# Development of anode catalysts for Proton Exchange Membrane Water Electrolyser

**A thesis submitted for the degree of**

**Doctor of Philosophy**

**by**


## Vinod Kumar Puthiyapura

**Supervisor: Prof. Keith Scott**




School of Chemical Engineering and Advanced Materials,

Newcastle University.

Newcastle Upon Tyne, United Kingdom.


March 2014

# Abstract

The proton exchange membrane water electrolyser (PEMWE) is a promising technology for the production of hydrogen from water. The oxygen evolution reaction (OER) has a high over potential cf. with the hydrogen evolution reaction and is one of the main reasons for the high energy demand of the electrolyser. $RuO_2$ and $IrO_2$ are the most active catalyst for OER, but are costly, making the electrolyser system expensive. In general, it is important to use stable, active and cheap catalysts in order to make a cost efficient electrolyser system. Supporting the active catalyst on a high surface area conducting support material is one of the approaches to reduce the precious metal loading on the electrode. Antimony tin oxide (ATO) and indium tin oxide (ITO) were studied as possible support materials for $IrO_2$ in the PEMWE anode prepared by the Adams method. The effect of the support material on the surface area, electronic conductivity, particle size and agglomeration were investigated. The $IrO_2$ showed highest conductivity (4.9 S $cm^{-1}$) and surface area (112 $m^2$ $g^{-1}$) and decreased with the decrease in the $IrO_2$ loading.

Using the catalysts in the membrane electrode assemblies (MEA) with Nafion®-115 membranes, at 80$^oC$ showed that the catalyst with better dispersion and conductivity gave better performance. The unsupported $IrO_2$ and 90% $IrO_2$ supported on ATO and ITO showed the best performance among all the catalysts tested, achieving a cell voltage of 1.73 V at 1 A $cm^{-2}$. A lower $IrO_2$ loading decreased the conductivity and surface area. The $IrO_2$ particle size and bulk conductivity of the supported catalyst significantly influenced the MEA performance. Overall, it is important to maintain a conductive network of $IrO_2$ on the non-conducting support to maintain the bulk conductivity and thus reduce the Ohmic potential drop.

Although $RuO_2$ is the most active catalyst for OER, it lacks stability on long term operation. $Ru_xNb_{1-x}O_2$ and $Ir_xNb_{1-x}O_2$ catalysts were synthesized and characterized, to try to develop stable electrodes for PEMWE. However the Adams method of catalyst synthesis formed a sodium–niobium complex making it unsuitable for preparation of Nb based catalysts. In both Adams and hydrolysis methods of synthesis, the addition of $Nb_2O_5$ decreased the anodic charge and electronic conductivity of the catalyst due to the dilution of the active $RuO_2$. The $RuO_2$ catalyst showed the best performance in MEA evaluation compared to the bimetallic catalyst (1.62 V and 1.75 V @1 A $cm^{-2}$ for

$RuO_2$(A) and $RuO_2$(H) respectively). A higher stability for bimetallic catalyst compared to the monometallic catalysts was obtained from the continuous CV cycling and MEA stability test.

# Acknowledgement

It has been a wonderful journey which is reaching an end. There are many without whom this thesis would have never finished. First of all I would like to express my sincere gratitude to my supervisor Prof. Keith Scott for all his guidance and support which helped me to finish the thesis on time. I also express my gratitude to EPSRC for the financial support for my PhD project.

I am deeply thankful to Dr. Mohammed Mamlouk (Moodie) for his invaluable help, support and guidance during all these three years. You have been a great mentor all these years. I am also grateful to all fuel cell group members- both past and present members- Dr. Senthil Kumar, Aris (Georgios), Xu Wu, Anca Dumitru, Asier, Ukrit (One), Ryan (Xu Wang), Georgina, Chenxi Xu (Paul), Ravikumar, Lei Xing (Chris), Luke Watkins, Terence (Xiaoteng Liu), Taiwo, Cao and Kemi for being such warm and friendly co-workers.

I would also like to express my sincere gratitude to Dr. Sivakumar Pasupathi and Prof. Bruno Pollet (HySA, University of Western Cape, South Africa) for their guidance and support during my stay in South Africa. Thanks to Huaneng Su, BJ Brown, Piotr Bujlo, Basheley and Joris for your help, support and fun at HySA. I cannot forget all the wonderful days in South Africa. I would like to express my sincere thanks and love to Sadiq Ali (Thirumeni), Ramesh Nepalli and Pritesh Sinha for making my stay in South Africa a memorable experience.

I would like to express my gratitude to Prof. Basu (IIT Delhi, India) for his supervision during my visit at IIT-Delhi, India. I am thankful to Varagunapandiyan, Pankaj Tiwari, Pawan kumar, Jyothsna Annepu, Rajalekshmi, Shashank sood and Sundar singh for their help and support during my stay at IIT-Delhi.

I am also thankful to all the technical and office staff at CEAM for their great support all these years. My special thanks to Maggie and Pauline Carrick for the XRD and SEM analysis.

Also, I would like to express my gratitude to all my dear friends in Newcastle who gave me wonderful memories in these 3 years of my life. Thanks Balamurugan, Abhijay Awasthi, Nutthapaon (Tom), Roney Joseph (Thirumeni), Vivek Dodduraj, Vineeth

Thoonoli, Nicolas (Nick), Ela, Simona Tibuloca, Rahul JP and Gayathri (Aishu). Thanks for all the fun!

I would also like to express my thanks to my dear friends for their support and for always being with me during the good and bad days. Thanks Jamsad Mannuthodukayyil, Midhun Chandran, Meera Mohan, Tharun Jose and Lishil Silvester (Arnold).

Finally, I would like to thank my parents and brother for all their love, support and encouragement during the hard days.

# Table of contents

# List of Figures

# List of Tables

# Symbols

| Symbol | Explanation | Section |
|---|---|---|
| $\eta_a$ | Anodic over potential | 1.4 |
| $\eta_c$ | Cathodic over potential | 1.4 |
| $\eta_{faradaic}$ | Faradaic efficiency of electrolysis | 1.4 |
| $\eta_{thermal}$ | Thermal efficiency of electrolysis | 1.4 |
| $\alpha$ | Transfer coefficient | 1.4 |
| $i_a$ | Anodic current | 1.4 |
| $i_c$ | Cathodic current | 1.4 |
| $i_o$ | Exchange current density | 1.4 |
| $d_{hkl}$ | Spacing between the lattice plane | 2.2.1 |
| θ | Peak position in XRD | 2.2.1 |
| λ | Wavelength of X-ray | 2.2.1 |
| β | Full width at half maximum | 2.2.1 |
| K | Shape factor of XRD spectral line | 2.2.1 |
| h | Planks constant | 2.2.2 |
| υ | Frequency of electromagnetic radiation | 2.2.2 |
| ϕ | Work function of the XPS instrument | 2.2.2 |
| ρ | Resistivity of the powder sample | 2.3.1 |
| σ | Conductivity of the powder sample/membrane | 2.3.1/2.3.4 |
| $i_p$ | Peak current in CV | 2.3.2 |
| D | Diffusion coefficient of the reactants | 2.3.2 |
| υ | Scan rate of CV | 2.3.2 |
| n | No of electrons transferred in the reaction | 2.3.2 |
| C | Capacitance | 2.3.2 |
| $C_\emptyset$ | Pseudo-capacitance | 2.3.2 |
| $C_{dl}$ | Double-layer capacitance | 2.3.2 |
| q* | Voltammetric charge | 2.3.2 |

# Abbreviations

| Abbreviation | Explanation |
|---|---|
| ATO | Antimony doped tin oxide |
| AWE | Alkaline water electrolyser |
| BA | Benzoic acid |
| BET | Brunauer-Emmet-Teller |
| BP | Boiling point |
| BSA | Benzene sulfonic acid |
| CCM | Catalyst coated membrane |
| CE | Counter electrode |
| CV | Cyclic voltammetry |
| DI water | De-ionised water |
| DMAc | Di-methyl acetamide |
| DMF | Di-methyl formamide |
| DSA | Dimensionally stable anode |
| EDX | Energy dispersive X-ray |
| HER | Hydrogen evolution reaction |
| HHV | High heating value of hydrogen |
| HOR | Hydrogen oxidation reaction |
| IP | Isopropanol |
| ITO | Indium tin oxide |
| LCD | Liquid crystal display |
| LHV | Low heating value of hydrogen |
| MEA | Membrane electrode assembly |
| MP | Melting point |
| MW | Molecular weight |
| OER | Oxygen evolution reaction |
| ORR | Oxygen reduction reaction |
| PA | Phosphoric acid |
| PAA | Phosphonoacetic acid |
| PAFC | Phosphoric acid fuel cell |

| | |
|---|---|
| PEMWE | Proton exchange membrane water electrolyser |
| PVD | Physical vapour deposition |
| RE | Reference electrode |
| SEM | Scanning electron microscopy |
| SOWE | Solid oxide water electrolyser |
| SPE | Solid proton exchange membrane |
| STP | Standard temperature and pressure |
| TEM | Transmission electron microscopy |
| TFMSA | Tri fluoro methane sulfonic acid |
| TGA | Thermo gravimetric analysis |
| WE | Working electrode |
| XPS | X-ray photoelectron spectroscopy |
| XRD | X-ray diffraction |
| YSZ | Yttria stabilised zirconia |

# Chapter-1. Introduction and objective

## 1.1 Hydrogen economy

Current energy demand of the world is mostly satisfied by fossil fuels. Fossil fuels are being burnt in order to use its energy content and a large portion of it is released to the atmosphere as waste heat making the process less efficient [1]. There are serious environmental consequences of fossil fuel combustion due to the greenhouse gas emissions such as $CO_x$, $NO_x$, $SO_x$, $C_nH_m$, ashes etc. [1, 2]. The global $CO_2$ emission has increased to about 30% after the industrial revolution due to the extensive use of fossil fuels [3]. Global petroleum reserves are also declining drastically and they are found only in certain parts of planet [1]. On the other hand, growth in the global population and industrial development, points towards high energy demand. This has led to the search for renewable energy sources such as wind energy, tidal energy, solar energy and geothermal energy as a possible alternate to fossil fuel based energy. One of the disadvantages with the renewable energy is that they have to match the supply with the demand and therefore energy storage is essential [4]. Batteries are one option for energy storage, however high cost for large storage requirements and loss of charge over time are the disadvantages of battery storage [4]. Hydrogen has been proposed as a suitable energy storage medium. Hydrogen ($H_2$) is one of the cleanest fuels available and emits nothing but only water on combustion. Hydrogen is proposed to play an important role in the future energy scenario to form a sustainable energy carrier [1, 2, 5].

$H_2$ is one of the lightest, simplest and most abundant elements in nature. However, it is invariably connected with other elements (mainly with carbon and oxygen) as different compounds and energy has to be applied to produce the molecular $H_2$. Hydrocarbons and water are the two major sources of $H_2$ on earth. Current $H_2$ production is mainly dominated by reforming hydrocarbons which have drawbacks as mentioned before. Electrolysis of water on the other hand is one of the most sustainable ways of hydrogen production when electricity from the renewable energy is used. However, currently only 4% of $H_2$ is produced by water electrolysis [6]. Hydrogen electrolysis generally uses electricity from the power grids which is produced by fossil fuel combustion, making the process expensive and eco-hostile. Using renewable energy as electricity instead of fossil fuel based electricity is the way towards a green and eco-friendly electrolytic hydrogen production. Whenever excess electricity is available from renewable energy

sources, it can be converted to $H_2$ by electrolysis and can be stored for further use. When electricity is not available, the so produced $H_2$ can be used in a fuel cell (which convert chemical energy of hydrogen to electrical energy) to generate electricity. This whole concept of energy cycle is known as hydrogen economy as given in Figure 1-1 [5, 7]. However such scenario requires large scale hydrogen production by water electrolysis in a sustainable way and the technology should be energy efficient and inexpensive.

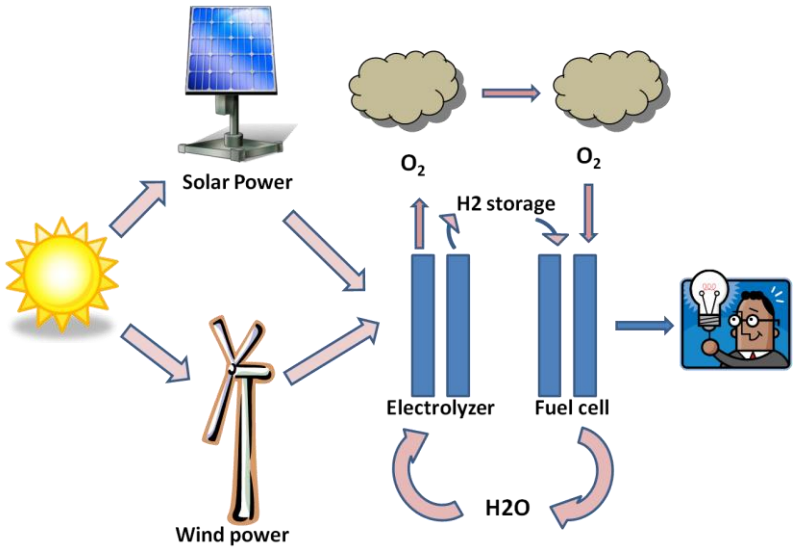


*Figure 1-1. Concept of hydrogen economy [7]. Reproduced with permission from John Wiley and Sons.*

Since the electrolytically produced hydrogen is much expensive than that derived from fossil fuels, electrolytic hydrogen is used only in very few areas such as food industry and electronics-semiconductor industry [8].

## 1.2 **Hydrogen production.**

Hydrogen is not a natural source like petroleum and so energy such as heat or electricity has to be applied to get molecular hydrogen [9]. $H_2$ is thus an energy carrier/energy storage medium like electricity but do not contain carbon and generate little or no pollutants at the point of use [9, 10]. Even though there is a need for hydrogen for various industries such as petroleum refining, ammonia production, metal refining, the current industrial hydrogen production is limited to steam reforming of natural gas and petroleum [11]. Hydrogen production mainly falls into three categories; thermal process, electrolytic process and photolytic process [12].

### 1.2.1 **Thermal process of hydrogen production**

Thermal process is the conventional and widely used method for the production of hydrogen known as reforming. Approximately 96% of the global hydrogen is produced by reforming. Fossil fuel is burnt to produce hydrogen in this process. The fossil fuel can be natural gas, coal or oil. Reforming produces a gas stream composed of mainly hydrogen, carbon dioxide and carbon monoxide. There are 3 major reforming process for $H_2$ production - steam reforming (SR), partial oxidation (POX) and auto thermal reforming (ATR) [12, 13]. The general reaction for these processes are given in the equation *(1-1)* to *(1-3)* [12].

| | | |
|---|---|---|
| **SR** | $C_mH_n + mH_2O \rightarrow mCO + (m + \frac{1}{2}n)H_2$ | *(1-1)* |
| **POX** | $C_mH_n + \frac{1}{2}mO_2 \rightarrow mCO + \frac{1}{2}H_2$ | *(1-2)* |
| **ATR** | $C_mH_n + \frac{1}{2}mH_2O + \frac{1}{4}mO_2 \rightarrow mCO + (\frac{1}{2}m + \frac{1}{2}n)H_2$ | *(1-3)* |

SR is the most widely used technology. It has advantages of high efficiency and lower operational and product cost [13]. SR does not require oxygen and has low operating temperature than ATR and POX, and have a high $H_2$/CO ratio [12]. SR is a two stage process. In the first stage the hydrocarbon is reacted with steam in the presence of catalyst (Ni oxide based) to form syn gas (CO + $H_2$). In the second stage, the CO produced is reacted with steam to form $CO_2$ and $H_2$ (water gas shift reaction) in the presence of an active copper catalyst as given in equation *(1-4)* increasing the overall $H_2$ yield [13, 14].

$$CO + H_2O \rightarrow CO_2 + H_2 \qquad (1\text{-}4)$$

POX converts hydrocarbon to hydrogen by partial oxidation with oxygen. It is a non-catalytic process and in comparison to SR, more CO is produced [13]. ATR is also similar to POX with an addition of steam. The heat from POX reduces the need for an external heat source [13]. The three processes are compared in Table 1-1. The current major contributor to $H_2$ production are the steam reforming of natural gas (~ 48%), coal (30%) and oil (~ 18%) [1, 6]. Since all three processes produce large amount of CO, it is an eco-hostile and non-sustainable process.

Pyrolysis involves the heating of organic material at a temperature of 500-900$^{o}$C in the absence of oxygen and air to give $H_2$ as given in equation *(1-5*) [12]. Since no oxygen is used, the emission of CO and $CO_2$ is negligible in this process.

$$C_nH_m \rightarrow nC + \frac{1}{2}mH_2 \qquad (1\text{-}5)$$

Coal gasification is another method where coal is heated up to 1800$^{o}$C with an oxidant to produce syngas. The syngas is then subjected to water gas shift reaction to get $H_2$ [14].

*Table 1-1.Comparison of different reforming technologies [12].*

| Technology | Advantage | Disadvantage |
|---|---|---|
| **Steam reforming** | Most extensive industrial experience,<br>Oxygen not required<br>Lowest process temperature<br>Best $H_2$/CO ratio for $H_2$ production | Highest air emissions |
| **Partial oxidation** | Lower process temperature than POX<br>Low methane slip | Limited commercial experience<br>Requires air or oxygen |
| **Auto thermal reforming** | Decreased desulfurization requirement<br>No catalyst required<br>Low methane slip | Low $H_2$/CO ratio<br>Very high processing temperatures<br>Soot formation/handling adds process complexity |

### 1.2.2 **Photolytic hydrogen production**

Photoelectrolysis uses semiconductor photo electrodes to absorb sunlight and produce the necessary voltage for the decomposition of water to $H_2$ and $O_2$ [12, 13, 15, 16]. Currently it is the most effective way to produce hydrogen from renewable energy sources. However the overall efficiency of the process is still lower than other hydrogen production methods. To achieve low-cost and efficient solar hydrogen energy production requires development of innovative materials, emerging physical phenomena, novel synthetic techniques and entirely new design concepts [9].

### 1.2.3 **Electrolytic hydrogen production**

About 96% of hydrogen currently produced by hydrocarbon reforming as mentioned before which produce greenhouse gases like CO and $CO_2$ [12]. Although several technologies have been used to produce hydrogen, water electrolyser is the most

sustainable one when electricity from renewable sources like wind energy and solar energy are used [1, 5, 14, 17, 18]. Currently water electrolysis contributes only 4% of overall hydrogen production [19, 20] and are mainly used for applications where large scale $H_2$ production is not possible and pure $H_2$ is required, such as marine, rockets, space crafts, electronic and food industries [11]. Water electrolysis has the advantages such as no carbon emission, very pure hydrogen, no dependence on hydrocarbon sources, simple small scale/real time hydrogen supply, utilisation of renewable primary energy sources, storage of renewable primary energy sources and pure oxygen as by-product [21]. The production cost of hydrogen to a large extent is affected by electric power consumption, which can be about 70% of the total $H_2$ production costs [22]. Overall efficiency improvement as well as cost reduction has to be achieved to make water electrolyser commercially viable.

## 1.3 History of water electrolysis

History of water electrolysis dates back to the discovery of hydrogen. British Scientist Henry Cavendish (1731-1810) first proposed the presence of an 'inflammable gas' in the air. He produced hydrogen by the reaction of zinc metal with hydrochloric acid and also proved that hydrogen is much lighter than the air. In 1783 Jacques Alexander Charles first launched the hydrogen balloon and flew at an altitude of 3 km. In 1785, Lavoisier repeated Cavendish's experiments and proved that water is not an element but a compound composed of $H_2$ and $O_2$. He produced $H_2$ and $O_2$ from water by heating it in a copper tube. Lavoisier coined the name hydrogen from two Greek word hydro (water) and genes (born of). Because of the lack of current sources, early year's hydrogen was produced by the reaction of metal with acid. The first application of hydrogen was not as fuel, but for hot air balloon [23, 24].

In 1800, William Nicholson and Anthony Carlisle first electrolysed water to produce hydrogen and oxygen. Water was the first substance to be electrolysed. In 1845 William Grove first demonstrated the concept of fuel cell to produce electricity from hydrogen and oxygen and is considered as the 'father of the fuel cell'. By 1902 more than 400 industrial water electrolyser were in operation and in 1939 the first large water electrolysis plant with a capacity of 10,000 $Nm^3H_2h^{-1}$ went into operation and in 1948 the first pressurized industrial electrolyser by Zdansky/Lonza was built [25]. The year 1920-1970 are known as the "golden period" for water electrolyser technology as most of the traditional electrolyser design were introduced in this stage [11]. After the energy

crisis in 1970's hydrogen was proposed as promising alternate fuel and water electrolyser received immense interest and significant researches were dedicated to improve the efficiency of the electrolytic hydrogen production [11]. The major landmarks in the development of electrolyser are tabulated in Table 1-2 [23, 24]. Major commercial electrolyser manufacturers and their hydrogen production capacity are given in appendix 8.7.

*Table 1-2. Major landmarks in the development of water electrolyser technology.*

| Year | Landmark event | Reference |
|---|---|---|
| **1766** | Discovery of hydrogen by Cavendish | [23] |
| **1785** | $H_2$ and $O_2$ separated from water by chemical reaction by Lavoisier | [23] |
| **1800** | Nicholson and Carlisle discovered electrolysis of water | [25] |
| **1920** | Several large 100 MW size plants were built | [11, 25] |
| **1939** | First large electrolysis plant went into operation<br>-capacity 10,000 $Nm^3H_2h^{-1}$ | [25] |
| **1948** | First pressurised electrolyser plant was built by Zdansky/Lonza | [11, 26] |
| **1966** | First SPE electrolyser was built by General Electric | [11, 25] |
| **1970** | First solid oxide water electrolyser | [11, 25] |
| **1980s** | Aswan installed electrolyser with 162 MW capacity and hydrogen generation capacity of 32,400 $m^3h^{-1}$ | [26] |

## 1.4 Theory of water electrolysis

A water electrolyser is a device which converts electrical energy to chemical energy which is achieved by passing current through water. Since water is a very stable compound, splitting of water requires a supply of energy. The total energy required to split water molecule is given by the enthalpy of formation of water ($\Delta H$).

At standard temperature and pressure, STP (298.15 K and 1 atm pressure), the enthalpy change, $\Delta H^o = 286\ kJmol^{-1}$ based on the higher heating value of hydrogen (HHV) as given by equation (1-6), free energy change, $\Delta G^o = 237.2\ kJmol^{-1}$ and entropy change, $\Delta S^o = 0.163\ kJmol^{-1}K^{-1}$ [27]. If steam is used instead of liquid water, lower heating value (LHV) of hydrogen should be used. i.e. $242\ kJ\ mol^{-1}$ (equation (1-7)) [28].

$$H_2O(l) \rightarrow \frac{1}{2}O_2(g) + H_2(g);\ \Delta H^o = 286\ kJ\ mol^{-1} \qquad (1\text{-}6)$$

$$H_2O(g) \rightarrow \frac{1}{2}O_2(g) + H_2(g);\ \Delta H^o = 242\ kJ\ mol^{-1} \qquad (1\text{-}7)$$

The difference between HHV and LHV is due to the enthalpy of vaporisation of water. For all chemical reaction a part of energy will be used for entropy change ($\Delta S$) which is related to the free energy change of reaction and enthalpy by the equation (1-8).

$$\Delta G = \Delta H - T\Delta S \qquad (1\text{-}8)$$

The difference between enthalpy change and free energy change gives the entropy change term ($T\Delta S$) [29].

$$T\Delta S^o = \Delta H^o - \Delta G^o = 285.83 - 238 = 47\ kJ\ mol^{-1} \qquad (1\text{-}9)$$

i.e. $47\ kJ\ mol^{-1}$ of energy will be used for entropy change during water splitting at STP. This energy will be spontaneously absorbed from the surroundings. So the total energy need to supply as electricity is $\Delta G^o$ ($237.2\ kJ\ mol^{-1}$) (equation (1-10)).

$$H_2O + electrical\ energy\ (\Delta G) + heat(T\Delta S) \rightarrow H_2 + \frac{1}{2}O_2 \qquad (1\text{-}10)$$

At STP, the amount of electricity required to split water is given by the equation *(1-11)*.

$$E^o = \frac{\Delta G^o}{nF} \qquad (1\text{-}11)$$

Where $E^o$ is equilibrium or reversible cell potential (the minimum voltage required to split water) which is obtained by subtracting the equilibrium potential of anode and cathode reaction (equation *(1-12)*), $n$ is the number of electrons transferred per mole of $H_2$ (n = 2), $F$ is the faradays constant ($96485\ C\ mol^{-1}$). Substituting the respective values in equation *(1-11)*, a potential of 1.23 V is obtained (equation *(1-13)*).

$$E^o = E^o_{anode} - E^o_{cathode} \qquad (1\text{-}12)$$

$$E^o = \frac{237.2\ kJ\ mol^{-1}}{2 \times 96485\ C\ mol^{-1}} = \mathbf{1.23\ V} \qquad (1\text{-}13)$$

In an isolated system, it is necessary to apply thermo-neutral potential ($E^o_{th}$) of 1.48 V in order to satisfy the thermodynamic requirement [29] as given by equation *(1-14)*.

$$E^o_{th} = \frac{\Delta H}{nF} = \frac{285.8\ kJ\ mol^{-1}}{2 \times 96485\ C\ mol^{-1}} = \mathbf{1.48\ V} \qquad (1\text{-}14)$$

i.e. at potential of 1.48 V, no heat exchange occur with the surroundings (thus the term thermoneutral). Below and above 1.48 V the reaction will be endothermic and exothermic respectively (Figure 1-2). Since most real electrolyser operate at potential greater than the $E^o_{th}$, an excess of heat is always produced in the cell which heats up the cell. The dependence of reversible potential ($E_{rev}$) on temperature without the pressure effect can be written as in *(1-15)* [30-34].

$$E_{rev} = 1.5184 - 1.5421 \times 10^{-3}T + 9.523 \times 10^{-5}T\ ln\ T + 9.84 \times 10^{-8}T^2 \qquad (1\text{-}15)$$

The efficiency of the water electrolyser is defined as the ratio of the total energy input to the total energy output [35]. The energy input can either be taken the free energy change of the reaction ($\Delta G$) or as the enthalpy change of the reaction ($\Delta H$) and thus two efficiency terms are defined such as faradaic efficiency ($\eta_{faradaic}$) and thermal efficiency ($\eta_{thermal}$) respectively [11, 26]. The two efficiency terms can be defined as in equation *(1-16)* and *(1-17)* where $E_{cell}$ is the cell voltage, $E_{\Delta G}$ and $E_{\Delta H}$ are the reversible cell voltage and thermo neutral voltage respectively [11].

$$\eta_{faradaic} = \frac{E_{\Delta G}}{E_{cell}} \qquad (1\text{-}16)$$

$$\eta_{thermal} = \frac{E_{\Delta H}}{E_{cell}} \qquad (1\text{-}17)$$

At 25$^{o}$C, the efficiencies can be written as in *(1-18*) and *(1-19*).

$$\eta_{faradaic} = \frac{1.23\ V}{E_{cell}} \qquad (1\text{-}18)$$

$$\eta_{thermal} = \frac{1.48\ V}{E_{cell}} \qquad (1\text{-}19)$$

When a current is passed through an electrolysis cell to produce hydrogen, the cell voltage increase with resepct to $E_{rev}$ due to the irreversibilities such as over potential for the electrode reaction and ohmic resistance losses. The electrolysis cell voltage thus can be attributed to addition of various voltage losses occur in the cell as given in (1-20) [27].

$$E_{cell} = E_{rev} + E_{ohm} + E_{act} + E_{con} \qquad (1\text{-}20)$$

Where $E_{rev}$ is the thermodynamic reversible cell potential, $E_{ohm}$ is the voltage loss due to the various ohmic resistance (electrode,electrolyte,current collectors, interconnections etc.) to the electron flow. $E_{ohm}$ varies linearly with the current flowing through the cell. $E_{act}$ is the activation overvoltage due to the electrode kinetics (activation energy required for the reaction to occur). $E_{con}$ is the concentration overpotential caused by the mass transport processes (convection and diffusion). Transport limitation reduces the reactant concentration at the electrode/electrolyte interface. Usually $E_{con}$ is much lower than that of $E_{act}$ and $E_{ohm}$ [27].

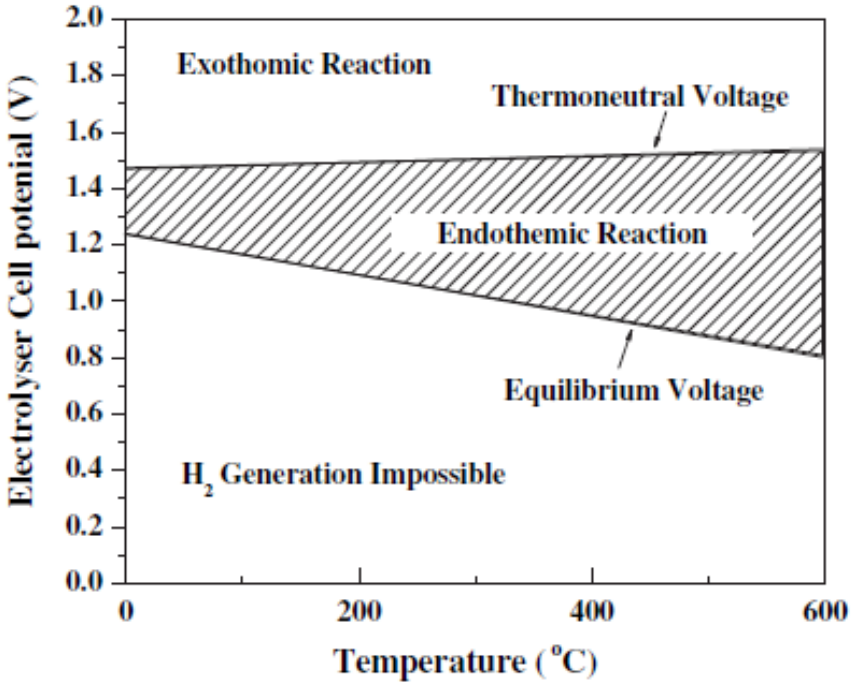


*Figure 1-2. Cell potential for $H_2$ production as a function of temperature [11].*

*Reproduced with permission from Elsevier.*

For a general electrochemical reaction,

$$O + ne^- \rightarrow R \qquad (1\text{-}21)$$

Gibbs free energy is given by equation (1-22)

$$\Delta G = \Delta G^o + RTlnQ = \Delta G^o + RTln\frac{[R]}{[O]} \qquad (1\text{-}22)$$

Where Q= reaction quotient, (at equilibrium Q=K, the equilibrium constant)

Since $\Delta G$ related to the potential by the equation (1-23), substituting in equation (1-22) gives Nernst equation for the reaction as given in (1-24).

$$\Delta G = -nFE \qquad (1\text{-}23)$$

$$E_{rev} = E^o + RTln\frac{[O]}{[R]} \qquad (1\text{-}24)$$

At equilibrium, anodic current $i_a$ and cathodic current $i_c$ are equal in magnitude and is called exchange current density $i_o$. At potential different from $E_{rev}$, the current can be calculated by using butler-volmer equation *(1-25*) [36].

$$i = i_o \left\{ \exp\left(\frac{-\alpha n F \eta_a}{RT}\right) - \exp\left(\frac{(1-\alpha) n F \eta_c}{RT}\right) \right\} \qquad (1\text{-}25)$$

Where $i$ is the current, $i_o$ is the exchange current density, $\alpha$ is the transfer coefficient, n is the number of electron transferred and $\eta_a$ and $\eta_c$ are the anodic and cathodic over potentials respectively. The transfer coefficient may be regarded as the fraction of over potential that leads to a change in the rate constant for the electron transfer and in general the value is taken as 0.5 [26]. At equilibrium condition ($i = 0$), butler-volmer equation reduces to Nernst equation [36].

Tafel slopes are derived from butler-volmer equation by considering anodic and cathodic current as negligible at high over potential for the cathodic and anodic reaction respectively [36].

$$\eta = \frac{2.303RT}{(1-\alpha)nF} log\ \frac{i_c}{i_o} = b_a log \frac{i_c}{i_o} \qquad (1\text{-}26)$$

$$\eta = \frac{2.303RT}{\alpha nF} log \frac{i_a}{i_o} = b_c log \frac{i_a}{i_o} \qquad (1\text{-}27)$$

Where *(1-26*) is the cathodic tafel equation and *(1-27*) is the anodic tafel equation. The slope of the linear plot between $\eta$ and $log\ i$ is called tafel slope ($b_a$ and $b_c$). The rate determining step of the reaction pathway can be determined from the tafel slope calculation (Table 1-5). More detailed discussion on the thermodynamics and kinetics of water electrolysis are available in literature [26, 30, 31, 35, 37, 38].

## 1.5 Types of water electrolysers

Depending upon the electrolyte used in the system, there are three main types of electrolysers (i) alkaline water electrolyser (AWE) (ii) solid oxide water electrolyser (SOWE) and (iii) proton exchange membrane water electrolyser (PEMWE).

### 1.5.1 Alkaline water electrolyser

Hydrogen production by alkaline electrolysis is a commercially well-established technology. Traditional alkaline electrolysers are based on the liquid alkaline electrolyte. All standard commercial alkaline electrolyser uses 30 wt.% KOH as the

electrolyte (due to the high conductivity of this composition) and operate at a typical current density of about < 0.4 A $cm^{-2}$ at moderate temperature of 70-90$^{o}$C with a cell voltage ranges from 1.85-2.2 V and conversion efficiencies range from 60-80% [27, 39]. For high temperature >120$^{o}$C, the electrolyte concentration may increase up to 40-47 wt.% above which the electrolyte solidifies [39]. Considering the practical aspect of hydrogen economy a much higher current density is required. Ni and Co based oxides are used as the cathode and the anode electrode respectively. Normal steels are used as cell construction materials [39]. The key factors favouring the alkaline electrolyser are that it obviates the need for expensive platinum-based catalysts; it is well proven at large scale and is usually of lower unit cost than a PEM electrolyser. The schematic of alkaline electrolyser is given in Figure 1-3 and the reaction occurring is given by the equations *(1-28*), *(1-29*) and *(1-30*).

Cathode $$2H_2O + 2e^- \rightarrow H_2 + 2OH^- \ (E^o = -0.83V \ vs. SHE) \qquad (1\text{-}28)$$

Anode $$2OH^- \rightarrow \frac{1}{2}O_2 + H_2O + 2e^- (E^o = 0.40 \ V \ vs. SHE) \qquad (1\text{-}29)$$

Net reaction $$H_2O \rightarrow \frac{1}{2}O_2 + H_2 \ (E^o = 1.23 \ V \ vs. SHE) \qquad (1\text{-}30)$$

A limitation of the alkaline electrolyser is that temperature of operation is less than 100$^{o}$C in order to avoid a strong increase in alkali corrosion of electrodes [40]. KOH electrolyte may react with $CO_2$ in the atmosphere to form carbonates and is a major drawback in an alkaline system. Conventional water electrolyser uses liquid alkaline solution, whereas an $OH^-$ ion conducting membranes is used in modern alkaline electrolysers (lab scale) [29]. But the current density associated with such alkaline membranes are still low (max. 1 A $cm^{-2}$) compared to Nafion® [29]. Significant improvement is still required in the development of anion exchange membrane based electrolyser.

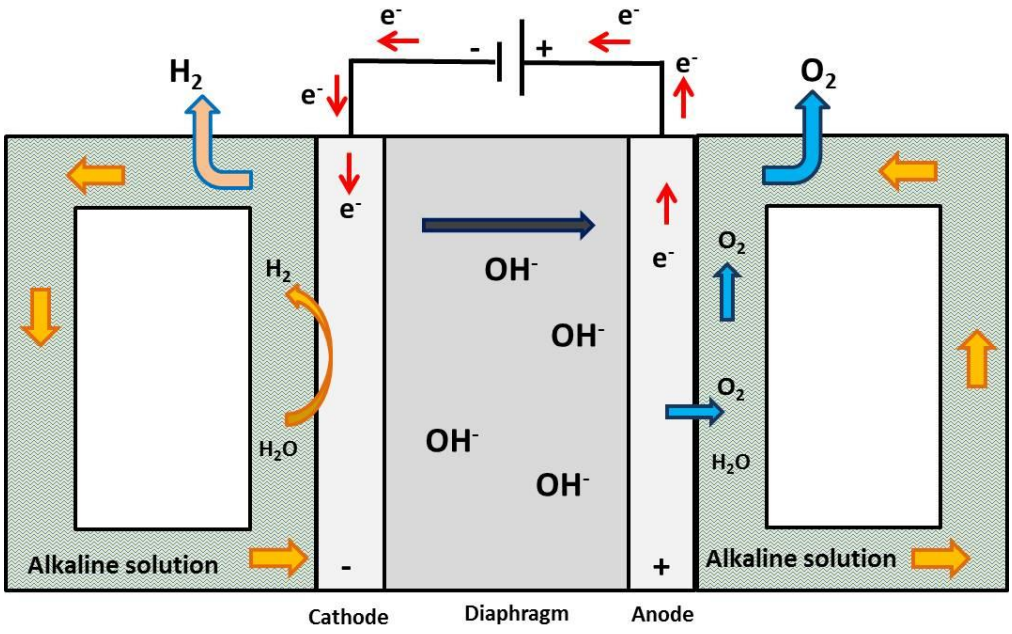


*Figure 1-3. Schematic of alkaline water electrolyser.*

### 1.5.2 **Solid oxide water electrolyser**

Solid oxide water (steam) electrolyser (SOWE) operates at high temperature ($600^{o}$-$900^{o}$C) range, which results in higher efficiency compared to alkaline and PEM water electrolysers. In solid oxide electrolyser steam is passed through the cathode side of the cell which split to form $H_2$ and $O^{2-}$ ion. The $O^{2-}$ ion is passed through a ceramic electrolyte to the anode side and $O_2$ is produced on the anode side as given by equations (1-31), (1-32) and (1-33). A schematic of SOWE is given in Figure 1-4. SOWE typically use yttria ($Y_2O_3$) stabilised zirconia ($ZrO_2$) (YSZ) as a solid oxide electrolyte. Since water electrolysis is endothermic with increase in temperature, the electrical energy demand at high temperature is low as the unavoidable joule heat produced is used in the $H_2O$ splitting process [4]. However high heat demand, thermal stability of materials and sealing issues still remain a challenge. Also the requirement of additional facilities to separate the hydrogen from the steam makes the overall system expensive [27]. A review of recent development of solid oxide water electrolyser is available with Ma et al [41]. SOWE will be beneficial as part of a combined heat and power (CHP) generation as the excess heat generated from many industries can be utilized in SOWE [42].

Cathode $H_2O + 2e^- \rightarrow H_2 + O^{2-}$ *(1-31)*

Anode $O^{2-} \rightarrow \frac{1}{2}O_2 + 2e^-$ *(1-32)*

Net reaction $2H_2O \rightarrow 2H_2 + O_2$ *(1-33)*

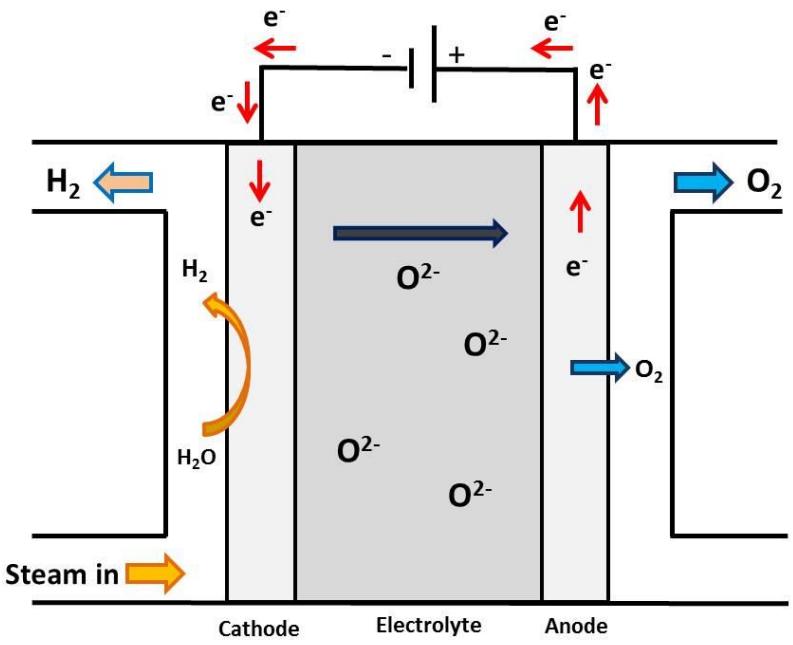


*Figure 1-4. Schematic of solid oxide water electrolysis cell for the electrolysis of steam.*

### 1.5.3 **Proton exchange membrane water electrolyser**

The introduction of per-fluorinated cation exchange membrane led to the development of PEMWE by General electric Co. in 1966 [17, 18, 43, 44] and it is considered as the most attractive and efficient method for the production of $H_2$ from water at low temperature [17]. PEMWE can operate at current density >1.5 A $cm^{-2}$, quite higher than alkaline counterpart [27].

A PEMWE consists of an anode, cathode and electrolyte (proton conducting membrane). The anode and cathode are normally bonded to the membrane electrolyte and is called a membrane electrode assembly (MEA). De-ionised water (DI water) is supplied to the anode where it splits into proton, electron and oxygen in the presence of a catalyst. The proton moves through the proton exchange membrane (PEM) to the cathode and electrons through the external circuit. Proton accepts electrons from the cathode side to produce $H_2$ whereas oxygen is evolved on the anode side [45, 46]. The

overall reaction is the splitting of 2 moles of water to produce 2 moles of $H_2$ and one mole of oxygen as given in equation (1-34), (1-35) and (1-36).

Anode $$2H_2O \rightarrow 4H^+ + O_2 + 4e^- \quad (1\text{-}34)$$

Cathode $$4H^+ + 4e^- \rightarrow 2H_2 \quad (1\text{-}35)$$

Net reaction $$2H_2O \rightarrow 2H_2 + O_2 \quad (1\text{-}36)$$

PEMWE has several advantages compared to the conventional alkaline electrolyser such as ecological cleanness, higher production rate, smaller mass to volume ratio, high power density, low power cost, high gas purity, and high level of safety [18]. Even though the working of PEMWE is just the reverse of proton exchange membrane fuel cell (PEMFC), commonly used materials in PEMFC such as carbon catalyst support, porous electrode structures (carbon fibre paper or carbon cloth) and graphite bi-polar plates cannot be used on the anode side of a PEMWE due to their corrosion [46]. The early stage PEMWE had very short life span but the introduction of Nafion® as PEM by DuPont has given higher lifetime to SPE electrolyser [44]. Nafion® is a per-fluorinated acid membrane consisting of sulfonic acid end group with acidity similar to that of 10-20 wt.% sulphuric acid solution [8, 47]. This acidic behaviour limits the use of only noble metal as the catalyst in PEM electrolyser, though it has the advantage of lower Ohmic resistance and compact design. However state of the art PEMWE has disadvantages such as high over-potential for oxygen evolution reaction (OER) and material component cost (PEM, bipolar plates and electrocatalysts).

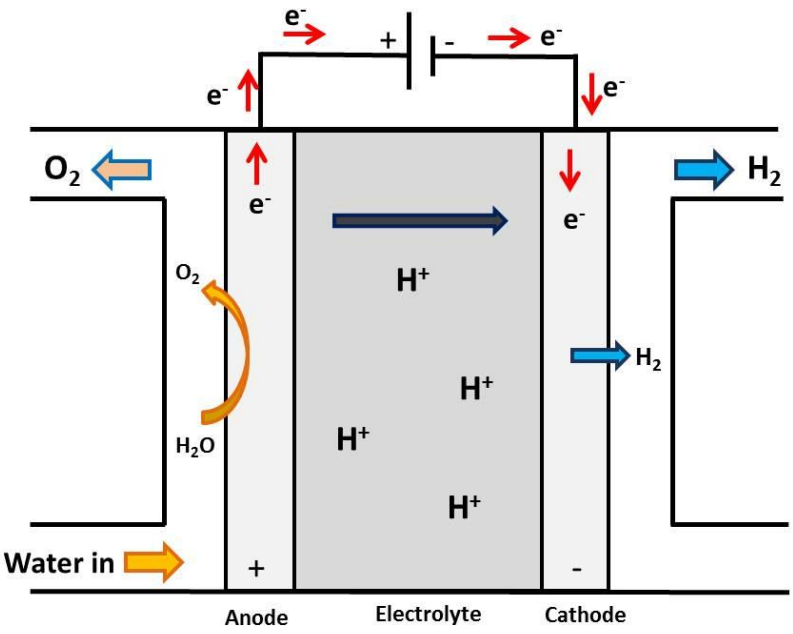


*Figure 1-5. Schematic of PEM water electrolyser*

The state of the art PEM water electrolyser operates at a temperature of 80$^{o}$C due to the possible dehydration of the Nafion® membrane at temperature ≥ 100$^{o}$C at atmospheric pressure. Recently, high temperature operation of electrolyser is also getting interest due to the advantages such as fast electrode kinetics, lower thermodynamic voltage, better utilization of waste heat and simplification of the cooling system [48-51]. Highly corrosion resistant materials are required for high temperature electrolyser operation [52].

Due to the poor efficiency and lower current density of commercial electrolyser, the cost of electrolytic $H_2$ is very high and it is currently being used in very few industries such as semiconductor and food industries where a high purity $H_2$ is required [8]. Current research in PEMWE is mainly focused on the development of (i) low cost membranes alternate to Nafion® (ii) low cost, stable and active OER catalysts (iii) high temperature PEMWE (iv) alkaline anion exchange membrane water electrolyser. Different types of electrolyser components are summarised in Table 1-3 and the advantages and disadvantages of the three types of electrolysers are compared in Table 1-4.

*Table 1-3. Different types of water electrolyser and their specifications [53].*

| Type | Alkaline | Acid | Polymer electrolyte | Solid-oxide |
|---|---|---|---|---|
| **Charge carrier** | $OH^-$ | $H^+$ | $H^+$ | $O^{2-}$ |
| **Reactant** | water | water | water | water, $CO_2$ |
| **Electrolyte** | NaOH or KOH | $H_2SO_4$ or $H_3PO_4$ | Polymer (e.g.: Nafion) | Ceramic |
| **Electrode** | Nickel | Graphite with Pt, polymer | Graphite with Pt, polymer | Nickel, ceramics |
| **Temperature** | 80°C | 150°C | 80°C | 850°C |

*Table 1-4. Advantages and disadvantages of the three electrolyser systems [54].*

| Alkaline electrolyser | PEM water electrolyser | Solid oxide electrolyser |
|---|---|---|
| | **Advantages** | |
| Well established technology | High current densities | Efficiency up to 100% range |
| Non-noble catalysts | High voltage efficiencies | Thermo neutral efficiency > 100% with hot steam |
| Long term stability | Good partial load range | Non-noble metal catalysts |
| Relatively low cost | Rapid system response | High pressure operation |
| Stacks in MW rang | Compact system design | |
| Cost effective | High gas purity | |
| | Dynamic operation | |
| | **Disadvantages** | |
| Low current densities | High cost of components | Laboratory stage |
| Cross over of gases(degree of purity) | Acidic corrosive atmosphere | Bulky system design |
| Low partial load range | Possibly low durability | Durability (brittle ceramics) |
| Low dynamics | Noble metal catalysts | No dependable cost information |
| Low operational pressure | Commercialisation | |
| Corrosive liquid electrolyte | Stacks below MW range | |

## 1.6 Electrocatalysts for PEMWE

Even though the thermodynamic potential for water electrolysis is 1.23 V, the kinetics of the reaction restricts the reaction to happen at this potential. An extra potential called over potential has to be applied for the reaction to occur (Figure 1-6). The over potential depends on the catalytic material used. i.e. electrocatalyst has to be chosen in such a way to give low over potential [55]. Both hydrogen evolution reaction (HER) and oxygen evolution reaction (OER) requires catalyst for the respective reaction to occur. Since HER is faster than OER, most of the over-potential loss in PEM electrolyser occurs on the anode side. Catalysts used for hydrogen oxidation reaction (HOR) such as Pt black, carbon supported Pt are used on the cathode side for HER.

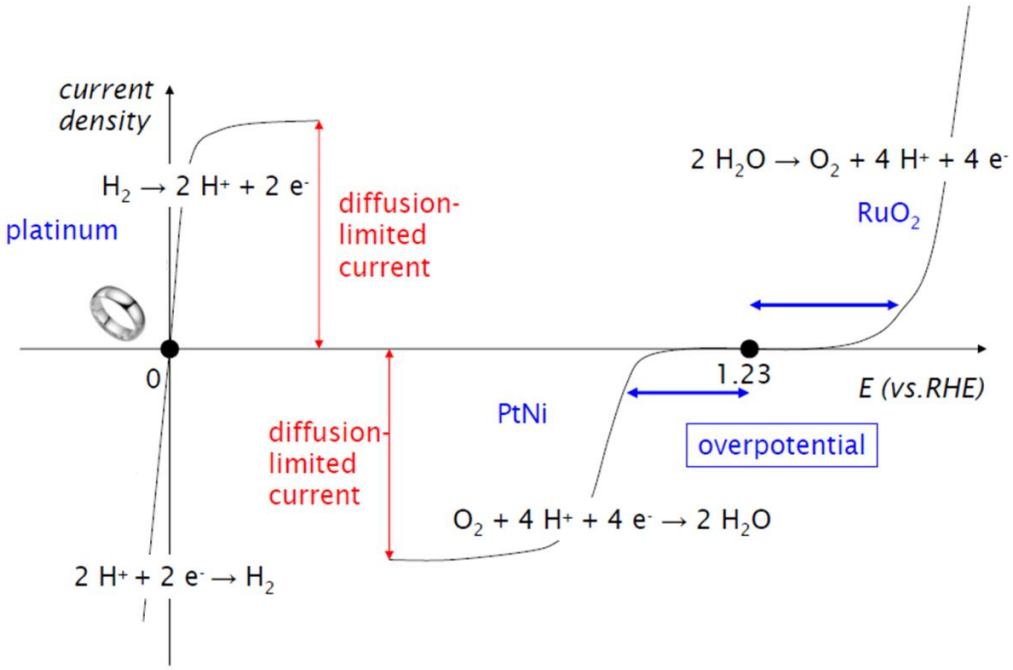


*Figure 1-6. Schematic of redox reaction of water [56]. Reproduced with permission from John Wiley & Sons,Inc.*

### 1.6.1 Oxygen evolution reaction (OER)

Oxygen evolution occurs on noble metal catalyst (e.g: Pt, Au, Ir, Rh, Ru, Ag). But it was found that evolution occurs only at potential higher than the standard oxidation potential of metal/metal-oxide or lower metal-oxide/higher metal-oxide couple [57, 58]. i.e. oxygen evolution from a metal surface occurs only after the oxidation of the metal surface and related to metal/metal oxide couple [57]. Since metal-oxygen bond (M-O) is always stronger than oxygen-oxygen(O-O) bond, OER always takes place on an oxide

surface [58, 59]. So it has been concluded that metal oxides are more active for OER than metal [60]. Because of the acidic environment and high anode potential during water electrolysis in PEMWE, non-noble catalytic metals like Ni and Co cannot be used on the PEMWE anode due to the corrosion [61]. Pt is also not suitable on the anode due to the formation of non-conducting PtO film [43]. The electrocatalytic activity of the oxides to a first approximation can be expressed in terms of the bond strength between the intermediates and the catalyst surface [62]. During oxygen evolution reaction, bonds between the surface metal ion and the oxygenated species are broken and formed. Since the oxidation state of the metal changes during the oxygen evolution, the enthalpy change in the transition of lower oxide to higher oxide ($\Delta H_t^o$) is correlated with the over potential for OER and a volcano shaped plot is obtained as given in Figure 1-7 [62, 63]. Oxides with intermediate $\Delta H_t^o$ value shows the highest catalytic activity for OER. Oxides which are oxidized too easily are not active as the intermediates adsorb too strongly. Oxides which are difficult to oxidize are also not active as the intermediates adsorb too weakly [62, 64]. Rutile type oxides $RuO_2$ and $IrO_2$ shows intermediate $\Delta H_t^o$ value and were found to be suitable catalyst for OER and they also have good electronic conductivity and chemical stability [64, 65]. Due to the high activity of $RuO_2$ for $O_2$ and $Cl_2$ evolution reaction 46% of the world's Ru production is used in chlor-alkali industry as dimensionally stable anode (DSA) electrode [66]. Ruthenium is relatively less expensive than Pt and $IrO_2$, but its corrosion on oxidation condition due to dissolution of $RuO_2$ and loss of inherent catalytic activity makes it unsuitable for practical electrolyser [67].

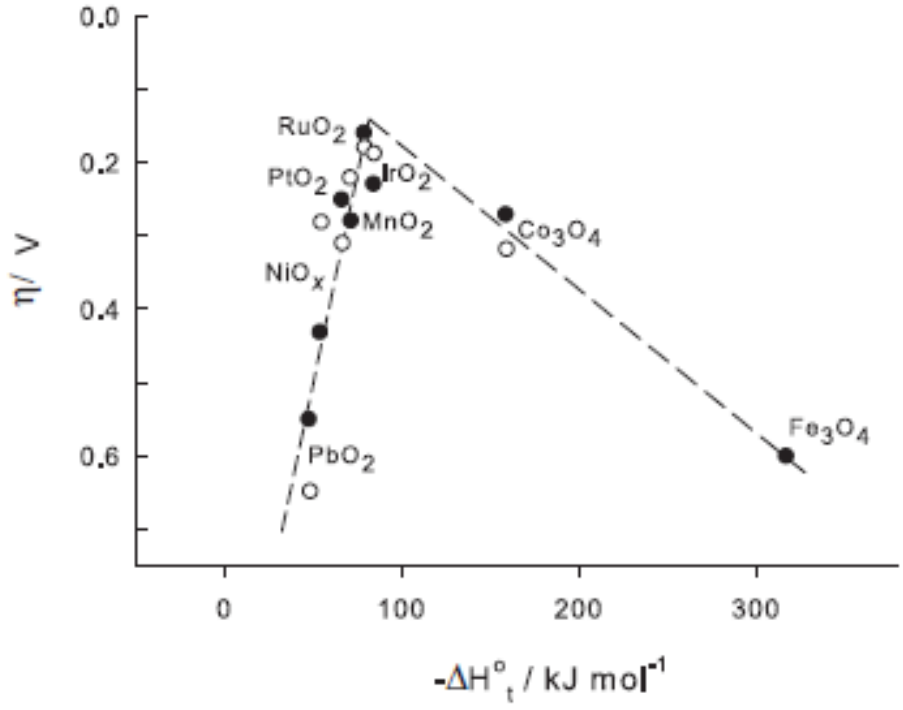


*Figure 1-7. Electrocatalytic activity of oxygen evolution reacion on various oxides as a function of enthalpy of lower oxide → higher oxide transition(●) acid solution and (○) alkaline solution [62]. Reproduced with permission from Elsevier.*

Different mechanisms have been proposed for OER. Three major proposed mechanisms are the electrochemical oxide path, the oxide path and the Krasil Shichikov path and are given in Table 1-5. More details on OER mechanism are available in literature [59, 68-72]. When one of the steps in the mechanism becomes the rate determining step (rds), a corresponding tafel slope can be derived and the values are given in Table 1-5 at low and high over potentials. Reaction mechanism and rds can be determined from the steady state polarisation analysis.

*Table 1-5.Various OER mechanism pathways in acidic media and their corresponding tafel slopes [68, 70].*

| Path | Reaction step (rds.) | $b_a$ at low η | $b_a$ at high η |
|---|---|---|---|
| Electrochemical Oxide path | $S + H_2O \leftrightarrows S—OH_{ads} + H^+ + e^-$ | 120 | 120 |
| | $S—OH_{ads} \leftrightarrows S—O + H^+ + e^-$ | 40 | 120 |
| | $2S—O \rightarrow 2S + O_2$ | 15 | ∞ |
| Oxide path | $S + H_2O \leftrightarrows S—OH_{ads} + H^+ + e^-$ | 120 | 120 |
| | $2S—OH_{ads} \rightarrow S - O + S + H_2O$ | 30 | ∞ |
| | $2S - O \rightarrow 2S + O_2$ | 15 | ∞ |
| Krasil Shichikov | $S + H_2O \leftrightarrows S—OH_{ads} + H^+ + e^-$ | 120 | 120 |
| | $S—OH_{ads} \rightarrow S - O^- + H^+$ | 60 | 60 |
| | $S - O^- \rightarrow S - O + e^-$ | 30 | 120 |
| | $2S - O \rightarrow 2S + O_2$ | 30 | ∞ |

Most of the OER catalysts studied in the earlier days were based on DSA electrode after its invention by Beer in 1967 [73]. DSA electrode is having general formula Me/$AO_x$-$BO_y$ containing a monometallic or bimetallic oxide ($AO_x$ and/or $BO_y$) one of which is conducting and the other is inert; coated on a suitable base metal (Me) such as Ti [60, 74]. The conducting oxide is active towards the desired reaction whereas the inert oxide ensure better dispersion of the active component, preventing the corrosion of the base metal and helps in better cohesion of the coating, increasing the stability of the oxide [60, 74]. Since the conducting coating, $RuO_2$ and $IrO_2$ are expensive and high loading in the electrode increase the system cost, a bimetallic catalyst system with non-precious metal mixed with the active oxide were widely used in commercial electrolyser system. Though, generally this decrease the active area, the life time significantly improves in this system which is important for the commercial operation.

$RuO_2$ is the most active catalyst for OER in PEMWE but suffers from instability on long term operation whereas $IrO_2$ is the most stable and second most active catalyst for OER [75, 76]. High cost of these catalysts limits the usage of its high loading on the

electrode. Reducing the loading of precious metal on the electrode without making significant compromise of the electrolyser performance is an important step towards the development of cost effective PEMWE. It is unlikely that a complete non-noble metal catalyst would be identified for PEM system, but a reduction in the noble-metal loading would be possible by suitable approaches such as making alloy with less precious/non precious metal or dispersing the catalyst on a suitable cheap and conducting support material [77].

### 1.6.2 **Hydrogen evolution reaction (HER)**

Hydrogen evolution/oxidation is one of the most studied electrochemical reactions. Hydrogen evolution reaction is kinetically feasible reaction compared to OER. The suitable catalyst for HER is also derived based on the bond strength between the catalyst and chemisorbed H (S-H). A volcano plot similar to Figure 1-7 is obtained and is given in Figure 1-8 [78, 79]. Metals with intermediate S-H bond strength (e.g. Pt) shows highest activity. Metals making too strong and too weak bonding with H shows lower activity for HER [80]. Pt is the most active catalyst for HER and HOR. The first step of the HER mechanism is the discharge of $H^+$ ion with the formation of adsorbed H (Volmer pathway). The second step can either be a chemical recombination (Tafel pathway) or an electrochemical recombination (Heyrovsky pathway)[81]. The slowest step determines the overall rate of the reaction. The different pathways for the HER and the tafel slopes corresponding to the different steps are given in Table 1-6.

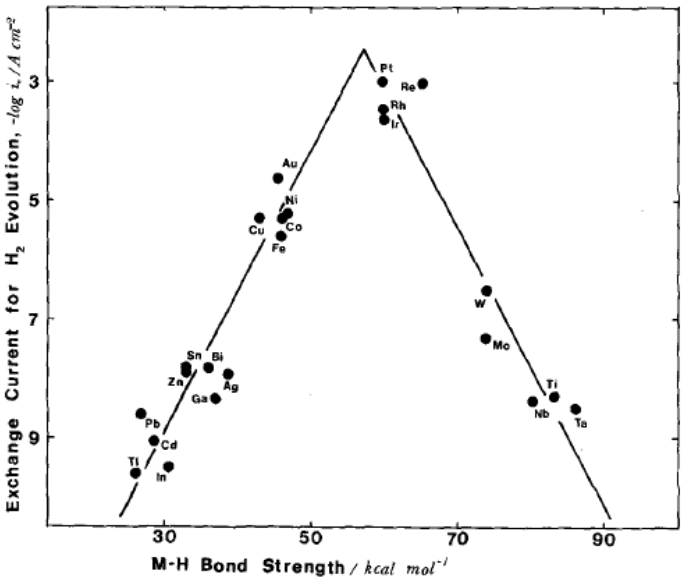


*Figure 1-8. Volcano plot of exchange current density for the HER vs. the M-H bond strength [78]. Reproduced with permission from Elsevier.*

*Table 1-6. The HER mechanism pathways in acid media and their corresponding tafel slopes [81, 82].*

| Path | Reaction step (rds.) | $b_a$ at low η | $b_a$ at high η |
|---|---|---|---|
| Volmer | $S + H^+ + e^- \leftrightarrows S—H_{ads}$ | 120 | 120 |
| Heyrovsky | $S—H_{ads} + H^+ + e^- \leftrightarrows S + H_2$ | 40 | 120 |
| Tafel | $2S—H_{ads} \rightarrow 2S + H_2$ | 30 | ∞ |

## 1.7 Objective of the thesis

The main objective of the thesis is to develop low cost, stable and active catalyst for the PEMWE. Little research has been performed to date on the use of supported catalyst for PEMWE anode. Supported catalysts were developed for PEMWE anode in order to have a lower precious metal loading on the electrode and thus reducing the cost of the electrode. The effects of various physical and electrochemical parameters affecting the performance of the supported catalysts were investigated in order to identify suitable composition of the supported catalyst. Various support materials such as indium tin oxide (ITO), antimony doped tin oxide (ATO) and titanium dioxides were investigated as support material for the $IrO_2$ catalyst. Since $RuO_2$ is the most active catalyst for OER, stabilisations of $RuO_2$ catalyst by adding niobium additive to form bimetallic systems were also investigated. The major objective can be summarized as,

- Explore various possible catalyst support material for OER catalyst in PEMWE.
- Investigation of various parameters affecting the performance of the supported catalyst in PEMWE anode and identify the optimum composition.
- Development of stable OER catalyst for PEMWE by utilizing Nb based bimetallic system of catalyst.
- Finding an alternate organic acid dopant to phosphoric acid for polybenzimidazole (PBI) membrane.

Chapter 1- gives a brief introduction and objective of the thesis. General principle of PEMWE and challenges are discussed.

Chapter 2- describes the synthesis of the catalyst and various physico-electrochemical techniques used for the characterization of the prepared catalyst. Brief descriptions of the theory of the techniques are also given in this chapter.

Chapter 3- describes the synthesis and characterization of the ATO supported $IrO_2$ as OER catalyst in PEMWE. Various physical properties affecting the performance of the supported catalysts are discussed.

Chapter 4- describes the study of ITO as support material for $IrO_2$ in PEMWE. The performance of the catalyst was compared with $TiO_2$ supported $IrO_2$ in order to study the effect of support conductivity on the catalyst performance.

Chapter 5- describes the $Ru_xNb_{1-x}O_2$ and $I_xNb_{1-x}O_2$ catalyst synthesis and characterization in detail. Two different methods, namely the Adams method and the hydrolysis method were adopted to prepare the catalyst.

Chapter 6- is a short chapter on the preliminary investigation of some alternate acid dopant to phosphoric acid for PBI membrane.

Chapter 8 summarizes the main findings and gives some recommendation for the future work.

# Chapter-2. Experimental

This chapter describes the methods used for the synthesis of OER catalysts and the characterization techniques used to analyse them. Principles of physical characterization techniques such as X-ray diffraction (XRD), X-ray photoelectron spectroscopy (XPS), scanning electron microscopy (SEM), energy dispersed X-ray analysis (EDX), transmission electron microscopy (TEM), Brunauer-Emmet-Teller (BET) and thermo gravimetric analysis (TGA) are briefly explained. The procedures and the principles of the electrochemical techniques used such as cyclic voltammetry (CV), membrane electrode assembly (MEA) polarisation as well as membrane and powder conductivity are also described.

## 2.1 Synthesis of the catalyst

Different methods have been adopted by various groups to prepare $RuO_2$ and $IrO_2$ based catalysts for OER such as the Adams fusion method [83], the hydrolysis method [84], the polyol process [85-87] and the borohydride reduction method [76]. All these methods involve preparation of a metal/metal compound intermediate followed by a thermal treatment to form the metal oxide. A calcination temperature ranging from 400-600$^{o}$C are generally used for the preparation of Ru and Ir based oxides [86-88]. The morphology, crystallinity, stoichiometry and electronic conductivity of the oxides depends on the preparation method and calcination temperature used [55].

Two major methods were adopted to prepare the unsupported and supported catalyst in this study. Specific details of the catalyst synthesis are given in their respective chapters. General principles of the synthesis methods and procedures are described here.

### 2.1.1 Adams fusion method

The Adams method was first introduced in 1923 by Roger Adams for the preparation of $PtO_2$ [83] and later used by various groups to prepare $RuO_2$, $IrO_2$ and mixed oxides [43, 76, 81, 83, 88-94].

In the Adams method the metal precursors (e.g. $RuCl_3$, $H_2IrCl_6$) as required by the stoichiometry are mixed in a suitable solvent (e.g. isopropanol, water or mixture). $NaNO_3$ is then added under constant stirring. For bimetallic and supported catalysts, the second metal precursor/support is added before the addition of $NaNO_3$. The solvent is then evaporated slowly and the dried mixture is transferred to a crucible and calcined at

high temperature (300°-600°C) in air to form the oxides. During the heat treatment the $NaNO_3$ (melting point = 308°C) forms an oxidizing melt, dissolving the precursors and reacting with them to form nitrates as given in equation (2-1) and (2-2) for $RuCl_3$ [83, 95] and equation (2-3) and (2-4) for $H_2IrCl_6$. The NaCl salt formed after the calcination was then dissolved in DI water. The sample was washed and centrifuged using excess DI water and dried in an air oven.

$$RuCl_3 + 3NaNO_3 \rightarrow 3\,NaCl + Ru(NO_3)_3 \qquad (2\text{-}1)$$

$$Ru(NO_3)_3 \rightarrow RuO_2 + 3NO_2\uparrow + \frac{1}{2}O_2\uparrow \qquad (2\text{-}2)$$

$$H_2IrCl_6 + 6NaNO_3 \rightarrow 6NaCl + Ir(NO_3)_4 + 2HNO_3 \qquad (2\text{-}3)$$

$$Ir(NO_3)_4 \rightarrow 4NO_2\uparrow + O_2\uparrow + IrO_2 \qquad (2\text{-}4)$$

The advantage of Adam's fusion method is that two of the bi-products formed are gases ($NO_2$ and $O_2$) and the third one is NaCl which can be removed easily by dissolving in water. A schematic of the procedure adopted is given in Figure 2-1.

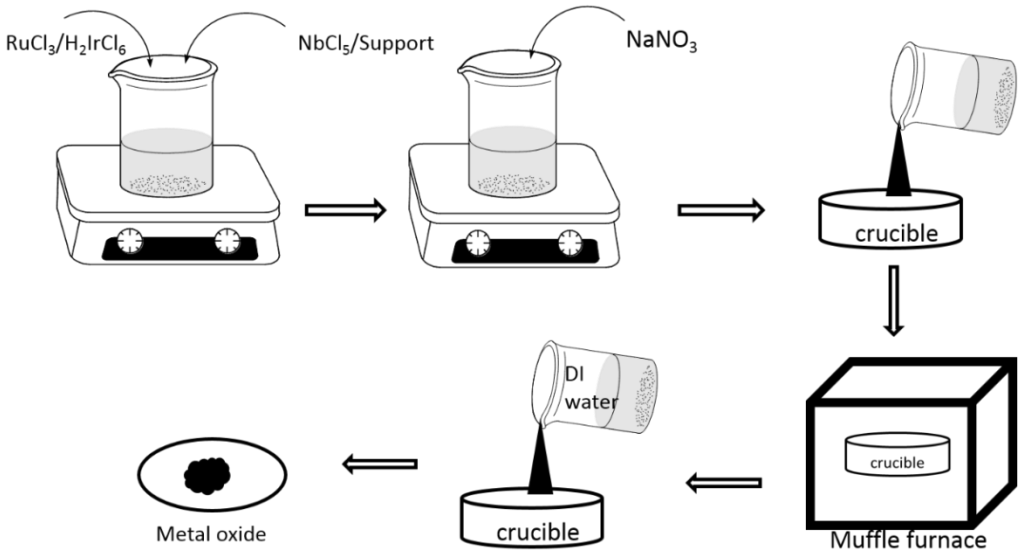


*Figure 2-1. Schematic of the Adams fusion method for the synthesis of metal oxide.*

### 2.1.2 Hydrolysis method

The aqueous hydrolysis method involves hydrolysis of metal precursor to form hydroxides (or hydrated oxide) and their subsequent decomposition at high temperature to form oxides. Suitable metal precursors (e.g. $RuCl_3$, $H_2IrCl_6$) or a mixture of metal precursors as required by the desired stoichiometry were hydrolyzed by aqueous alkaline solution (e.g. NaOH) at 80$^o$C. For supported catalysts, the support material was introduced before the addition of the alkaline solution. A gradual color change was observed during hydrolysis at 80$^o$C, eventually reaching a deep blue colored complex. This is attributed to the substitution of chlorine with a hydroxide group [96]. 1M $HNO_3$ was then added drop wise until the pH of the solution measured using a pH meter (Hanna instruments) reached 7-8 where a controlled precipitation occurs [97, 98]. If the pH decreased below 7, the unreacted Ru species will still present in the solution while if the pH remained more than 7, sodium ions will be present as an impurity in the catalyst [97]. The precipitate formed may be either a hydrated metal oxide, metal hydroxide or hydrated metal hydroxide [97]. The precipitate nature also depends on the extension of hydrolysis and will be different for Ru and Ir species since their hydrolysis tendency varies [99].

The solution after the hydrolysis stage was stirred overnight, washed with plenty of water and separated by a centrifuge. The precipitate was then calcined at high temperature to form the respective metal oxide. The hydrolysis method permits the use of lower calcination temperature compared to the Adams method [76]. A calcination temperature of 400$^o$C-500$^o$C was reported to give best catalytic performance [84, 100-102]. A higher calcination temperature will lead to particle sintering which will decrease the active surface area [100] whereas catalysts prepared at lower temperatures will be amorphous and have poor stability for OER [102]. The hydrous $RuO_2$, on heat treatment at 300$^o$C or above gives an anhydrous compound with crystalline structure [97, 103].

Reactions of $H_2IrCl_6$ with NaOH are given by Ioroi et al [100]. The $H_2IrCl_6$ dissolves in NaOH to form $[IrCl_6]^{3-}$(equation (2-5)). After heating for a sufficient time, $Cl^-$ is substituted by $OH^-$ ion (equation (2-6)), the hydroxide complex formed is then precipitated by adding $HNO_3$ solution (equation (2-7)),

$$2[IrCl_6]^{2-} + 2OH^- \rightarrow 2[IrCl_6]^{3-} + \frac{1}{2}O_2 + H_2O \qquad (2\text{-}5)$$

$$[IrCl_6]^{3-} + 6OH^- \rightarrow [Ir(OH)_6]^{3-} + 6Cl^- \quad (2\text{-}6)$$

$$[Ir(OH)_6]^{3-} + 3H^+ \rightarrow Ir(OH)_3(H_2O)_3 \quad (2\text{-}7)$$

The precipitate formed is then washed and heat treated at high temperature to form the $IrO_2$. A schematic of the procedure adopted in given in Figure 2-2.

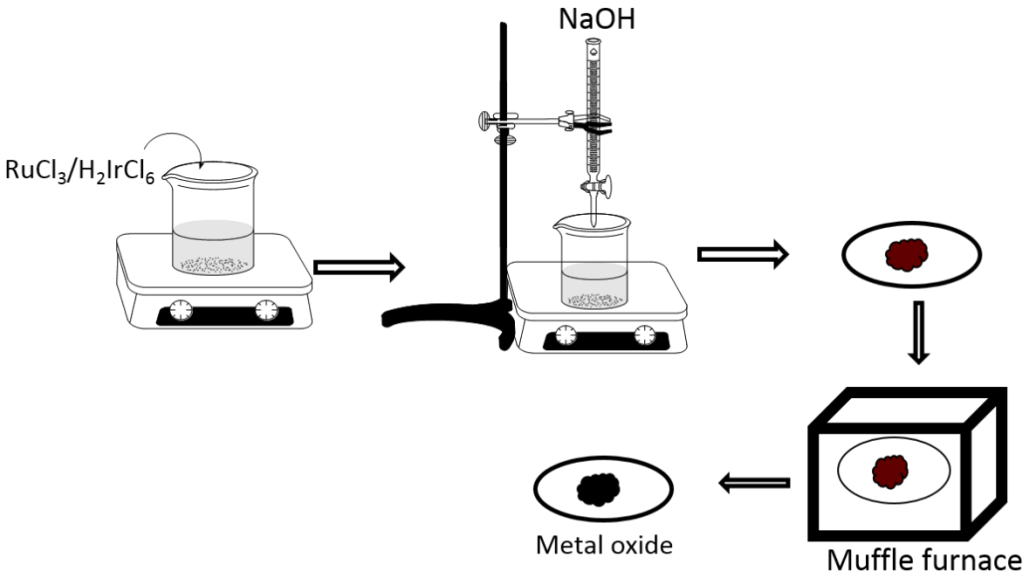


*Figure 2-2. Schematic of the hydrolysis method for the synthesis of metal oxide.*

## 2.2 Physical Characterization

### 2.2.1 X-ray diffraction

The X-ray diffraction (XRD) technique is the most widely used technique for the characterization of crystalline materials. It can be used for both qualitative and quantitative analysis.

The principle of XRD lies in the diffraction of radiation. Crystalline solids have periodical arrangements of constituents (atoms, ions or molecules) and the wavelength of X-ray (0.1 – 100 Å) and interatomic spacing in crystals are of the same magnitude [104]. Thus crystals act as a 3-D diffraction grating for X-rays [105]. As an X-ray (an electromagnetic radiation which has an oscillating electric field) interacts with the electrons in the sample, the electron starts oscillating in the same frequency as the incident X-ray. An oscillating electron will always emit radiation with the frequency of oscillation. Thus the electron from the sample emits radiation in all direction (Thomson

scattering) which can have constructive and destructive interference. Figure 2-3 shows the diffraction of X-rays from crystal planes. When the Bragg condition (equation (2-8)) is satisfied, scattered X-rays constructively interfere and an intense peak is obtained.

$$2d_{hkl}sin\theta = n\lambda \qquad (2\text{-}8)$$

Here $d_{hkl}$ is the spacing between the lattice planes with Miller indices h, k and l. n is the order of diffraction (1, 2, 3 etc.) and $\lambda$ is the wavelength of the incident X-ray.

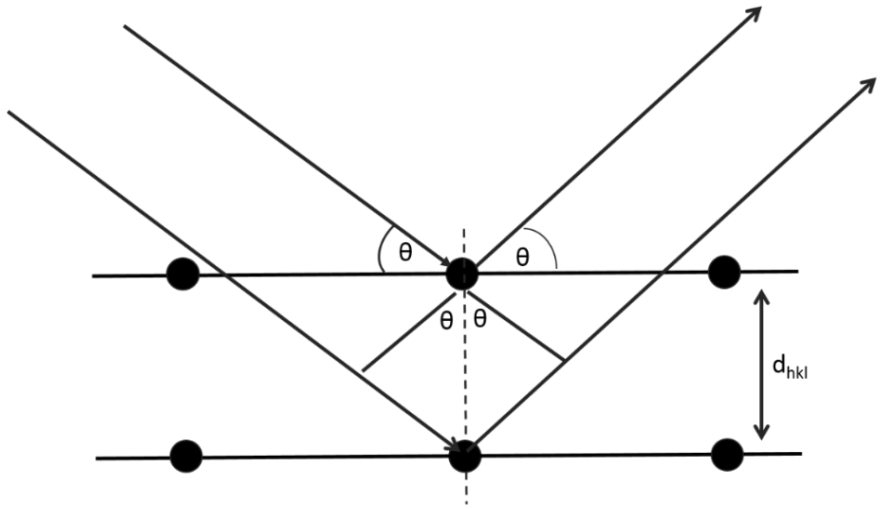


*Figure 2-3. Bragg's reflection from a set of hkl crystal planes.*

Unlike in a single crystal, a powder crystal sample contains a very large number of small crystals called crystallites which are randomly arranged in all possible orientations [104, 105]. Thus for every set of crystal plane some of the crystals will be in a position to satisfy Bragg's equation and a peak is obtained in XRD spectra.

The X-rays are generated in an X-ray tube by bombarding accelerated electrons produced from a heated filament (tungsten) with an anode metal target (e.g.: Cu, Al, Mo and Mg) at a potential difference of about 20-50 kV in vacuum (Figure 2-4). The high speed electron collides with the metal target and eject electron from its core level. As a result, a hole is created in the core level and an electron in an upper level falls into this level releasing energy in the form of an X-ray [106].

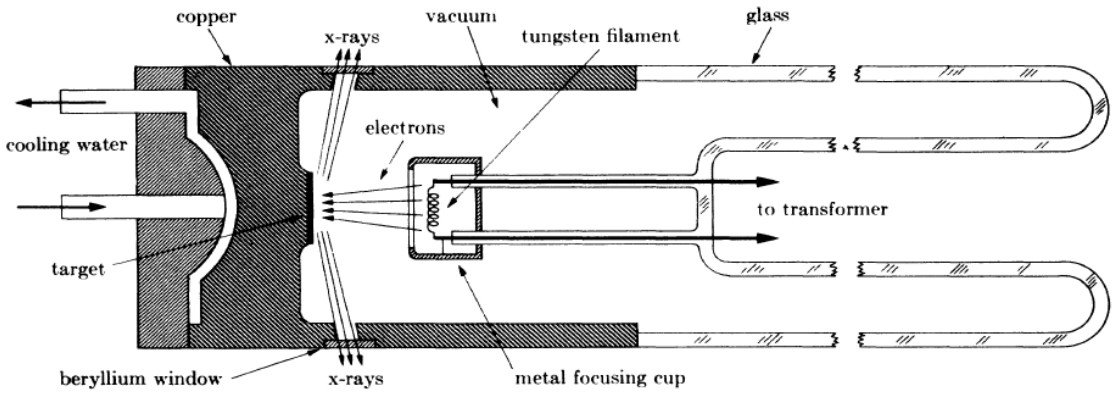


*Figure 2-4. Schematic of the cross section of sealed-off filament x-ray tube [106].*

The X-ray bombards the sample at different angles. The emitted ray is then analysed using a suitable detector (Figure 2-5). The sample or the detector is rotated at an angle 2θ and the result is plotted as angle vs. intensity of peak.

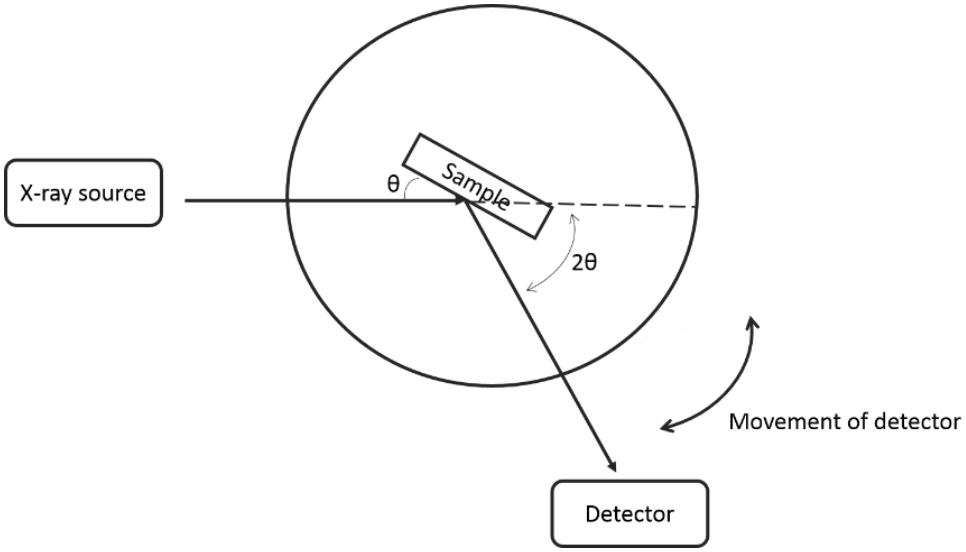


*Figure 2-5. Basic instrumental set up of XRD.*

The XRD analysis can be used only for a crystalline substance and not for amorphous compounds. An amorphous or partially crystalline substance shows broad peaks in XRD. It was found that the peak also broadens as the crystallite size decreases. The broadness of the peak is used to calculate the crystallite size using Debye-Scherrer formula (equation (2-9)) [104],

$$t = \frac{K\lambda}{\beta cos\theta} \qquad (2\text{-}9)$$

Where $\lambda$ is the wavelength of incident X-ray, $\beta$ is the full width at half maximum($2\theta$), and K is the shape factor which usually takes the value of 0.9 [104] assuming spherical crystallite shape.

In this study, the X-ray diffraction (XRD) analyses of the samples were carried out using a PANalytical X'Pert Pro MPD, (powered by a Philips PW3040/60 X-ray generator and fitted with an X'Celerator) with Cu-Kα radiation (λ = 1.541874 Å) . The data were collected over a range of 5-100$^o$ 2θ with a step size of 0.0334$^o$ 2θ and nominal time per step of 200 seconds. All scans were carried out in 'continuous' mode using the X'Celerator RTMS detector. Phase identification was carried out by means of the X'Pert accompanying software program PANalytical High Score Plus in conjunction with the ICDD Powder Diffraction File 2 database (1999) and the Crystallography Open Database (September 2011; www.crystallography.net).

### 2.2.2 X-ray photoelectron spectroscopy (XPS)

X-ray photoelectron spectroscopy or Electron Spectroscopy for chemical analysis (ESCA) is an important surface analysis technique used to analyse the composition and the bonding on the surface of solid materials.

XPS analysis works based on the principle of the photoelectric effect. X-rays generated from a suitable X-ray source (e.g. Al $K_\alpha$ or Mg $K_\alpha$) are introduced on the sample surface. This primary beam interacts with the sample in different ways (Figure 2-7). The X-ray ejects an electron from the core-level of an atom on the sample surface. The electron leaves the surface with a kinetic energy which depends on the energy of the introduced beam and binding energy of the electron (equation (2-10)).

$$h\nu = B.E + E_k + \phi \qquad (2\text{-}10)$$

Where $B.E$ and $E_k$ are the binding energy and kinetic energy of the electron and $\phi$ is the work function of the instrument. By measuring $E_k$ of the ejected electron, $B.E$ of the electron can be calculated from the equation (2-10). Since each electron has characteristic $B.E$, it can be used to identify the chemical oxidation state, electronic structure and atomic composition of the sample surface [107]. The binding energy not only depends on the element but also its oxidation state and chemical environment which help to analyse the stoichiometry and bonding of elements on the surface.

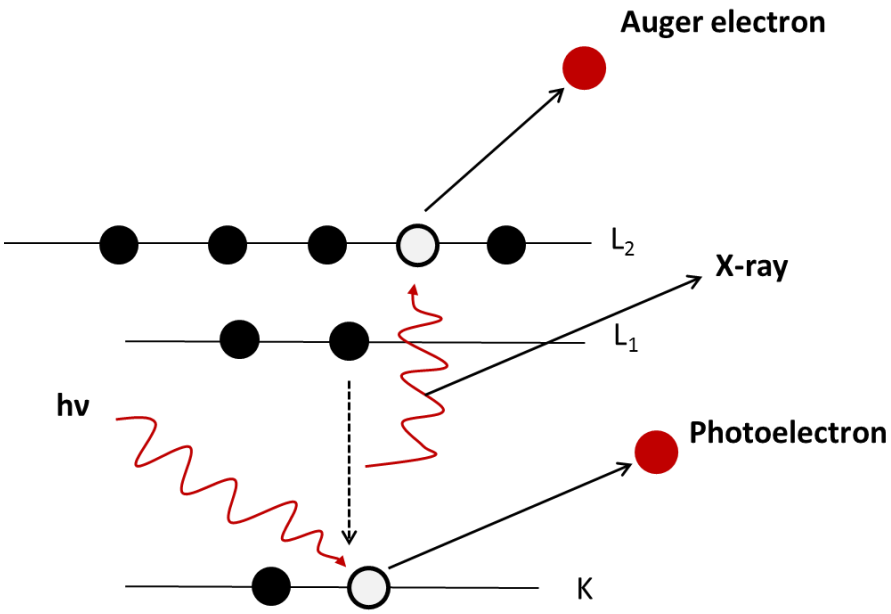


*Figure 2-6. Schematic of the electron transition in XPS analysis.*

As given in Figure 2-6, when the incident beam ejects electron from the core level, a hole is created and an electron in an upper level falls into this level releasing energy in the form of an X-ray which in turn is utilised to eject an electron from the upper shell (Figure 2-6). The electron ejected in this way is called an Auger electron. These electrons have very low energy and are ejected from the outer atomic layer on the surface (Figure 2-8). It has to be noted that photoionization can produce both photoelectrons and auger electrons whereas electron ionization can produce only auger electrons [108]. The KE of an auger electron is independent of the introduced photon energy whereas the KE of photoelectron is dependent on the energy of the introduced photon electron [108]. Both auger electron and X-ray generation are competitive processes. At high energy, X-ray generation dominates and at low energy, auger electron generation dominates. Since conventional XPS instruments use low energy X-rays (Al Kα=1486.6 eV, Mg Kα=1253.6 eV), the X-ray generation is not prominent [107].

The XPS analysis in this study was carried out in a K-Alpha (Thermo Scientific) instrument with a micro focused monochromatic Al- Kα source.

### 2.2.3 Scanning electron microscopy (SEM)

Scanning electron microscopy is an important electron microscopy technique used to study the topography, morphology and composition of solid materials.

In this technique, an electron beam produced from an electron gun (primary electron beam) is bombarded vertically on to the sample surface in vacuum. The electron beam interacts with the sample and undergoes both elastic and inelastic scattering (Figure 2-7). In the elastic scattering the kinetic energy and the velocity of electron remains constant (called a backscattered electron if it escapes the surface). In the inelastic scattering, the electron collides with the atoms in the sample and ejects electrons from them (called secondary electrons). Secondary electrons are generally produced up to a depth of 10 nm and are considered as the depth limit of SEM. The number of secondary electrons depends on various factors such as atomic number of the atom, angle which the surface forms with the introduced beam, shape, thickness and particle position etc. [109]. Thus it helps to form a 3-D topographical image of the surface. The energy of the backscattered electron is generally >50 eV whereas for secondary electron it is $\leq$ 50 eV. X-rays and auger electron can also be emitted by the sample due to the relaxation of the excited atom (Figure 2-7). This forms the basis of elemental analysis. Detectors are placed on a proper position suitable to detect the various forms of rays coming from the sample. Based on the detection of the emitted beams three types of images are formed. Backscattered electron image, secondary electron image and elemental mapping. Backscattered electron images are produced when a high accelerating voltage is used which gives high penetration depth and wider diffusion area, but reduces the image contrast and cannot be used for fine structure analysis. Secondary electron image are generally used for the fine structure analysis by using low accelerating voltage [109].

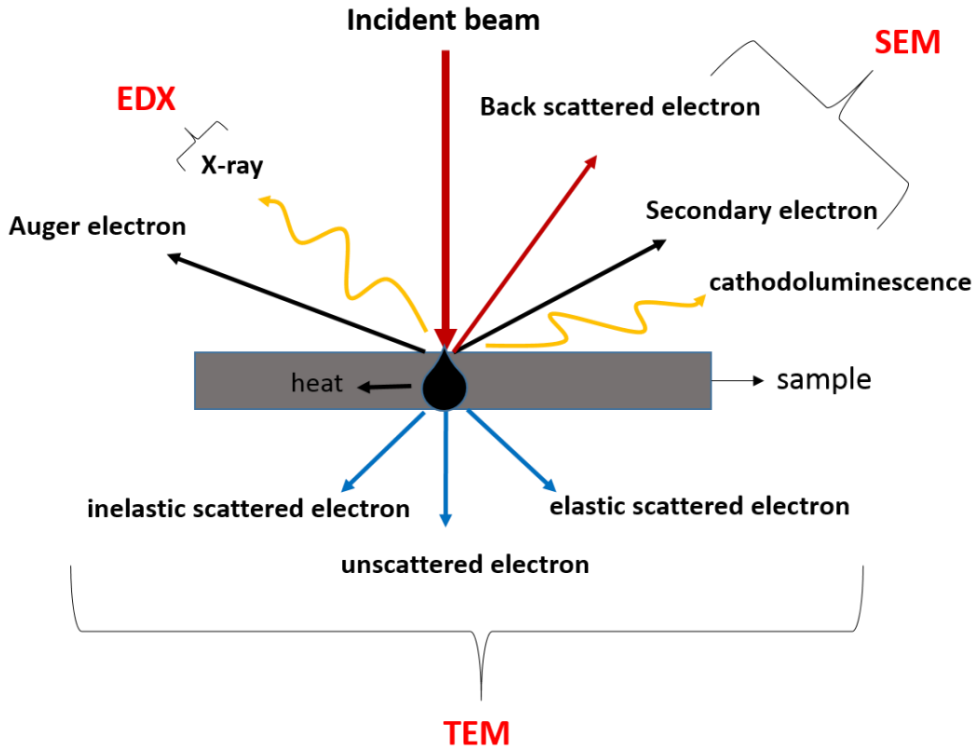


*Figure 2-7. Various effect of electron bombardment on the sample and characterization technique associated with it [109] .*

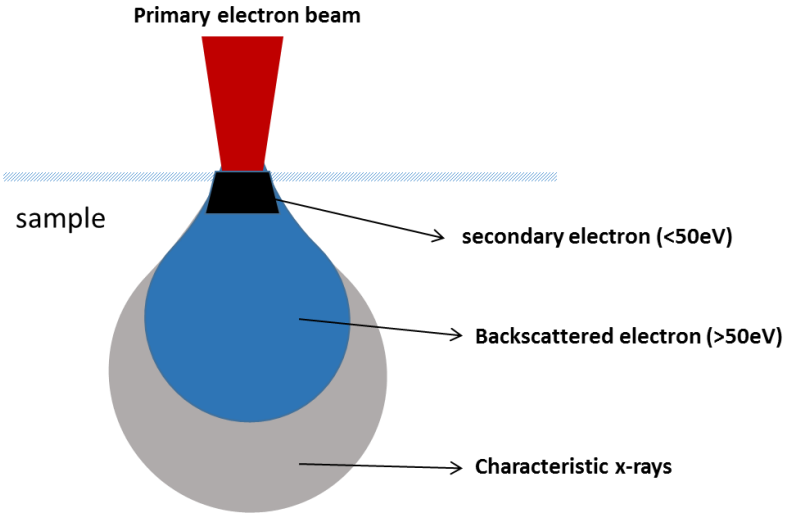


*Figure 2-8. Depth profile in a sample where characteristic interaction occur with the electron beam.*

### 2.2.4 Energy dispersive X-ray technique (EDX)

Energy dispersive spectroscopy (EDS) or Energy dispersive X-ray analysis (EDX) is an analysis technique used in conjunction with the SEM analysis. EDX analysis utilise the emitted X-ray from the sample during the interaction of electron beam with the sample (Figure 2-7) to quantitatively analyse the elemental composition. When a primary electron beam interacts with the sample and ejects secondary electron, a hole is created and the electrons from higher shell transferred to the hole by releasing an X-ray photon (Figure 2-6). Since the energy of the X-ray depends on the energy difference between the shells which in turn depends on the specific element, EDX can be used to identify elements present in the sample.

In this study, the SEM and Energy dispersive X-ray spectroscopy (EDX) analyses were carried out in FEI Xl30 ESEM-FEG (Environmental Scanning Electron Microscope-Field Emission Gun) at 20kv for elemental analysis on uncoated samples in low vacuum mode and at 10 kV on gold coated samples in high vacuum mode for the images. The EDX system was from Rontec using Quantax software.

### 2.2.5 Transmission electron microscopy (TEM)

Transmission electron microscopy has similar basic principle of SEM except that the electrons pass through the sample. TEM utilises three types of transmitted electrons from the sample, i.e. elastic scattered electron, inelastic scattered electron and unscattered electrons (Figure 2-7). The unscattered and elastic scattered electron intensity will be proportional to the thickness of the sample and will be shown as light and dark areas in the image. Also elements with higher atomic number will scatter more electrons than those with lower atomic number, creating different intensity regions.

In our study, TEM analysis was carried out in a Philips CM100 operated at 100kV.The CCD camera is optronics 1824x1824 pixel with AMT40 version 5.42 image capture engine supplied by Deben UK. Sample for TEM were dried onto carbon-coated copper 400 mesh grids supplied by TAAB Laboratories Equipment Ltd, Aldermaston, UK.

### 2.2.6 Thermo-gravimetric analysis (TGA)

Thermo-gravimetric analysis (TGA) is a widely used technique to study the thermal behaviour of the sample. It can be used to study the chemical composition and thermal stability of the sample.

In this technique, mass change of the sample is monitored while heating the sample in a controlled atmosphere ($N_2$, $O_2$, air etc.) with a controlled temperature programme. The mass change versus the temperature (or time) is plotted for the analysis. A decrease in mass implies a destruction of the sample whereas an increase weight in an oxidising atmosphere indicates an oxide formation. TGA analysis was used in our study mainly to study the thermal stability of the support material and its thermal oxidation behaviour. Since most of the synthesis method for the $RuO_2$ and $IrO_2$ catalyst requires a thermal treatment at high temperature of up to 600$^o$C, it is important to know the thermal behaviour of the species involved.

In our study, the TGA of the samples were carried out using TGAQ500V20.10 Build 36 instrument in air atmosphere with temperature ramp from 30$^o$C to 900$^o$C at 10$^o$ C.min$^{-1}$.

### 2.2.7 BET surface area analysis

The Brunauer-Emmet-Teller (BET) method is widely used for the surface area analysis of solid samples using $N_2$ physical adsorption. BET consider multilayer adsorption of $N_2$ considering the fact that the enthalpy of adsorption for the first mono layer are higher than the subsequent layer. Using the BET equation (equation (2-11)), the surface area (m$^2$ g$^{-1}$) is calculated [110].

$$\frac{P}{V(P_o - P)} = \frac{1}{V_m C} + \frac{(C-1)}{V_m C}.\frac{P}{P_o} \qquad (2\text{-}11)$$

Where $P_o$ is the saturation pressure of the gas (atmospheric pressure if the process is carried out atmospheric pressure and above the boiling point of $N_2$), V is the volume of the gas adsorbed per unit mass of material at pressure P, $V_m$ is the volume of the gas required to cover a monolayer on the surface per unit mass and C is a constant.

The $N_2$ adsorption BET surface area was measured in Tristar II 3020 V1.01 instrument.

## 2.3 Electrochemical Methods

### 2.3.1 Powder conductivity

Electronic conductivity of powder sample was calculated using an in-house built conductivity set up. The schematic of the setup is given Figure 2-9 and photograph in Figure 2-10.

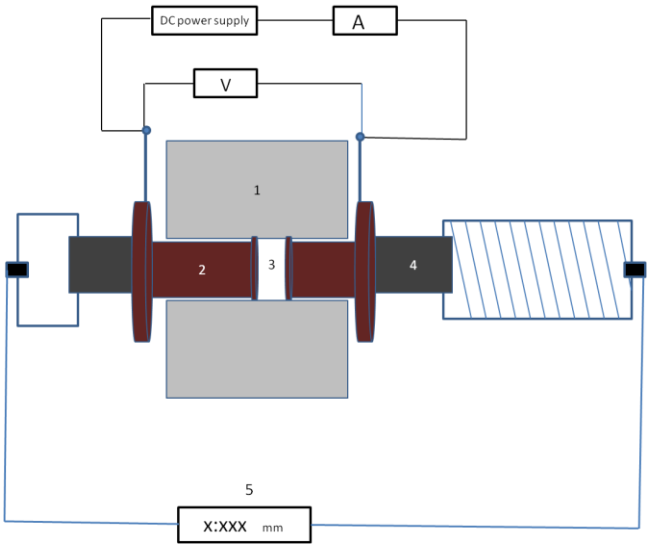


*Figure 2-9. Schematic of the powder conductivity cell. (1) insulator cover (2) copper piston (3) powder sample (4) plastic (5) thickness display on micrometre.*

Since the powder sample prepared was at the milligram level, a smaller set up which can also fit into a standard micrometre was designed and built using copper rod and an insulating plastic disk (Figure 2-10). The sample was placed in between the two copper pistons and pressed using the micrometre. The micrometre thus applies pressure and measures thickness simultaneously. The resistance of the sample was measured at different thicknesses by varying the pressure. A similar set up for measuring conductivity of powder sample under compression are described elsewhere [111-113].


*Figure 2-10. The powder conductivity cell.*

The conductivity was measured in a two probe method by passing a dc-voltage across the piston and measuring the current at room temperature. A slope voltage vs. current plot gives the resistance (equation (2-12).

$$R = \frac{V}{I} \qquad (2\text{-}12)$$

The resistance of the powder at each thickness was measured. A plot of thickness vs. resistance gives a linear relation and its gradient gives the resistivity (ρ) according to the equation ((2-13).

$$R = \rho . \frac{l}{A} \qquad (2\text{-}13)$$

Where $l$ is the thickness of the sample and $A$ is the cross section of the piston (5mm diameter) in contact with the sample. The resistivity was calculated from the gradient of $l$ vs. $R$ plot (equation (2-14) and conductivity from its inverse (equation (2-15).

$$\rho = \frac{\Delta R}{\Delta l} . A \qquad (2\text{-}14)$$

$$\sigma = \frac{1}{\rho} \qquad (2\text{-}15)$$

Where $R$ is the resistance (Ω), $l$ is the thickness of the sample pellet (cm), $A$ is the area of the pellet in contact with the piston ($cm^2$), $\rho$ is the resistivity (Ω.cm) and $\sigma$ is the conductivity ($S.cm^{-1}$). It should be noted that, powder conductivity of a compressed sample depends on various factors, such as conductivity of individual particles, the degree of contact between the particles, the packing density, impurities present in the sample and the external pressure applied [114, 115]. As the conductivity is calculated from the resistance values at different thickness, this method eliminates any contact

resistance between the powder sample and piston and the difference in packing density of samples. The conductivity of Vulcan XC-72 and $TiO_2$ nanoparticle in the same set up were 1.78 S $cm^{-1}$ and $2.61\times10^{-6}$ S $cm^{-1}$ respectively. A conductivity of 4 - 4.5 S $cm^{-1}$ for Vulcan XC-72 was reported in literature in a set up similar to ours [116, 117].

### 2.3.2 Cyclic voltammetry

Cyclic voltammetry (CV) is one of the dynamic electrochemical methods for the study of electro active species and is a popular technique for initial electrochemical studies of new systems [36, 118]. In CV the potential is cycled at fixed scan rate and the resulting current is measured [119]. The theory and principle of CV is well described in the literatures [118-124]. The CV experiment is normally carried out in a three electrode cell. The voltage is measured between a working electrode (WE) and reference electrode (RE) whereas current is measured between the WE and counter electrode (CE).

For a reversible reaction (reaction rate is fast), the equilibrium establishes quickly and the Nernst equation applies to the equilibrium. In this case the peak current depends on the mass transport (slowest step) and not on the kinetics [123] and is given by the Randles-Sevich equation (equation (2-16) [36, 125]. Mass transport in CV is only by diffusion as other forms of mass transports are eliminated.

$$i_p = (2.69 \times 10^5) A n^{3/2} D^{1/2} \upsilon^{1/2} C_o \qquad (2\text{-}16)$$

Where $i_p$ =Peak current (A), A= area of electrode ($cm^2$), D= diffusion coefficient of reactant ($cm^2$ $s^{-1}$), n= number of electrons transferred, ν = scan rate (V $s^{-1}$), $C_o$ = analyte concentration (mol $cm^{-3}$).

An ideal reversible couple is characterised by sharp and symmetrical anodic and cathodic peak, peak current proportional to $\nu^{\frac{1}{2}}$, no change in peak potential with scan rate, and peak potential separation of $\frac{59mV}{n}$ [119, 123]. Both anodic and cathodic peak potential are independent of the scan rate for a reversible couple [125].

The peak separation increases and peaks broaden as the rate of charge transfer decreases and/or the scan rate is increased [118, 123]. Most real systems are not fully reversible but a quasi-reversible system. A quasireversible system is where the rate of the reaction is in between the reversible and irreversible extreme cases ($10^{-1} < k^o < 10^{-5}$ cm $s^{-1}$). In this

case the Nernst equation is only approximately valid. If the reaction rate is slower than the scan rate, the equilibrium will not occur rapidly compared to the voltage ramp, so the peak will shift to a more over potential position and the difference between the redox peaks will increase.

For an irreversible process the charge transfer at the electrode is extremely slow ($k^o < 10^{-5}$ cm/s) and thus the current is controlled by charge transfer reaction rate (kinetic control) which is the slow reaction [123]. Since the surface concentration of the redox species are not at thermodynamic equilibrium, the Nernst equation cannot be applied [123]. The individual peaks are reduced in size and widely separated [125].

Also it should be noted that since the potential is continuously changing in CV, a charging current $i_c$ always flows (capacitive current). This is non-Faradaic current due to the charging of the double layer without any charge transfer between electrode and electrolyte [123, 126].

CV of Pt in acid solution gives well defined peaks (Figure 2-11) showing the adsorption process during the potential scan. Three regions are defined in the CV, the hydrogen region, the oxygen region and the double layer region respectively. The hydrogen region is where $H_2$ is adsorbed/desorbed on Pt and the oxygen region where Pt forms an oxide layer during anodic potential scan (~ +0.8V vs. NHE). The double layer region is at the centre where only capacitive processes occur. During the cathodic scan the oxide layer is reduced to form Pt metal (~ +0.7 V vs. NHE). The electrochemical active surface area of Pt can be calculated by integrating the hydrogen region [121, 127].

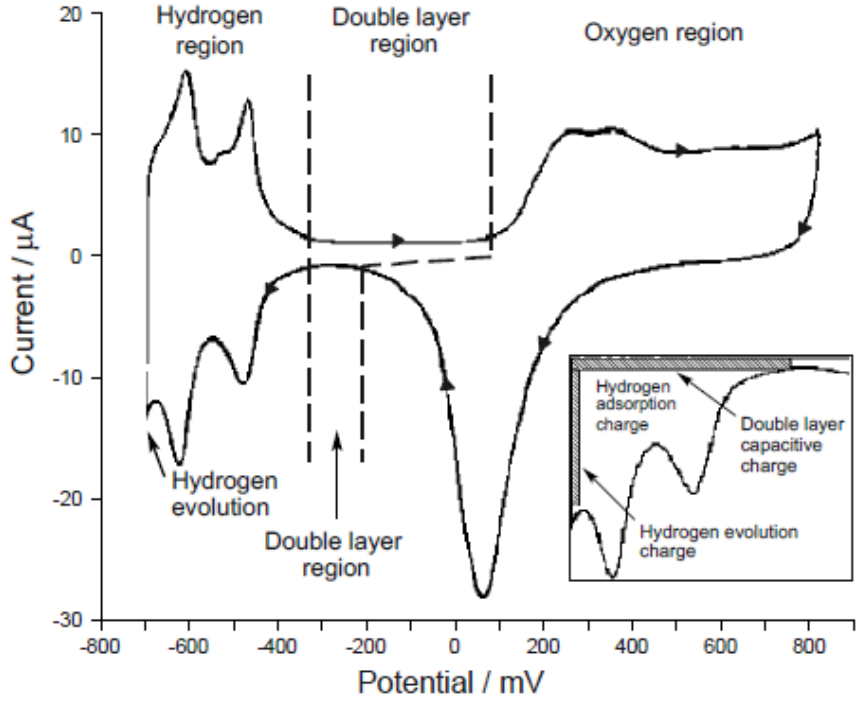


*Figure 2-11. Typical CV curve for a Pt electrode in 0.5 M $H_2SO_4$ solution. The potential is wrt. mercury sulphate reference electrode (MSE) (0.64 V wrt. NHE) [121].*

Rutile oxides, $IrO_2$ and $RuO_2$ show different characteristic features in CV (Figure 2-12). The broad peaks are characteristic of $RuO_2$ and $IrO_2$ with no well-defined double layer region [60]. When $RuO_x$ or $IrO_x$ is placed in acid solution and its potential is varied, the valence state of the surface metal atoms changes while compensating for the charge with proton (transition metal has the capacity to exhibit difference valence states)[128]. During a voltammetric curve, the surface is oxidized and reduced reversibly through a mechanism involving proton exchange with the solution (pseudo-capacitance, faradaic process) [129]. During the forward positive potential scan the proton is expelled into the solution and an electron into the electrode. This may be accompanied by anionic adsorption or cation ejection. Similarly during the cathodic scan the proton is inserted into the electrode with electron from the source. This may be accompanied by anion desorption or cation insertion [130]. The double layer capacitance on the other hand arise due to the charge separation at the electrode/electrolyte interface (non-faradaic process) and is given by the equation(2-17) [131]. The capacitance in the CV, thus involves both double layer and pseudo capacitances as given in equation (2-18) [132]. Characteristics of both the capacitance processes are compared in Table 2-1 [131, 133].

$$C_{dl} = \frac{dq}{dV} \quad (2\text{-}17)$$

$$C = C_{\emptyset} + C_{dl} \quad (2\text{-}18)$$

*Table 2-1.Comparison of double layer and pseudocapacitance [131, 133].*

| **Double layer capacitance** | **Pseudo capacitance** |
|---|---|
| Non-faradaic | Involve faradaic process |
| ~20-50 µF $cm^{-2}$ | 2000 µF $cm^{-2}$ for single-state process; 200–500 µF $cm^{-2}$ for multi-state, overlapping processes |
| 'C' fairly constant with potential, except through the point of zero charge | 'C' fairly constant with potential for $RuO_2$; for single-state process, exhibits marked maximum, Can exhibit several maxima for overlapping, multi-state processes, as for H at Pt |
| Highly reversible charging/discharging | Quite reversible but has intrinsic electrode-kinetic rate limitation determined by faradaic resistance |
| Has restricted voltage range | Has restricted voltage range |
| Exhibits mirror-image voltammograms | Exhibits mirror-image voltammograms |

For $RuO_2$, The peaks at around +0.4 V and +1.0 V (vs. Ag/AgCl) are commonly attributed to the Ru (III)/Ru(IV) and Ru(IV)/Ru(V) surface transitions respectively [76, 89] due to the redox charge transition between the hydrogen ion ($H^+$) and $RuO_2$ surface [88, 128, 129, 134] as given in equation ((2-19),

$$RuO_x(OH)_y \leftrightarrows RuO_{x+\delta}(OH)_{y-\delta} + \delta H^+ + \delta e^- \quad (2\text{-}19)$$

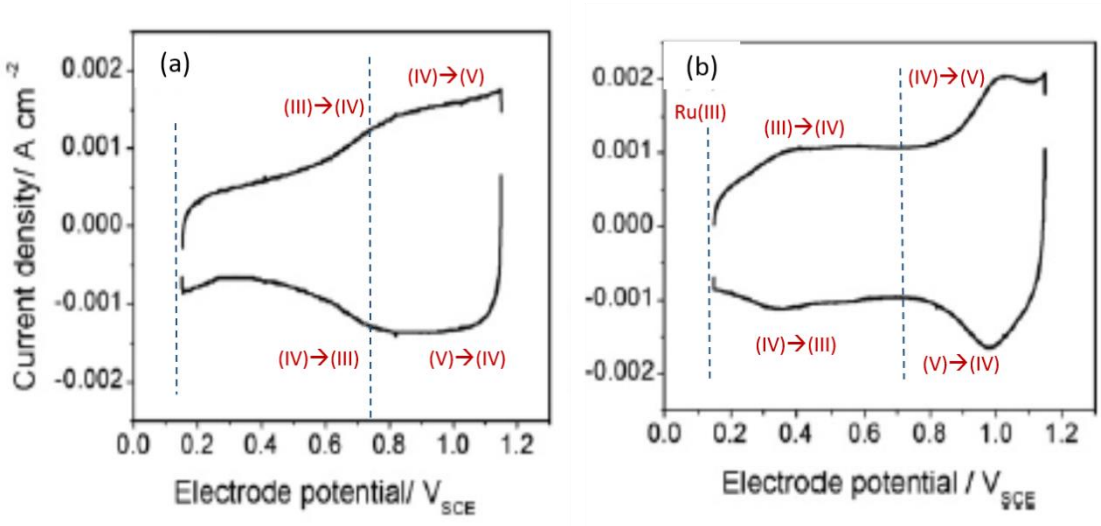


*Figure 2-12. Typical CV of (a) $IrO_2$ (b) $RuO_2$ in 0.5M $H_2SO_4$ solution [91].*

The redox transitions of $IrO_2$ are not as well distinguishable as for $RuO_2$. The characteristic peaks for $IrO_2$ at ~0.75 V and ~1 V (vs.Ag/AgCl) are attributed to the redox transition of Ir(III)/Ir(IV) and Ir(IV)/Ir(VI) (equation 2-18) [75, 135-137].

$$IrO_x(OH)_y + \leftrightarrows IrO_{x+\delta}(OH)_{y-\delta} + \delta H^+ + \delta e^- \qquad (2\text{-}20)$$

The integration of the CV curve gives the voltammetric charge (q*) values associated with the proton transfer in the potential window used. A direct correlation between the voltammetric charge and the active area was reported and is generally used to indicate the active surface area of the metal oxide catalyst [60].

Since glassy carbon is not suitable at anodic potential in acid solution due to possible corrosion and gold is not stable in phosphoric acid at anodic potential [138], A Ta working electrode was fabricated due to its high stability in 85% $H_3PO_4$ [52]. Ta metal rod was purchased from Advent Research Material, UK (4mm diameter, Purity 99.9%). The working electrode was fabricated by inserting PTFE outer body to the Ta metal (Figure 2-13). The Ta metal was surrounded by a heat shrinked PTFE tube (pro power-STFE4 9.5-1.2mnat - heatshrink) before inserting the Teflon outer body. The electrode was polished well using SiC paper (1200, 2400 and 4000 grade) until a mirror finish was obtained. This electrode was used for all the CV analysis described in this thesis.

*Figure 2-13. The Ta working electrode fabricated in-house.*

### 2.3.3 MEA preparation and electrolyser test

The membrane electrode assembly (MEA) was prepared by the catalyst coated membrane (CCM) method [139-141]. Nafion®-115 membrane was used for all MEA described in this thesis. Nafion® membrane was pre-treated with 3% $H_2O_2$, 0.5M $H_2SO_4$ and DI-water as described elsewhere [139, 141, 142]. The catalyst ink for anode and cathode were prepared by mixing the catalyst, ethanol and Nafion® binder. The catalyst ink was ultra sonicated until a uniform solution is obtained. Both anode and cathode catalyst were coated by spraying method on both sides of the membrane (Figure 2-14) which was kept on a hot plate at temperature of 50-80$^oC$ using a spray gun (Badger No 100LG, USA) with $N_2$ gas pressure. The loading of anode catalyst in literature generally varies from 1.5 - 3 mg $cm^{-2}$ and that of cathode catalyst (Pt black or Pt/C) normally varies from 0.3 - 1 mgPt $cm^{-2}$. The cathode catalyst can be either Pt black or carbon supported Pt [84, 143].

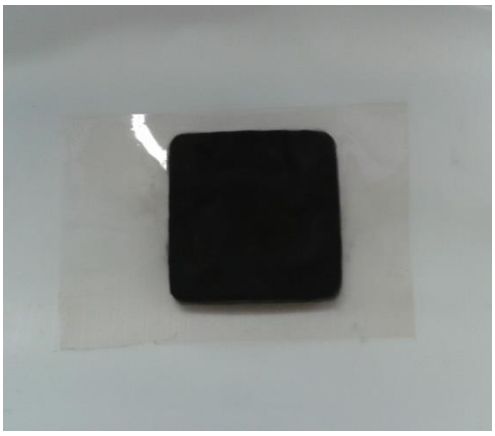

*Figure 2-14. The catalyst coated Nafion-115 membrane obtained by spraying method.*

The cell body was made up of a titanium parallel flow field of 1 $cm^2$ area (Figure 2-15(b)). The flow field plate was gold coated on both anode and cathode side by a physical vapour deposition method (PVD), in order to make a better contact with the electrode and to protect the Ti from oxidation on the anode. The PVD was carried out by sputtering at ACMA, Newcastle University. A gold coated titanium mesh and toray carbon paper were used as GDL/current collector on the anode and cathode side respectively. Toray carbon paper, [144, 145], titanium fibre [141], titanium sintered disc [143] etc. were used as anode current collector in the literature. The MEA prepared was sandwiched between the current collectors and assembled in the cell body with a torque of 2 N m. The anode catalyst loading was ~1.8-2 mg $cm^{-2}$ and the cathode loading was ~ 0.5 mg Pt $cm^{-2}$. The loading was calculated by spraying the catalyst ink on a PTFE sheet and weighing it before and after spraying. This method was adopted as it is difficult to weigh the Nafion® membrane accurately due to the high water uptake from the atmosphere. It was assumed that the same amount is deposited on the membrane. A silicone gasket was used to ensure proper seal of anode and cathode compartments. All MEA except for $Ru_xNb_{1-x}O_2$ (Chapter 6) were tested using the cell described above.

MEA tests of $Ru_xNb_{1-x}O_2$ (Chapter 6) were carried out at HySA, University of Western cape, South Africa using a cell made of stainless steel with an interdigitated flow field of 4$cm^2$ area with two porous titanium sinters (White washers, CSIR, South Africa, thickness 1 mm, 30% porosity) (Figure 2-15(a)). Titanium fibre (Bekenit, Japan, thickness 0.3 mm, porosity 60%) and carbon cloth were used as current collector on anode and cathode respectively. A Neware Battery testing system (Neware technology Ltd, China) was used as the power source. A schematic of the experimental set up is given in Figure 2-16.

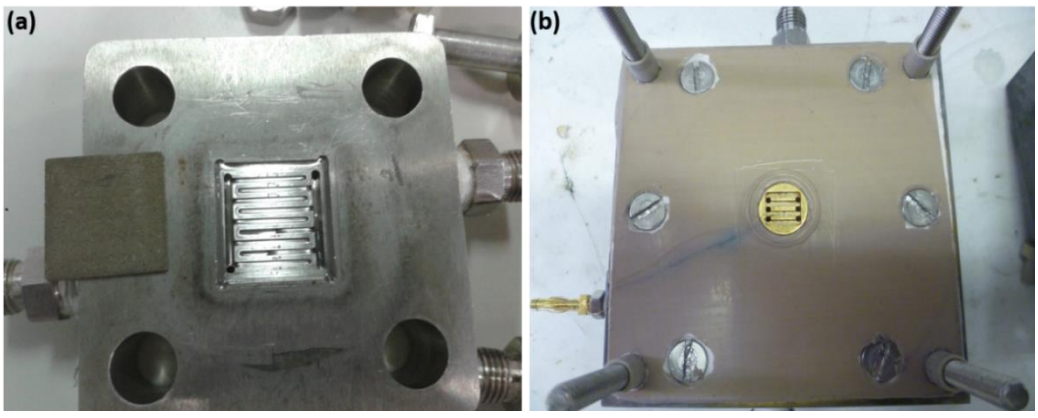


*Figure 2-15. The cell used for MEA analysis (a) stainless steel electrolyser cell (4 $cm^2$) and titanium porous sinter (b) titanium cell with gold coated flow field (1 $cm^2$).*

DI water was pumped using a peristaltic pump to the anode side of the cell which was heated to the required temperature by a heating rod using a temperature controller. The cathode was kept dry as there will be water transfer to the cathode through electro osmotic drag. Potential was applied using a power source (Thurlsby Thandar Instruments, PL3320) and current was recorded at various potentials. The experimental set up is schematically shown in Figure 2-16.

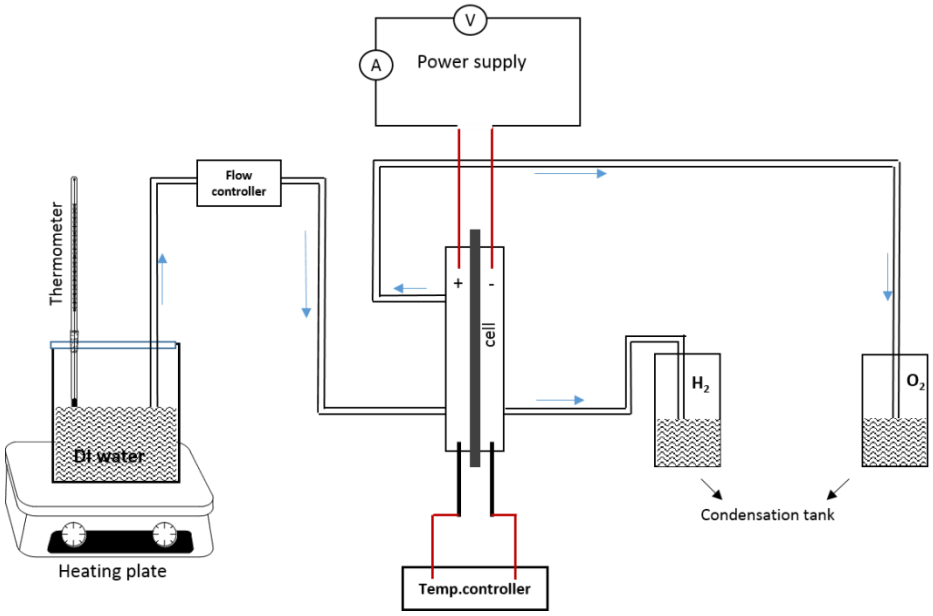


*Figure 2-16. Schematic of PEM water electrolyser set up for MEA analysis.*

### 2.3.4 Membrane conductivity measurement

The membrane proton conductivity is an important factor in a PEM system in order to achieve a high current density with a low ohmic resistance. Proton transfer in membrane can take place in two directions (i) in plane (ii) through plane. Through plane conductivity is more relevant in fuel cell operation. However since the through plane resistance when using thin membranes can be overwhelmed by the contact resistance between the membrane and the probes, leading to large errors in measurement, in plane conductivity measurement is more widely reported [146, 147]. Since the membrane is isotopic, the in plane and through plane conductivity should ideally be similar [147]. Four point and two point probe technique are generally used for in plane conductivity measurement. The four-point method has an advantage compared to two probe as it eliminates the probe resistance and resistance between the probe and the membrane surface [146].

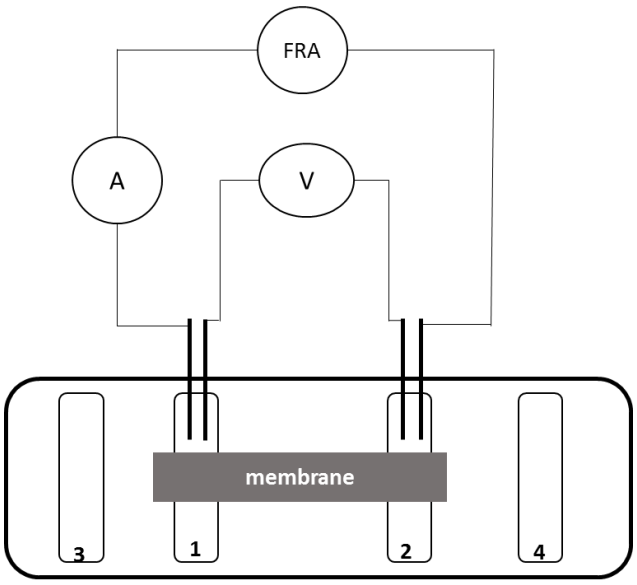


*Figure 2-17. Schematic diagram of two point probe technique for the measurement of in-plane membrane conductivity [146].*

Since the membrane resistance measured is significantly higher than the resistance of the probes (>1000 times), a two point probe is used in our study. The conductivity cell consists of four equally spaced (0.5 cm) Pt probes (Figure 2-17) and the membrane was sandwiched in the cell in contact with the two Pt probes (1 and 2). In the two points probe technique used, the current source and voltmeter was connected to two probes (1 and 2). The membranes were cut into 1 cm × 1 cm strips and placed across two Pt foils. AC impedance measurements were carried out between frequencies of 1 and 20 kHz by frequency response analyser (Voltech TF2000, UK). Figure 2-18 and Figure 2-19 gives the conductivity cell and experimental set up to measure the conductivity.

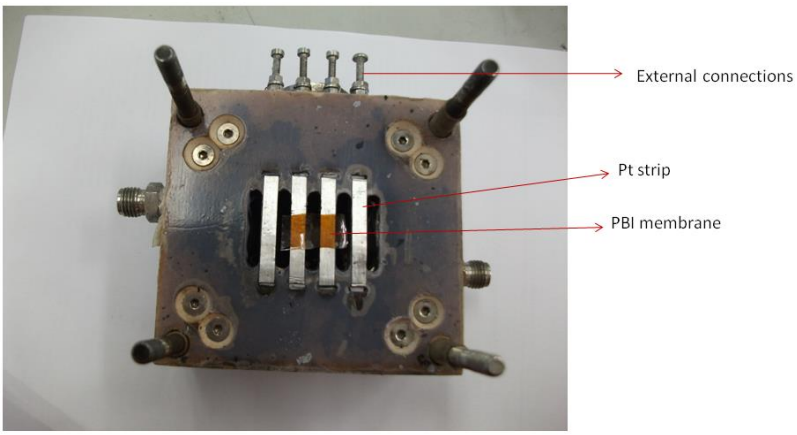


*Figure 2-18. The conductivity cell used to measure the conductivity of the membrane.*

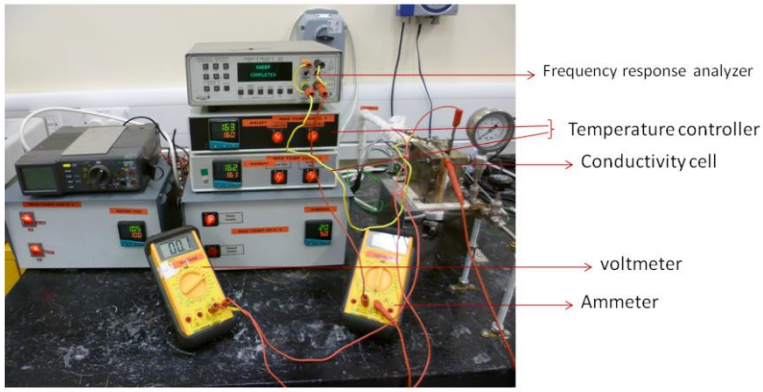


*Figure 2-19.Conductivity cell arrangement for measuring the conductivity of membrane.*

The conductivity of the membrane was calculated using the equation ((2-21).

$$\sigma = \frac{1}{R} \times \frac{l}{a} \qquad (2\text{-}21)$$

Where σ = conductivity (S $cm^{-1}$), R= Resistance (Ω), $l$ = length of the membrane (length between two Pt strips) (cm), $a$ = area of the membrane in between the two Pt strips = thickness × width of membrane ($cm^2$).

# Chapter-3. Investigation of supported anode catalyst for PEM water electrolyser

Antimony doped tin oxide (ATO) was studied as a potential support material for $IrO_2$ in PEMWE. $IrO_2$ of various loadings was deposited on the ATO support using the Adams method. The physical and electrochemical characterization of the catalyst was carried out using XRD, SEM, TEM, powder conductivity, CV and MEA polarisation.

## 1.8 Introduction

Proton exchange membrane water electrolysis (PEMWE) is a promising technology for the production of hydrogen from water. However state of the art PEMWE have drawbacks such as high material cost (PEM, catalyst and bipolar plates), high over potential for the OER, and low operating temperature due to possible dehydration of the Nafion® membrane at temperature above 100$^{o}$C. $IrO_2$ and $RuO_2$ are the most active electrocatalyst for the OER in PEMWE [148], but the stability of $RuO_2$ at high anodic potential is poor [76]. $IrO_2$ on the other hand has very good stability and gives the highest activity for the OER after $RuO_2$, but has higher cost. An on-going aim of electrocatalyst research is to increase the performance of the electrode while reducing the cost [149], which is an important step towards commercialisation of PEMWE. There are different approaches to reduce precious metal loading on an electrode, such as adding a non-precious element to form an alloy/bimetallic mixture or support the active catalyst on a cheap and conductive high surface area support material [111, 150]. Support materials for electrocatalysts help in increasing the dispersion of the catalyst particles and thus increasing the specific surface area of the catalyst. The support also helps to reduce the agglomeration of the active catalyst during long term operation [149, 151]. High surface area carbon supports are typically used in fuel cells, but their high corrosion rate (equation (3-1) restricts its use in the PEMWE anode [151, 152].

$$C + 2H_2O \rightarrow CO_2 + 4H^+ + 4e^- \ (0.207\ \text{V vs. SHE}, 25^{o}\text{C}) \qquad (3\text{-}1)$$

The standard electrode potential for the reaction ((3-1) at 25 °C is 0.207 V vs. SHE [152] which means that carbon is thermodynamically unstable above this potential. However severe oxidation occurs only at potential above 0.9 V vs. SHE in presence of water [153, 154]. Since a typical electrolyser operates at a potential >1.5 V vs. SHE, it is not possible

to use carbon on the electrolyser anode. An alternate material has to be investigated to take advantage of supported catalysts in a PEMWE environment. Due to the high oxidation atmosphere present in the electrolyser anode (high anodic potential up to +2 V vs. SHE and oxygen evolution), materials that can be used as support at electrolyser anode are limited. An ideal catalyst support should have high surface area, good electrical conductivity, thermal and electrochemical stability in the PEMWE environment [150, 155, 156].

Ma et al [150] studied TiC supported Ir as OER catalyst. Commercial TiC powder (Fujian Sinocera Advanced Materials Co.Ltd) with BET surface area of 14.41 $m^2 g^{-1}$ was used as support material for Ir. 20 wt.% Ir was deposited on the TiC by chemical reduction and deposition with ultrasonic dispersion. A broadening of the Ir peak was observed in XRD for the 20 wt.% Ir-TiC compared to the pristine Ir indicating a better dispersion of Ir on the TiC forming smaller crystallites [150]. TEM imaging showed the TiC particle size of 50-150 nm and Ir particle size of 10-40 nm. Higher performance of Ir/TiC compared to pristine Ir was obtained in cyclic voltammetry studies in 0.5M $H_2SO_4$ [150]..The current density value at potential 1.5 V of the kinetic region for the 20% Ir-TiC was about 9 times that of the pristine Ir for the OER [150].

An effect of Ir loading on the MEA performance was evaluated later by the same author [157]. It was found that MEA performance (Nafion-112 membrane, 80$^oC$, atmospheric pressure) increased with an increase in Ir loading (10 wt.%, 20 wt.% and 40 wt.% Ir/TiC) [157]. A current density of 1002 mA $cm^{-2}$ @ 1.8 V was obtained for 40% Ir-TiC compared to 840 mA $cm^{-2}$ for 20 wt.% Ir-TiC [157]. The MEA performance and stability comparison of the unsupported Ir catalyst and 20% Ir-TiC showed a higher activity and stability up to 4 hr for the 20% Ir-TiC compared to pristine Ir [17]. However it was reported elsewhere that corrosion of the TiC occured at anodic potential >0.8 V vs. SHE forming $Ti^{4+}$, CO and $CO_2$ [158-161]. At a potential of ~1.05 V a passivation occurs due to the $TiO_2$ layer formation and severe corrosion is observed at a potential >1.75 V [161]. The non-conducting $TiO_2$ layer formation will reduce the conductivity and performance of the catalyst during long term operation.

Other carbides such as Si doped SiC (Si-SiC) [112] and TaC [162] were also studied as support material for an OER catalyst. $IrO_2$ supported TaC prepared by the Adams method was found to be forming sodium-tantalum complex during the synthesis stage [162]. Even though TaC has good electronic conductivity (118 S $cm^{-1}$), it decreased by 10 orders of

magnitude after the Adams method of synthesis due to the $NaTaO_3$ complex formation [162]. TaC has also a very low BET surface area (2.4 $m^2 g^{-1}$) [162]. The TGA analysis of TaC showed that TaC starts oxidizing to $Ta_2O_5$ at a temperature > 330$^oC$ and severe oxidation occur at a temperature > 600$^oC$ with complete conversion to $Ta_2O_5$ [162]. A performance similar to $IrO_2$ was observed for $IrO_2$ content of ≥ 50 wt.% from a half-cell study [162]. Si-SiC support also has very low electronic conductivity ($1.8\times10^{-5}$ S $cm^{-1}$) and surface area (6 $m^2$ $g^{-1}$) [112]. $IrO_2$ supported on Si-SiC was prepared with various loadings by the Adams method [112]. The pristine $IrO_2$, 90% $IrO_2$/Si-SiC and 80% $IrO_2$/Si-SiC showed crystallite size of approximately 5.5 nm, 3 nm and 2.5 nm respectively [112]. The CV studies of the catalyst in $H_3PO_4$ showed a higher active area for 90% $IrO_2$/Si-SiC and 80% $IrO_2$/Si-SiC compared to the pristine $IrO_2$ [112]. This was explained based on the high dispersion of the $IrO_2$ forming smaller particles on Si-SiC resulting in higher active surface area.

Tungsten carbide (WC) is one of the most widely studied fuel cell catalyst supports among the transition metal carbides due its high thermal stability, high electronic conductivity ($10^5$ S $cm^{-1}$ at 20$^oC$) and catalytic behaviour similar to Pt [163-166]. However at anodic potential above +0.8 V, WC forms a semi conductive oxide $WO_3$ [163, 167, 168] which is an n-type semiconductor with band gap of 2.6-2.8 eV [169]. $WO_3$ is not stable and dissolves in acid as the tungstate ion $H_xWO_3$ [168, 170, 171] making it unsuitable as a support in anodic, acidic environment. Among the metal nitrides, TiN is the most studied nitride due to its good electrical conductivity (4000 S $cm^{-1}$) and corrosion resistance [156]. But TiN forms a native oxynitride layer on its surface due to atmospheric oxidation [172] and at anodic potential of about +0.8-0.9 V, it forms passivating $TiO_2$ layer on the surface [172] limiting its use as support material at high anodic potential.

Metal oxides generally have good corrosion resistance, though their electronic conductivity is poor. Different methods were adopted to increase the conductivity of the oxides such as doping with a foreign element and using reduced forms of the oxide [152, 173]. $Ti_4O_7$, commercially known as Ebonex is the major component in the homologous series of titanium sub oxides with general formula $Ti_nO_{2n-1}$ ($4 \leq n \leq 10$) and have conductivity of about 1000 S $cm^{-1}$ [152] and has been used as support material for oxygen reduction reaction (ORR) and OER catalysts [174]. But on long term polarisation at high anodic potentials, a non-conductive $TiO_2$ layer was formed on this material limiting it use as support material [175].

$SnO_2$, though it is a poor electron conductor, on doping with Sb(V), In(III) or $F^-$ can increase its conductivity significantly [176, 177]. $Sb_2O_5$ forms a solid solution with $SnO_2$ and around 20 wt.% of $Sb_2O_5$ can be added forming an n-type semiconducting oxide [178]. ATO is widely used in electronic conducting coatings, gas sensors, solar battery transparent electrodes [179, 180] and is stable in acidic media [181].

Marshall et al [182] studied ATO nanoparticle incorporated $IrO_2$ DSA type electrode for OER. A particle size of around 100 nm for $IrO_2$ and 20 nm for ATO was obtained in TEM analysis [182]. The $IrO_2$ electrode showed a more compact structure whereas the ATO nanoparticle incorporated $IrO_2$ electrode showed more rough and particle like structure [182]. It was assumed that ATO nanoparticles act as reinforcing material in the DSA electrode where the cracks between the $IrO_2$ particles were filled with ATO nanoparticles. This stabilises the electrode by reducing the penetration of acid to the titanium base metal [182]. Half-cell studies carried out with the prepared DSA electrode in 0.5M $H_2SO_4$ solution showed a higher activity with 10 wt.% ATO nanoparticle addition. This was attributed to the higher dispersion of active $IrO_2$ on inactive ATO nanoparticles [182]. A bimetallic $IrO_2$-$RuO_2$ supported on commercial ATO nanoparticle prepared by thermal decomposition at 450$^oC$ for 1 hour with metal loadings of 5, 10 and 20 wt.% was also studied by Marshall et al [183]. XRD of the supported catalysts showed peaks of $SnO_2$ only with no evidence of $IrO_2$ and $RuO_2$ crystalline phase and was assumed that the particles are amorphous and small $Ir_xRu_{1-x}O_2$ clusters are formed on the ATO support. CV studies in 0.5M $H_2SO_4$ showed high activity for 20 wt.% $Ru_{0.25}Ir_{0.75}O_2$/ATO on normalising the current with the catalyst loading. The OER performance decreased with a decrease in catalyst loading and Ru content in the bimetallic oxide [183]. It was also proposed by the author that some penetration of $IrO_2$ into the ATO particle is also possible which will help in stabilising the electrode [182, 184].

Yin et al [185] used ATO-carbon composite supported Pt catalyst for ORR. A 5 mol% Sb addition was found to give the maximum conductivity for ATO (0.83 S $cm^{-1}$ and 1.1 S $cm^{-1}$ at room temperature and 130$^oC$ respectively) and an ATO-carbon composite was prepared as support material for Pt. The ORR activity of the 20 wt.% Pt on ATO, carbon and ATO-carbon composite support were studied using CV and a rotating disk electrode (RDE) technique in 0.5 M $H_2SO_4$. The Pt/C-ATO was found to be a more efficient ORR catalyst than Pt/C from the RDE analysis [185], however the stability test at 3000 potential cycles showed higher stability for Pt/ATO than the Pt/C and Pt/C-ATO

composite. This was attributed to the electronic interaction between ATO and Pt as well as the high electrochemical stability of ATO [185].

A high stability of Pt supported on ATO in 85% phosphoric acid was reported by Tseung et al [149]. An unsupported Pt and ATO supported Pt (~10 wt.% Pt) were potentiostatically held at +700 mV vs. DHE in 85% $H_3PO_4$ at 150$^oC$ for 720 h. It was found that unsupported Pt lost 63% of initial surface area whereas ATO supported Pt lost only 25% of its initial surface area [149]. The performance of the ATO supported Pt after the stability test was also higher than that of the unsupported Pt [149]. This was attributed to the lower agglomeration of the Pt crystallites on the ATO [149].

ATO was recently used as support for a $IrO_2$-Pt catalyst in a unitised regenerative fuel cell [186]. A 50:50 wt.% ratio of $IrO_2$-Pt was supported on ATO nanoparticles (30 wt.% loading). XRD, TEM and BET analysis showed a particle size of 4-6 nm and surface area of 115.7 $m^2\ g^{-1}$ for the ATO support. The MEA analysis with Nafion-115 membrane at 80$^oC$ showed better performance for OER than ORR and was attributed to the Pt oxide formation at high anodic potential which affects the ORR reaction but not significantly affect the OER [186].

ATO was selected as the support material here due to its high electronic conductivity, stability in acidic conditions [149], electrochemical stability at anodic potential [187] and commercial availability with reasonably good surface area (20-40 $m^2\ g^{-1}$). The objective of this chapter was to systematically investigate the effect of various parameters such as particle size, electronic conductivity and surface area on the performance of the ATO supported $IrO_2$ catalyst in PEMWE anode.

## 3.1 Experimental:

Commercially available ATO nanoparticles, Nanotek, 99.5% ($Sb_2O_5$:$SnO_2$ 10:90 wt.%) from Alfa aesar (particle size of 22-44 nm, BET surface area 20-40 $m^2\ g^{-1}$) were used as the support. $H_2IrCl_6.xH_2O$ (Alfa aesar), $NaNO_3$ (Sigma Aldrich) were used as Ir precursor and oxidizing agent respectively.

### 3.1.1 Synthesis of catalyst

Supported $IrO_2$ catalyst was prepared by the modified Adams fusion method. The $H_2IrCl_6$ solution was prepared in isopropanol (0.01 M). The ATO support was well dispersed in isopropanol to which the $H_2IrCl_6$ solution was added drop wise. This enabled good dispersion of Ir precursor on the ATO support. The solution was stirred well for 3 hours

followed by $NaNO_3$ addition and further stirring overnight. The solvent was evaporated slowly and the obtained mixture was dried well and calcined at 500$^oC$ for 1 hour in a muffle furnace. The reactions occurring in the Adams method is given by equation ((2-3) and ((2-4) [111]. The NaCl residue formed was dissolved in water and the catalyst was washed with a copious amount of DI water and dried in open air oven.

## 3.2 Characterization of the catalysts

Physical characterizations of the catalysts were carried out by XRD (section 2.2.1), SEM (section 2.2.3), TEM (section 2.2.5) EDX (section 2.2.4), XPS (section 2.2.2) and BET surface area (section 2.2.7) analysis. The powder conductivity was measured using the set up described in section 2.3.1.

### 3.2.1 Electrochemical characterization

The electrochemical characterization was carried out in a voltalab PGZ50 potentiostat. The catalyst ink was prepared in isopropanol: water (3:2) solvent with Nafion® binder content of 20 wt.%. The ink was dispersed well in an ultra-sonic bath for half an hour before drop casting 10 µl on the Ta working electrode. The loading on the electrode was ~500 µg $cm^{-2}$. An Ag/AgCl (sat.KCl) and Pt wire were used as reference and counter electrode respectively. The electrolyte was deoxygenated by passing $N_2$ gas through the electrolyte for 15 minutes before carrying out the test. Cyclic voltammetry were carried out at a potential between +0 and +1.25 V vs. Ag/AgCl. A precondition was carried out between these potentials for 10 cycles at 100 mV $s^{-1}$. CV's at different scan rates starting from 200 mV $s^{-1}$ to 5 mV $s^{-1}$ were carried out at room temperature and at 20 mV $s^{-1}$ for higher temperatures. Total of 3 cycles were carried out and the third cycle was recorded whereby a stable CV was obtained. Current values were normalised to the total catalyst weight on the electrode.

MEA with the prepared catalysts as anode were prepared using Nafion® -115 membrane by the CCM method. Catalyst ink was prepared with catalyst, Nafion® and ethanol solvent and sprayed directly on the membrane. Pt/C (20 wt.%) from Alfa aesar was used as cathode catalyst. The Nafion® content on both electrodes was 15 wt.%. The Nafion® membrane was pre-treated with $H_2O_2$, $H_2SO_4$ and DI-water successively before use. The cell body was made up of gold coated titanium with 1 $cm^2$ flow field area (Figure 2-15b). A gold coated Ti mesh and carbon paper (Torray) was used as current collector on the anode and cathode respectively. The MEA prepared was sandwiched between the current

collectors and assembled in the cell body with a torque of 2 N m. The anode and cathode catalyst loadings were ~1.8 - 2 mg $cm^{-2}$ and ~ 0.5 mg Pt $cm^{-2}$ respectively.

DI water was pumped using a peristaltic pump to the anode side of the cell which was pre-heated to the required temperature by a heating rod and controller. The cathode was kept dry. The voltage applied and the current values were measured using power source (Thurlsby Thandar Instruments, PL3320).

## 3.3 Result and Discussion

### 3.3.1 Thermal stability

The thermal stability of the support materials was studied using TGA analysis. It is important to understand the thermal stability of the support materials at temperatures of up to 600$^{o}$C, as it is normally used for the preparation of the oxide catalyst and there is a possibility of thermal oxidation/decomposition of the support at high temperature. The TGA of some of the commercially available materials such as titanium carbide (TiC) (Alfa aesar, 30-50 nm APS powder), titanium nitride (TiN) (Sigma Aldrich, <3 μm), tungsten carbide (WC) (Sigma Aldrich, powder, 2 μm, 99%) indium tin oxide (ITO) (Alfa aesar, 17-28 nm) and antimony tin oxide (ATO) (Alfa aesar, 22-44 nm) are given in Figure 3-1.

The TiC did not show any significant weight loss below 330$^{o}$C. A slight weight loss (0.9224%) was observed below 330$^{o}$C which might be due to desorption of water adsorbed on the surface. A significant weight gain (25%) from 330$^{o}$C to 650$^{o}$C indicates that oxidation of TiC starts at this temperature, forming $TiO_2$ and $CO_2$. Both stoichiometric and non-stoichiometric oxides ($TiO_2$, $Ti_3O_5$, $Ti_2O_3$ and TiO) can be formed during the oxidation [188, 189]. The colour of the sample changed from black to white after the analysis indicating the $TiO_2$ formation. TiN on other hand showed a much higher thermal stability up to 400$^{o}$C. A weight gain was observed only above 400$^{o}$C (29% up to 820$^{o}$C). WC showed thermal stability up to 500$^{o}$C with an onset of oxidation > 500$^{o}$C (17.65% weight gain up to 800$^{o}$C). Even though the bulk oxidation occurred at the mentioned onset temperature for all samples, a surface oxidation will occur even at low temperature. It has been proposed that carbides replace oxygen from the air forming oxy carbides on the surface before the bulk oxidation begins [190]. The $TiO_2$ surface layer formed as a result of oxidation will reduce the conductivity of the support. ITO and ATO showed excellent thermal stability up to 800$^{o}$C with no significant weight gain/loss. A

higher thermal stability of ITO and Pt supported ITO up to 1000$^{o}$C was reported elsewhere [152]. ITO and ATO were selected as support material in this study. The ITO support is described in chapter 4.

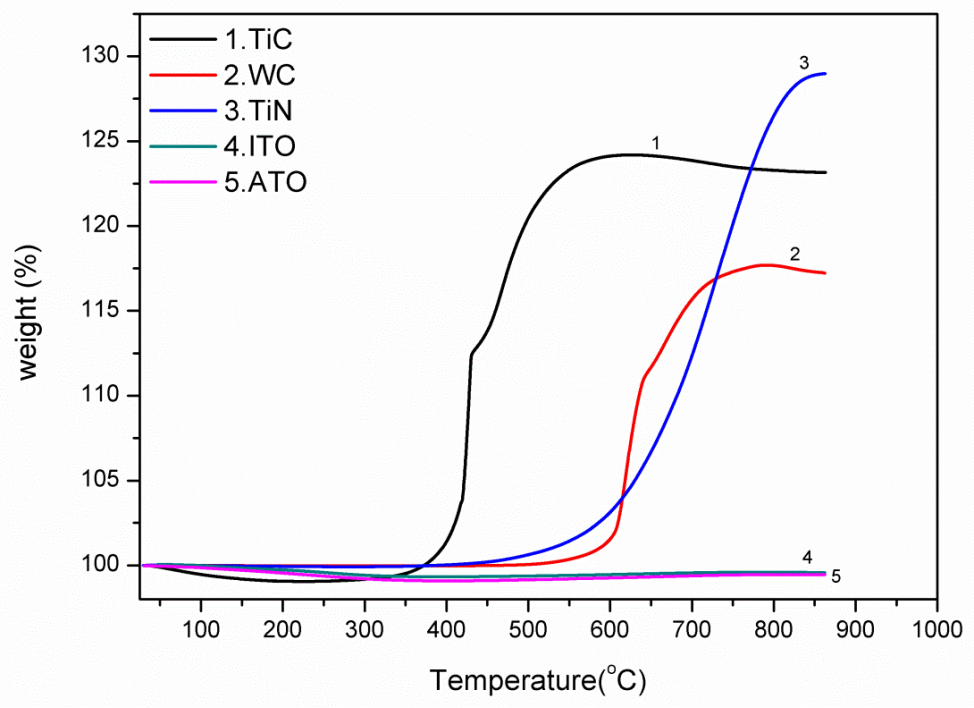


*Figure 3-1. TGA of some of the common commercial support materials.*

### 3.3.2 Powder conductivity

The conductivity (σ) measured at room temperature using the cell described in section 2.3.1 gives a linear relationship between the thicknesses and resistance (Figure 3-2) for the catalyst powder samples. The conductivity was calculated from the slope of the plot using the equations ((2-14) and ((2-15) and is given in Table 3-2 .

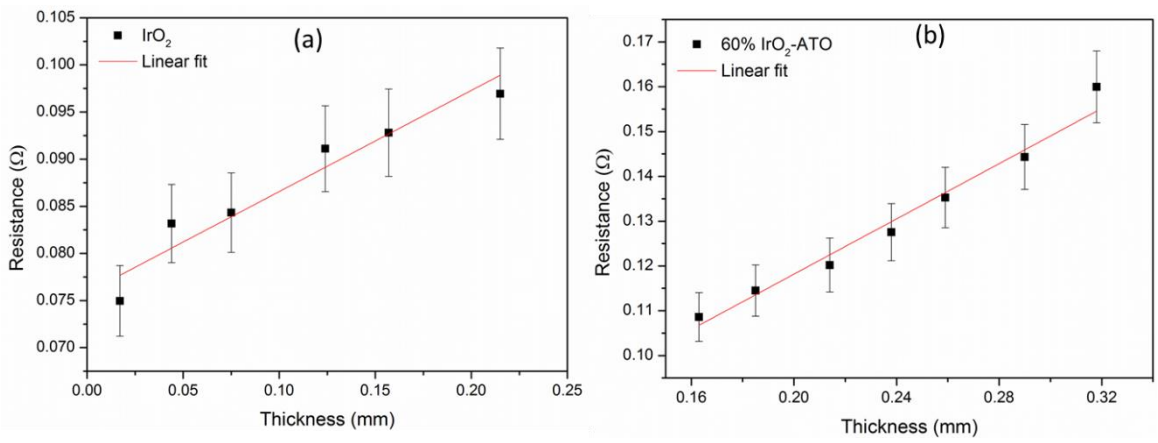


*Figure 3-2. Thickness (l) vs. resistance (R) plot of (a) $IrO_2$ and (b) 60% $IrO_2$-ATO.*

The conductivity of the pristine $IrO_2$ (4.9 S $cm^{-1}$) was 3 orders of magnitude higher than that of the ATO support ($4.3\times10^{-3}$ S $cm^{-1}$). A conductivity of the same order of magnitude as that of the pristine $IrO_2$ was reported elsewhere [111]. The conductivity of the supported catalyst decreased with a decrease in $IrO_2$ loading (Figure 3-4) indicating that the conductivity was contributed mainly by the $IrO_2$. A 60% $IrO_2$ (1.4 S $cm^{-1}$) loading has a conductivity of 3 orders of magnitude higher compared to the ATO support ($4.3\times10^{-3}$ S $cm^{-1}$). It was thus clear that even though the support itself has lower conductivity, addition of $IrO_2$ increases the conductivity of the supported catalyst particles significantly. An increase in conductivity of 5 orders of magnitude was observed for 60% $Pt/TiO_2$ compared to $TiO_2$ support elsewhere [191]. The resistivity in oxides was reported to mainly come from the inter grain region and the conduction mainly occurs by a 'hopping mechanism' between the grains [111]. Thus, the conductivity depends on various factors such as the conductivity of individual particles, contact between the particles, their packing and applied pressure [115]. Compared to DSA type electrode, where the oxide film is formed on a metal support such as titanium, a powder catalyst system will have higher resistivity due to large number of grain regions [192]. Lodi et al [192] reported that, DSA electrode with cracked morphology of $RuO_2$ has two orders of magnitude higher resistivity compared to compact $RuO_2$ due to the breakdown of conduction paths in the cracked morphology. The conductivity of the supported $IrO_2$ for loading up to 60% $IrO_2$-ATO was of the same order of magnitude to that of the pristine $IrO_2$. Conductivity decreased by 10 times from 60% $IrO_2$-ATO (1.4 S $cm^{-1}$) to 40% $IrO_2$-ATO ($2.0\times10^{-1}$ S $cm^{-1}$). The large conductivity at higher loading can be attributed to the higher $IrO_2$ amount as well as the full coverage of ATO surface by the conductive $IrO_2$

forming a continuous network. Since conductivity of the ATO ($4.3\times10^{-3}$ S $cm^{-1}$) was 3 orders of magnitude lower than the pristine $IrO_2$ (4.9 S $cm^{-1}$), a partial coverage of the ATO by $IrO_2$ will reduce the conduction network formed by the $IrO_2$ (Figure 3-3) [193]. A similar behaviour in conductivity was also observed for ITO supported $IrO_2$ (Chapter-4). For the same reason of conductivity, a lower loading of below 20% is not being used in the DSA electrode, as $TiO_2$ is non-conductive [55, 187]. The loss in conductivity of catalysts will contribute to the performance loss of the MEA in PEMWE [111].

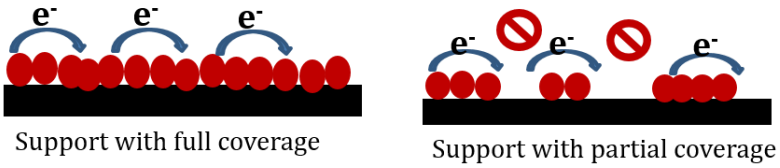


*Figure 3-3. Schematic of breakdown of electron conduction path due to the partial coverage of the support.*

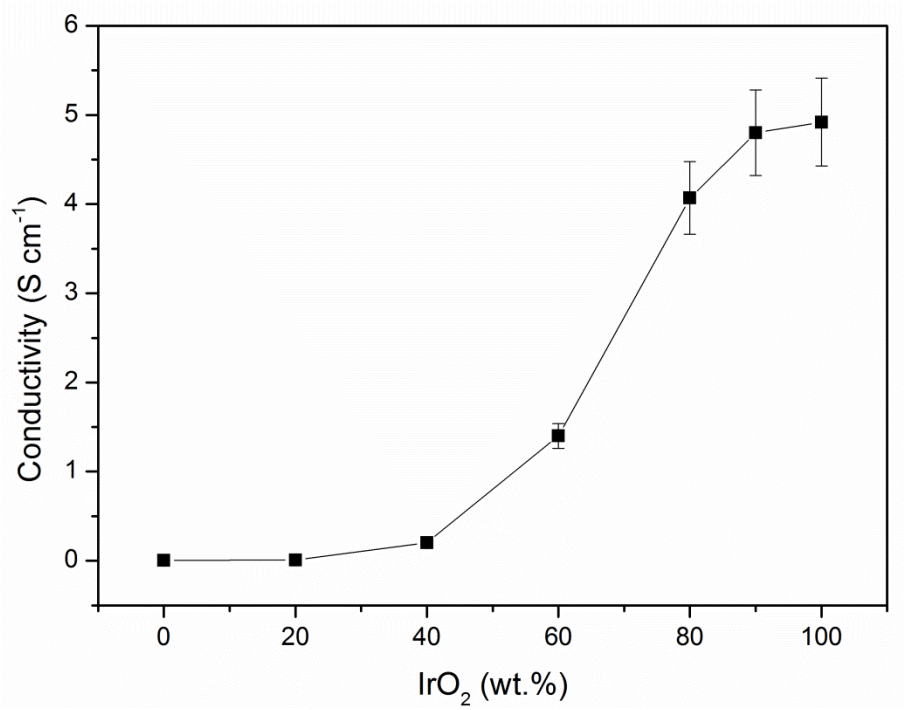


*Figure 3-4. Conductivity of the $IrO_2$-ATO catalyst with respect to the $IrO_2$ loading.*

Polonsky et al [162] reported a decrease by 10 orders of magnitude in conductivity of TaC from 118 S $cm^{-1}$ after the Adams method of synthesis and was attributed to the sodium-tantalum complex formation during the synthesis. No peaks other than for ATO

and $IrO_2$ were found in XRD or EDX analysis in our system and it can be concluded that no side reaction occurred between the ATO and $NaNO_3$.

Assuming anode catalyst loading as 1-3 mg $cm^{-2}$, the catalyst layer thickness will be around 5-10 μm. The ohmic drop by the catalyst will be thus approximately 0.05-0.1, 0.5-1, 5-10 and 50-100 mV at 1 A $cm^{-2}$ for oxide resistivity's of 0.1, 1, 10 and 100 Ω cm respectively [111]. Taking an acceptable ohmic drop on the anode electrode as 5-10 mV, Marshall et al [111] proposed a resistivity value of 10 Ω $cm^{-1}$ or less as acceptable conductivity for the anode catalyst in PEMWE. According to this, a loading of ≥ 40% $IrO_2$-ATO can be used as anode catalyst in PEMWE without having significant Ohmic drop in the electrode. However, resistivity of the membrane and ionomer needs to be considered in real electrolyser operation.

### 3.3.3 XRD

The XRD plot of the pristine $IrO_2$ and the ATO support is given in Figure 3-5. The ATO showed the characteristic peaks of $SnO_2$ (JCPDS-041-1445) at 26.6, 33.9, 38.0 and 51.8$^o$. No peaks of $Sb_2O_5$ were observed in ATO due to the entrance of $Sb_2O_5$ (10 wt.%) dopant in the $SnO_2$ lattice [185]. The $IrO_2$ showed the rutile structure with characteristic peak at 28.0, 34.7 and 54.1$^o$ (JCPDS-015-0876). The peaks of ATO were sharp and narrow compared to $IrO_2$, indicating a larger crystallite size of the ATO particles. The characteristic peaks of $IrO_2$ and $SnO_2$ in the supported catalysts are shown in Figure 3-6 for 60% $IrO_2$-ATO as representative example.

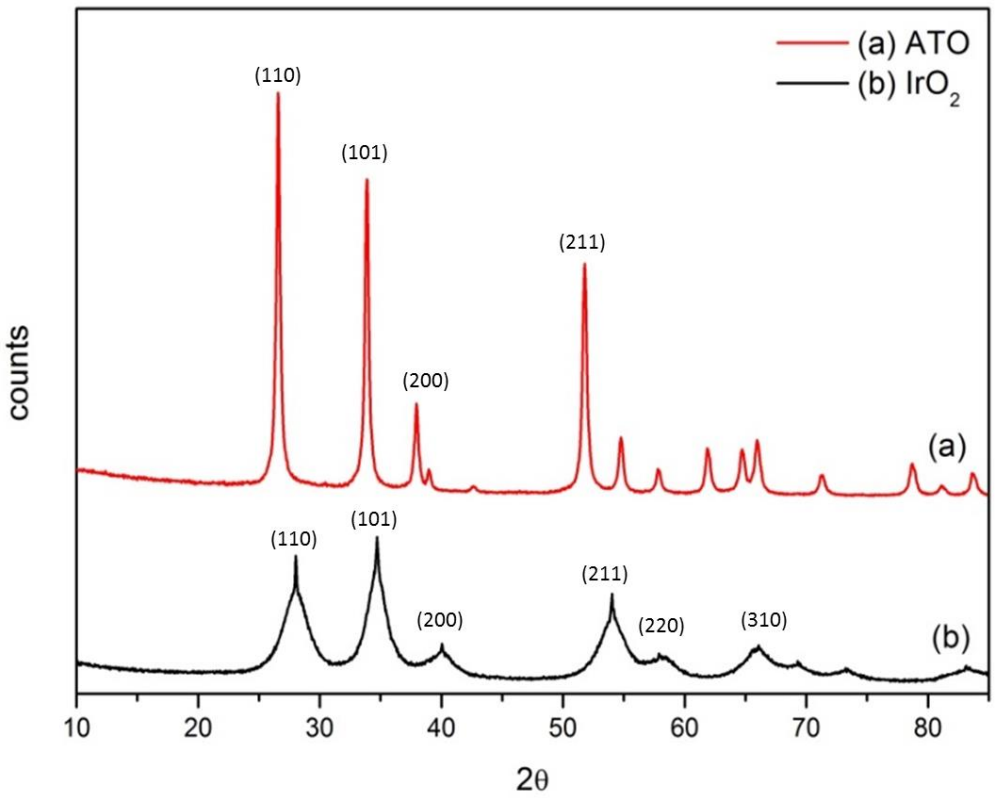


*Figure 3-5. XRD spectra of (a) ATO support and (b) unsupported $IrO_2$.*

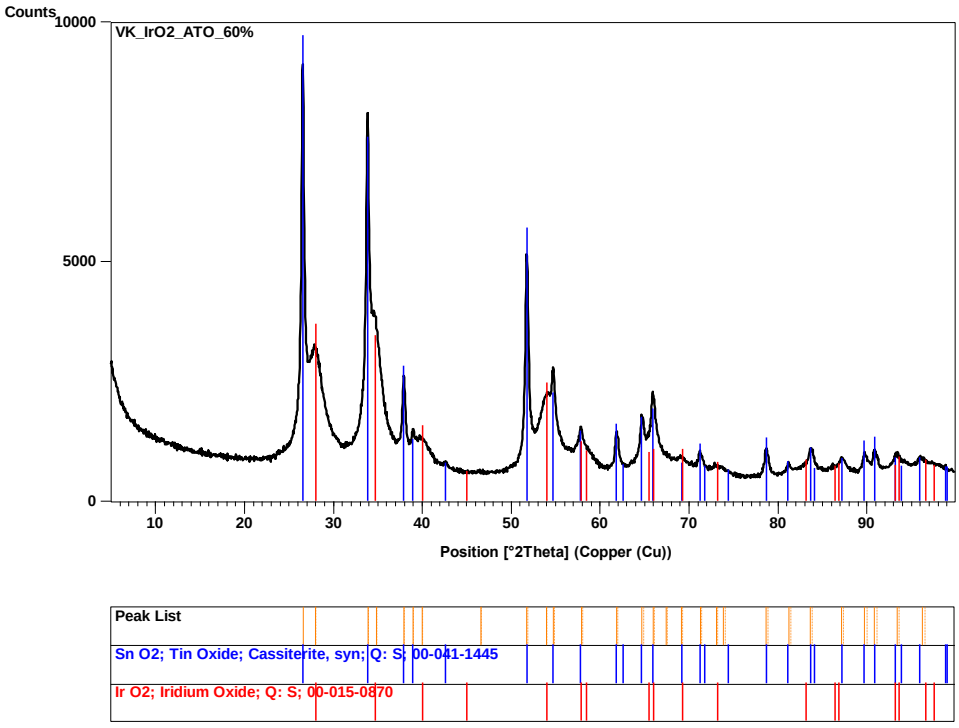


*Figure 3-6. XRD spectra of 60% $IrO_2$-ATO showing characteristic peaks of $IrO_2$ and $SnO_2$.*

The XRD of the supported catalysts with different $IrO_2$ loading is compared in Figure 3-7. The intensity of the $IrO_2$ peaks disappear gradually and $SnO_2$ peaks becomes prominent with the increase of the ATO wt.%. Two separate peaks for $SnO_2$ and $IrO_2$ were clear but were closely positioned. No shift in $IrO_2$ and $SnO_2$ peak position with composition was observed. This indicates that $IrO_2$ and ATO were present as separate phase and a single phase solid solution between the $IrO_2$ and $SnO_2$ was not formed. $SnO_2$ has a rutile structure similar to $IrO_2$ and the ionic radii of $Ir^{4+}$ (0.077 nm) is close to that of $Sn^{4+}$ (0.083 nm) [111]. According to Hume-Rothery theory, a solid solution/meta stable solution formation between the two oxides is possible. The solid solution formation was reported to help in the adhesion between the catalyst and the support and increase the stability of supported catalyst as in DSA electrode [182, 194-196]. Since the ATO was added as single phase to the Ir precursor for the synthesis of supported catalyst, an atomic level interaction between the two to form solid solution is unlikely whereas in an alloy catalyst preparation the both Ir and Sn precursor interact each other before the calcination and forms solid solution during the calcination.

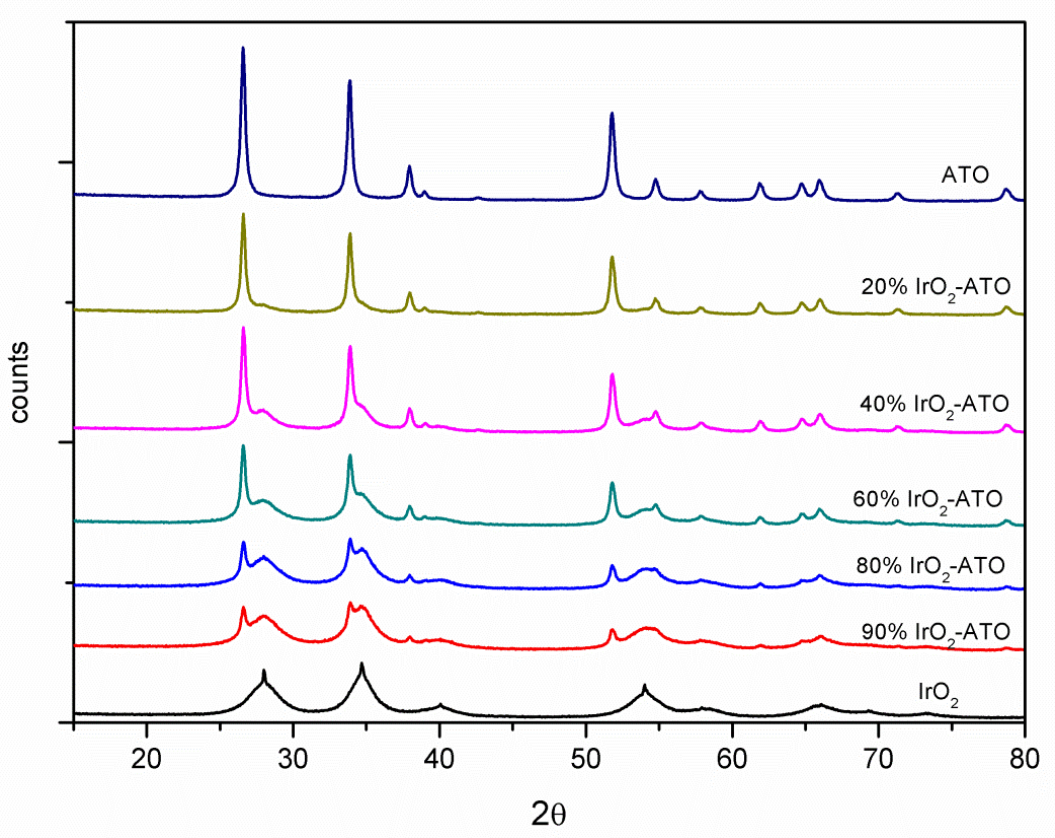


*Figure 3-7. XRD of $IrO_2$-ATO at different $IrO_2$ loading.*

Since the $IrO_2$ and $SnO_2$ peaks were closely positioned, a peak fitting (lorrenzian model) was adapted to de-convolute the peaks for all supported catalysts as given in Figure 3-8. The crystallite size calculated using the model is given in Table 3-1. The average crystallite sizes were calculated from the peaks at $28^o$ and $34.7^o$ for $IrO_2$ (Table 3-2) and $26.6^o$ and $33.9^o$ for $SnO_2$. The evolution of crystallite size with $IrO_2$ loading is plotted in Figure 3-9. The pristine $IrO_2$ showed an average crystallite size of 6 nm which decreased with decrease in $IrO_2$ loading up to 60% $IrO_2$-ATO and starts increasing on reducing $IrO_2$ loading further (Figure 3-9). The lowest $IrO_2$ crystallite size was obtained for 90% $IrO_2$-ATO (3.8 nm). The lower crystallite size for supported catalysts indicates that the support affects the crystallisation of $IrO_2$. Better particle dispersion on the support might have been achieved giving rise to smaller particles. The increase in crystallite size at lower $IrO_2$ loading may be explained based on the nucleation sites available for the crystallite formation [162]. Pure $IrO_2$ is formed as a homogenous phase where it has to cross a significant energy barrier for the formation of the first $IrO_2$ nucleation site, whereas a supported catalyst is a heterogeneous system whereby may $IrO_2$ nucleation sites are formed on the support. The energy barrier in the latter case is lower than the former. Once a nucleation centre is formed, it is energetically favourable for $IrO_2$ to grow on it. At lower loading the first nucleation centre is formed easily due to the lower activation energy for the first $IrO_2$ crystallite formation and subsequently $IrO_2$ grows on it leading to a large particle size [162]. The average crystallite size of $SnO_2$ did not change significantly with composition and had more or less same crystallite size (22-24 nm) (Figure 3-9).

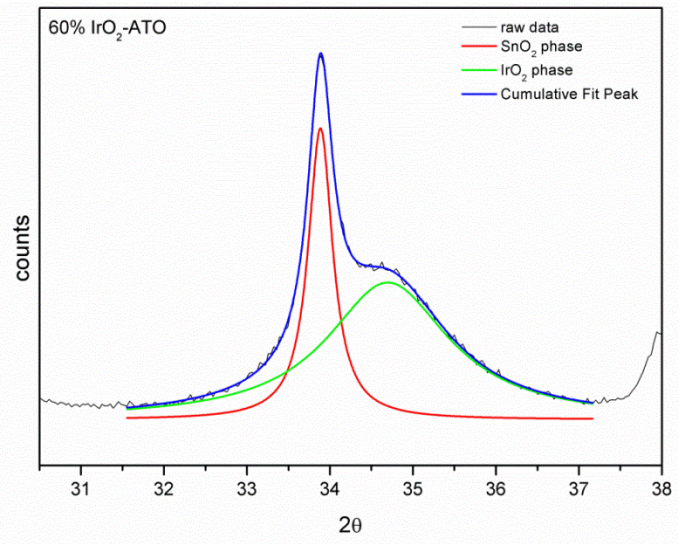


*Figure 3-8. Representative example of the peak fitting of the XRD peak.*

*Table 3-1. Crystallite size of $IrO_2$-ATO calculated using Scherrer equation.*

| $IrO_2$ loading (wt. %) | Crystallite size of $IrO_2$ /nm (28°) | Crystallite size of $IrO_2$ /nm (34.7°) | Average crystallite size of $IrO_2$/nm | Crystallite size of ATO /nm (26.6°) | Crystallite size of ATO /nm (33.9°) | Average crystallite size of ATO/nm |
|---|---|---|---|---|---|---|
| 100 | 5.7 | 6.3 | 6 ± 0.3 | - | - | - |
| 90 | 3.1 | 4.6 | 3.8 ± 0.8 | 23.9 | 21.8 | 22.9 ± 1.1 |
| 80 | 3.3 | 4.8 | 4.1 ± 0.8 | 24.3 | 22.9 | 23.6 ± 0.7 |
| 60 | 3.5 | 4.6 | 4.1 ± 0.6 | 24.0 | 23.2 | 23.6 ± 0.4 |
| 40 | 4.6 | 5.9 | 5.3 ± 0.7 | 23.6 | 22.7 | 23.2 ± 0.5 |
| 20 | 5.3 | 6.4 | 5.9 ± 0.6 | 24.1 | 24.2 | 24.2 ± 0.1 |
| 0 | - | - | 23.2* | 23.3 | 23.1 | 23.2 ± 0.1 |

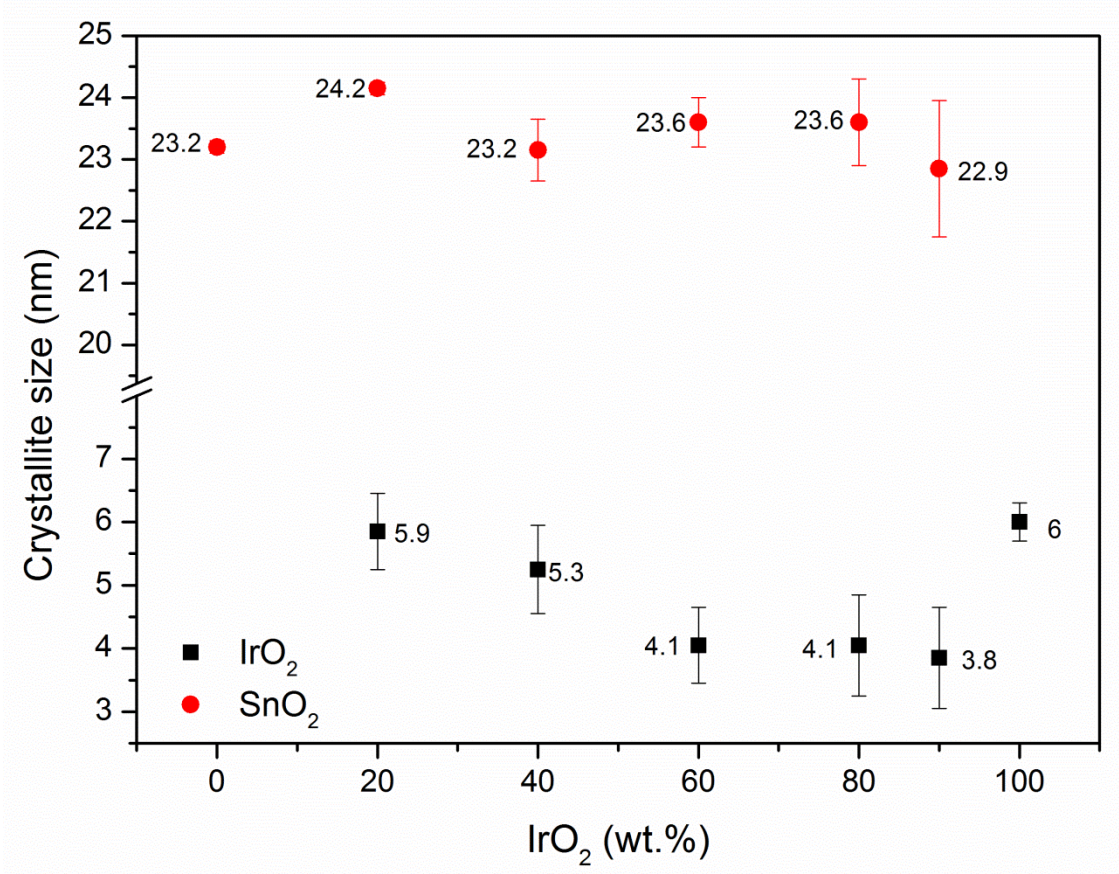


*Figure 3-9. Average crystallite sizes of $IrO_2$ and ATO in $IrO_2$-ATO catalysts calculated from the XRD using the Scherrer equation.*

### 3.3.4 BET surface area

The BET surface areas of the supported catalysts are given in Table 3-2. The pristine $IrO_2$ (112 $m^2$ $g^{-1}$) has BET surface area of approximately 3 times higher than the ATO support (20-40 $m^2$ $g^{-1}$). The BET surface area of the supported catalysts increased quite linearly with an increase in the $IrO_2$ loading (Figure 3-10) except for 90% $IrO_2$-ATO which showed a slightly higher BET surface area (126 $m^2$ $g^{-1}$) than the pristine $IrO_2$ (112 $m^2$ $g^{-1}$). The increases in BET surface area with the increase in the $IrO_2$ loading indicates that the surface area was mainly contributed by the $IrO_2$ with negligible contribution from the support. A BET surface area of 121 $m^2$ $g^{-1}$ was reported elsewhere for the pristine $IrO_2$ prepared by the Adams method [112, 162]. The large difference in the surface area of the support and the active catalyst will help in the dispersion of the active catalyst with full coverage on the support. It is very important to maintain a film of active component on the support to make catalyst electronically conductive as described in the section 3.3.2. A higher surface area for the 90% $IrO_2$-ATO (126 $m^2$ $g^{-1}$) than the unsupported $IrO_2$ (112 $m^2$ $g^{-1}$) indicates that the $IrO_2$ was well dispersed on the support forming small particles. It was clear from the XRD analysis that 90% $IrO_2$-ATO has smaller crystallite (3.8 nm) compared to the pristine $IrO_2$ (6 nm) (Table 3-2). The support material acts as nuclei for the dispersion and oxidation of $IrO_2$ intermediate during the synthesis.

It is important to know the surface area of the $IrO_2$ deposited on the ATO without the contribution of the support, in order to have an idea of its dispersion on the support. For this, the BET surface area of the support by itself was subtracted from the surface area of the supported $IrO_2$ catalyst normalised to $IrO_2$ loading. The obtained normalised $IrO_2$ specific surface area is given in Table 3-2. Considering $IrO_2$ as a hard sphere with diameter ('t' m) and density $\rho$ (11.6 g $cm^{-3}$) having specific surface area SSA ($m^2$ $g^{-1}$), and considering the BET surface area as equal to SSA, the particle size (t) can be calculated using equation ((3-2),

$$t = \frac{6}{SSA \times \rho} \qquad (3\text{-}2)$$

The particle size so obtained is given in Table 3-2. The particle size calculated from the BET surface area is more or less same as the crystallite size calculated from the XRD indicating a good dispersion of the $IrO_2$ on the support. Supported catalysts up to 60% $IrO_2$-ATO showed a higher normalised surface area than the pristine $IrO_2$ (112 $m^2$ $g^{-1}$)(Table 3-2). The surface area decreased for loading < 60% $IrO_2$-ATO. The 40% $IrO_2$-

ATO (76 $m^2$ $g^{-1}$) showed lower normalised surface area compared to the 60% $IrO_2$-ATO (125 $m^2$ $g^{-1}$). The particle size calculated from the normalised BET surface area showed an increase in $IrO_2$ particle size from 60% $IrO_2$-ATO (4.1 nm) to 40% $IrO_2$-ATO (6.8 nm).

Even though a higher surface area of support material is generally prescribed; it will be advantageous only when the support has higher or similar conductivity to that of active component. A higher surface area of poor conducting support will decrease the performance due to the overall decrease in conductivity of the catalyst layer.

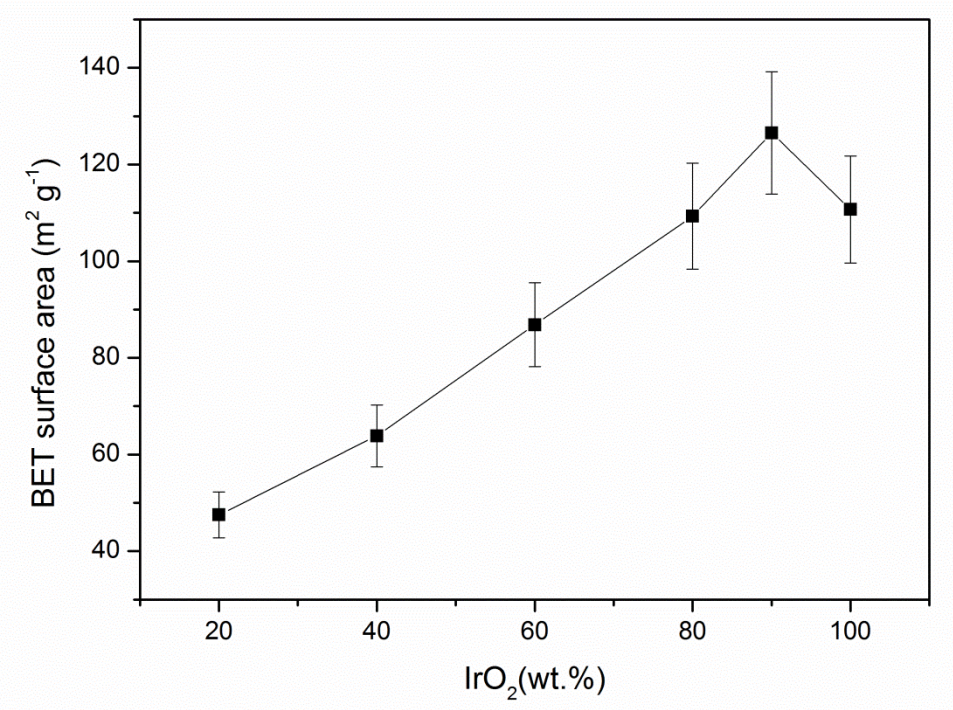


*Figure 3-10. BET surface area of the $IrO_2$-ATO catalyst with respect to $IrO_2$ wt.%.*

*Table 3-2. Physical properties of $IrO_2$-ATO catalyst with respect to $IrO_2$ loading. # data from the manufacturer, * crystallite size of $SnO_2$.*

| **$IrO_2$ loading (wt.%)** | **Conductivity (S $cm^{-1}$)** | **BET surface area ($m^2$ $g^{-1}$)** | **Average crystallite size of $IrO_2$ (nm)** | **BET surface area normalised to $IrO_2$ loading ($m^2$ $g^{-1}$)** | **Particle size calculated from the BET surface area (nm)** |
|---|---|---|---|---|---|
| 100 | 4.9 ± 0.5 | 112 ± 11 | 6 ± 0.3 | 112 ± 11 | 4.6 ± 0.5 |
| 90 | 4.8 ± 0.5 | 126 ± 13 | 3.8 ± 0.8 | 137 ± 14 | 3.8 ± 0.4 |
| 80 | 4.1 ± 0.4 | 109 ± 11 | 4.1 ± 0.8 | 129 ± 13 | 4.0 ± 0.4 |
| 60 | 1.6 ± 0.2 | 87 ± 9 | 4.1 ± 0.6 | 125 ± 13 | 4.1 ± 0.4 |
| 40 | $2.0 \times 10^{-1}$ | 64 ± 6 | 5.3 ± 0.7 | 76.3 ± 8 | 6.8 ± 0.7 |
| 20 | $8.6 \times 10^{-3}$ | 48 ± 5 | 5.9 ± 0.6 | 79.4 ± 8 | 6.5 ± 0.7 |
| 0 | $4.3 \times 10^{-3}$ | 20-40[#] | 23.2* | | 22.1 - 44 |

### 3.3.5 XPS analysis

The XPS peak analysis was carried out using Casaxps software (version 2.3.16). A typical survey spectrum of supported catalyst is given in Figure 3-11. The peaks of Sb $3d_{5/2}$ and O1s (530.1 eV) as well as Sn $3d_{3/2}$ and Ir $4p_{3/2}$ (496.2 eV) overlap each other. The distinguishable peaks of Ir were Ir $4d_{3/2}$ (313.65 eV), Ir $4d_{5/2}$ (298.1 eV) and Ir 4f peaks. The distinguishable peak for Sn was Sn $3d_{5/2}$ (487.19 eV). The survey spectra from 400 eV to 600 eV of various catalysts prepared is compared in Figure 3-12. A gradual decrease in the Sb $3d_{3/2}$ and Sn $3d_{5/2}$ peaks can be seen with increase in $IrO_2$ loading indicating coverage of the ATO surface by the $IrO_2$. A Sn 3d narrow scan is given in Figure 3-13 and a gradual decrease in intensity can be seen with an increase in $IrO_2$ loading. This is in consistent with the XRD (Figure 3-7) whereby a similar increase in intensity of $SnO_2$ with decrease in $IrO_2$ loading was observed.

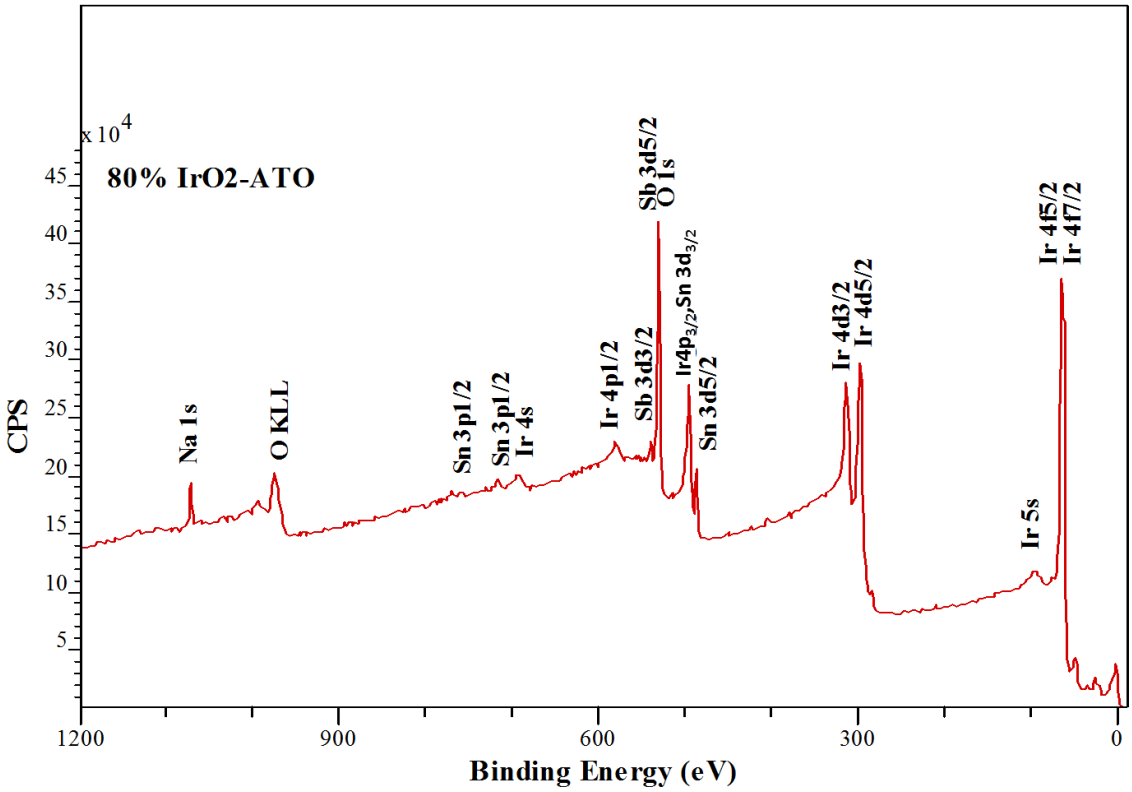


*Figure 3-11. XPS survey spectra of 80% $IrO_2$-ATO.*

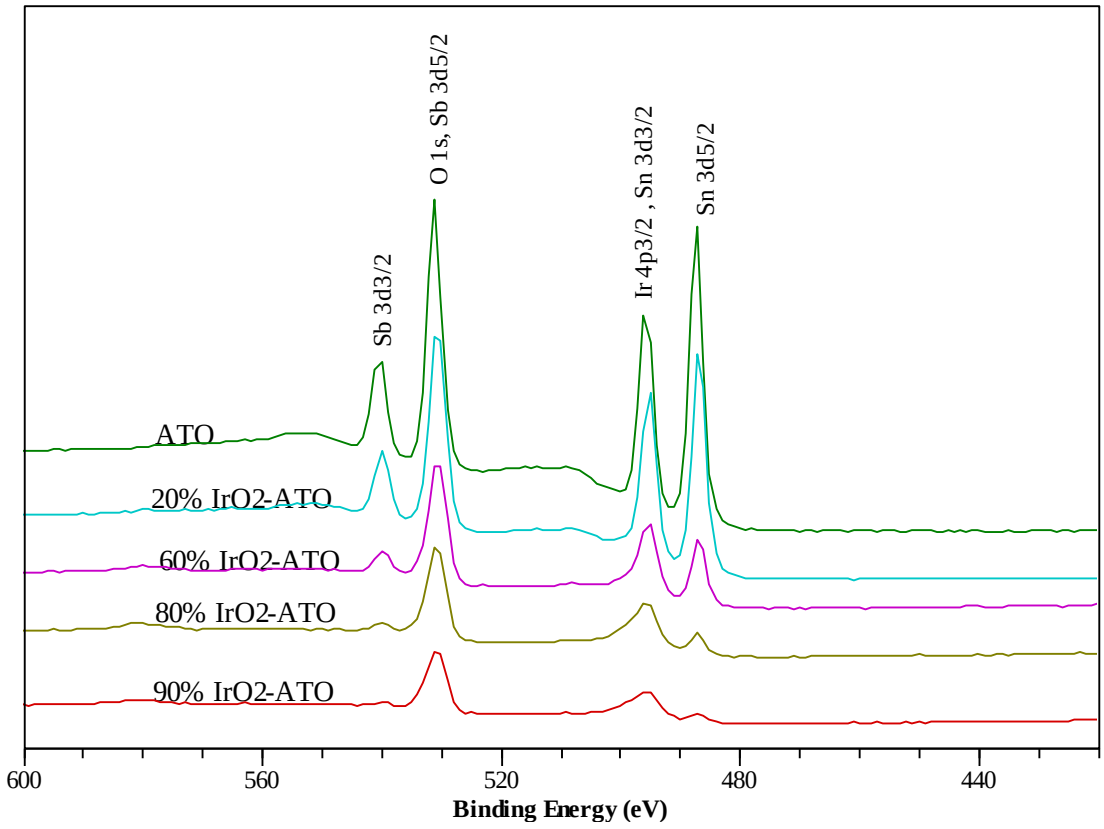


*Figure 3-12. XPS survey spectra of various $IrO_2$-ATO catalysts.*

The Ir 4f scan of 90% $IrO_2$-ATO is given in Figure 3-14. A similar peak fitting was reported elsewhere [111, 197]. Analysis of Ir 4f peak is difficult to due to considerable disagreement in the literature about the nature of 4f peaks [111, 197]. However the two pairs of peaks indicate the Ir is present in more than one valence state [111]. The 5$^{th}$ peak located at ~67.58 eV was suggested to be due to the final state screening and was required to fit the peak properly [197]. The BE for Ir $4f_{5/2}$ (64.8 eV) and Ir $4f_{7/2}$ (61.9 eV) are higher than for the metallic Ir (60.9 eV for $4f_{7/2}$ and 63.8 eV for $4f_{5/2}$) and was assigned to $Ir^{4+}$ chemical state in literature [111, 198-202]. The pair of peaks at ~63 eV and ~66.2 eV are higher BE than Ir $^{4+}$ and may be attributed an existence of higher oxidation state of Ir [199]. Slavcheva [200] and Hara et al [203] on other hand assigned the lower BE peak pair (61.9 eV) to $Ir^{3+}$ and the higher BE peak pair (~62.9 eV) to $Ir^{4+}$. It is thus not possible to conclude exactly which Ir species is present due to the considerable disagreement in the literature [197]; however it is certain that all the Ir species present are oxidised Ir and no metallic Ir was present. The Sn $3d_{5/2}$ peak at BE of 487.2 eV (484.6 eV for Sn $3d_{5/2}$ in metallic Sn) represents $SnO_2$ in a stoichiometric state [198, 201].

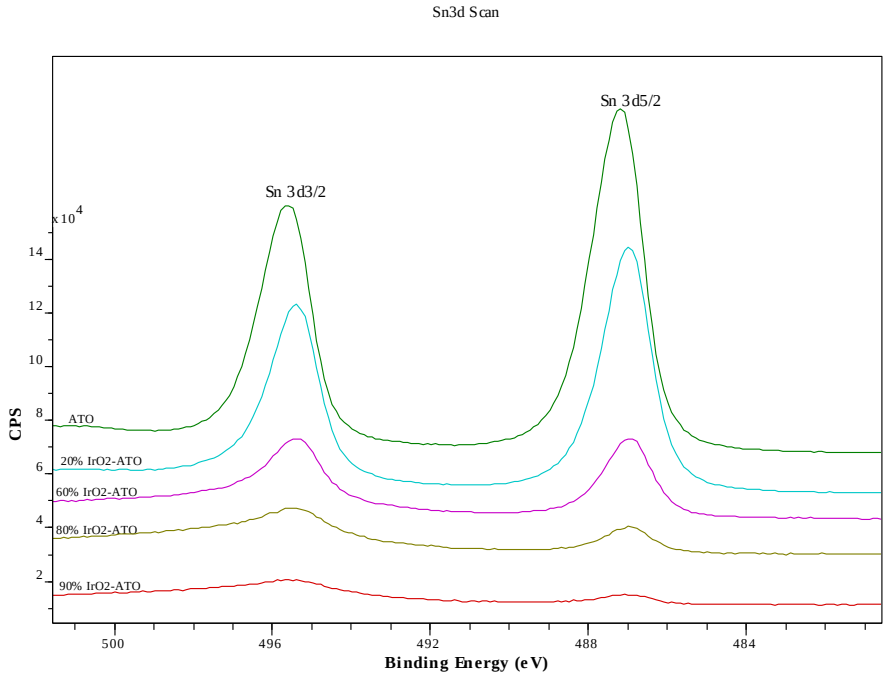


*Figure 3-13. XPS spectra of the Sn 3d narrow scans of $IrO_2$-ATO catalyst.*

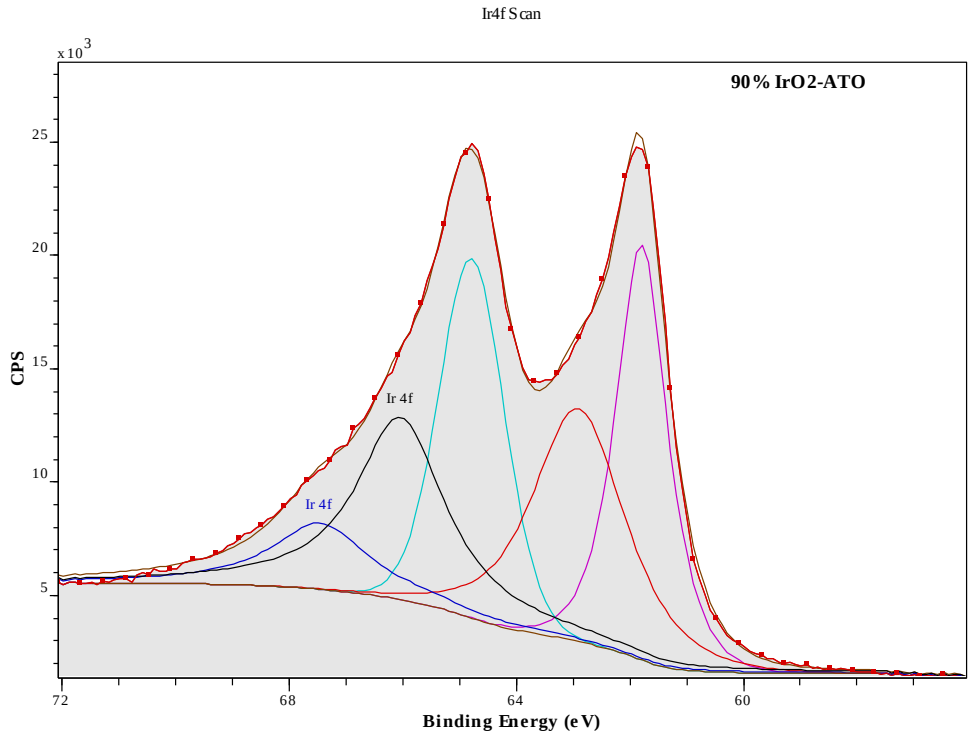


*Figure 3-14. A typical Ir 4f narrow scan XPS spectra of $IrO_2$-ATO catalysts.*

### 3.3.6 Morphology

The SEM of the catalyst is given in Figure 3-15. It is not possible to distinguish between the ATO and $IrO_2$ particles from the SEM picture. The pristine $IrO_2$ showed a uniform aggregate morphology. All supported catalysts showed more or less similar morphology and no significant difference was observed on varying the $IrO_2$ loading.

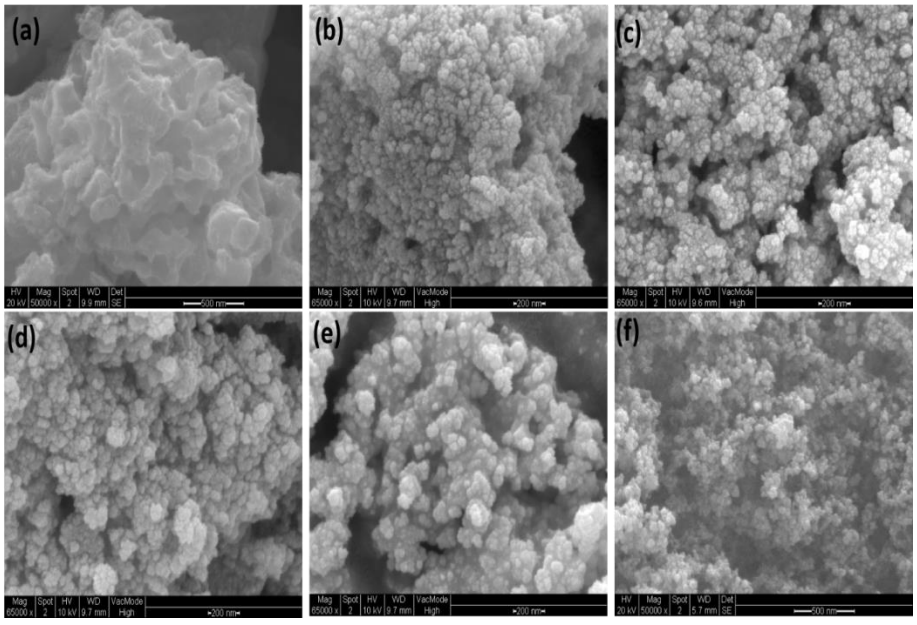


*Figure 3-15. SEM picture of $IrO_2$-ATO catalyst (a) $IrO_2$ (b) 80% $IrO_2$-ATO (c) 60% $IrO_2$-ATO (d) 40% $IrO_2$-ATO (e) 20% $IrO_2$-ATO (f) ATO.*

The Ir wt.% obtained from the EDX analysis of the supported catalysts is given in Table 3-3. The loading was almost the same as that of precursor used and indicates that there was no material loss during the synthesis and washing stage of the catalyst preparation.

*Table 3-3. Ir composition in $IrO_2$-ATO catalyst from the EDX analysis.*

| Catalyst | Ir wt.% obtained from EDX | Ir wt.% required |
|---|---|---|
| 20% $IrO_2$-ATO | 17.9 ± 3.8 | 17.2 |
| 40% $IrO_2$-ATO | 33.6 ± 3.6 | 34.3 |
| 60% $IrO_2$-ATO | 50.3 ± 4.1 | 51.4 |
| 80% $IrO_2$-ATO | 71.2 ± 2.4 | 68.6 |
| 90% $IrO_2$-ATO | 76.2 ± 1.9 | 77.2 |

TEM images of the samples are given in Figure 3-16. Particle sizes in the range of 3-6 nm can be seen for 90% $IrO_2$-ATO whereas particle with two different sizes was observed for 40% $IrO_2$-ATO (Figure 3-16). Even though it is difficult to clearly distinguish between the $IrO_2$ and ATO particles in TEM, a higher number of larger particles is clear for 40% $IrO_2$-ATO which can be attributed to the large ATO nanoparticles. Crystallite size in the range of 22-24 nm for ATO was evident from the XRD analysis (Table 3-1).

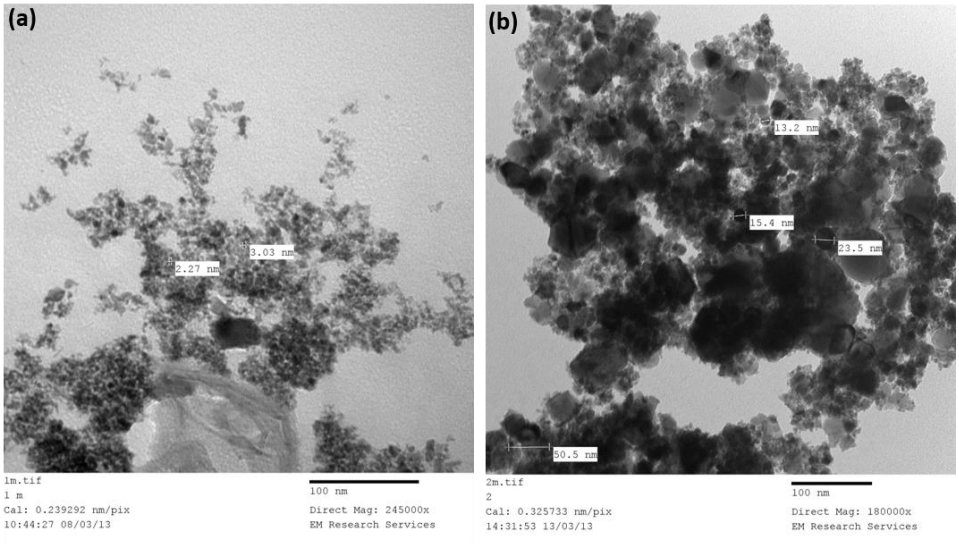


*Figure 3-16. TEM images of (a) 90% $IrO_2$-ATO (b) 40% $IrO_2$-ATO.*

### 3.3.7 Cyclic voltammetry

The cyclic voltammogram (CV) of the pristine $IrO_2$ in 0.5M $H_2SO_4$ and 85% $H_3PO_4$ at room temperature recorded at scan rate from 5 to 200 mV $s^{-1}$ are given in Figure 3-17 and Figure 3-18 respectively. The CV's showed characteristic shape of $IrO_2$ with a narrow region at potential lower than +0.5 V and wider region above +0.5 V vs. Ag/AgCl indicating the high charge storage capacity of $IrO_2$ [204]. The unsupported $IrO_2$ and supported $IrO_2$ give characteristic peaks of $IrO_2$ at ~0.78 V and ~1 V (vs. Ag/AgCl) in 85% $H_3PO_4$ attributed to the redox transition of Ir(III)/Ir(IV) and Ir(IV)/Ir(VI) (equation 2-18) [75, 135-137]. A similar CV shape for $IrO_2$ was reported in literature [76, 136, 205]. The capacitance behaviour in the $IrO_2$ comes from the pseudo-capacitance (due to the proton exchange reaction) and the standard double layer capacitance (due to the ion adsorption).

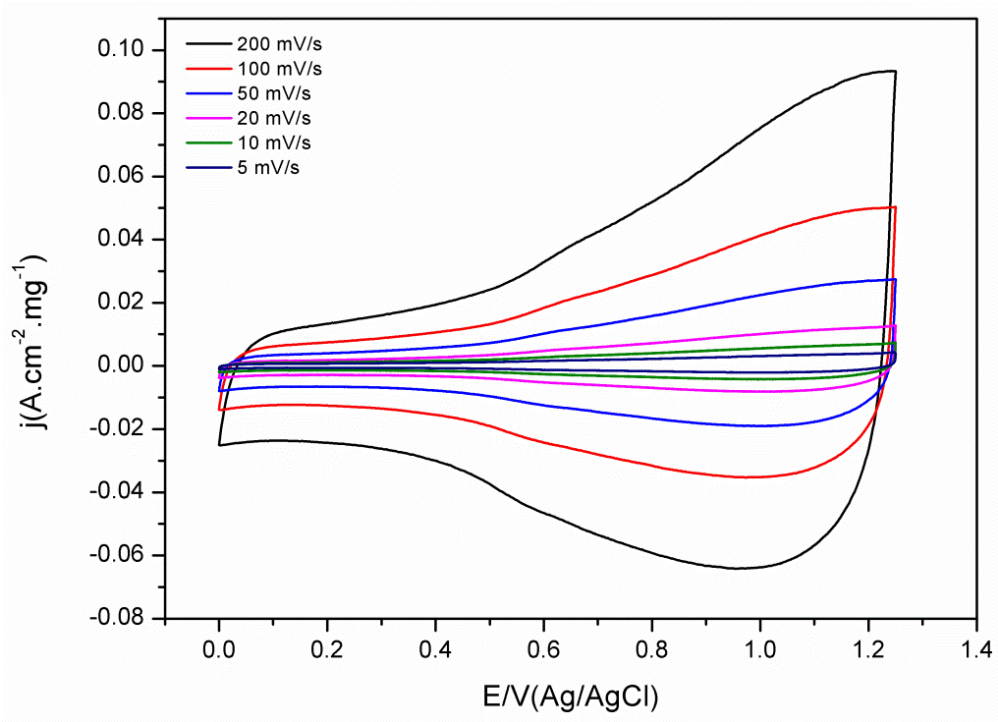


*Figure 3-17. CV of $IrO_2$ in 0.5M $H_2SO_4$ at room temperature.*

The CV of ATO support in 85% $H_3PO_4$ is given in Figure 3-19. The CV showed capacitive behaviour without any distinguishable features during the anodic scan. A similar CV response for ATO was reported elsewhere [176, 181, 206]. The reduction peak lower than +0.5 V is due to the irreversible reduction Sn(II)/Sn(IV) and Sb(III)/Sb(V) and the hydrogen evolution reaction [187, 206]. A corresponding anodic

peak was not observed due to the irreversible nature of the reactions. Since it is difficult to oxidise Sn(II) and Sb(III) at lower anodic potential [187]. This in turn indicates that ATO is suitable at anodic potential and not at cathodic potential [187]. The charging current response obtained from the ATO at all potentials was approximately 10 times lower than that from the 20% $IrO_2$-ATO (Figure 3-20), indicating that the current observed in $IrO_2$-ATO mainly arises from the $IrO_2$.

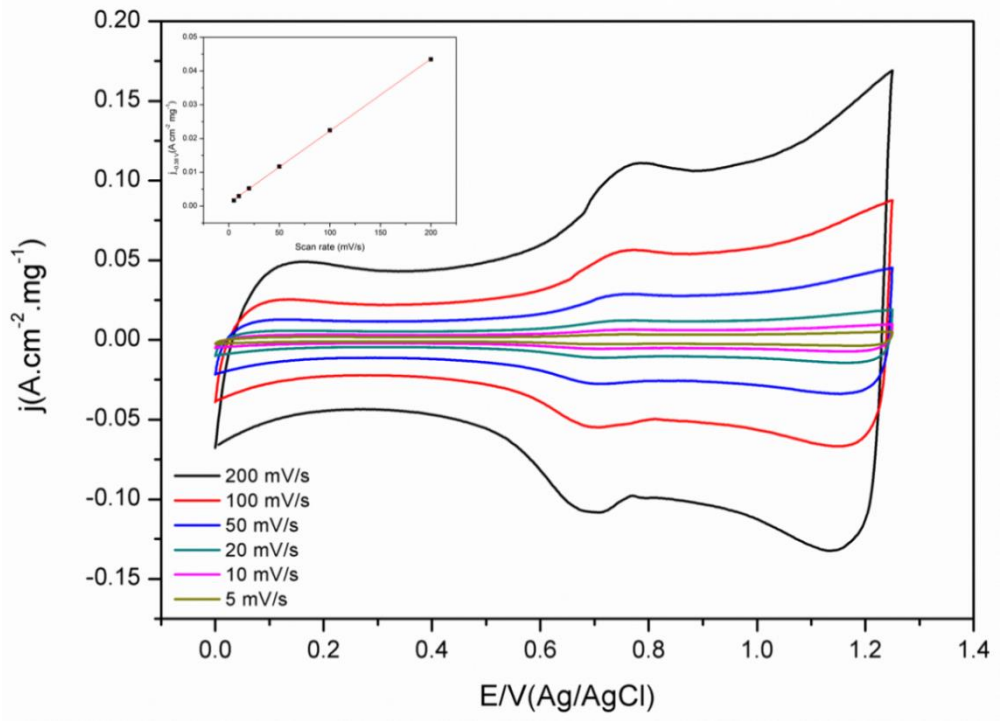


*Figure 3-18. CV of $IrO_2$ with respect to scan rate in 85% $H_3PO_4$ at room temperature. Inset shows the linear relation between the current density vs. scan rate at 0.38 V.*

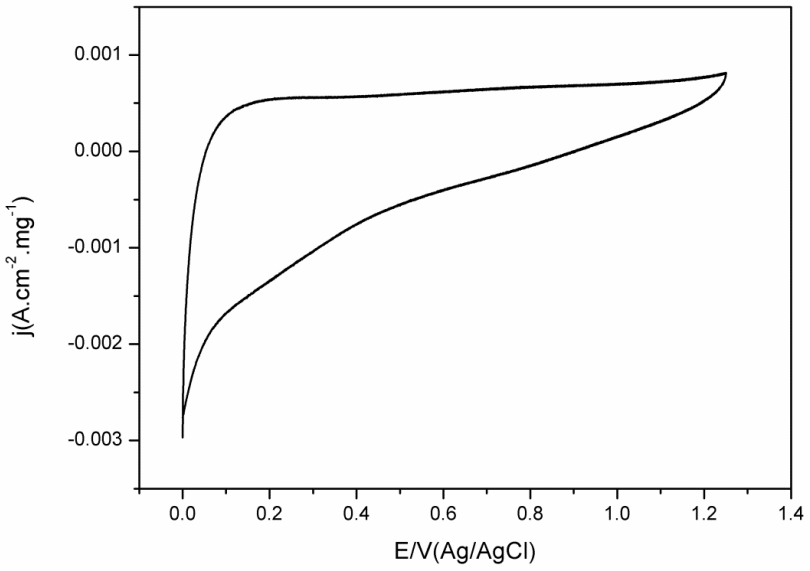


*Figure 3-19. CV of ATO support in 85% $H_3PO_4$ at room temperature.*

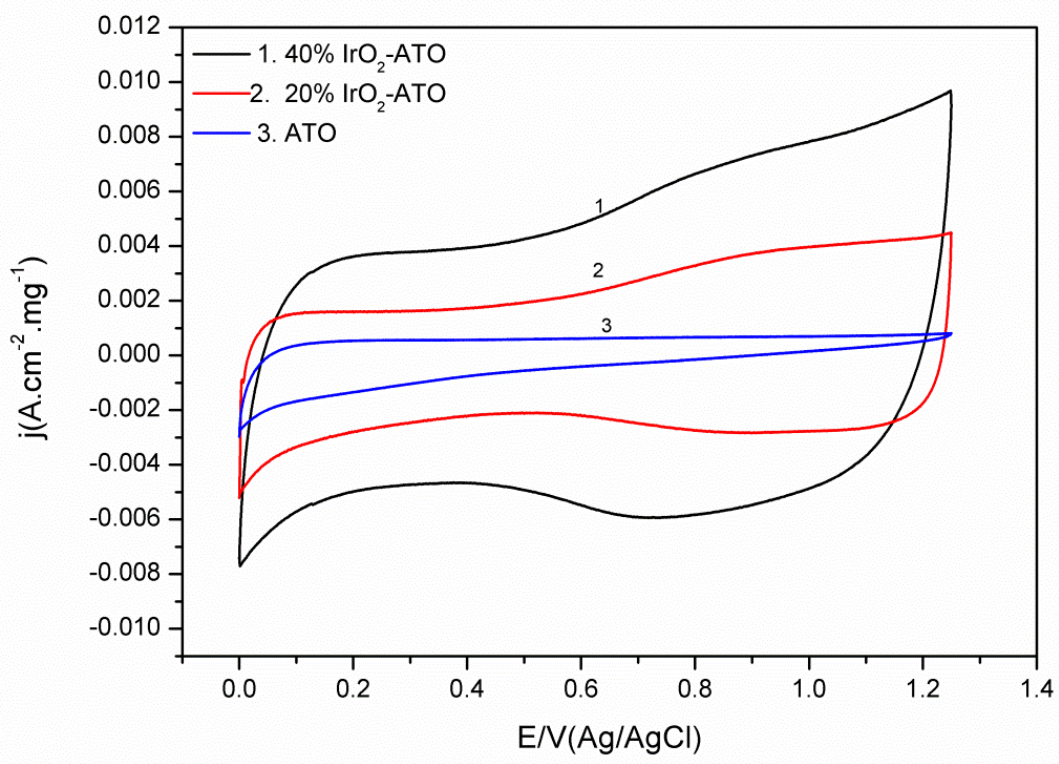


*Figure 3-20. CV comparison of ATO with 20% $IrO_2$-ATO and 40% $IrO_2$-ATO in 85% $H_3PO_4$ at room temperature.*

The CV of $IrO_2$ was symmetrical with respect to the zero current axes independent of the scan rate (Figure 3-18) suggesting a reversible reaction at the surface. The capacitance can be calculated from the CV using the equation ((3-3) and ((3-4).

$$C = \frac{dq}{dV} = \frac{i.dt}{dV} \qquad (3\text{-}3)$$

$$i = C.\frac{dV}{dt} = C.\upsilon \qquad (3\text{-}4)$$

Where C is the capacitance (F), $i$ is the current (A) and $\upsilon$ is the scan rate (V $s^{-1}$). A plot of $i$ vs. $\upsilon$ gives a straight line and the slope of which gives the capacitance (Figure 3-18 inset). The anodic current value at 0.38 V, where no redox reaction observed, was used to calculate the capacitance using the equation ((3-4) and the capacitance obtained was 214 mF $cm^{-2}$ $mg^{-1}$. The peak current for Ir(III)/Ir(IV) transition around ~0.75 V was plotted against the scan rate (Figure 3-21) and a linear plot was obtained as in Figure 3-18 inset. The capacitance calculated from the slope of this linear plot according to equation (3-4 was 545 mF $cm^{-2}$ $mg^{-1}$. Though the proportionality between the current and scan rate is indicative of double layer capacitive behaviour, a peak will not be observed for pure

double layer capacitive behaviour. The linear relation indicates that the proton insertion reaction was not influenced by diffusion [207] and the reactants were confined at the interface [118, 208].

The integration of the CV curve gives the voltammetric charge (q*) which represents the charging/discharging of the redox pseudo capacitance and the double layer capacitance. The voltammetric charge is thus a measure of the number of active sites available to exchange a proton with the solution. i.e. electrochemical active surface area [129, 209] and is often used in literature to indicate the electrochemical active surface area of the noble metal oxides [91, 129, 209]. The q* calculated for the supported catalysts are given in Table 3-4. The 90% $IrO_2$-ATO (1990 mC $cm^{-2}$ $mg^{-1}$) and 80% $IrO_2$-ATO (1840 mC $cm^{-2}$ $mg^{-1}$) gave higher voltammetric charge than the pristine $IrO_2$ (1700 mC $cm^{-2}$ $mg^{-1}$). The active surface area for the supported catalyst from Figure 3-22 are in the order 90% $IrO_2$-ATO > 80% $IrO_2$-ATO > $IrO_2$ > 60% $IrO_2$-ATO > 40% $IrO_2$-ATO > 20% $IrO_2$-ATO. The higher active area of 90% $IrO_2$-ATO and 80% $IrO_2$-ATO is in agreement with the observation by Nikiforov et al [112] whereby a higher active surface area for 90% $IrO_2$/Si-SiC in comparison to pristine $IrO_2$ was obtained in 85% $H_3PO_4$ and was attributed to smaller $IrO_2$ particles (~ 3 nm for 90% $IrO_2$/Si-SiC compared to 5.5 nm for pristine $IrO_2$) and better dispersion of $IrO_2$ on the support.

It is clear from the BET surface area analysis (Figure 3-10) that the 90% $IrO_2$-ATO (126 $m^2$ $g^{-1}$) has higher surface area compared to the pristine $IrO_2$ (112 $m^2$ $g^{-1}$). The 80% $IrO_2$-ATO has smaller crystallite size (4.1 nm) as well as comparable BET surface area (109 $m^2$ $g^{-1}$) and conductivity (4.1 S $cm^{-1}$) to that of the pristine $IrO_2$ (6 nm, 112 $m^2$ $g^{-1}$, 4.9 S $cm^{-1}$) (Table 3-2). Normalising the voltammetric charge (q*) with the $IrO_2$ loading gave a higher charge for all the supported catalysts compared to the pristine $IrO_2$ (Table 3-4). The 60% $IrO_2$-ATO showed the highest normalised voltammetric charge (2616 mC $cm^{-2}$ $mg^{-1}$) which is ~1.5 times higher than that of the pristine $IrO_2$ (1700 mC $cm^{-2}$ $mg^{-1}$). The higher normalised voltammetric charge on the supported catalysts indicate that the $IrO_2$ dispersion increased with a decrease in $IrO_2$ loading [183] and can be attributed to the smaller particles and better dispersion of $IrO_2$ on the support. This was supported by the XRD analysis whereby a lower $IrO_2$ crystallite sizes for all the supported catalysts were observed (Table 3-1).

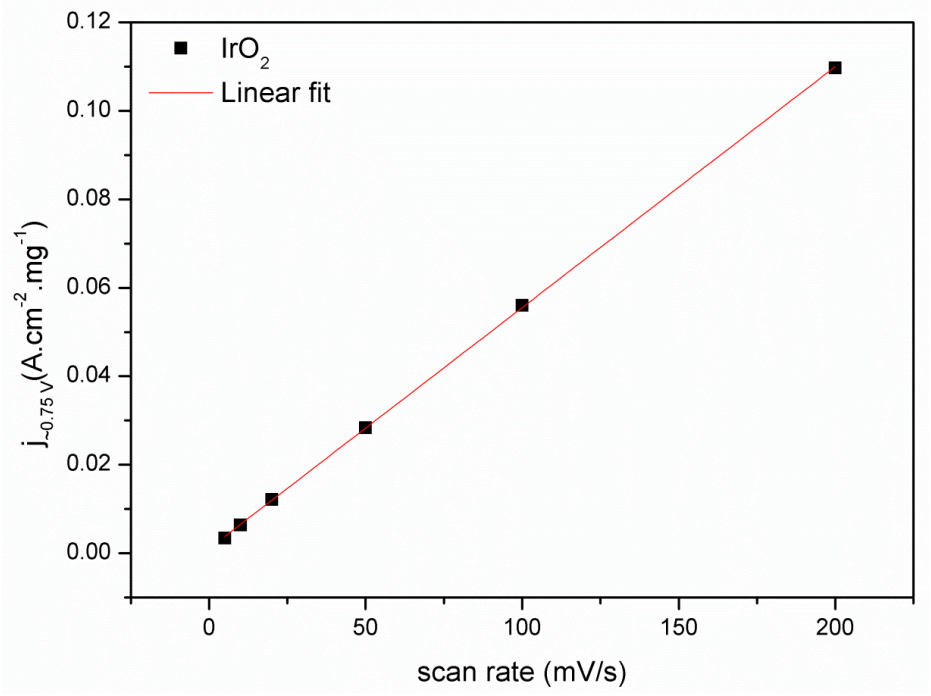


*Figure 3-21. Peak current (~0.75 V) vs. scan rate plot of pristine $IrO_2$ in 85% $H_3PO_4$ at room temperature.*

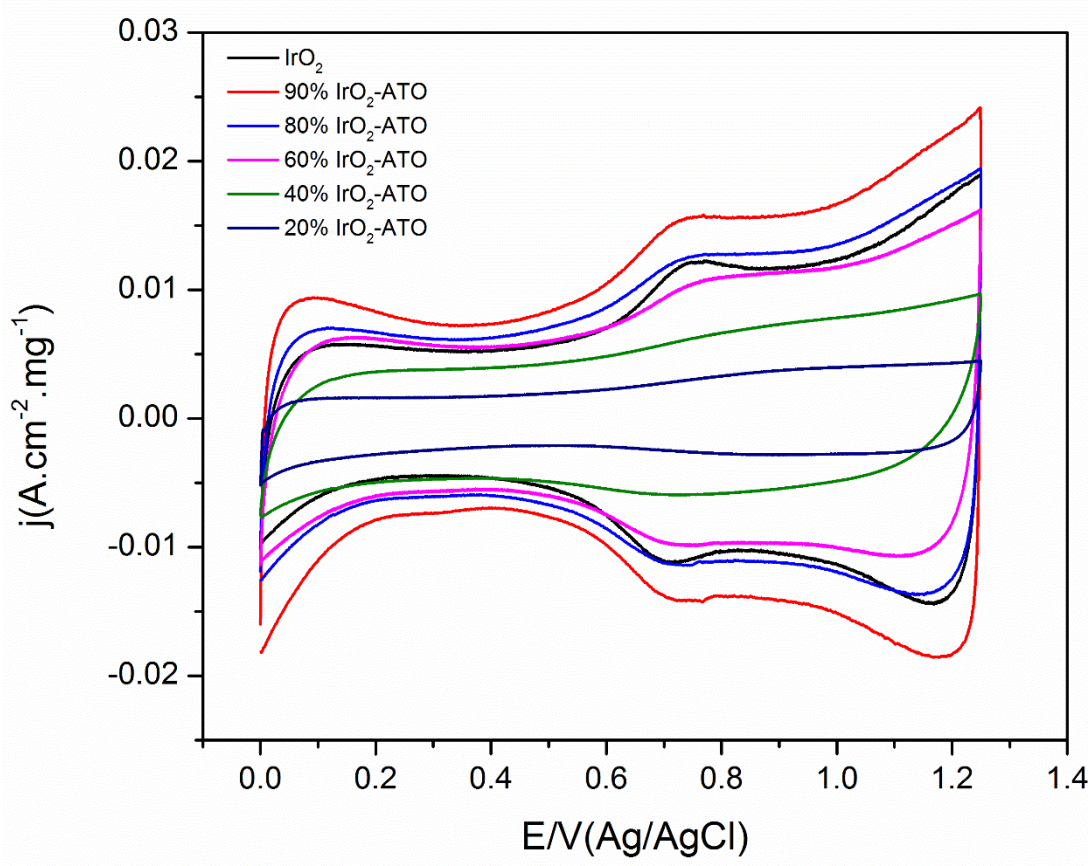


*Figure 3-22. CV of $IrO_2$-ATO with different $IrO_2$ composition in 85% $H_3PO_4$ at room temperature and scan rate 20 $mVs^{-1}$.*

*Table 3-4. Voltammetric charge of $IrO_2$-ATO at room temperature in 85% $H_3PO_4$. Scan rate 20 mV $s^{-1}$*

| Electrode | Voltammetric charge (q*) at room temperature (mC $cm^{-2}$ $mg^{-1}$) | |
|---|---|---|
| | **q* as measured** | **q* normalised to $IrO_2$ loading** |
| $IrO_2$ | 1700 ± 85 | 1700 ± 85 |
| 90% $IrO_2$-ATO | 1990 ± 100 | 2211 ± 111 |
| 80% $IrO_2$-ATO | 1840 ± 92 | 2300 ± 115 |
| 60% $IrO_2$-ATO | 1570 ± 79 | 2616 ± 131 |
| 40% $IrO_2$-ATO | 980 ± 49 | 2450 ± 123 |
| 20% $IrO_2$-ATO | 493 ± 25 | 2465 ± 123 |

Since phosphoric acid doped PBI membrane was proposed to be a promising membrane for high temperature operation, the prepared catalysts were tested in 85% $H_3PO_4$ at temperatures up to 120$^oC$. The electrode was placed into the electrolyte at room temperature and heated using a heating plate to the required temperature. A standard mercury thermometer was used to measure the temperature of the electrolyte. The reference electrode compartment was cooled by passing cold water through the outer jacket during high temperature operation. The CV of the pristine $IrO_2$ and supported catalyst in 85% $H_3PO_4$ at various temperatures are given in Figure 3-23. The evolution of voltammetric charge (q*) with increase in temperature is given in Figure 3-24. It can be seen that as the temperature increased voltammetric charge decreased and the characteristic peaks of $IrO_2$ diminish. The q* decreased to ~70% of its value at room temperature for the pristine $IrO_2$. Since reaction kinetics is faster at high temperature, an increase in catalyst activity is expected [207]. An increase in the catalyst activity with increase in temperature was observed in the MEA analysis using $IrO_2$ catalyst as anode (Nafion 115 membrane, 80$^oC$, Pt/C cathode) (Figure 3-27). So the decrease in active area with increase in temperature in CV cannot be attributed to the decrease in activity of the catalyst. It is difficult to identify an exact reason for the decrease in the active surface area with the increase in temperature. One of the possible reasons could be the decreased double layer capacitance with increase in temperature. Since adsorption is an exothermic

process, as temperature increases, the phosphate adsorption will decrease reducing the double layer capacitance. However the pseudo capacitance which is the major contributor to the voltammetric charge will increase with increase in temperature and thus voltammetric charge should increase with an increase in temperature. So the double layer capacitance will not be able to explain the decrease in the q*. Thus it may be concluded that a loss of the catalyst from the electrode occurred with increase in electrolyte temperature.

Since direct heating was used for heating the electrolyte, this might have created a non-uniform convectional movement of phosphoric acid making the catalyst come off the smooth tantalum electrode. In order to confirm this, a glass cell with an external jacket and provision to pass pre-heated oil through the cell was used to heat the electrolyte. This set up is likely to provide relatively uniform heating unlike a direct heating, avoiding the severe non-uniform convectional movement of phosphoric acid during the direct heating of the electrolyte. The CV of 80% $IrO_2$-ATO obtained by using this set up is given in Figure 3-25 and the change in voltammetric charge (q*) with increase in temperature is given in Figure 3-26. An increase in the q* with increase in temperature up to $80^oC$ is evident from the study which decreased at temperature > $80^oC$. The increase in q* up to a temperature of $80^oC$ can thus be attributed to the increase in kinetics whereas the steep decrease at temperature > $80^oC$ can be attributed to a loss of the catalyst from the electrode surface at high temperature. It has to be noted that Nafion® used as a binder has a glass transition temperature of ~$105^oC$ [210] and so a higher temperature will reduce the binding ability of the Nafion which will accelerate the loss of the catalyst at high temperature. This could be the reason for the loss of the active surface area at temperature > $80^oC$. CV was also carried out after cooling the electrolyte and no increase in q* was observed confirming the assumption of the loss of the catalyst from the electrode.

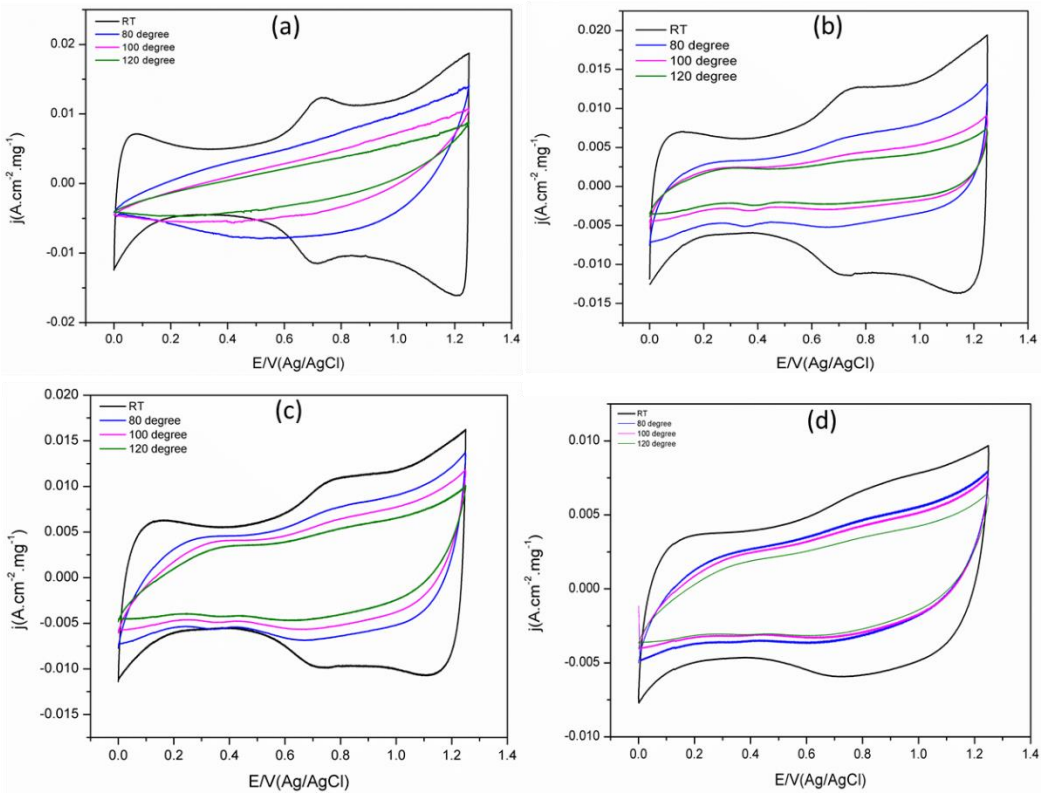


*Figure 3-23. CV at different temperature in 85% $H_3PO_4$ for (a) $IrO_2$ (b) 80% $IrO_2$-ATO (c) 60% $IrO_2$-ATO (d) 40% $IrO_2$-ATO.*

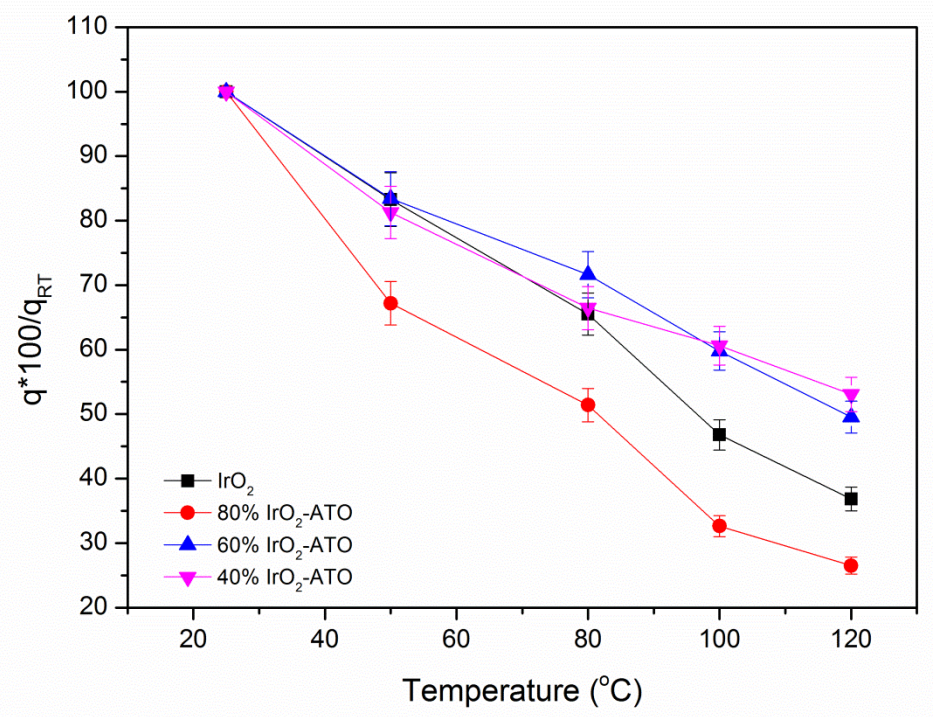


*Figure 3-24. Voltammetric charge (q*) with respect to temperature of $IrO_2$-ATO catalysts at 20mV $s^{-1}$. q* is the voltammetric charge at the specific temperature and $q_{RT}$ is the voltammetric charge at room temperature.*

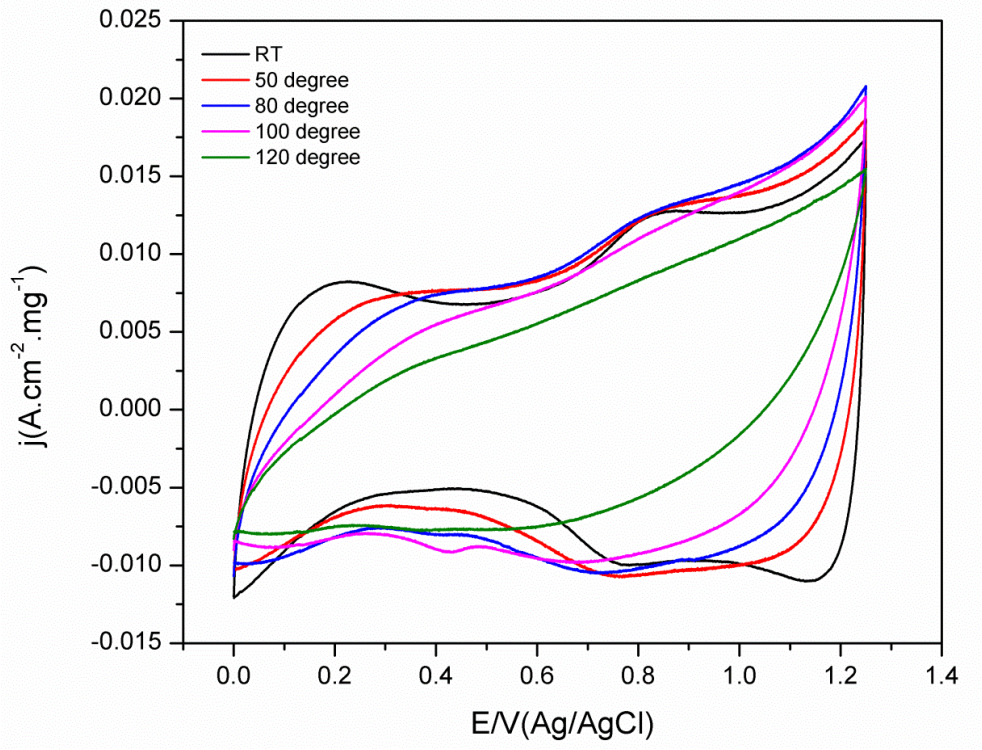


*Figure 3-25. CV of 80% $IrO_2$-ATO with respect to temperature using the cell with external jacket and heated using pre heated oil.*

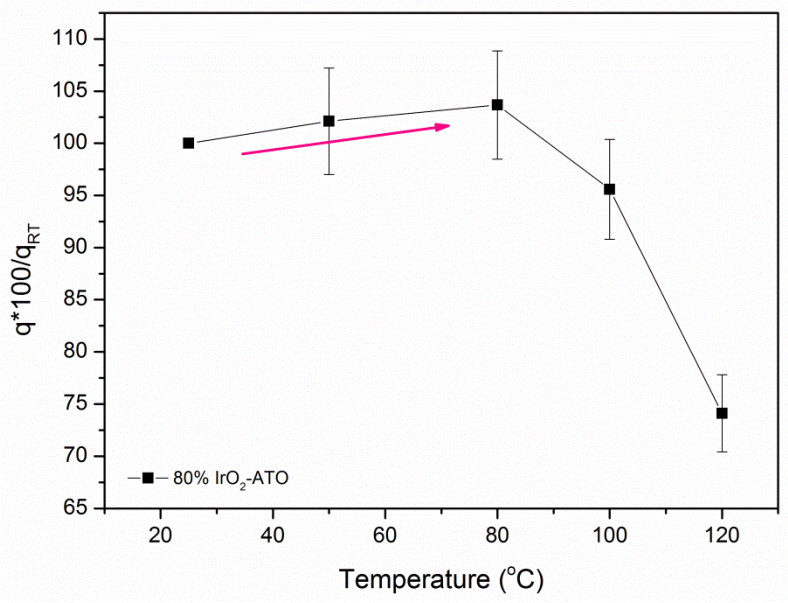


*Figure 3-26. Voltammetric charge with respect to temperature for 80% $IrO_2$-ATO using the cell with an external jacket and heated using pre heated oil.*

Due to the time limitation of the PhD project, further studies on high temperature CV were not able to be carried out. However an increase in activity with temperature is

evident from Figure 3-26. A new experimental set up would need to be designed with a provision to have uniform heating of the electrolyte up to a temperature of 150$^{o}$C in order to study the CV at high temperature. A thermally stable binder such as PTFE solution may be adopted to study any effect of the binder on the performance of the catalyst at high temperature.

### 3.3.8 MEA Performance

Membrane electrode assemblies (MEA) were prepared with Nafion-115 membranes using the CCM method as described in the experimental section 3.2.1 in order to evaluate the performance of the catalyst in electrolyser operation. The polarisation plot of the MEA with pristine $IrO_2$ anode catalyst at various temperatures is given in Figure 3-27. The current densities at 1.8 V for 25$^{o}$C, 50$^{o}$C, 80$^{o}$C were 497, 856 and 1344 mA cm$^{-2}$ respectively for the $IrO_2$. The current density @1.8 V and 80$^{o}$C was ~2.7 times higher than at 25$^{o}$C and can be attributed to the faster electrode kinetics and increased Nafion® conductivity with increase in temperature [193, 211]. Since at high current density, ohmic resistance and bubble formation influence the performance [141, 212], a low current density of 0.1 A cm$^{-2}$ was used to compare the performance of the anode catalyst and the cell voltage at 0.1 A cm$^{-2}$ for $IrO_2$ anode catalysts at different temperatures are given in Table 3-5. The cell potential @ 0.1 A cm$^{-2}$ decreased by 120 mV on increasing the temperature from 25$^{o}$C (1.62 V) to 80$^{o}$C (1.5 V). The voltage at 1 A cm$^{-2}$ (which involves ohmic and bubble effect) gives an idea of the performance under real electrolyser condition. The cell voltage @ 1A cm$^{-2}$ for $IrO_2$ at 25$^{o}$C and 80$^{o}$C were 1.99 V and 1.73 V (260 mV decrease) respectively (Table 3-5). The voltage value in literature for $IrO_2$ based catalysts with loading of 1.5 - 3 mg cm$^{-2}$ using a Nafion-115 membrane range from 1.65 - 1.8 V at 1 A cm$^{-2}$ at 80$^{o}$C [86, 141, 213, 214]. The performance of MEA with $IrO_2$ anode at 1 A cm$^{-2}$ and 80$^{o}$C (cell voltage 1.73 V) equates to a cell efficiency ($\varepsilon_{\Delta G}$) of 68.4% (Appendix 8.3).

*Table 3-5. MEA performance of $IrO_2$ anode catalyst at different temperature.*

| Temperature ($^oC$) | Voltage @ 0.1 A $cm^{-2}$ (V) | Voltage @ 1A $cm^{-2}$ (V) | Current density @ 1.8 V (mA $cm^{-2}$) | Efficiency ($\varepsilon_{\Delta G}$) @ 1 A $cm^{-2}$ | Energy consumption @1A $cm^{-2}$ (kWhNm$^{-3}$) |
|---|---|---|---|---|---|
| 25$^o$C | 1.62 | 1.99 | 497 | 61.8 | 4.8 |
| 50$^o$C | 1.57 | 1.83 | 856 | 66.0 | 4.4 |
| 80$^o$C | 1.5 | 1.73 | 1344 | 68.4 | 4.1 |

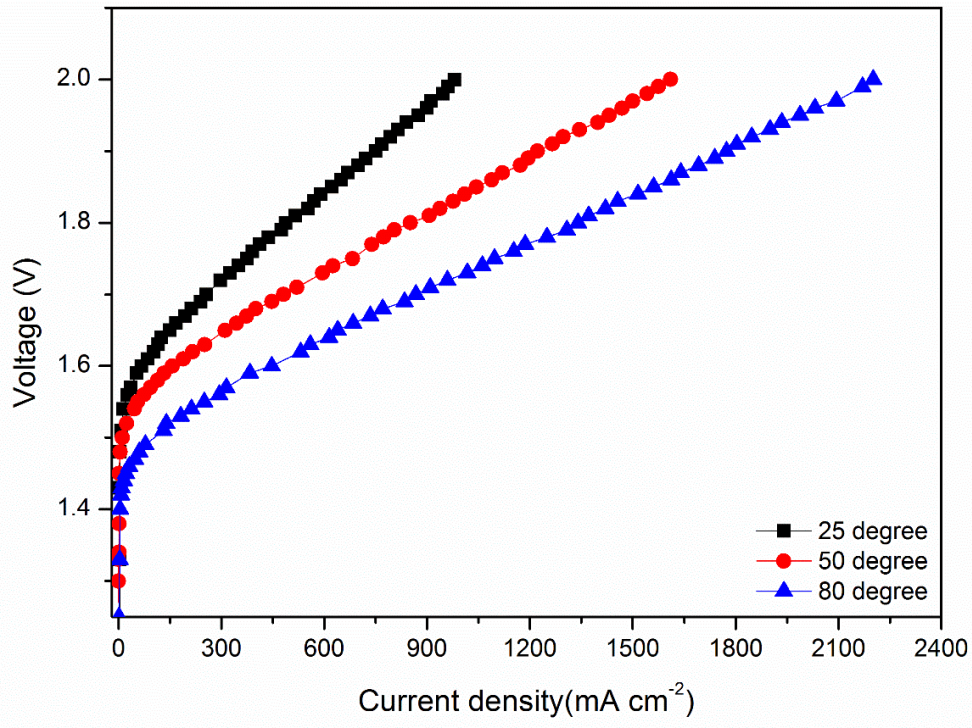


*Figure 3-27. Effect of temperature on the MEA polarisation of $IrO_2$ anode. Nafion-115 membrane, Pt/C (20%) cathode. Temperature 80$^o$C and ambient pressure.*

MEAs prepared with $IrO_2$-ATO with various $IrO_2$ loading at 80$^o$C are compared in Figure 3-28. The unsupported $IrO_2$ and 90% $IrO_2$-ATO gave the best performance among all the tested MEAs with a potential of 1.73 V at 1 A $cm^{-2}$ which equates to a cell efficiency of ($\varepsilon_{\Delta G}$) of 68% and energy consumption of 4.1 kWhr $Nm^{-3}$ $H_2$ at 80$^o$C. The 80% $IrO_2$-ATO gave slightly lower performance (1.74 V@ 1A $cm^{-2}$) compared to that of unsupported $IrO_2$ (1.73 V @ 1 A $cm^{-2}$). The performances of various MEAs are tabulated in Table 3-6. The pristine $IrO_2$ showed a current density of 1341 mA $cm^{-2}$ at 1.8 V and decreased with decrease in $IrO_2$ loading except for 90% $IrO_2$-ATO which showed a higher current density (1327 mA $cm^{-2}$ @ 1.8 V) than the pristine $IrO_2$. The current density at 1.8 V normalised to $IrO_2$ loading is also given in Table 3-6. The normalised current density

@1.8 V increased with a decrease in $IrO_2$ loading up to 60% $IrO_2$-ATO and decreased with a further decrease in $IrO_2$ loading. The 60% $IrO_2$-ATO (1625 mA $cm^{-2}$ @1.8 V) has normalised current density about 1.2 times higher than that of the pristine $IrO_2$. This indicates that the performance of the supported catalysts up to 60 wt.% $IrO_2$ loading is better than that of the pristine $IrO_2$. The performance decreased for 40% $IrO_2$-ATO (normalised current density 1133 mA $cm^{-2}$@ 1.8 V) and can be attributed to the low conductivity ($2\times10^{-1}$ S cm) and large crystallite size (5.3 nm) for 40% $IrO_2$-ATO compared to $IrO_2$ loading > 60 wt.% $IrO_2$ (Table 3-2).

The cell voltage at low current density of 100 mA $cm^{-2}$ where ohmic resistance and bubble effects does not significantly influencing the MEA performance is used to compare the performance of the anode catalyst. The cathode performance can be considered equal for all MEA especially at low current density due to the faster kinetics of HER on Pt electrode. A cell voltage of 1.5 V was observed for the pristine $IrO_2$, 90% $IrO_2$-ATO and 80% $IrO_2$. The 60% $IrO_2$-ATO showed only 50 mV (1.55 V @ 0.1 A $cm^{-2}$) lower voltage compared to the pristine $IrO_2$ (1.5 V @ 0.1 A $cm^{-2}$). The difference between the cell voltage @ 0.1 A $cm^{-2}$ and 1 A $cm^{-2}$ increased from 230 mV (90% $IrO_2$-ATO) to 330 mV for 40% $IrO_2$-ATO (Table 3-6) indicating a higher ohmic drop at lower $IrO_2$ loading. The powder conductivity analysis (Table 3-2) showed a decrease in conductivity with decrease in $IrO_2$ loading.

The relatively good performance of 60% $IrO_2$-ATO (1.55 V@ 0.1 A $cm^{-2}$) which equates to an efficiency of 66% and energy consumption of 4.3 kWhr $Nm^{-3}$ $H_2$ at 80$^{o}$C compared to pristine $IrO_2$ (1.50 V @0.1 A $cm^{-2}$) with 68% efficiency and 4.1 kWhr $Nm^{-3}$ $H_2$ at 80$^{o}$C is a significant achievement in terms of the cost of electrocatalyst as the precious $IrO_2$ can be reduced by about 40 wt.% by utilising the support. The energy consumption of commercial electrolysers normally ranges from 3.9 to 7 kWhr $Nm^{-3}$ $H_2$ (Appendix 8.7).

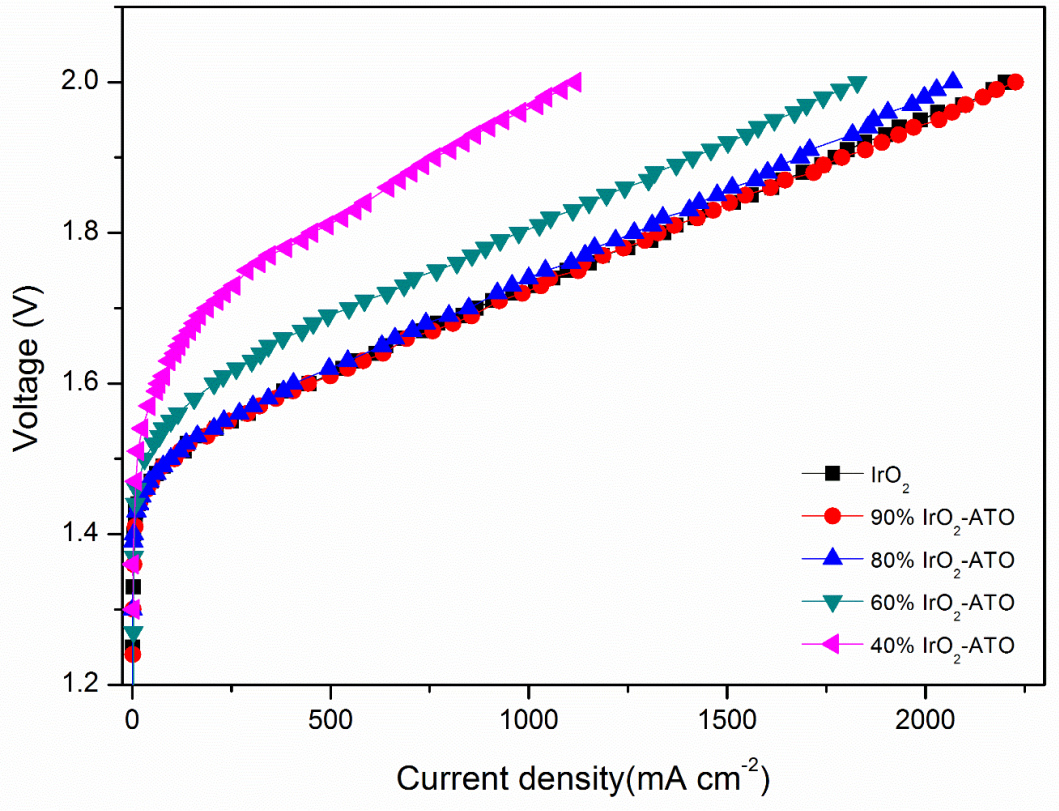


*Figure 3-28. MEA polarisation of $IrO_2$-ATO catalyst at 80$^o$C (Nafion® -115 membrane, Pt/C (20 wt.%) cathode).*

*Table 3-6. MEA performance of $IrO_2$-ATO at various $IrO_2$ loading at 80$^o$C.*

| $IrO_2$ loading (wt.%) | Current density @1. 8V (mA cm$^{-2}$) | Current density@1.8 V normalised to $IrO_2$ loading (mA cm$^{-2}$) | Cell voltage @1A cm$^{-2}$ (V) | Cell voltage @ 0.1 A cm$^{-2}$ (V) | Efficiency ($\varepsilon_{\Delta G}$) @ 1 A cm$^{-2}$ | Energy consumption @1 A cm$^{-2}$ kWhNm$^{-3}$ |
|---|---|---|---|---|---|---|
| 100 | 1341 | 1341 | 1.73 | 1.50 | 68 | 4.1 |
| 90 | 1327 | 1474 | 1.73 | 1.50 | 68 | 4.1 |
| 80 | 1266 | 1583 | 1.74 | 1.50 | 68 | 4.2 |
| 60 | 975 | 1625 | 1.80 | 1.55 | 66 | 4.3 |
| 40 | 453 | 1133 | 1.96 | 1.63 | 60 | 4.7 |

## 3.4 Conclusion

ATO nanoparticles (22-44 nm) were studied as a support material for $IrO_2$ in PEMWE anode. A modified Adams method was adapted for the synthesis. The supported catalysts showed lower crystallite size compared to pristine $IrO_2$. A gradual increase in the intensities of the $SnO_2$ peaks with a decrease in $IrO_2$ loading was also clear from XRD (Figure 3-7) and XPS analysis (Figure 3-12) indicating a coverage of ATO support by the $IrO_2$. Both the powder conductivity and the BET surface analysis increased with an increase in $IrO_2$ loading indicating that the conduction and the surface area were controlled primarily by $IrO_2$. The surface area of ATO (20-40 $m^2 g^{-1}$) was ~3 times lower than that of unsupported $IrO_2$ (112.7 $m^2 g^{-1}$) whereas the conductivity of ATO ($4.29\times10^{-3}$ S $cm^{-1}$) was 3 orders of magnitude lower than that of pristine $IrO_2$ (4.92 S $cm^{-1}$). However a loading of ≥ 60% $IrO_2$-ATO gave conductivity of the same order of magnitude to that of unsupported $IrO_2$, indicating that the $IrO_2$ forms a continuous electrical network at ≥ 60% $IrO_2$-ATO loading below which a significant decrease in conductivity was observed. A continuous film of conducting $IrO_2$ is required to be formed on the support in order to maintain the bulk conductivity of the catalyst. The crystallite size of $IrO_2$ (~6 nm) was ~4 times lower than that of ATO particle (~21-23 nm).

Electrochemical characterization in 85% $H_3PO_4$ at room temperature showed characteristic peaks of $IrO_2$ and the $IrO_2$ loading ≥ 80% $IrO_2$-ATO showed better performance than unsupported $IrO_2$ indicating a higher active surface area for these compositions. The voltammetric charge normalised to $IrO_2$ loading showed a higher voltammetric charge (q*) for all the supported catalysts indicating that the supported catalysts have higher active surface area than the pristine $IrO_2$. A decrease in active area was observed in the CV analysis with increase in temperature. This was attributed to a loss of the active catalyst from the electrode rather than the decrease in activity of the catalyst. The loss of the catalyst may be attributed to the non- uniform heating effect and poor binder stability at high temperature. An increase in activity up to 80$^oC$ was evident from the half-cell study and MEA analysis. MEA analyses with a Nafion-115 membrane and the prepared catalyst as anode electrode were also in agreement with the CV analysis. An $IrO_2$ loading ≥ 60% $IrO_2$ and above showed a better specific mass activity compared to unsupported $IrO_2$ and the performance decreased on further decrease in $IrO_2$ loading.

It can be assumed from the analysis that, support effects in dispersion of the catalyst and maintaining bulk conductivity is important when preparing the supported catalyst. From

the analysis a 60% $IrO_2$-ATO can be recommended as suitable catalyst for the PEMWE anode with a 40 wt.% reduction of precious metal oxide.

# Chapter-4. ITO supported $IrO_2$ as OER catalyst in PEMWE.

Indium tin oxide (ITO) was studied as support material for $IrO_2$ in a PEMWE anode. A modified Adams method was used to synthesis the catalysts. Physical and electrochemical characterizations of the catalysts were carried out using TGA, XRD, SEM, BET surface area and MEA polarisation. A 60 wt.% $IrO_2$ supported on $TiO_2$ was also studied and its MEA performance was compared with the $IrO_2$-ITO catalysts.

## 4.1 Introduction

Precious metal catalyst based electrodes are one of the major cost enhancing factors in PEMWE. Reduction of the precious metal loading on the electrode is an important step towards the commercialisation of the water electrolyser technology. Supporting the active catalyst on a cheap support material is one of the strategies to reduce the precious metal loading on the electrode. Titanium carbide TiC [150, 157], tantalum carbide TaC [215] and silicon carbide-silicon SiC-Si [112] have been studied as OER catalyst supports. Higher activity and stability for Ir/TiC compared to Ir black was observed [17, 150]. The MEA performance increased with increased loading of Ir (10%, 20% and 40% Ir) for Ir/TiC catalysts [157]. But TiC forms non-conductive $TiO_2$ layer at high anodic potential [158]. TaC has a very low BET surface area (2.4 $m^2\ g^{-1}$) and its electronic conductivity decreased by 10 orders of magnitude from 118 S $cm^{-1}$ due to the formation of $NaTaO_3$ [162]. Ti sub-oxide with general formula $Ti_nO_{2n-1}$ ($4 \leq n \leq 10$) has a good conductivity around 1000 S $cm^{-1}$ [152] and has been used as support material for ORR and OER catalysts [174]. But over long term polarisation at high anodic potentials, a non-conductive $TiO_2$ layer was formed on the surface limiting its use [175].

Tin doped indium oxide (ITO) is a well-known transparent conducting oxide widely used as a thin coating film in LCD display, cathode ray tubes, solar cells and electro chromic devices [216, 217]. ITO is a non-stoichiometric oxide where the Sn atom replaces some of the $In^{3+}$ atom in the indium oxide structure and gives rise to n-type conduction [218-220]. The high electrical properties of ITO arise from the combination of conducting carrier-oxygen vacancies in the cubic $In_2O_3$ structure and the dopant ($Sn^{4+}$) that is added to the $In_2O_3$ matrix.

Chhina et al [152] studied the electrochemical stability of an ITO supported Pt catalyst. 40 wt.% of Pt was deposited on both ITO and Vulcan XC-72. The XRD analysis gave a particle size of 13 nm for Pt and 38 nm for the ITO support. The TGA analysis up to a temperature of 1000$^{o}$C in air showed a good thermal stability for the pristine ITO with only 1 wt.% loss after 1000$^{o}$C [152]. An electrochemical study in 0.5M $H_2SO_4$ showed that 40 wt.% Pt/ITO has good electrochemical stability up to +1.8 V vs. RHE compared to a carbon support counterpart [152]. The inert nature of ITO up to +1.8 V vs. RHE in 1M $HNO_3$ was also reported elsewhere [221]. ATO was studied in the previous chapter and an improvement in the performance was observed. ITO has higher conductivity than ATO [220, 222]. Electrical conductivity of the order of $10^2$-$10^3$ S cm$^{-1}$ was reported for ITO [152, 222, 223] whereas ATO has reported conductivity of the order of 10-$10^2$ S cm$^{-1}$ [224]. The aim of this work is to use ITO nanoparticles as a support material for the $IrO_2$ catalyst and study any effect of the support conductivity on the performance of the catalyst.

## 4.2 Experimental:

### 4.2.1 Synthesis of catalyst

$H_2IrCl_6.xH_2O$ (Alfa aesar), tin doped indium oxide (ITO), 10 wt.% $SnO_2$ (Alfa aesar, 17-28 nm particle size and BET surface area 30-50 m$^2$ g$^{-1}$), $NaNO_3$ (Alfa aesar) and isopropanol were used for the catalyst synthesis.

$IrO_2$ supported on ITO was prepared by the modified Adams fusion method. A required amount of support was well dispersed in isopropanol and to this $H_2IrCl_6$ solution was added drop wise while stirring followed by $NaNO_3$. The mixture was stirred well and the solvent was evaporated slowly till dry. It was then transferred to a ceramic crucible and calcined at 500$^{o}$C for 1 hour. The NaCl residue formed after the calcination was dissolved in DI water and the catalyst was washed with copious amount of DI water. A 60% $IrO_2$ on $TiO_2$ (anatase, particle size <25 nm, BET surface area 45-55 m$^2$ g$^{-1}$) was also prepared for comparison using the same method. The reactions in the Adams method are given by equations ((2-3) and ((2-4) [111].

### 4.2.2 Characterization of the catalyst

Physical characterization of the catalysts was carried out by XRD (section 2.2.1), SEM (section 2.2.3), TEM (section 2.2.5), EDX (section 2.2.4) and TGA (section 2.2.6). Powder conductivity was measured using the conductivity set up (section 2.3.1).

The MEA was prepared by the CCM method on a Nafion®-115 membrane using the prepared catalyst as anode and commercial 20% Pt/C (Alfa aesar) as cathode. The membrane was pre-treated in 3% $H_2O_2$, 0.5M $H_2SO_4$ and DI water successively before use. The ink for spraying was prepared with the catalyst, Nafion® ionomer and ethanol. It was then sprayed directly on to the membrane using a spray gun. The Nafion® content on both electrodes was 15 wt.%. The cell body was made up of titanium with 1 $cm^2$ flow field area. A gold coated titanium mesh and carbon paper (Toray) was used as gas diffusion layers/current collectors on the anode and cathode respectively. The prepared CCM was sandwiched between the two gas diffusion layers forming the MEA and assembled in the cell body with a torque of 2 N m.

DI water was pumped using a peristaltic pump to the anode side of the cell. The cell was heated to the required temperature using two heating rods and temperature controllers (Figure 2-15). The cathode was kept dry as there will be water transfer to cathode through electro osmotic drag (movement of water accompanying with proton transfer under a potential difference). Cell polarisation was carried out in a potentiostatic mode using a power source (Thurlsby Thandar instruments, PL3320).

## 4.3 Result and Discussion:

### 4.3.1 XRD

The XRD spectra of the $IrO_2$ and ITO support is given in Figure 4-1 showing highly crystalline structures. The peaks were identified to be rutile structure for $IrO_2$ (JCPDS: 015-0870) and cubic for ITO (JCPDS: 006-0416). The XRD spectra of 60% $IrO_2$-ITO is given in Figure 4-2 as representative example showing the characteristic peaks of $IrO_2$ and ITO in the supported catalysts. The XRD of supported catalysts with various $IrO_2$ loading is compared in Figure 4-3. The strong peak at 30.57$^o$ is the (222) peak for $In_2O_3$ (JCPDS: 6-0416) from ITO. The (222), (400), (440) and (622) peaks of ITO were intense and clearly visible in all the supported catalysts except for the 90% $IrO_2$-ITO. A broadening of the $IrO_2$ (110) and (101) peak was observed for 90% $IrO_2$-ITO compared to other supported catalysts indicating that 90% $IrO_2$-ITO has smaller $IrO_2$ crystallites.

Smaller crystallites usually have more crystal lattice defects which are mostly the high active sites. Smaller crystallites thus increase the density of the active sites and subsequently reduce the electrode over potential [150]. Since the characteristic peaks of ITO and $IrO_2$ were present separately in the XRD and no change in peak position was observed with respect to composition, it may be assumed that the $IrO_2$ forms a physical mixture with ITO and no solid solution was formed between the two oxides [194].

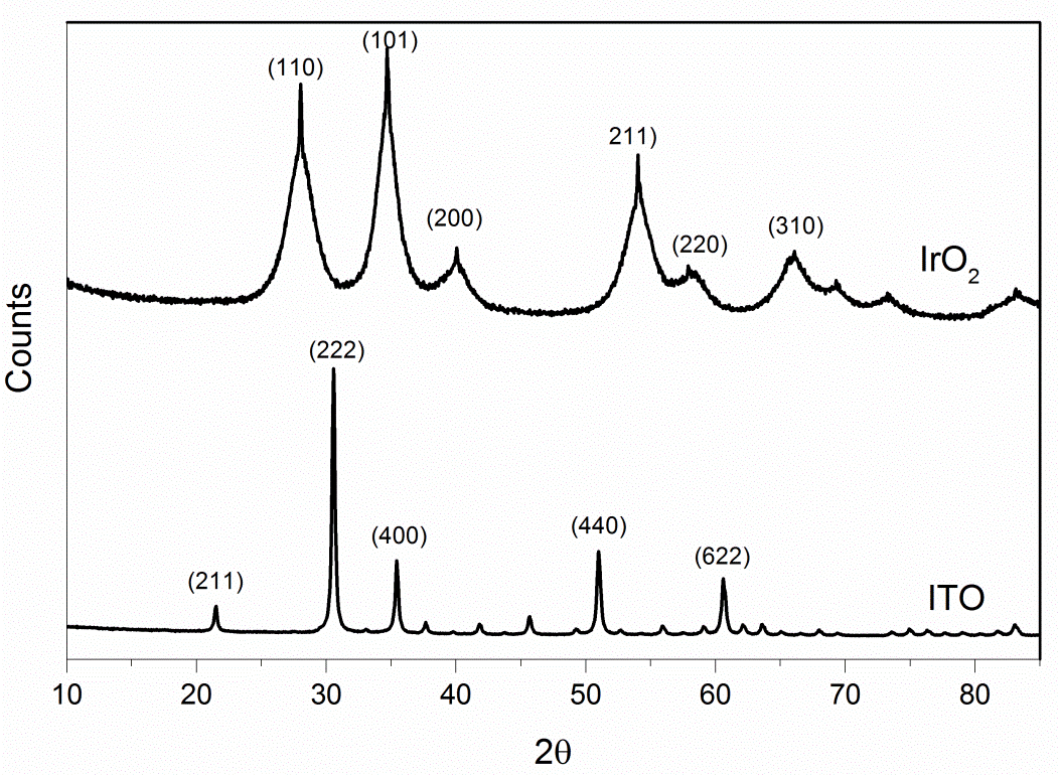


*Figure 4-1. XRD spectra of $IrO_2$ prepared and ITO commercial.*

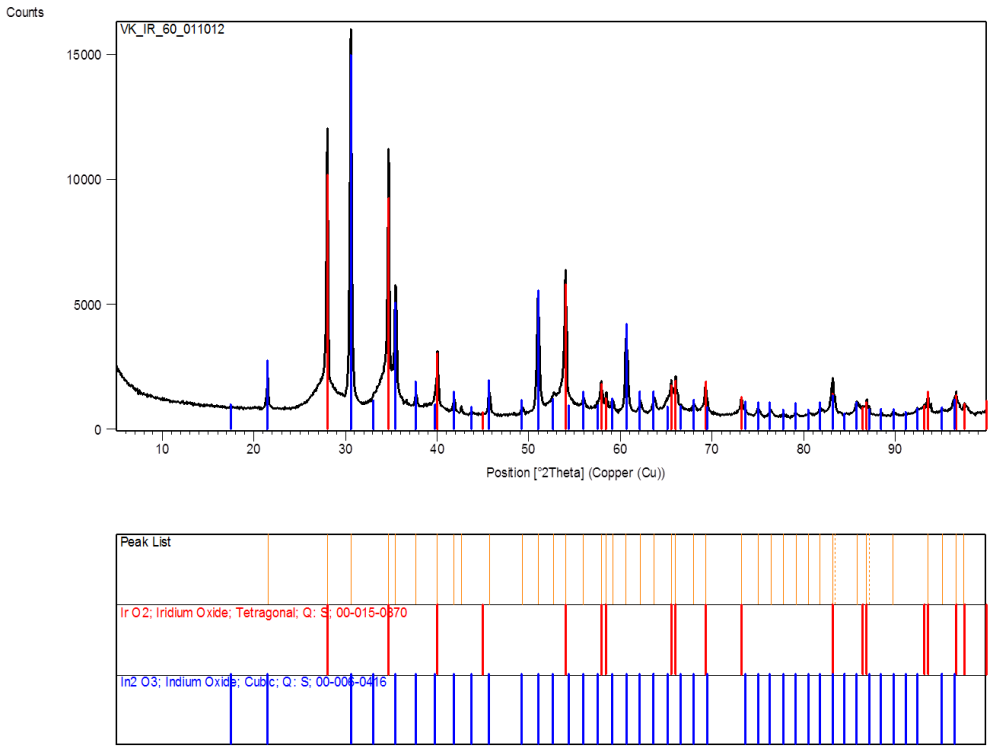


*Figure 4-2. XRD spectra of 60% $IrO_2$-ITO showing the characteristic peaks of $IrO_2$ and $In_2O_3$.*

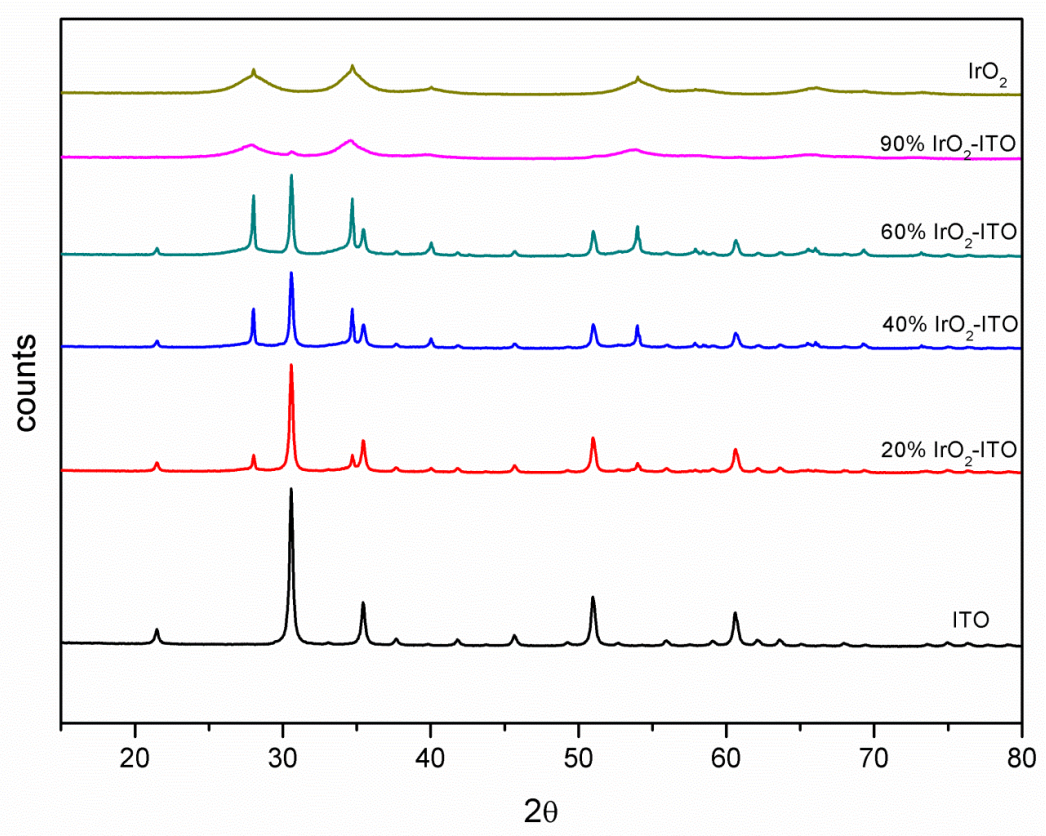


*Figure 4-3. XRD spectra of $IrO_2$-ITO at various $IrO_2$ loading.*

Average crystallite sizes of the $IrO_2$ on the supported catalysts were calculated from the Scherrer equation (equation 2.9) using the two major peaks at $28^o$ and $34.5^o$ and are given in Table 4-1. The peak at $30.6^o$ was used for the crystallite size calculation of ITO. The average $IrO_2$ crystallite sizes in pristine $IrO_2$ and 90% $IrO_2$-ITO were 6.0 nm and 5.0 nm respectively. The pristine ITO showed crystallite size of 30.5 nm which is more or less the same as the particle size given by the supplier (28 nm). The crystallite size of ITO (30.5 nm) was 5 times larger than that of $IrO_2$ (6 nm). A steep increase in the crystallite size was observed from 90% $IrO_2$-ITO (5 nm) to ≤ 60% $IrO_2$-ITO (47-50 nm). A lower crystallite size at lower $IrO_2$ loading was observed for $IrO_2$-ATO catalysts in the previous chapter and was explained based on the dispersion of the $IrO_2$ on the ATO support forming smaller crystallites. The lower $IrO_2$ crystallite size obtained for 90% $IrO_2$-ITO (5 nm) compared to pristine (6 nm) is in quite agreement with the results of $IrO_2$-ATO catalysts (Chapter 3). However in contrary to $IrO_2$-ATO catalysts, a steep increase in $IrO_2$ crystallite size of ~9 times for 60% $IrO_2$-ITO (47.2 nm) compared to 90% $IrO_2$-ITO (5 nm) was observed for $IrO_2$-ITO. This is quite unusual and it may imply that an agglomerate of $IrO_2$ was formed on the ITO support for loading < 90% $IrO_2$-ITO and the $IrO_2$ might have formed islands on the ITO instead of forming a continuous network. The $IrO_2$ agglomeration will reduce the electronic conduction network as well as the surface area which was confirmed from the conductivity and surface area analysis (Table 4-1) and is discussed in the section 4.3.3 and section 4.3.4 respectively. It is difficult to identify the exact reason for agglomeration. It may assumed to be mainly due to a lack of proper precursor mixing during the synthesis resulting in a low interaction between the catalyst and the support. Since the dispersion of the active catalyst occurs during the precursor mixing stage prior to the calcination, it is important to maintain a good mixing in order to obtain a good dispersion.

### 4.3.2 Morphology

The morphology of the supported catalyst was studied using SEM and TEM. The SEM images of the catalyst are given in Figure 4-4. The pristine $IrO_2$ (Figure 4-4a) showed good uniform morphology whereas the supported catalysts showed a slightly different morphology. It is difficult to distinguish between $IrO_2$ and ITO in the supported catalyst from the SEM. The 40% $IrO_2$-ITO showed some agglomeration as clear from Figure 4-4(c). A lower conductivity and higher crystallite size ($6.9\times10^{-3}$ S $cm^{-1}$, 50.1 nm) of the 40% $IrO_2$-ITO compared to the 20% $IrO_2$-ITO ($2\times10^{-2}$ S $cm^{-1}$, 47.2 nm) was clear from

the XRD and the conductivity analysis (Table 4-1) which may be attributed to the $IrO_2$ agglomeration.

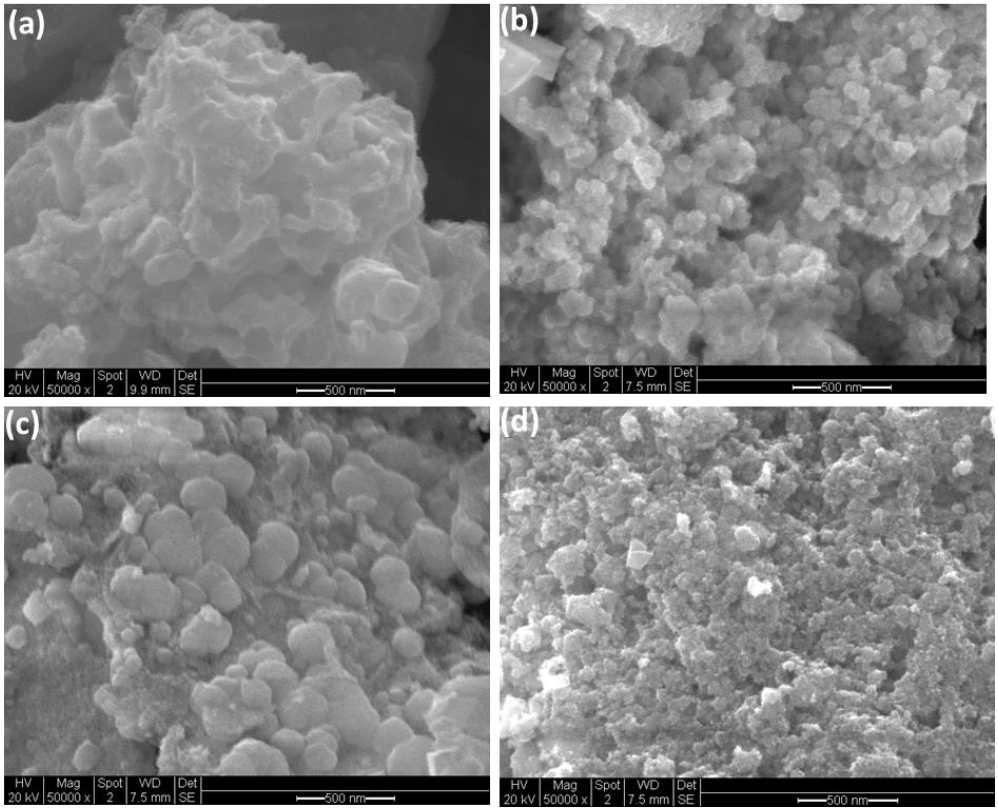


*Figure 4-4. SEM micrograph of (a) $IrO_2$ (b) 60% $IrO_2$-ITO (c) 40% $IrO_2$-ITO (d) 20% $IrO_2$-ITO.*

TEM images showed very uniform particle distribution for the $IrO_2$ and 90% $IrO_2$-ITO (Figure 4-5). A particle size of 3-4 nm was obtained for $IrO_2$ and 90% $IrO_2$-ITO and is more or less same as the crystallite size calculated from the XRD (5-6 nm) (Table 4-1). It is difficult to distinguish between the $IrO_2$ and ITO from the TEM. The 60% $IrO_2$-ITO showed both small and large particles. The large particles can either be $IrO_2$ agglomerate or the ITO support. Since XRD gave crystallite size of around 47.2 and 30.5 nm respectively for $IrO_2$ in 60% $IrO_2$-ITO and ITO, it is difficult to specifically assign the large particle to one of them.

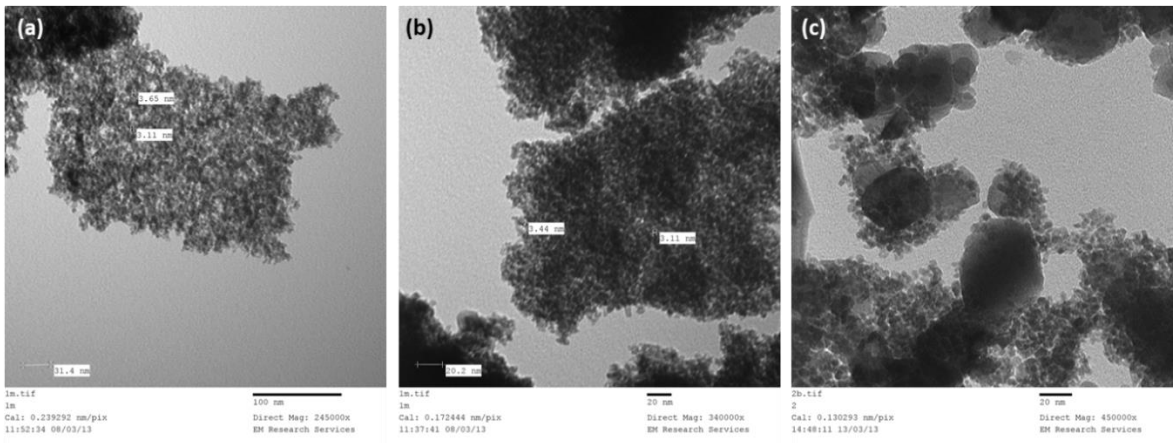


*Figure 4-5. TEM images of (a) $IrO_2$ (b) 90% $IrO_2$-ITO (c) 60% $IrO_2$-ITO.*

### 4.3.3 Electronic conductivity

The conductivity measured using the cell described in section 2.3.1 gives a linear relationship between the thicknesses vs. resistance for all samples (Figure 4-6). The conductivity was calculated from the slope of the linear plot using equations (2-14) and (2-15). The conductivities obtained are given in Table 4-1.

$IrO_2$ showed the highest conductivity amongst all samples (4.9 S $cm^{-1}$) which is three orders of magnitude higher than that of the ITO support ($6.3\times10^{-3}$ S $cm^{-1}$). The conductivity decreased by 10 times whereas the crystallite size decreased by ~9 times from 90% $IrO_2$-ITO (3.5 S $cm^{-1}$, 5 nm) to 60% $IrO_2$-ITO ($1.3\times10^{-1}$ S $cm^{-1}$, 47.2 nm). The significant decrease in conductivity at $IrO_2$ loading < 90% $IrO_2$-ITO can be attributed to $IrO_2$ agglomeration as discussed in section 4.3.1. The 40% $IrO_2$-ITO ($6.9\times10^{-3}$ S $cm^{-1}$) showed a lower conductivity than 20% $IrO_2$-ITO ($2\times10^{-2}$ S $cm^{-1}$) though the $IrO_2$ content is higher in 40% $IrO_2$-ITO. This may be attributed to the much higher agglomeration on this composition as clear from SEM (Figure 4-4) whereby larger particles are seen on 40% $IrO_2$-ITO compared to 20% $IrO_2$-ITO. On comparing the conductivity of the $IrO_2$-ITO catalyst with the conductivity of the $IrO_2$-ATO (chapter 3), it is clear that a significant decrease in conductivity is obtained for $IrO_2$ loading < 60 wt. % on both the ITO and the ATO supported $IrO_2$ catalyst. A decrease in conductivity of one order of magnitude was observed for ATO supported $IrO_2$ from 60% $IrO_2$-ATO (1.6 S $cm^{-1}$) to 40% $IrO_2$-ATO ($2\times10^{-1}$ S $cm^{-1}$) whereas for ITO supported catalysts, a decrease in conductivity of two orders of magnitude was observed from 60% $IrO_2$-ITO ($1.3\times10^{-1}$ S $cm^{-1}$) to 40% $IrO_2$-ITO ($6.9\times10^{-3}$ S $cm^{-1}$). The larger difference is conductivity decrease

in the case of the ITO supported catalyst can be attributed to a significantly higher agglomeration of it. Since the conductivity is predominantly contributed by the $IrO_2$ particles, any $IrO_2$ agglomeration on the support will reduce the continuous $IrO_2$ network decreasing the overall conductivity of the supported catalyst. Since the conductivity of the ITO support ($6.3\times10^{-3}$ S $cm^{-1}$) is much lower than the $IrO_2$ (4.9 S $cm^{-1}$), it is very important to maintain good electrical conductivity by forming a continuous $IrO_2$ network on the support.

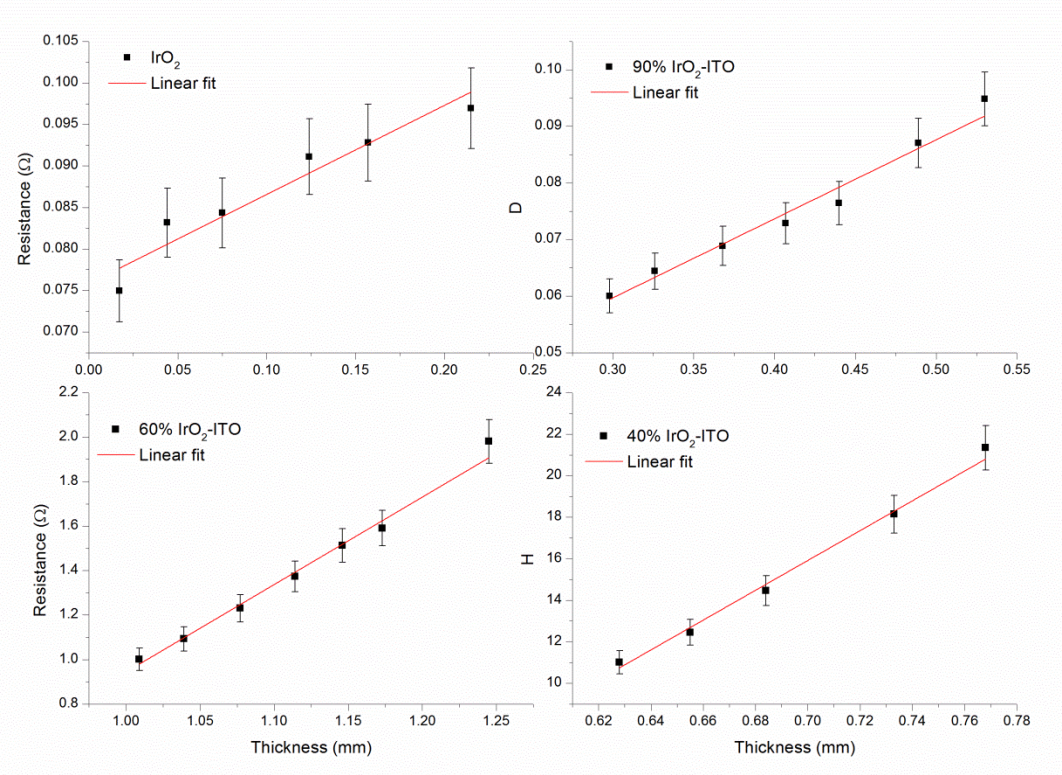


*Figure 4-6. Resistance vs. thickness plots of the $IrO_2$-ITO catalyst powder.*

### 4.3.4 BET surface area

The BET surface area was used to measure the $N_2$ adsorbed surface area of catalyst dispersed on the ITO nano particle. Pristine $IrO_2$ gave a higher surface area of 112 $m^2$ $g^{-1}$ compared to the ITO supported material (35 $m^2$ $g^{-1}$). A BET surface area of 121 $m^2$ $g^{-1}$ was reported elsewhere for $IrO_2$ prepared by the Adams method [112, 162]. The BET surface area of the supported catalysts increased with increase in the $IrO_2$ loading (Figure 4-7) indicating that the surface area was contributed mainly by $IrO_2$. The 90% $IrO_2$-ITO showed a higher BET surface area (122.5 $m^2$ $g^{-1}$) than the pristine $IrO_2$ (112.8 $m^2$ $g^{-1}$) and thus can be attributed to lower $IrO_2$ crystallite size (5 nm compared to 6 nm for pristine

$IrO_2$) and better dispersion on the support. A higher BET surface area for 90% $IrO_2$-ATO (126.5 $m^2$ $g^{-1}$) compared to pristine $IrO_2$ (121 $m^2$ $g^{-1}$) was obtained in the previous chapter (Chapter 3) with a decrease in crystallite size from 6 nm (for pristine $IrO_2$) to 3.8 nm (for 90% $IrO_2$-ATO).

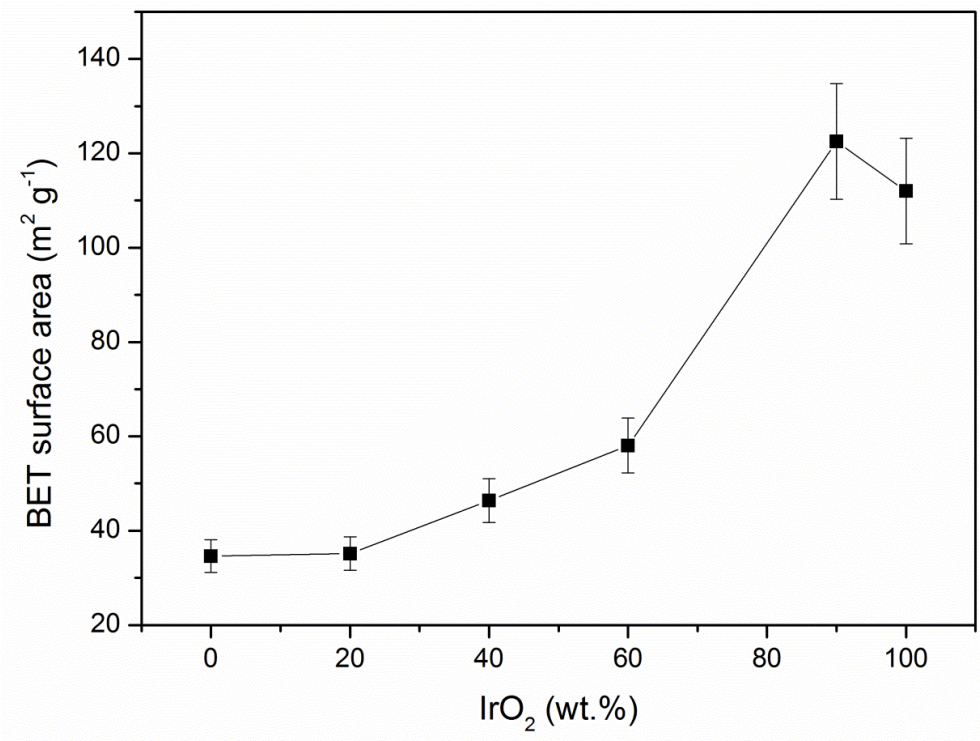


*Figure 4-7. BET surface area of the supported catalyst with respect to the $IrO_2$ loading.*

The steep decrease in the surface area from 90% $IrO_2$-ITO (122.5 $m^2$ $g^{-1}$) to 60% $IrO_2$-ITO (58.1 $m^2$ $g^{-1}$) was mainly because of the higher $IrO_2$ particle size in 60% $IrO_2$-ITO (47.2 nm) compared to 90% $IrO_2$-ITO (5 nm) caused by agglomeration of $IrO_2$ as mentioned in the XRD (section 4.3.1) and conductivity (section 4.3.3) analysis. Correlating the decrease in surface area with the corresponding increase in crystallite size and decrease in conductivity (Table 4-1) from 90% $IrO_2$-ITO (122.5 $m^2$ $g^{-1}$, 5 nm, 3.5 S $cm^{-1}$) to 60% $IrO_2$-ITO (58.1 $m^2$ $g^{-1}$, 47.2 nm, $1.3\times10^{-1}$ S $cm^{-1}$), the $IrO_2$ agglomeration on the ITO supported catalyst with loading < 90% $IrO_2$-ITO can be confirmed.

The BET surface area normalised to $IrO_2$ loading is also given in Table 4-1 and the particle size was calculated from the normalised surface area considering $IrO_2$ as a hard sphere using equation (3-2). The 90% $IrO_2$-ITO showed the highest normalised surface area (132 $m^2$ $g^{-1}$). A steep decrease in the normalised surface area is clear on decreasing the $IrO_2$ loading to 60% $IrO_2$-ITO (74 $m^2$ $g^{-1}$) confirming the $IrO_2$ agglomeration. The

particle sizes calculated from the surface area were significantly different from the crystallite size calculated from the XRD for $IrO_2$ loading ≤ 60% $IrO_2$-ATO. Since the particle size calculated from the surface area is by considering an ideal case of hard sphere, the large difference indicates that the $IrO_2$ crystallites were agglomerated in reality for loading ≤ 60% $IrO_2$-ITO.

*Table 4-1. Physical properties of the $IrO_2$-ITO catalyst. * Values obtained from the supplier, # crystallite size of the support particle.*

| Catalyst | BET surface area ($m^2\ g^{-1}$) | Electronic conductivity ($S\ cm^{-1}$) | Average crystallite size of $IrO_2$ (nm) | BET surface area normalised to $IrO_2$ loading ($m^2\ g^{-1}$) | Particle size calculated from the BET surface area (nm) |
|---|---|---|---|---|---|
| $IrO_2$ | 112 ± 11 | 4.9 ± 0.6 | 6.0 ± 0.3 | 112 ± 11 | 4.6 ± 0.4 |
| 90% $IrO_2$-ITO | 122.5 ± 12 | 3.5 ± 0.4 | 5.0 ± 0.4 | 132 ± 13 | 3.9 ± 0.5 |
| 60% $IrO_2$-ITO | 58.1 ± 6 | $1.3\times10^{-1}$ | 47.2 ± 1 | 74 ± 7 | 7 ± 0.8 |
| 40% $IrO_2$-ITO | 46.4 ± 5 | $6.9\times10^{-3}$ | 50.1 ± 1.2 | 42 ± 4 | 12.2 ± 1 |
| 20% $IrO_2$-ITO | 35.2 ± 4 | $2\times10^{-2}$ | 47.2 ± 1.7 | 9 ± 1 | 57.5 ± 6 |
| 60% $IrO_2$-$TiO_2$ | 121 ± 12 | $3.8\times10^{-1}$ | 4.0 ± 0.5 | 168 ± 17 | 3.1 ± 0.3 |
| ITO | 35 ± 4 | $6.3\times10^{-3}$ | 30.5 ± 0.4# | | 24 ± 2 |
| $TiO_2$ | 45-55* | $2.6\times10^{-6}$ | <25*# | | |

### 4.3.5 Cyclic voltammetry

As mentioned in the chapter 4, the CV in 85% $H_3PO_4$ gives clearer redox peaks for $IrO_2$. The CV of $IrO_2$-ITO in 85% $H_3PO_4$ at room temperature is given in Figure 4-8. The unsupported $IrO_2$ and supported $IrO_2$ gives characteristic peaks of $IrO_2$ at ~0.78 V and ~1 V (vs.Ag/AgCl) in 85% $H_3PO_4$ and is attributed to the redox transition of Ir(III)/Ir(IV) and Ir(IV)/Ir(VI) (equation 2-18) [75, 135-137]. As mentioned in Chapter 3, the voltammetric charge (q*) is a measure of the number of active sites available to exchange proton with the solution. i.e. electrochemical active surface area [129, 209]. The q* calculated for the $IrO_2$-ITO catalyst in 85% $H_3PO_4$ with 20 mV $s^{-1}$ scan rate at room temperature is given in Table 4-2. The 90% $IrO_2$-ITO was found to give higher voltammetric charge (2160 mC $cm^{-2}$ $mg^{-1}$) compared to pristine $IrO_2$ (1700 $m^2\ g^{-1}$) as in the case of the ATO supported $IrO_2$ (Table 3-4). However a large active surface area

decreases can be seen for the $IrO_2$ loading ≤ 60% wt.% unlike for the ATO supported catalyst counterpart (Table 3-4). The voltammetric charge was decreased by ~4.5 times for 60% $IrO_2$-ITO from 90% $IrO_2$-ITO (Table 4-2) compared to ~1.3 times decrease for ATO supported catalysts counterpart. This decrease can be attributed to the large crystallite size (47.2 nm) and lower electronic conductivity ($1.3\times10^{-1}$ S $cm^{-1}$) of the 60% $IrO_2$-ITO catalyst compared to the pristine 90% $IrO_2$-ITO (5 nm, 3.5 S $cm^{-1}$) (Table 4-1).

The voltammetric charge normalised to the $IrO_2$ loading was also given in Table 4-2. The normalised voltammetric charge is higher for 90% $IrO_2$-ITO (2400 mC $cm^{-2}$ $mg^{-1}$) compared to the pristine $IrO_2$ (1700 mC $cm^{-2}$ $mg^{-1}$). The normalised charge also showed a steep decrease to 60% $IrO_2$-ITO (639 mC $cm^{-2}$ $mg^{-1}$) about ~3.7 times lower than that of 90% $IrO_2$-ITO (2400 mC $cm^{-2}$ $mg^{-1}$). This once again confirms the assumption of $IrO_2$ agglomeration on the ITO support.

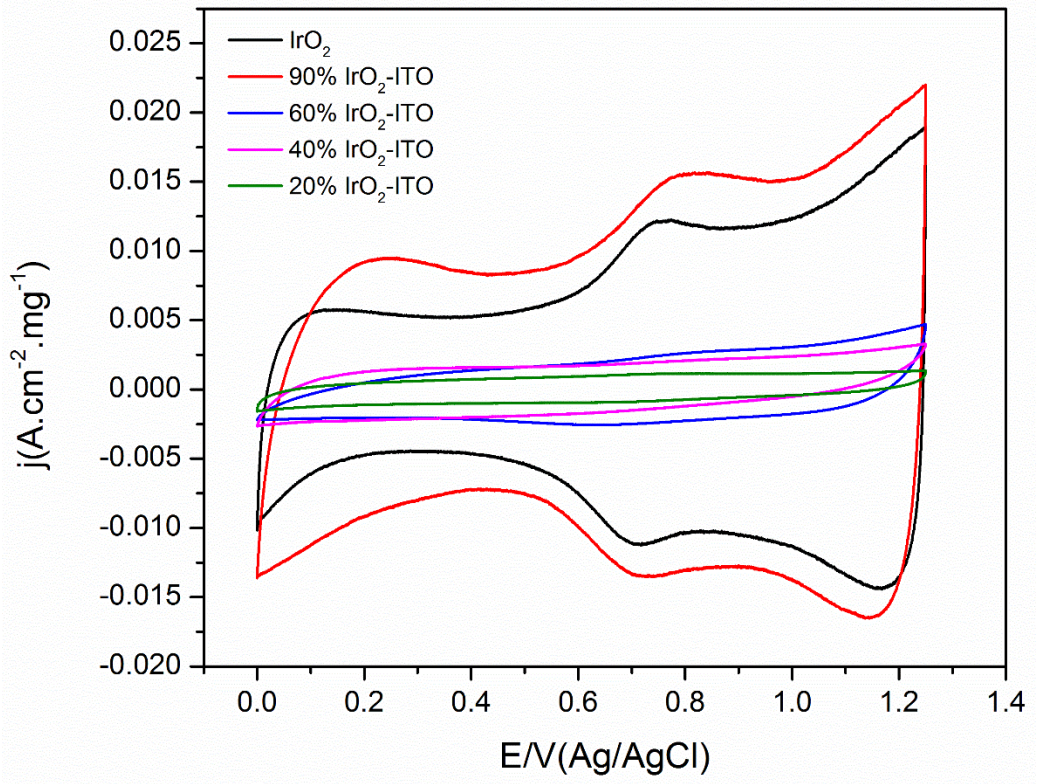


*Figure 4-8. CV of $IrO_2$-ITO catalyst at room temperature in 85% $H_3PO_4$ solution (Scan rate 20 mV $s^{-1}$).*

*Table 4-2. Voltammetric charge of $IrO_2$-ITO at room temperature in 85% $H_3PO_4$*

| Catalyst | Voltammetric charge (q*) (mC $cm^{-2}$ $mg^{-1}$) | Voltammetric charge (q*) normalised to $IrO_2$ loading (mC $cm^{-2}$ $mg^{-1}$) |
|---|---|---|
| $IrO_2$ | 1700 ± 85 | 1700 ± 85 |
| 90% $IrO_2$-ITO | 2160 ± 108 | 2400 ± 120 |
| 60% $IrO_2$-ITO | 383 ± 19 | 639 ± 32 |
| 40% $IrO_2$-ITO | 319 ± 16 | 797 ± 40 |
| 20% $IrO_2$-ITO | 159 ± 8 | 795 ± 40 |

### 4.3.6 PEMWE performance

The MEA performance of $IrO_2$-ITO with different $IrO_2$ loadings at 80°C is compared in Figure 4-9 and the performance of the various MEA's are tabulated in Table 4-3. The 90% $IrO_2$-ITO catalyst (1276 mA $cm^{-2}$@ 1.8 V) showed more or less similar performance to that of the pristine $IrO_2$ (1341 mA $cm^{-2}$ @1.8 V) (Table 4-3). The 60% $IrO_2$-ITO (524 mA $cm^{-2}$ @1.8 V) showed ~ 2.4 times lower current density compared to the 90% $IrO_2$-ITO (1276 mA $cm^{-2}$@ 1.8 V). The current density @ 1.8 V normalised to $IrO_2$ loading is also given in Table 4-3. The 90% $IrO_2$-ITO showed a higher normalised current density (1418 mA $cm^{-2}$@ 1.8 V) compared to the pristine $IrO_2$ (1341 mA $cm^{-2}$@ 1.8 V). The 60% $IrO_2$-ITO (873 mA $cm^{-2}$@ 1.8 V) showed ~1.6 times lower normalised current density compared to the 90% $IrO_2$-ITO (1418 mA $cm^{-2}$@ 1.8 V) (Table 4-3). The cell voltages of the MEA with the ITO supported $IrO_2$ anode catalysts at current density of 100 mA $cm^{-2}$ were compared in order to evaluate the performance of the catalyst without significant ohmic and bubble formation effects. The cell voltages of the MEAs at 0.1 A $cm^{-2}$ at 80°C are given in Table 4-3. The 90% $IrO_2$-ITO and the pristine $IrO_2$ showed a cell voltage of 1.50 V @ 0.1 A $cm^{-2}$ whereas the 60% $IrO_2$-ITO showed a higher cell voltage of 1.61 V @0.1 A $cm^{-2}$. The difference in the cell voltage at 0.1 A $cm^{-2}$ and 1 A $cm^{-2}$ for 90% $IrO_2$-ITO and 60% $IrO_2$-ITO were 240 mV and 320 mV respectively. The large difference in cell voltage at high current density can be attributed to lower electronic conductivity of 60% $IrO_2$-ITO ($1.3\times10^{-1}$ S $cm^{-1}$) compared to the 90% $IrO_2$-ITO (3.5 S $cm^{-1}$) resulting in large ohmic drop at high current density. It is noticeable that the cell voltage differences for the $IrO_2$-ATO counterpart at the same condition were 230 mV and 250 mV which may be attributed to the comparable conductivity of 60% $IrO_2$-ATO (1.6 S $cm^{-1}$) to that of 90% $IrO_2$-ITO (4.8 S $cm^{-1}$).

From the Table 4-1, it was clear that 90% $IrO_2$-ITO have comparable crystallite size, conductivity and surface area (5 nm, 3.5 S $cm^{-1}$, 123 $m^2$ $g^{-1}$) to that of the pristine $IrO_2$ (6 nm, 4.9 S $cm^{-1}$, 112.8 $m^2$ $g^{-1}$) which explains the similar performance of the 90% $IrO_2$-ITO (1.74 V@ 1 A $cm^{-2}$) to that of pristine $IrO_2$ (1.73 V@ 1 A $cm^{-2}$). It can be assumed that the active $IrO_2$ was well dispersed on the ITO support in 90% $IrO_2$-ITO and support material assisted in the dispersion. A significantly lower performance for 60% $IrO_2$-ITO can be attributed to their higher particle size (47.2 nm) compared to 90% $IrO_2$-ITO (5 nm) and pristine $IrO_2$ (6 nm) which produced particles of lower surface area and conductivity (Table 4-1). The results clearly indicate the effect of particle size and dispersion of the catalyst on the performance of the electrode. Larger particles have lower surface area and failed to provide a continuous electron conducting network on the support which in turn decrease the performance of the MEA.

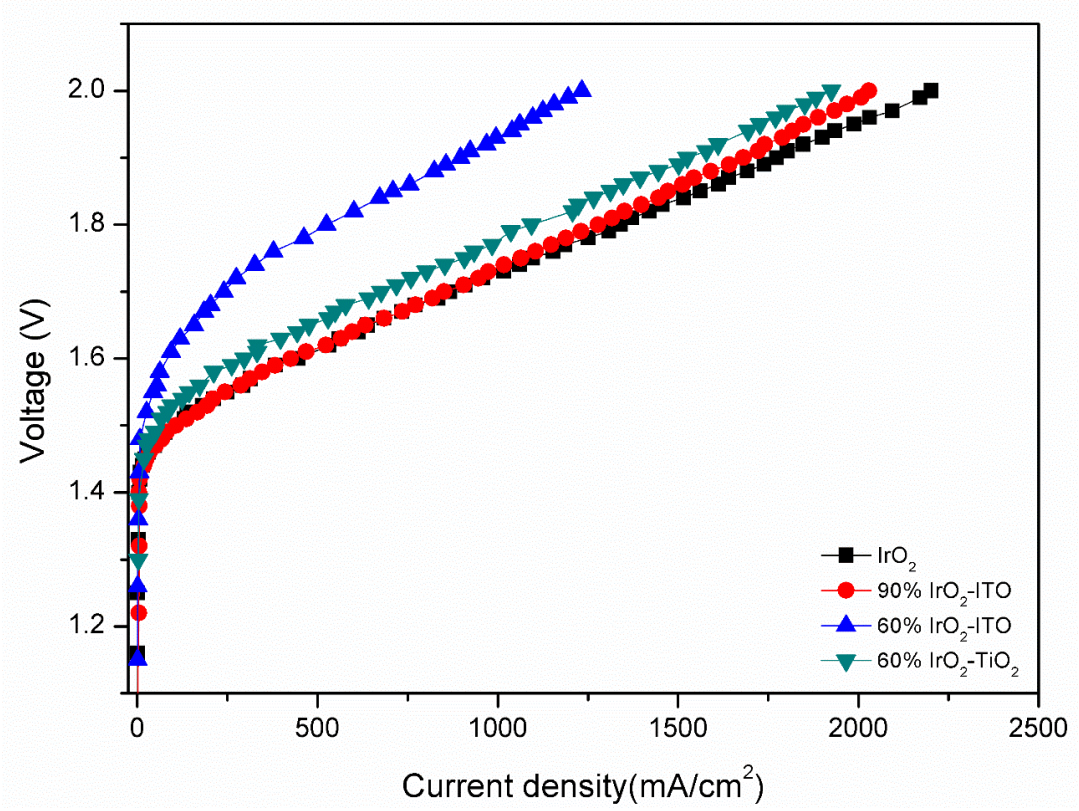


*Figure 4-9. MEA polarisation of $IrO_2$-ITO and 60% $IrO_2$-$TiO_2$ catalysts at 80$^oC$. Nafion-115 membrane, Pt/C (20 wt.%) cathode.*

### 4.3.7 Effect of support conductivity

In order to confirm the agglomeration and to understand the effect of conductivity of the support on the performance of the catalyst, a 60% $IrO_2$ supported on a non-conducting $TiO_2$ was prepared using the Adams fusion method. The anatase form of $TiO_2$ was chosen as it was reported to give better performance than the rutile structure [173, 191]. The XRD spectrum of the prepared catalyst is given in Figure 4-10 and an anatase $TiO_2$ structure (JCPDS: 021-1272) was confirmed with characteristic peaks at 25.3$^o$, 37.7$^o$ and 48$^o$. An average crystallite size of 4 nm was obtained for $IrO_2$ from the peaks at 28$^o$ and 34.5$^o$.

The MEA performance of the 60% $IrO_2$-$TiO_2$ anode is given in Figure 4-9. The performance of $TiO_2$ and ITO supported $IrO_2$ is compared in Table 4-3. The current density @ 1.8V for 60% $IrO_2$-$TiO_2$ (1094 mA cm$^{-2}$ @1.8 V) was two times higher than that of 60% $IrO_2$-ITO (524 mA cm$^{-2}$ @1.8 V). The current density normalised to $IrO_2$ loading also showed two times higher current density for 60% $IrO_2$-$TiO_2$ (1823 mA cm$^{-2}$ @1.8 V) compared to 60% $IrO_2$-ITO (873 mA cm$^{-2}$ @1.8 V). Table 4-1 compares the conductivity and crystallite sizes of the ITO and $TiO_2$ supported $IrO_2$ for the 60 wt.% $IrO_2$ loading. The conductivity of 60% $IrO_2$-ITO ($1.3\times10^{-1}$ S cm$^{-1}$) and 60% $IrO_2$-$TiO_2$ ($3.8\times10^{-1}$ S cm$^{-1}$) were of the same order of magnitude but the crystallite sizes were approximately 9 times lower for the latter (47.2 nm for 60% $IrO_2$-ITO compared to 4 nm for 60% $IrO_2$-$TiO_2$). The BET surface area was ~2 times lower for 60% $IrO_2$-ITO (58 m$^2$ g$^{-1}$) compared to 60% $IrO_2$-$TiO_2$ (121 m$^2$ g$^{-1}$). An interesting observation is that, even though the conductivity of the ITO and $TiO_2$ supports alone were 3 orders of magnitude different ($6.3\times10^{-3}$ S cm$^{-1}$ for ITO and $2.6\times10^{-6}$ S cm$^{-1}$ for $TiO_2$), a 60% $IrO_2$ loading gave conductivity of the same order of magnitude which confirms the behaviour described in section 4.3.3, that the conductivity was predominantly contributed by $IrO_2$. The cell voltage at current density of 100 mA cm$^{-2}$ of 60% $IrO_2$-$TiO_2$ is compared with 60% $IrO_2$-ITO in Table 4-3. The 60% $IrO_2$-$TiO_2$ (1.53 V @0.1 A cm$^{-2}$) showed 80 mV lower voltage compared to 60% $IrO_2$-ITO (1.61 V @0.1 A cm$^{-2}$).

The large difference in the performance of MEA for ITO and $TiO_2$ supported catalysts can thus be attributed to the difference in the crystallite size rather than to the conductivity. The smaller $IrO_2$ crystallite size (4 nm) on the 60% $IrO_2$-$TiO_2$ gave a higher surface area (121 m$^2$ g$^{-1}$) compared to the lower surface area (58 m$^2$ g$^{-1}$) of 60% $IrO_2$-ITO due to its larger $IrO_2$ crystallite size (47.2 nm). An enhanced activity of 60% Ir-Ru catalyst supported on anatase $TiO_2$, compared to an pristine Ir-Ru catalyst, was reported

elsewhere [173] and was attributed to better dispersion of the particle on the support surface giving rise to higher surface area.

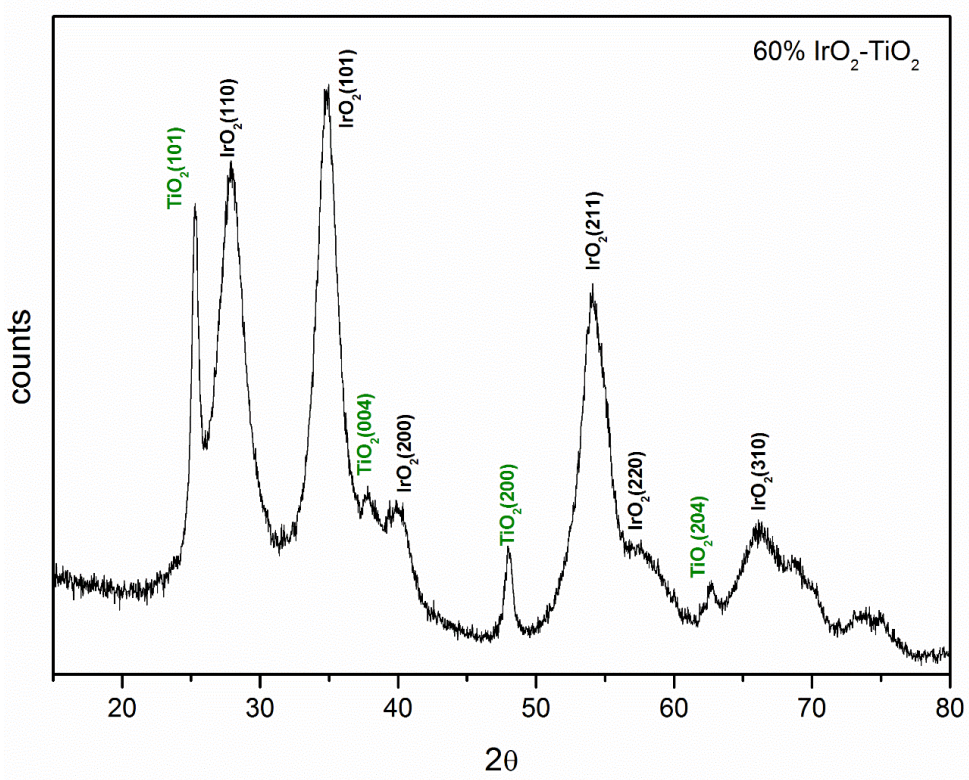


*Figure 4-10. XRD spectra of 60% $IrO_2$-$TiO_2$.*

*Table 4-3. MEA performance of $IrO_2$-ITO catalyst.*

| **Anode catalyst** | **Current density @ 1.8 V (mA cm$^{-2}$)** | **Current density @ 1.8 V normalised to $IrO_2$ loading (mA cm$^{-2}$)** | **Cell voltage @1A cm$^{-2}$ (V)** | **Cell voltage @0.1 A cm$^{-2}$ (V)** | **Efficiency ($\varepsilon_{\Delta G}$) @ 1 A cm$^{-2}$** | **Energy consumption @1A cm$^{-2}$ (kWhNm$^{-3}$)** |
|---|---|---|---|---|---|---|
| $IrO_2$ | 1341 | 1341 | 1.73 | 1.50 | 68 | 4.1 |
| 90% $IrO_2$-ITO | 1276 | 1418 | 1.74 | 1.50 | 68 | 4.2 |
| 60% $IrO_2$-ITO | 524 | 873 | 1.93 | 1.61 | 61 | 4.6 |
| 60% $IrO_2$-$TiO_2$ | 1094 | 1823 | 1.78 | 1.53 | 67 | 4.3 |

## 4.4 Conclusions

$IrO_2$ nanoparticles were deposited in various loadings on commercially available ITO nanoparticles 17-28 nm in size using the modified Adam's fusion method. The prepared catalysts were characterised using XRD, SEM, TEM, conductivity and MEA polarisation. The BET surface area of the support (35 $m^2.g^{-1}$) was 3 times lower than the pristine $IrO_2$ (112.7 $m^2.g^{-1}$) and increased with an increase in the $IrO_2$ loading indicating that the surface area was contributed mainly by $IrO_2$. The electrical conductivity of the catalyst also increased with the increase in $IrO_2$ loading. A large agglomeration of the catalyst was observed for the loading ≤ 60% $IrO_2$-ITO. This was mainly attributed to the lack of proper precursor interaction with the support during the synthesis. The 90% $IrO_2$-ITO (1.74 V @1 A $cm^{-2}$) gave similar performance to that of the pristine $IrO_2$ (1.73 V @1A$cm^{-2}$) in MEA polarisation tests which was attributed to a better dispersion of the active $IrO_2$ on the electrochemically inactive ITO support in 90% $IrO_2$-ITO, giving rise to lower particle size (5 nm) and higher surface area (123 $m^2$ $g^{-1}$) catalyst compared to pristine $IrO_2$ (6 nm, 112 $m^2$ $g^{-1}$). A significant decrease in the performance was observed for 60% $IrO_2$-ITO (1.93 V@1 A $cm^{-2}$) and was attributed to the large crystallite size (47.2 nm) and lower surface (58 $m^2$ $g^{-1}$) compared to 90% $IrO_2$-ITO (5 nm, 123 $m^2$ $g^{-1}$). Larger particle give low surface area and failed to form conducting network on the support. The effect of the conductivity of the support on the performance was studied by using poor conducting $TiO_2$ ($2.6\times10^{-6}$ S $cm^{-1}$) as support material. The 60% $IrO_2$-$TiO_2$ (1.78 V@1 A $cm^{-2}$) showed better performance than 60% $IrO_2$-ITO (1.93 V @1 A $cm^{-2}$) and were comparable to 90% $IrO_2$-ITO (1.74 V@1 A $cm^{-2}$) confirming the effect of active catalyst particle size on the MEA performance. Comparing the conductivity of the 60% $IrO_2$-ITO and 60% $IrO_2$-$TiO_2$, it may be concluded that the conductivity of the support itself is not significant as long as a conducting film of active catalyst formed on it and a 60% $IrO_2$ loading on $TiO_2$ gives sufficient conductivity to the catalyst ($3.8\times10^{-1}$ S $cm^{-1}$). Supported $IrO_2$ will be promising catalyst at PEMWE anode with reduced precious metal loading if smaller active catalyst formed on the support with full coverage to provide conducting network on it.

# Chapter 5. $Ru_xNb_{1-x}O_2$ catalyst for the oxygen evolution reaction in PEMWE

This chapter describes the synthesis and characterization of $Ru_xNb_{1-x}O_2$ and $Ir_xNb_{1-x}O_2$ catalyst. The physical and electrochemical characterization of the catalyst was carried out by XRD, SEM, conductivity and CV. The performance and stability of the as prepared catalysts were investigated in PEMWE.

## 5.1 Introduction

The oxygen evolution reaction (OER) on the electrolyser anode has a higher over potential compared to the hydrogen evolution reaction (HER) and is one of the major cause of energy loss in water electrolysis. A suitable catalyst is required for the reaction to occur on the anode and the cathode. $IrO_2$ and $RuO_2$ are found to be the most active catalyst for the OER [225]. $RuO_2$ is the most stable oxide of Ru in a wide temperature range [226] and is widely used as an electrocatalyst in the chlor alkali industry [66]. It has good electronic conductivity [134] and high capacitance and thus used for electrochemical capacitors [97]. The high capacitance in $RuO_2$ arises from the pseudo capacitance by the reaction of proton ($H^+$) with the $RuO_2$ at the interface [97].

Most of the metal oxides electrodes reported for electrolysis process are based on dimensionally stable anode (DSA) electrode developed by H. Beer in 1965 for the chlor-alkali industry [73]. In DSA type electrodes, metal oxides ($RuO_2$ or $IrO_2$) are formed on Ti metal substrates by thermal decomposition of their precursors. $RuO_2$ is the most active catalyst for OER. However $RuO_2$ is unstable in the anodic environment of an electrolyser and does not have long term stability [67]. It must be stabilised by addition of a second metal in order to be used for practical purposes. Mixtures of $RuO_2$ and $IrO_2$ have been studied as anode catalysts and found to have considerable stability and activity [66]. The $Ir_{0.6}Ru_{0.4}O_2$ has been found to show the best performance by Marshall et al [84]. However both $IrO_2$ and $RuO_2$ are expensive materials making the electrolyser systems expensive. Various non-noble metal oxides such as $SnO_2$, $TiO_2$, $Ta_2O_5$ were added to the $RuO_2$ and $IrO_2$ in view of increasing activity, stability and reduce the precious metal content [66, 84, 88, 227]. Increasing the number of components in the catalyst can lead to a finer morphology because of poor mixing and

can increase the surface area [97, 228-230]. Depending upon the effectiveness of the mixing and the calcination temperature used, different outcomes can be obtained in mixed oxides [231]. It can either form a solid solution or simply a physical mixture of both metal oxides [60]. Metal oxides with similar structure and ionic radii to $RuO_2$ such as $SnO_2$ or $TiO_2$ may form a solid solution with $RuO_2$ whereas oxides with different crystal structure such as $Nb_2O_5$ and $Ta_2O_5$ may not be able to form such a solid solution. However there are discrepancies in various reports regarding the solid solution formation. $IrO_2$ & $Ta_2O_5$ was reported to be not forming solid solution because of the different crystalline forms of both [60], however some authors reported that at a certain composition, a solid solution between the two can be formed [232]. The discrepancies could be because of different conditions used for the preparation. The proper solid solution formation depends on various factors such as oxidation and precipitation kinetics of the two metal ions, the solvent used to mix the precursors, the heating rate etc. [231]. Also in many cases a bi-metallic system resulted in a surface, richer in one metal than the other [231].

A bimetallic catalyst of $IrO_2$-$Ta_2O_5$ (70:30 mol %) was found to be most active and stable DSA electrode for OER [60, 232-240] and is widely used in commercial electrolyser cells. $Ta_2O_5$ is stable during anodic electrolysis and protects the Ti base metal from corrosion [60, 238]. The effect of calcination temperature on this composition was studied by Versesi et al [241]. At temperatures $\leq 350^oC$, the coating was found to be amorphous and crystallisation increases with an increase in temperature whereas at very high temperature $\geq 750^oC$, both $IrO_2$ and $Ta_2O_5$ crystalline compounds separate from each other. At intermediate temperature $IrO_2$ is present as crystalline compound with amorphous $Ta_2O_5$ [240-242]. $IrO_2$ does not form a solid solution with $Ta_2O_5$ [241]. Since a lower $IrO_2$ content was found to be increasing the resistance, the $IrO_2$ content in DSA electrode is limited to $\geq 40\%$ [243]. Recently Marshall et al [84] studied the effect of $Ta_2O_5$ addition to the Ir+Ru oxide system. The particle size and resistivity of the catalyst was found to increase with Ta content. MEA performance with Nafion -115 membrane at $80^oC$ showed that the cell potential increased with Ta addition due to the inertness of $Ta_2O_5$ towards the OER. However it was concluded that approximately 20 mol% of Ta could be added to Ir-Ru mixed oxides without significant decrease in the activity and stability of the catalyst [84].

$Nb_2O_5$ is chemically similar to $Ta_2O_5$ but lower in cost [244] and have excellent anodic corrosion stability [245]. First DSA electrode containing $Nb_2O_5$ was developed by

Terezo et al [227] using the polymeric precursor method. It was found that 70:30 mol% ratio of Ti/$RuO_2$-$Nb_2O_5$ yielded the highest anodic voltammetric charge (thus higher electrochemical active area) and the highest stability among the other compositions studied. $RuO_2$ and $Nb_2O_5$ were present as two different crystal structures (rutile and orthorhombic) at 600$^oC$ calcination temperature and $Nb_2O_5$ was amorphous at calcination temperatures below 500$^oC$ [227, 243]. Low temperature processing is normally preferred for the preparation of high surface area and small particle size $RuO_2$ polycrystalline material [246].

In a study by Santana et al [225, 247] on DSA electrode, $Nb_2O_5$ was found to had a stabilizing effect on the Ru+Ti+Ce oxide system. They systematically substituted $Nb_2O_5$ for $CeO_2$ and found that the addition of Nb increased the stability of the catalyst. The effect of calcination temperature, precursor salt, molar ratios of the reducing agents for a $IrO_2$-$Nb_2O_5$ DSA electrode has also been reported by Santana et al [243]. Sanatana et al [245] studied $IrO_2$-$Nb_2O_5$ DSA electrode with 40, 45 and 50 mol% $IrO_2$ for the electrochemical ozone production in acid electrolyte. It was reported that at a temperature of 450$^oC$, the $Nb_2O_5$ was amorphous in nature [245]. Though normally $IrO_2$ forms crystalline structure at 450$^oC$, due to the amorphous nature of $Nb_2O_5$, the bimetallic system showed amorphous nature. So the bimetallic system was considered as a mixture of crystalline and amorphous structure [245].

The objective of the study was to investigate the catalytic activity and stability of the $RuO_2$-$Nb_2O_5$ and $IrO_2$-$Nb_2O_5$ bimetallic system. To our knowledge a $RuO_2$-$Nb_2O_5$ and a $IrO_2$-$Nb_2O_5$ powder catalyst system for OER have never been studied before. The effect on the physical and electrochemical properties of a $RuO_2$ and $IrO_2$ catalyst by the addition of $Nb_2O_5$ was investigated. Two preparation methods are compared here namely the Adams method and the hydrolysis method, in an attempt to prepare an optimum $RuO_2$-$Nb_2O_2$ mixture.

## 5.2 Electrocatalyst Syntheses

$RuCl_3$ (Ru content 45-55%), $NbCl_5$ (99.995 trace metal basis) from Sigma Aldrich and $H_2IrCl_6.xH_2O$ (Alfa aesar, 99%, metals basis, Ir 38-42%) were used as Ru, Nb and Ir precursors respectively. $NaNO_3$ (99.5% assay) reagent grade from Merck, 2 propanol from Fischer scientific were used as reagent and solvent respectively. $Ru_xNb_{1-x}O_2$ with different molar ratios of Ru and Nb was prepared using the Adams and hydrolysis method.

### 5.2.1 **Adams fusion method**

$RuCl_3$ precursor as required by the stoichiometry was dissolved in isopropanol (IP) and stirred for 3 hours. To this $NbCl_5$ solution (solution in IP) was added as required by the stoichiometry. The total metal concentration was approximately 0.01M. To this 20g of finely grounded $NaNO_3$ was added and stirred well for 4-5 hours. The solvent was then evaporated slowly in an air oven at 75-80$^oC$. The sample was transferred to a silica crucible and calcined in a muffle furnace at 500$^oC$ for 1 hour. The reactions occurring in the Adams method are given in equation ((2-1) and ((2-2). The sample was kept in the furnace until the temperature cooled back to room temperature. The NaCl salt formed was then dissolved in DI water. The sample was washed and centrifuged using an excess de-ionised (DI) water and dried in the air oven at 70-80$^oC$ overnight. $Ru_xNb_{1-x}O_2$ (x=1, 0.8, 0.6, 0.4, 0) were prepared using this procedure by varying the precursor ratio.

### 5.2.2 **Hydrolysis Method.**

The $RuCl_3$ and $NbCl_5$ (as solution in IP) according to the required stoichiometry were dissolved in DI water to yield a total metal concentration of 0.01M. To this, 0.5 M NaOH solution was added. Metal:NaOH molar ratio was maintained as 1:20. This mixture was then heated at 80$^oC$ with stirring for 1 hour. A deep blue coloured complex was formed on heating and this was precipitated by adding 1M $HNO_3$ drop wise until the pH of the solution reaches 7-8. A gradual colour change was observed during the heating and was attributed to the replacement of chlorine with a hydroxide group [96]. The solution was stirred overnight, centrifuged, dried in air oven and heat treated in a muffle furnace at 400$^oC$ for 30 minutes to form the oxide. Synthesis of $Nb_2O_5$ by the same method was also attempted. A white jelly precipitate was formed but the precipitate was not dense enough to separate. The difficulty in obtaining a precipitate of $Nb_2O_5$ was also reported elsewhere [248]. An $Ir_xNb_{1-x}O_2$(H) was also prepared using similar method. The precipitate obtained was calcined at 450$^oC$ for 1 hour to prepare the metal oxide.

The catalysts prepared by the Adams fusion method are represented as $Ru_xNb_{1-x}O_2$(A) and those prepared by the hydrolysis method are represented as $Ru_xNb_{1-x}O_2$(H) and $Ir_xNb_{1-x}O_2$(H) throughout this thesis, where x and (1-x) represent the mol% of respective metals in the mixed oxide.

## 5.3 Electrocatalyst Characterization

### 5.3.1 Physical Characterization

The physical characterizations of the catalyst were carried out using XRD (section 2.2.1), SEM (section 2.2.3) and EDX (Section 2.2.4).

### 5.3.2 Electrochemical Characterization

CV analysis of the catalysts were conducted using a potentiostat/galavanostat (Aultolab) and a homemade tantalum working electrode (4mm diameter) which was polished well with SiC paper (1200, 2400 and 4000 grade) before use. A Ag/AgCl (sat. KCl) and a Pt wire were used as reference and counter electrode respectively. The catalyst ink was prepared by dispersing the catalyst in 0.5 ml solvent (3:2 water:ethanol mixture) and Nafion® solution (25 wt.%). The mixture was sonicated in an ultrasonic bath for 30 minutes before drop casting 10 μl on to the electrode using a micropipette. It was then dried in the air and introduced in the three electrode cell containing 0.5M $H_2SO_4$ solution. The electrolyte was deoxygenated by purging with nitrogen for 15 minutes before the experiment. Cyclic voltammetry were carried out at a potential between +0 and +1.25 V vs. Ag/AgCl. A precondition was carried out between these potentials for 10 cycles at 100 mV $s^{-1}$ before recording the CV. CV's at different scan rates starting from 200 mV $s^{-1}$ to 5 mV $s^{-1}$ were carried out at room temperature. Total of 3 cycles were carried out and the third cycle was recorded whereby a stable CV was obtained. Current values were normalised to the total catalyst weight on the electrode. All potentials in this study are denoted with respect to Ag/AgCl electrode unless otherwise specified.

Powder conductivity of the sample was measured using the in house built powder conductivity set up (Figure 2.8) as described in section 2.3.1.

The MEA of the as prepared catalysts were used as the anode for the CCM utilising Nafion® 115 membrane. Hispec Pt/C (40%) was used as cathode. Nafion® solution (Sigma Aldrich) was used as the ionomer. The cell set up is described in section 2.3.3. Pre-heated DI water from the reservoir was pumped to the cell with the aid of a peristaltic pump at atmospheric pressure and the cell temperature was maintained at 80$^{o}$C. The polarization curves (V/I) were recorded potentiostatically from +1 V to +2 V using Neware battery testing system (Neware technology Ltd, China).

## 5.4 Result and Discussion:

### 5.4.1 X-ray diffraction

The XRD spectra of $Ru_xNb_{1-x}O_2$(A) are given in Figure 5-2. The peaks indicate rutile structure for the $RuO_2$ catalysts (JCPDS: 40-1290). The peaks at 28°, 35°, 40° and 54° are $RuO_2$ (110), (101), (111) and (211) respectively. No $Nb_2O_5$ peaks were observed due to its amorphous nature at the preparation temperature [60, 227, 243]. Peaks at 22.9°, 32.59°, 46.7°, 14.54° and 17.26° started appearing upon $Nb_2O_5$ addition. These peaks were identified to be $NaNbO_3$ (JCPDS: 19-1221) and $Na_2Nb_4O_{11}$ (JCPDS: 020-1145) as given in Figure 5-1. These peaks are represented as NaNb in Figure 5-2. This sodium-niobium complex formation was due to the reaction between $NaNO_3$ and $Nb_2O_5$ at high temperature as reported for Nb and Mo elsewhere [89, 249].

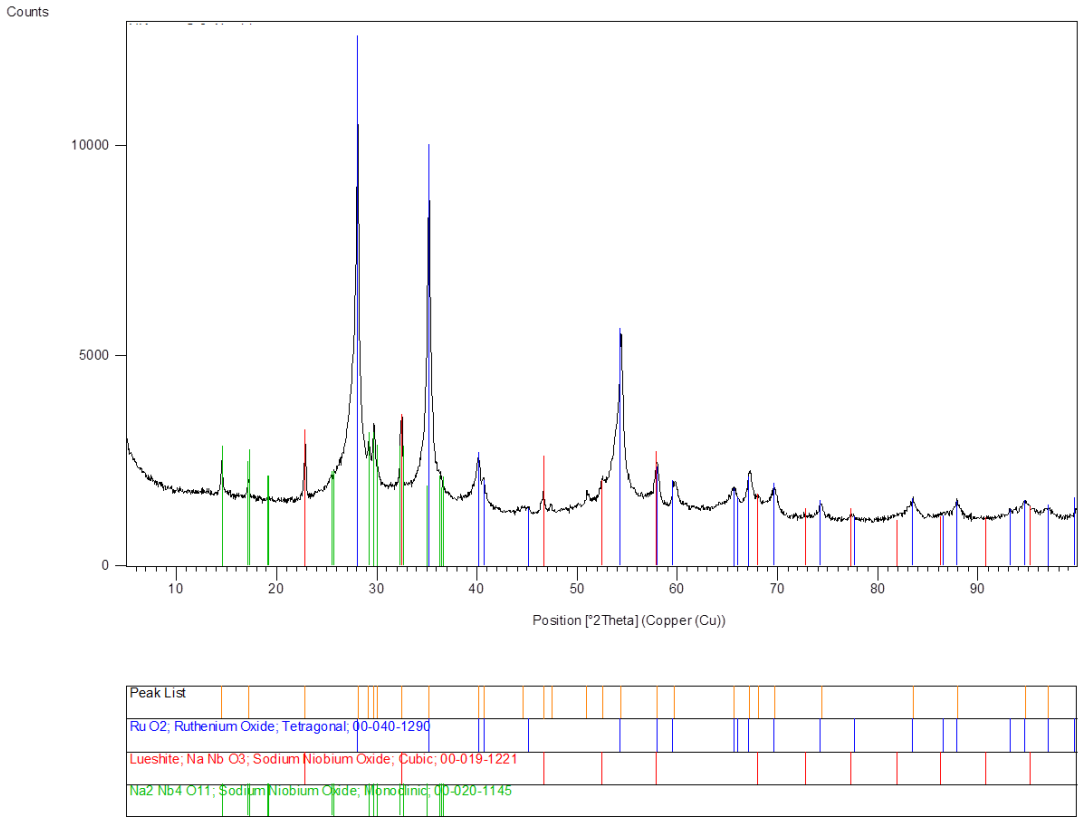


*Figure 5-1. XRD spectra of $Ru_{0.6}Nb_{0.4}O_2$(A) showing the characteristic peaks of Ru and Nb oxide.*

Peak intensities of NaNb oxide were low for $Ru_{0.8}Nb_{0.2}O_2$(A) and is due to the low amount of $Nb_2O_5$ in the catalyst. $RuO_2$ peaks were clearly visible even in $Nb_2O_5$ rich compositions and it can be concluded that $RuO_2$ was crystallized well at the experimental conditions. Since there was no shift in the peak position of $RuO_2$ with $Nb_2O_5$ addition, a solid solution between the two oxides might not have formed. In a

mixed oxide system, a complete solid solution formation is not required, in order to have an influence on catalyst activity, but a fine mixing is sufficient [227, 250]. In DSA electrodes, $IrO_2$-$Ta_2O_5$ catalysts was found to be the best catalysts for OER which cannot be explained based on the solid solution formation between the two metal oxides [60, 227]. In fact since the $RuO_2$ and $Nb_2O_5$ possess two different crystalline structures, a tension between the two species will be predominantly present at higher crystallinity and this tension tends to increase on $Nb_2O_5$ crystallization in turn decreasing the catalytic activity [227].

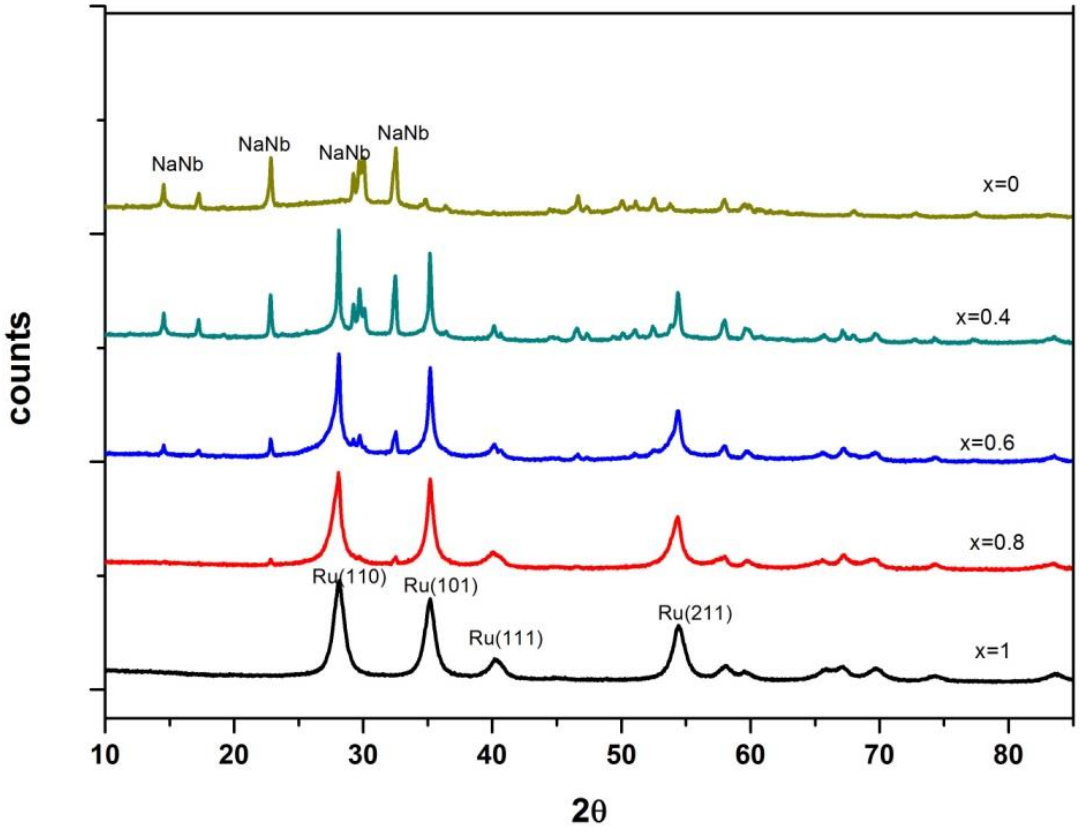


*Figure 5-2. XRD spectra of $Ru_xNb_{1-x}O_2$ (A) with respect to composition.*

The average crystallite size ($t_{average}$) of the $RuO_2$ were calculated using Scherrer equation (2-9) [97] from the two peaks at 28° and 35°. The $RuO_2$ crystallite sizes in the $Ru_xNb_{1-x}O_2$(A) are given in Table 5-1. $RuO_2$(A) showed the lowest crystallite size (8.7 nm) which gradually increased on Nb addition up to 39.4 nm for $Ru_{0.4}Nb_{0.6}O_2$(A). The crystallite sizes of $RuO_2$(A) (8.7 nm) and $Ru_{0.8}Nb_{0.2}O_2$(A) (12.4) were similar and increased significantly at Nb concentration > 20 mol%. There was a steep increase in the crystallite size from $Ru_{0.6}Nb_{0.4}O_2$(A) (20.8 nm) to $Ru_{0.4}Nb_{0.6}O_2$(A) (39.4 nm). Since the crystallisation of $RuO_2$ was complete at the prepared condition as evident from the

XRD, the increase in crystallite size may be attributed to an agglomeration of $RuO_2$ in presence of $Nb_2O_5$ in the bimetallic catalyst.

*Table 5-1. Average crystallite size of $RuO_2$ in $Ru_xNb_{1-x}O_2$ (A) calculated from the XRD.*

| x value | $t_1$/nm | $t_2$/nm | $t_{average}$/nm |
|---|---|---|---|
| 1 | 8.3 | 9.1 | 8.7 ± 0.4 |
| 0.8 | 10.6 | 14.1 | 12.4 ± 1.8 |
| 0.6 | 19.0 | 22.5 | 20.8 ± 1.8 |
| 0.4 | 40.9 | 37.9 | 39.4 ± 1.5 |

In order to study the effect of NaNb complex formation with respect to temperature, the $Ru_{0.8}Nb_{0.2}O_2$(A) composition was prepared at different calcination temperatures. The XRD of $Ru_{0.8}Nb_{0.2}O_2$(A) prepared at various calcinations temperatures is given in Figure 5-3.

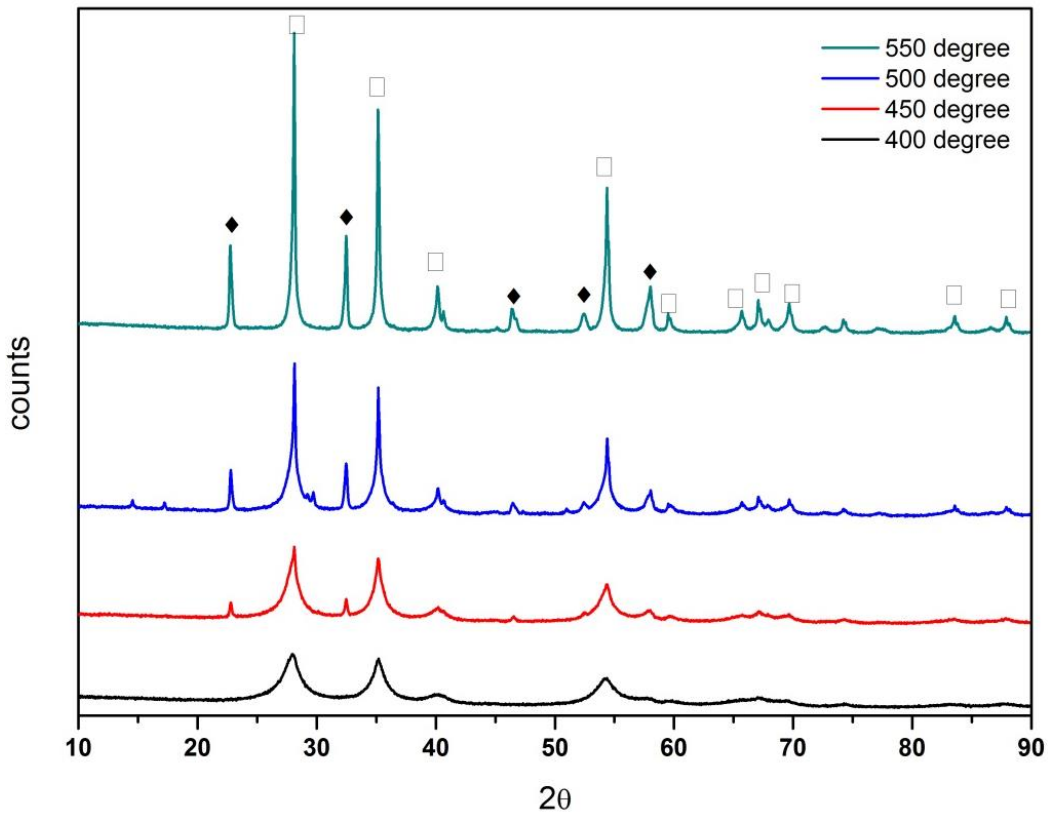


*Figure 5-3. XRD spectra of $Ru_{0.8}Nb_{0.2}O_2$ prepared by the Adams fusion method at different calcination temperatures.(□=$RuO_2$, ◆= NaNb).*

The $RuO_2$ peak intensity increased with an increase in calcination temperature indicating an increase in crystallization at high temperature. The increases in intensity of the NaNb oxide peaks were very clear as the calcination temperature increased above 400$^o$C. The NaNb oxide peak started appearing from calcination temperature ≥ 450$^o$C. It can be concluded that crystalline NaNb oxide forms at temperature > 400$^o$C in Adams method. An increase in the $RuO_2$ crystallite size with increase in the calcination temperature was observed (Table 5-2) and may be attributed to sintering and crystallisation at high temperature [192] which is also clear from the SEM images (Figure 5-7). The increase in the crystallite size was smaller from 400$^o$C (5.7 nm) to 450$^o$C (9.9 nm), but from 450$^o$C (9.9 nm) to 500$^o$C (28 nm), a steep increase was observed. This may be attributed to the NaNb oxide formation which might be leading to agglomeration of $RuO_2$ significantly as mentioned in the previous paragraph. The effect of NaNb oxide on $RuO_2$ crystallite size is also clear by comparing the crystallite size of $Ru_{0.8}Nb_{0.2}O_2$(A) (12.4 nm) in Table 5-1 and Table 5-2 (28 nm) due to the low NaNb oxide formation in the former.

*Table 5-2. Average crystallite size of $RuO_2$ in $Ru_{0.8}Nb_{0.2}O_2$ (A) calcined at different temperature calculated from the XRD.*

| **Calcination temperature ($^o$C)** | **$t_1$/nm** | **$t_2$/nm** | **$t_{average}$/nm** |
|---|---|---|---|
| 400 | 5.31 | 7.5 | 5.7 ± 1.1 |
| 450 | 8.6 | 11.1 | 9.9 ± 1.3 |
| 500 | 28.2 | 27.8 | 28 ± 0.2 |
| 550 | 39.0 | 37.9 | 38.4 ± 0.6 |

The hydrolysis method was adopted in order to avoid the NaNb oxide complex formation in the Adams method. A lower temperature of calcination (400$^o$C for 0.5 hr) was used in the hydrolysis method. The XRD of $Ru_xNb_{1-x}O_2$(H) are given in Figure 5-4. The XRD behaviour of $RuO_2$(H) was similar to that of $RuO_2$(A). Both showed well defined rutile structures, however Nb addition gave different patterns in both methods of preparation.

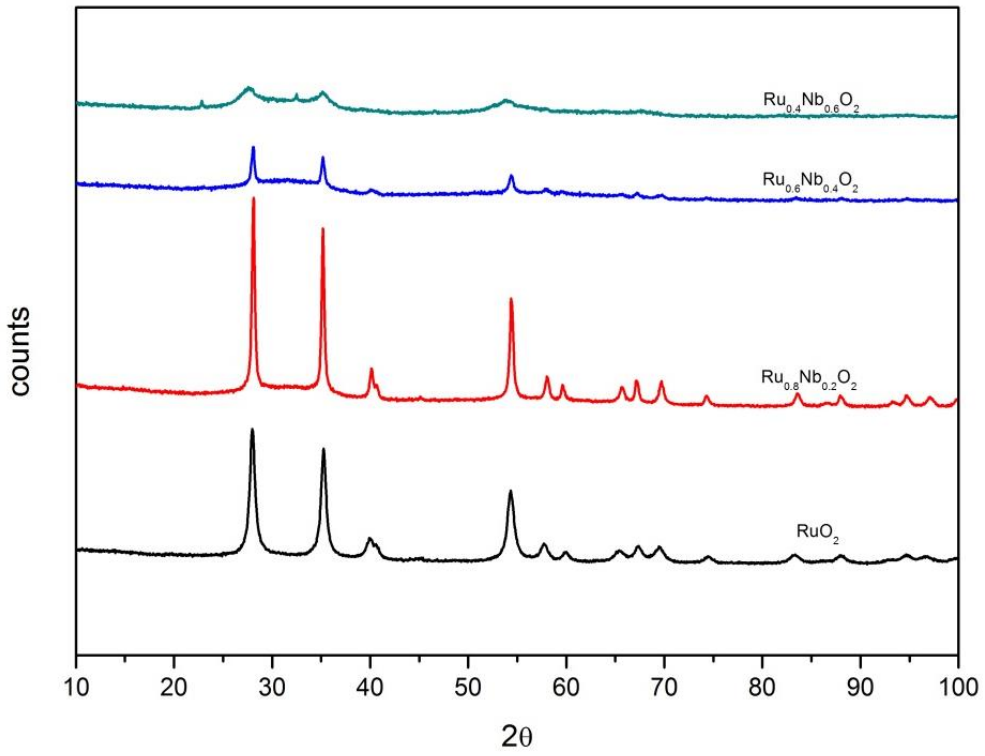


*Figure 5-4. XRD spectra of $Ru_xNb_{1-x}O_2$ (H) with different x values.*

Figure 5-4 shows that the intensity of the $RuO_2$ peak decreases with decrease in Ru content. The $Nb_2O_5$ peaks were not visible in any of these spectra due to the amorphous nature of $Nb_2O_5$ at the prepared conditions [243, 247]. However the presences of Nb in all bimetallic compositions were detected in EDX analyses. The small peaks which appear only at higher Nb content ($Ru_{0.4}Nb_{0.6}O_2$) at around $22^o$ and $33^o$ are associated to NaNb oxide complex probably formed from the reaction between NaOH impurity and $NbCl_5$. The $RuO_2$ showed broader peaks at high $Nb_2O_5$ content indicating that the crystallisation of $RuO_2$ was not complete, which implies that crystallisation of $RuO_2$ was affected by the presence of $Nb_2O_5$. It was reported elsewhere that amorphous nature of $Nb_2O_5$ makes $IrO_2$ crystallization difficult [243]. The niobium aqua-hydroxide complex formed during the hydrolysis stage may cover the active sites of ruthenium aqua-hydroxide complex intermediate making the $RuO_2$ crystallisation difficult [99, 243].

Crystallite sizes of $RuO_2$ in $Ru_xNb_{1-x}O_2$(H) are given in Table 5-3. $RuO_2$(H) showed a crystallite size of 13.4 nm which increased on Nb addition. The $Ru_{0.4}Nb_{0.6}O_2$(H) (8 nm) showed lower crystallite size compared to other composition prepared by the same method. The crystallite size of this composition calculated from the Scherrer equation

may not be accurate since the wide peak in XRD is more likely due to amorphous nature of the material. It was reported elsewhere that $RuO_2$ formed on DSA electrode prepared at 450$^{o}$C are mixture of 30% amorphous and 70% rutile crystalline phases and complete crystallisation occur only above 650$^{o}$C whereby the complete removal of $OH^-$, $H_2O$ and $Cl^-$ groups occurs [99]. It may be expected that there can be a mixture of the crystalline and amorphous phase of $RuO_2$ as well in the hydrolysis method of synthesis.

The crystallite sizes of bimetallic system prepared by the Adams method were lower than that of the hydrolysis method. The reason for this is not very clear. It cannot be explained based on the crystalline nature of the catalyst since the hydrolysis method gives more amorphous nature, its crystallite size should be smaller than that in Adams method. It may be assumed that the crystal growth of $RuO_2$ was affected more significantly by the addition of $Nb_2O_5$ in the hydrolysis method than in the Adams method.

*Table 5-3. Average crystallite size of $RuO_2$ in $Ru_xNb_{1-x}O_2$ (H) calculated using the Scherrer equation from the XRD.*

| x- value | $t_1$/nm | $t_2$/nm | $t_{average}$/nm |
|---|---|---|---|
| 1 | 13.2 | 13.6 | 13.4 ± 0.2 |
| 0.8 | 24.1 | 26.9 | 25.5 ± 1.4 |
| 0.6 | 24.8 | 23.1 | 24.0 ± 0.8 |
| 0.4 | 6.0 | 10.0 | 8.0 ± 2 |

A distinction has to be made in both synthesis processes as nitrates are the intermediate in the fusion method for decomposition and hydroxides are the intermediates for decomposition in the hydrolysis method. The decomposition of nitrates produces less crystalline $RuO_2$ [251]. This is clearly given in Figure 5-5 where $Ru_{0.8}Nb_{0.2}O_2$ prepared using the two methods are compared. The broader diffraction peaks for $Ru_{0.8}Nb_{0.2}O_2$(A) compared to $Ru_{0.8}Nb_{0.2}O_2$(H), both calcined at 400$^{o}$C, indicate a lower crystallite size for catalysts prepared by the Adams method. Peaks were not well resolved for the catalysts prepared by the fusion method at 400$^{o}$C but were well resolved in the hydrolysis method prepared at the same temperature. Crystallization in the hydrolysis method was easier than in the fusion method. This could be due to the fact that, in the fusion method the oxide formation reaction takes place in many steps, for example (i) dispersion of precursor in $NaNO_3$ (ii) melting of $NaNO_3$ (308$^{o}$C) (iii) reaction of the precursor with the melt $NaNO_3$ to form nitrates (iv) decomposition of nitrates to form

their respective oxides by releasing $NO_2$ gas, whereas in the hydrolysis method, the overall mechanism is governed by the thermal decomposition of the hydroxide which is formed before the calcination stage. The numbers of intermediate steps involved in the hydrolysis method are less than that in the fusion method during the oxide formation.

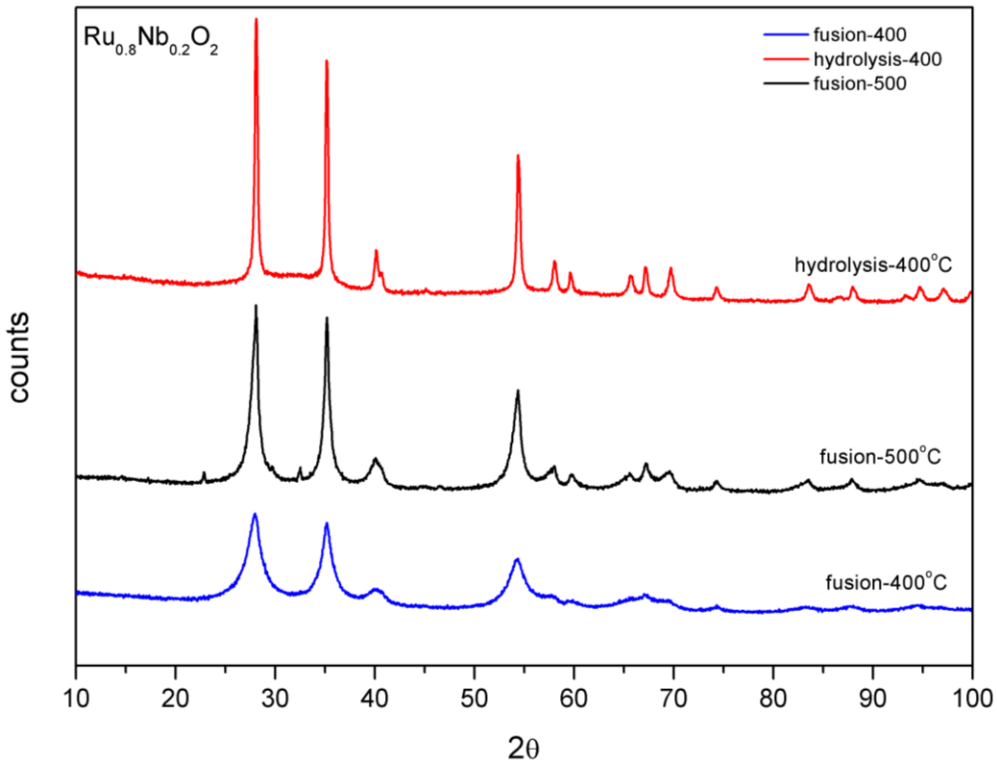


*Figure 5-5. XRD spectra of $Ru_{0.8}Nb_{0.2}O_2$ catalyst prepared by the Adams fusion method (at 400°C and 500°C calcination temperature) and hydrolysis method (400°C calcination temperature).*

### 5.4.2 **Morphology**

SEM was used to observe the morphology of the catalysts. The SEM micrographs of the catalysts prepared by both Adams and hydrolysis method are given in Figure 5-6. The $RuO_2$(A) and $Ru_{0.8}Nb_{0.2}O_2$(A) showed a dense and aggregated particle structure (Figure 5-6 a,b). The agglomerated structure may be due to the high temperature used for the synthesis. The hydrolysis method gives more uniform particles compared to the Adams method. The difference in morphology may be due to difference in the preparation method and the calcination temperature used. Since the temperature used for the hydrolysis method was 400°C in comparison to 500°C for the Adams method, the formed oxide is likely to contain some amorphous oxides as well. The EDX analysis (Figure 5-8) showed Ru mol% more or less the same as required by the precursor ratio

used, except for $Ru_{0.6}Nb_{0.4}O_2$(A) which showed slightly lower Ru mol% than the desired ratio. This may be due to some precursor loss during the synthesis and washing.

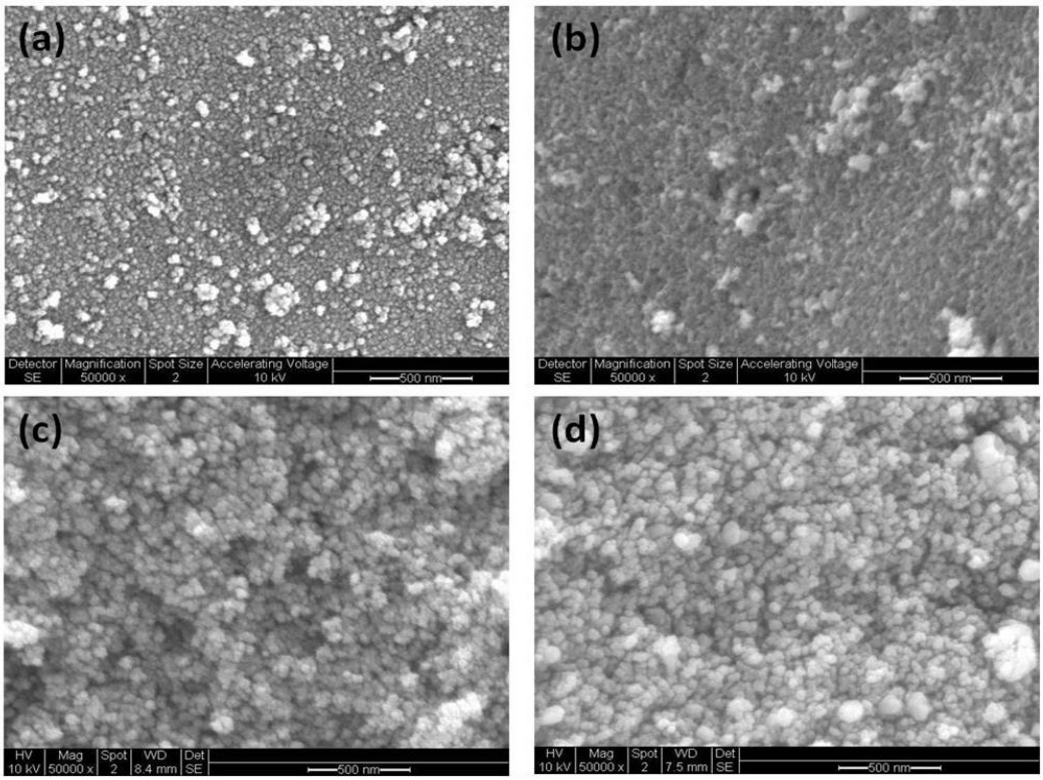


*Figure 5-6. SEM picture of (a) $RuO_2$(A) (b) $Ru_{0.8}Nb_{0.2}O_2$(A) (c) $RuO_2$(H) (d) $Ru_{0.8}Nb_{0.2}O_2$(H) (magnification 50×k).*

The SEM of $Ru_{0.8}Nb_{0.2}O_2$(A) calcined at different temperature is given in Figure 5-7. An increase in crystallization with temperature can be seen from the Figure 5-7. At 550$^{o}$C calcination temperature, large crystals are formed which was also evident from the XRD analysis (Figure 5-3).

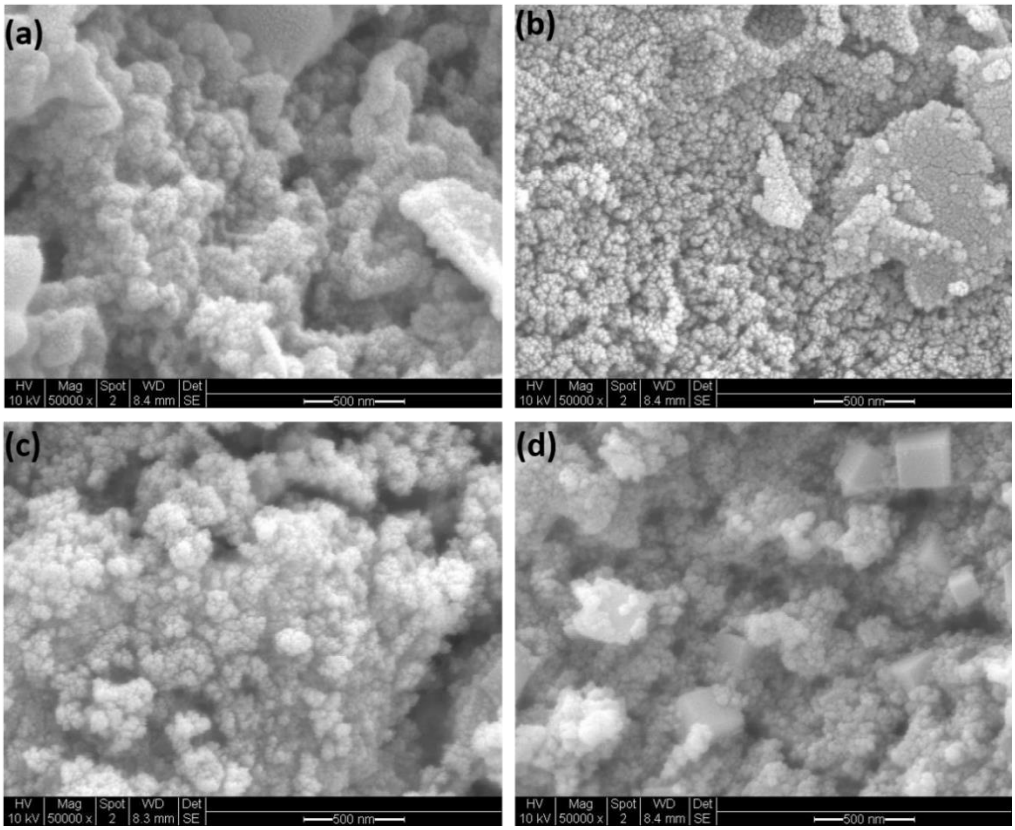


*Figure 5-7. SEM picture of $Ru_{0.8}Nb_{0.2}O_2$(A) with different calcination temperature (a) 400°C (b) 450°C (c) 500°C (d) 550°C.*

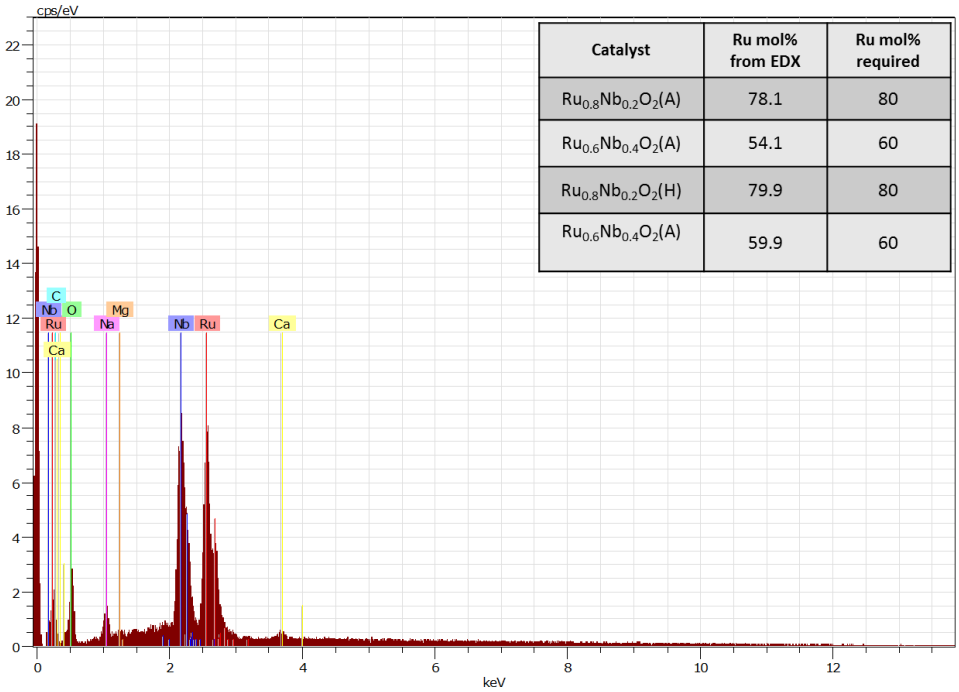


| Catalyst | Ru mol% from EDX | Ru mol% required |
|---|---|---|
| $Ru_{0.8}Nb_{0.2}O_2$(A) | 78.1 | 80 |
| $Ru_{0.6}Nb_{0.4}O_2$(A) | 54.1 | 60 |
| $Ru_{0.8}Nb_{0.2}O_2$(H) | 79.9 | 80 |
| $Ru_{0.6}Nb_{0.4}O_2$(A) | 59.9 | 60 |

*Figure 5-8. EDX spectra of $Ru_{0.6}Nb_{0.4}O_2$(A). Inset shows Ru mol% of the various catalyst prepared.*

### 5.4.3 **Powder conductivity:**

The powder conductivity of the catalyst prepared by both methods is given in Figure 5-9. A linear relationship was observed for the thickness vs. resistance plot for the powder catalysts (Figure 5-9 inset) indicating ohmic behaviour of the samples. The electronic conductivity of $Ru_xNb_{1-x}O_2$ prepared by both methods decreased on $Nb_2O_5$ addition. The $RuO_2$(A) (5.3 S $cm^{-1}$) showed higher conductivity than $RuO_2$(H) (2.1 S $cm^{-1}$). This is mainly due to the higher crystallinity of the catalysts prepared at 500$^oC$ compared to $RuO_2$(H) prepared at 400$^oC$. A higher crystallinity increases the electronic conductivity of the particles. The conductivities of $Ru_{0.8}Nb_{0.2}O_2$(A) (1.3 S $cm^{-1}$) and $RuO_2$(A) (5.3 S $cm^{-1}$) were of the same order of magnitude which decreases by two orders of magnitude for $Ru_{0.6}Nb_{0.4}O_2$(A) ($1.3\times10^{-2}$ S $cm^{-1}$). The similar conductivity between $RuO_2$(A) and $Ru_{0.8}Nb_{0.2}O_2$(A) indicate that the $RuO_2$ nano particles were well connected to form a continuous network (Figure 5-9). A sharp decrease in conductivity for Nb mol% > 60 can be attributed to the reduced electron conducting network.

The conductivity of $RuO_2$(H) (2.1 S $cm^{-1}$) decreased by an order of magnitude for $Ru_{0.8}Nb_{0.2}O_2$(H) ($3.7\times10^{-1}$ S $cm^{-1}$) and two orders of magnitude for $Ru_{0.6}Nb_{0.4}O_2$(H) ($5.4\times10^{-2}$ S $cm^{-1}$) indicating that a proper network of $RuO_2$ was not maintained in $Ru_xNb_{1-x}O_2$(H). The XRD analysis showed that crystallite sizes between $RuO_2$(A) (8.7 nm) and $Ru_{0.8}Nb_{0.2}O_2$(A) (12.4 nm) are lower than that of the $RuO_2$(H) (13.4 nm) and $Ru_{0.8}Nb_{0.2}O_2$(H) (25.5 nm) indicating an $RuO_2$ agglomeration in $Ru_{0.8}Nb_{0.2}O_2$(H). The agglomeration will affect the conductivity of the bimetallic catalyst by reducing the conducting network formation.

A sharper decrease in the conductivity was observed for the catalysts prepared by the Adams method than by the hydrolysis method. This is attributed to the Na-Nb oxide formed in the Adams method at high Nb concentration > 80 mol%. The electrical conductivity in the catalyst is mainly contributed by the $RuO_2$ network as $Nb_2O_5$ is non-conductor. The presence of non-conducting particles in the catalyst restricts the electron conduction path increasing the overall resistance of the catalyst layer. An increased resistivity in bimetallic system of $IrO_2$-$SnO_2$ with increase in non-conducting $SnO_2$ content was reported by Marshall et al [86].

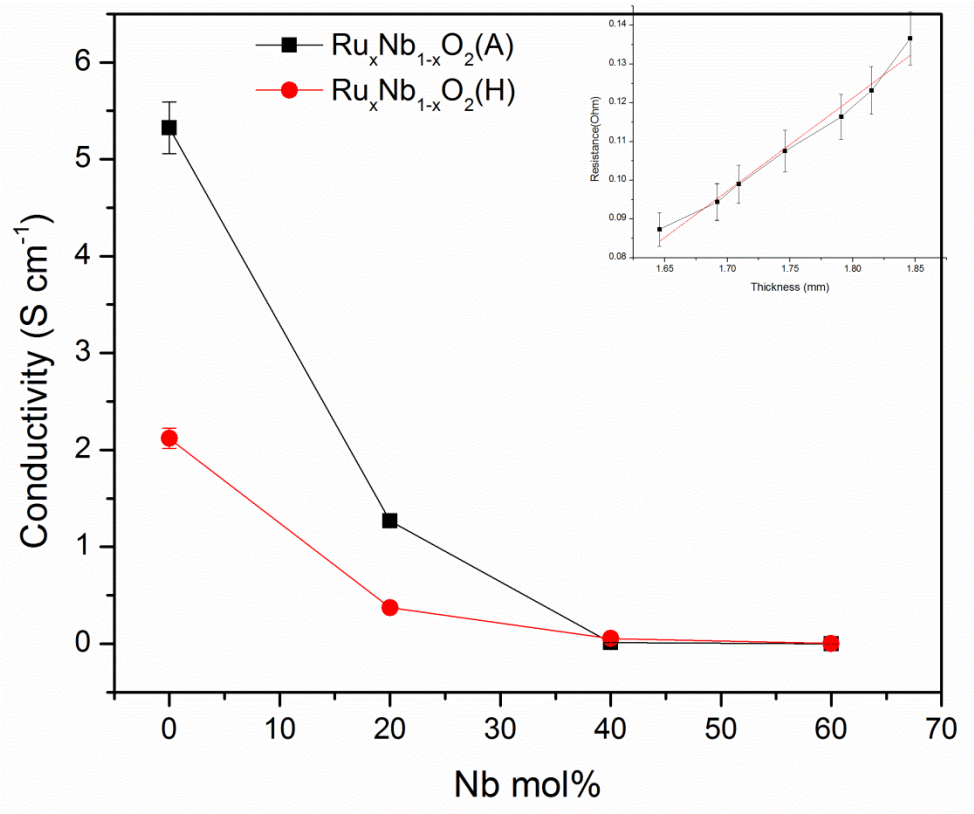


*Figure 5-9. Powder conductivity of $Ru_xNb_{1-x}O_2$ catalyst as a function of composition prepared by the Adams and the hydrolysis method. Inset shows the thickness vs.resistance plot for $RuO_2$(H).*

The effect of calcination temperature on the powder conductivity of $Ru_{0.8}Nb_{0.2}O_2$(A) is given in Figure 5-10. The conductivities of the catalyst prepared at 400$^o$C and 450$^o$C were similar and decreased significantly at higher calcination temperature. Since the crystallinity increases at high temperature, an increase in conductivity was expected. But in contrast, the conductivity decreased with an increase in calcination temperature. This may be attributed to the non-conducting Na-Nb complex formation at high temperature ≥ 450$^o$C (Figure 5-3).

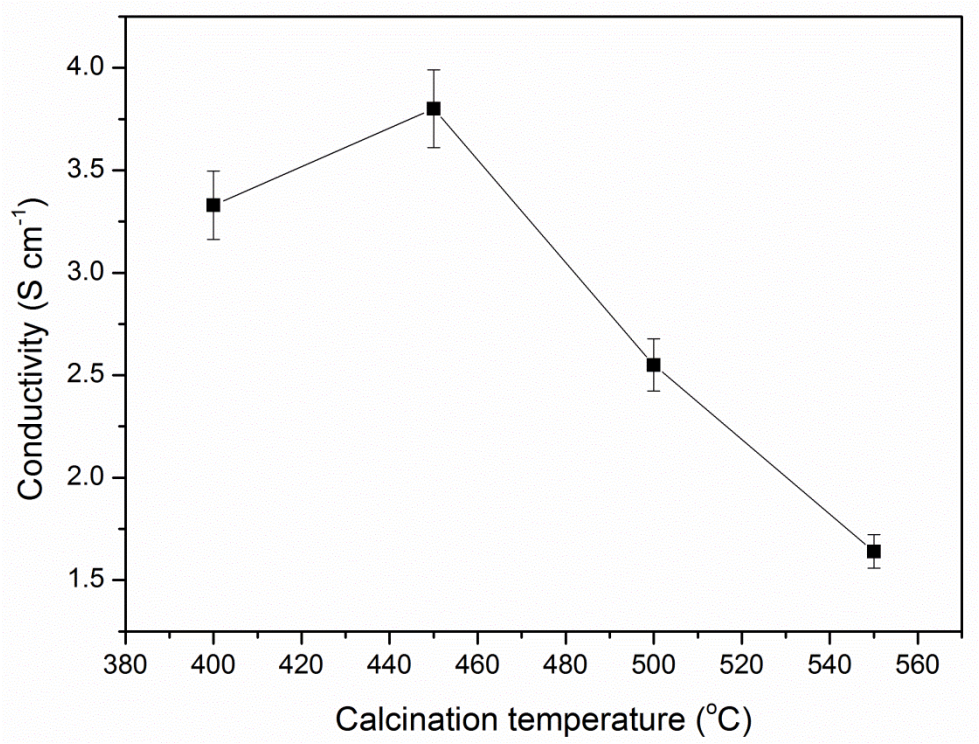


*Figure 5-10. Powder conductivity of $Ru_{0.8}Nb_{0.2}O_2$(A) as a function of calcination temperature.*

### 5.4.4 **Cyclic Voltammetry**

The CV of the catalysts between the potential +0 V to 1.25 V vs. Ag/AgCl in 0.5M $H_2SO_4$ was used to study the electrochemical property of the catalyst. The CV plot of $Ru_xNb_{1-x}O_2$(A) at different scan rate is given in Figure 5-11. The $RuO_2$(A) showed common shape and features of the rutile $RuO_2$ [97, 252]. The broad peaks with no well-defined double layer region are characteristic of $RuO_2$. The peaks at around +0.4 V and +1.0 V (vs. Ag/AgCl) are commonly attributed to the Ru(III)/Ru(IV) and Ru(IV)/Ru(V) surface transitions respectively [76, 89] due to the redox charge transition between the proton ($H^+$) and $RuO_2$ surface [129, 134] as given in equation ((2-15).

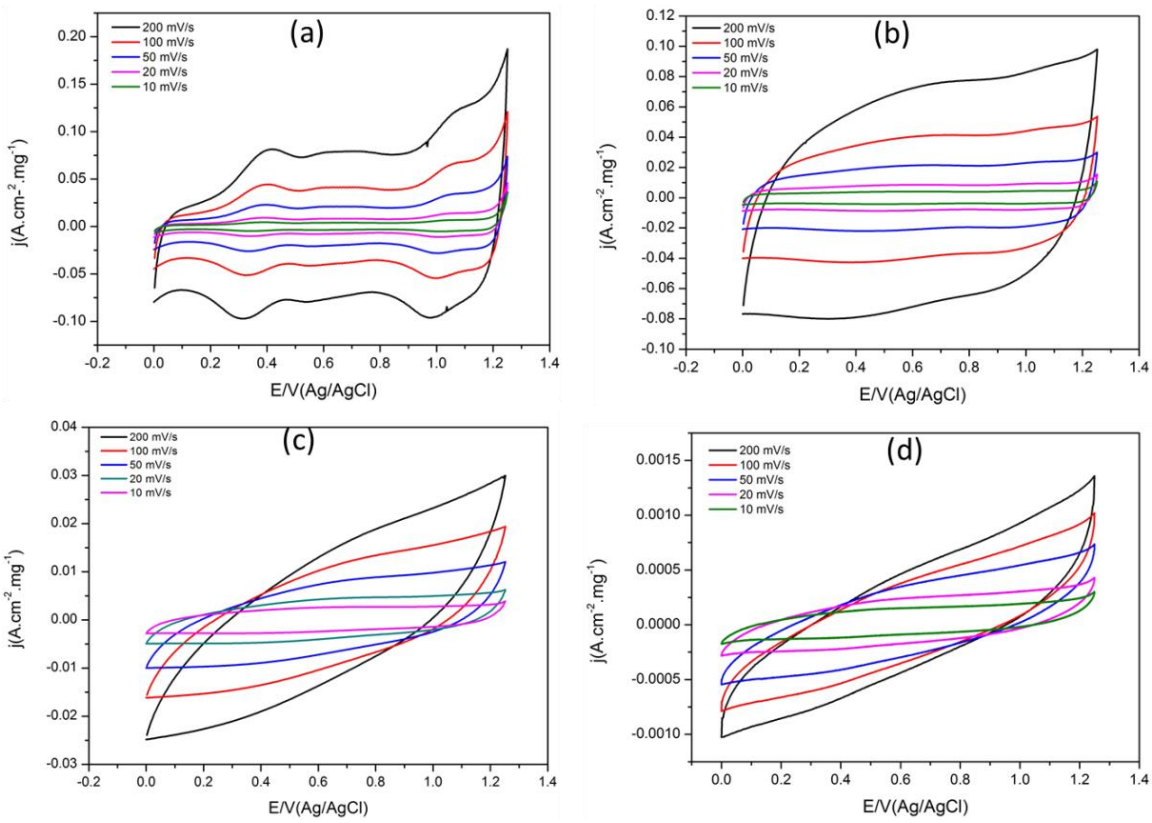


*Figure 5-11.CV $Ru_xNb_{1-x}O_2$(A) with respect to scan rate (a) $RuO_2$ (b) $Ru_{0.8}Nb_{0.2}O_2$ (c)$Ru_{0.6}Nb_{0.4}O_2$ (d) $Ru_{0.4}Nb_{0.6}O_2$ at different scan rate in 0.5M $H_2SO_4$ .*

The voltammetric charge (q*) was calculated by integrating the CV at 20 mV $s^{-1}$. As described in Chapter 3 before, the q* is proportional to the active surface area of the catalyst. The q* calculated for both $Ru_xNb_{1-x}O_2$(A) and $Ru_xNb_{1-x}O_2$(H) are given in Figure 5-13. The q* decreased with Nb addition. The voltammetric charge of $RuO_2$(A) and $Ru_{0.8}Nb_{0.2}O_2$(A) were 1613 mC $cm^{-2}$ $mg^{-1}$ and 1418 mC $cm^{-2}$ $mg^{-1}$ respectively. Voltammetric charge of ~1600 mC $cm^{-2}$ $mg^{-1}$ for $RuO_2$ was reported elsewhere [88]. The q* obtained is significantly higher than the charge value reported for DSA electrodes (~50-100 mC $cm^{-2}$ $mg^{-1}$) [244] due to high surface area of the powder sample. The $RuO_2$(A) and $Ru_{0.8}Nb_{0.2}O_2$(A) CVs were symmetrical around zero current indicating a capacitive behaviour in the potential window. A distortion of the symmetry of the curves was observed at Nb > 20 mol%. This could be due to the lower electron conduction of $Nb_2O_5$ [230]. Since $Nb_2O_5$ is a poor conductor, the current values in CV mainly comes from the $RuO_2$ network [225, 227, 230]. Powder conductivity analysis showed that the conductivity of $Ru_xNb_{1-x}O_2$(A) decreased on Nb addition (Figure 5-9). The voltammetric charge of $RuO_2$ decreased on Nb addition and the decrease is quite

large above 20 mol% Nb (Figure 5-13). The q* decreased from 1481 mC $cm^{-2}$ $mg^{-1}$ for $Ru_{0.8}Nb_{0.2}O_2$(A) to 686 mC $cm^{-2}$ $mg^{-1}$ for $Ru_{0.6}Nb_{0.4}O_2$(A). This may be attributed to the dilution of $RuO_2$ as well as the large $RuO_2$ crystallite size at Nb > 20 mol% (Table 5-1) decreasing the active surface area of the catalyst. The crystallite size and conductivity of $Ru_{0.8}Nb_{0.2}O_2$(A) (12.4 nm, 1.3 S $cm^{-1}$) was comparable to that of $RuO_2$(A) (8.7 nm, 5.3 S $cm^{-1}$) which explains the similar voltammetric charge between the two in Figure 5-13. The specific capacitance values of the catalysts were calculated from the equation (5-1), where C is the specific capacitance (F $g^{-1}$), $q^*$ is the voltammetric charge (C $g^{-1}$), and $\Delta E$ is the potential window (V).

$$C = \frac{q^*}{2 \times \Delta E} \qquad (5\text{-}1)$$

In metal oxides, the double layer capacitance and pseudo-capacitance coexist, making it difficult to differentiate between the two [60]. Thus the calculated capacitance C includes both the double layer and pseudo-capacitance contribution. The specific capacitance of $RuO_2$(A) and $Ru_{0.8}Nb_{0.2}O_2$(A) calculated from the Figure 5-13 using equation ((5-1) were 81.1 F $g^{-1}$ and 74.4 F $g^{-1}$ respectively. The value is lower than the typical amorphous $RuO_2$ electrode (> 600 F $g^{-1}$) [253] and is due to the crystalline nature of the $RuO_2$. A capacitance of 100 F $g^{-1}$ for crystalline $RuO_2$ prepared at 300$^o$C calcination temperature was reported elsewhere [254]. It is clear from the result that higher conductivity and smaller particle size gives higher active area and 20 mol% Nb addition gives comparable conductivity and particle size to that of pristine $RuO_2$. Higher Nb content > 20 mol% and the NaNb oxide formation in the catalyst reduces the active area of the catalyst [97].

The CV of $Ru_xNb_{1-x}O_2$(H) at different scan rates in 0.5M $H_2SO_4$ is given in Figure 5-12. The trend of CV with respect to Nb addition was the same as that in the Adam's method. Redox peaks were clear in the pristine $RuO_2$(H). The very clear peak as observed in the case of $RuO_2$(A) was not obtained indicating that the $RuO_2$(H) was not completely crystalline [97]. The voltammetric charge (q*) of $Ru_xNb_{1-x}O_2$(H) is given in Figure 5-13. The $RuO_2$(H) showed a q* of 1527 mC $cm^{-2}$ $mg^{-1}$ which is similar to the value given by $RuO_2$(A) (1613 mC $cm^{-2}$ $mg^{-1}$). The q* decreased on Nb addition as in the case of $Ru_xNb_{1-x}O_2$(A). The $Ru_{0.8}Nb_{0.2}O_2$(H) gave a q* value of 982 mC $cm^{-2}$ $mg^{-1}$. This is lower than the q* of $Ru_{0.8}Nb_{0.2}O_2$(A) (1481 mC $cm^{-2}$ $mg^{-1}$). The lower value can be attributed to the larger crystallite size of $Ru_{0.8}Nb_{0.2}O_2$(H) (25.5 nm) compared to

$Ru_{0.8}Nb_{0.2}O_2$(A) (12.4 nm). A decrease in voltammetric charge on adding $SnO_2$ to $IrO_2$ was also reported by Marshall et al [86].

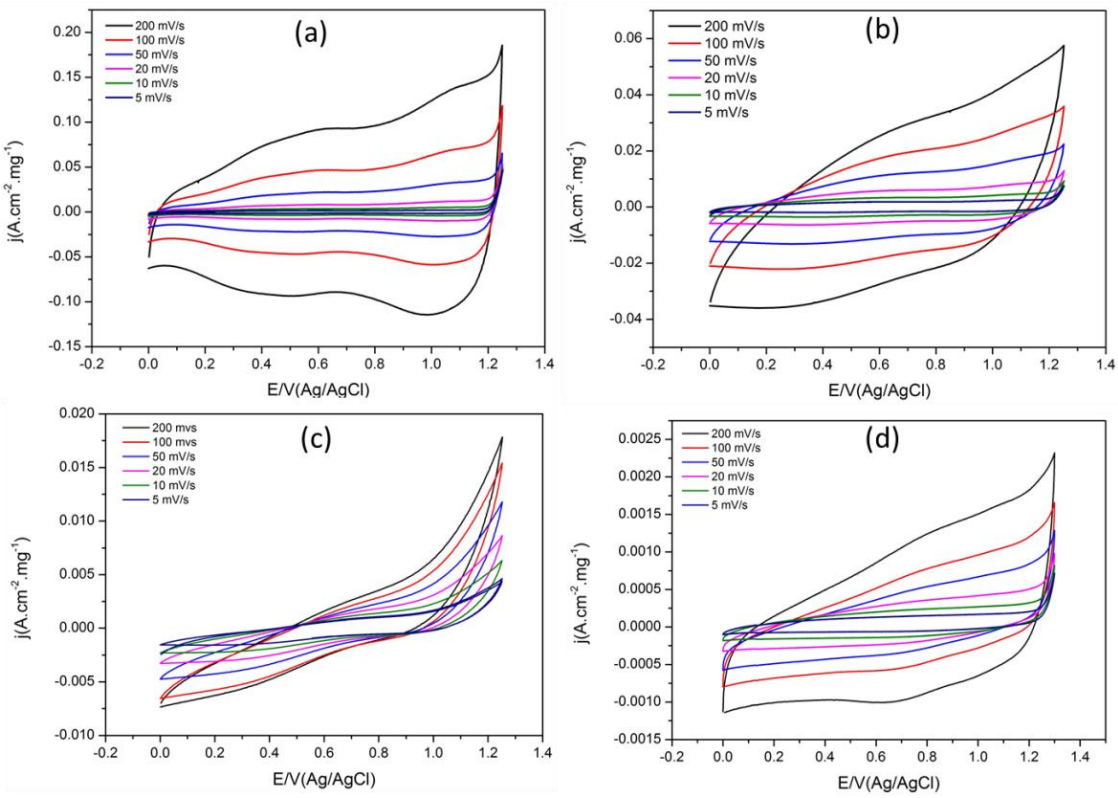


*Figure 5-12. CV of $Ru_xNb_{1-x}O_2$ (H) at 20 mV $s^{-1}$.(a) $RuO_2$ (b) $Ru_{0.8}Nb_{0.2}O_2$ (c) $Ru_{0.6}Nb_{0.4}O_2$ (d) $Ru_{0.4}Nb_{0.6}O_2$.*

The specific capacitance of $RuO_2$(H) and $Ru_{0.8}Nb_{0.2}O_2$(H) were 76.7 F $g^{-1}$ and 49.3 F $g^{-1}$ respectively calculated from equation (5-1. The difference in capacitance is very high on adding 20% $Nb_2O_5$ addition for the hydrolysis method unlike in Adams method. This may be attributed to the large difference in crystallite size between $RuO_2$(H) (13.4 nm) and $Ru_{0.8}Nb_{0.2}O_2$(H) (25.5 nm) compared to $RuO_2$(A) (8.7 nm) and $Ru_{0.8}Nb_{0.2}O_2$(A) (12.4 nm).

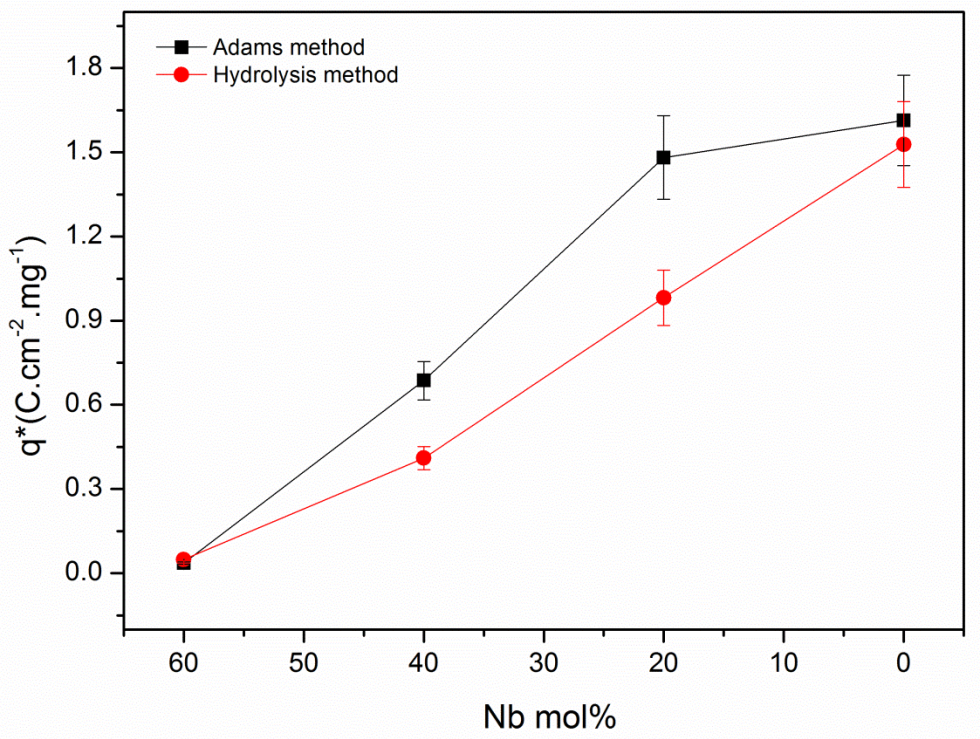


*Figure 5-13. Voltammetric charge ($q_*$) of $Ru_xNb_{1-x}O_2$ prepared by both the Adams and the hydrolysis method. Calculated from CV @20mV $s^{-1}$ scan rate.*

### 5.4.5 **Effect of calcination temperature**

Since $Ru_{0.8}Nb_{0.2}O_2$(A) showed comparable voltammetric charge to that of $RuO_2$(A), an effect of calcination temperature on this composition was studied. A set $Ru_{0.8}Nb_{0.2}O_2$(A) catalysts calcined at different temperatures of 400°, 450°, 500° and 550°C were prepared for this purpose. The XRD of these catalysts was discussed in section 5.4.1. The CVs of these catalysts in 0.5M $H_2SO_4$ at 20 mV $s^{-1}$ are compared in Figure 5-14. Characteristic redox peaks for $RuO_2$ can be seen in the CV. No significant change in the active area was observed for the samples calcined at 400°C and 450°C whereas above 450°C, a decrease in the active area was observed which was attributed to the sintering and grain growth of the catalyst at high temperature [208, 240, 244]. The voltammetric charge (q*) of the catalyst calculated from the CV is given in Figure 5-15. The highest q* value was obtained for the sample calcined at 450°C (2404 mC $cm^{-2}$ $mg^{-1}$). The charge decreased with increase in calcination temperature. A steep decrease was observed for the sample calcined at 500°C (1257 mC $cm^{-2}$ $mg^{-1}$) to 550°C (430.4 mC $cm^{-2}$ $mg^{-1}$) (Figure 5-14). A change in shape of CV curve with respect to calcinations temperature was reported for $RuO_2$ and $IrO_2$ and a decrease in active area with respect to calcination temperature was observed elsewhere [43, 97]. The lower

active area for the samples prepared above 500°C is partly due to the sintering of particles and partly may also be due to the sodium niobium oxide formation at this temperature which was clear from the XRD peaks (Figure 5-5).

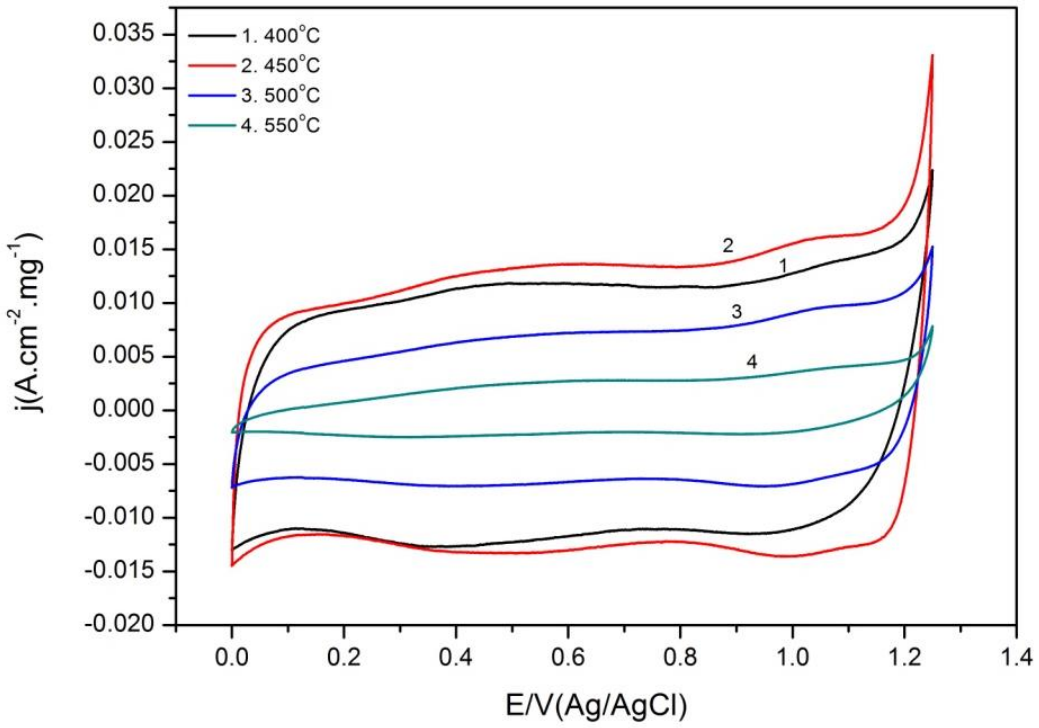


*Figure 5-14. CV of $Ru_{0.8}Nb_{0.2}O_2$(A) calcined at different temperature at 20 mV $s^{-1}$ in 0.5M $H_2SO_4$.*

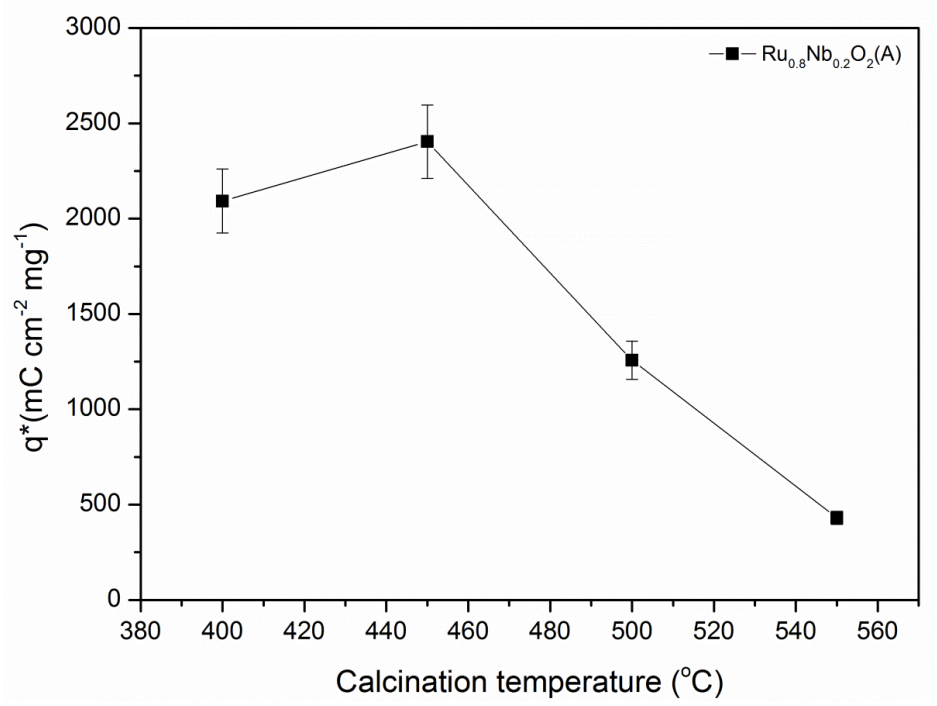


*Figure 5-15. Voltammetric charge of $Ru_{0.8}Nb_{0.2}O_2$(A) calcined at different temperature calculated from the CV in 0.5M $H_2SO_4$ at 20 mV $s^{-1}$.*

### 5.4.6 **Stability of the catalyst**

The stability of the catalyst was assessed using continuous CV cycling (600 cycles) within the potential range +0 to +1.25 V (vs.Ag/AgCl) and is given in Figure 5-16. The active area as well as the OER current decreased after several cycles of potential scans. This may be attributed to the erosion/dissolution of the catalyst or the agglomeration of the catalyst on cycling. The characteristic peaks of $RuO_2$ are lost after few potential cycles and the decrease in active area was gradual with the increased number of cycles. The $RuO_2$(A) voltammetric charge (q*) decreased by 50% from its initial value after 600 cycles whereas $Ru_{0.8}Nb_{0.2}O_2$(A) has lost only 32% of voltammetric charge in the same conditions. The hydrolysis method also showed a similar trend. The $RuO_2$(H) lost 40% of voltammetric charge after 600 cycles whereas $Ru_{0.8}Nb_{0.2}O_2$(H) lost only 25% of voltammetric charge in the same conditions. This shows that $Nb_2O_5$ stabilises the $RuO_2$ catalyst. It was reported in literature that the stability of $RuO_2$ is unsatisfactory as it forms low conducting and soluble $RuO_4$ at high anodic potential [67, 255]. An addition of $Nb_2O_5$ stabilized the $RuO_2$ in both synthesis methods. MEAs were then fabricated with the prepared catalyst in order to investigate the behaviour of the catalyst in 'real' electrolyser operations.

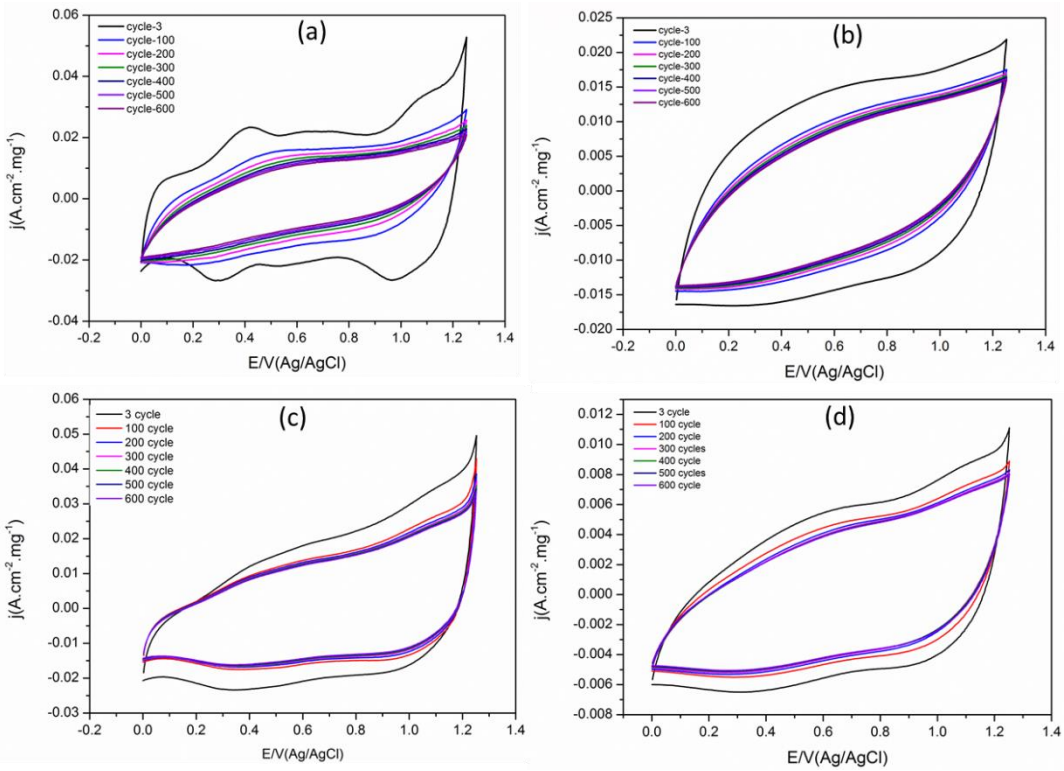


*Figure 5-16. Stability of the catalysts (a) $RuO_2$(A) (b) $Ru_{0.8}Nb_{0.2}O_2$(A) (c) $RuO_2$(H) (d) $Ru_{0.8}Nb_{0.2}O_2$(H) at scan rate of 50 $mVs^{-1}$ for 600 cycles.*

### 5.4.7 **MEA performance**

MEA performances of the $Ru_xNb_{1-x}O_2$ catalyst at 80°C with Nafion 115 membrane are given in Figure 5-17. The $RuO_2$(A) gave the best performance (1.62 V at 1 A $cm^{-2}$) among all the MEA tested. The $RuO_2$(A) and $RuO_2$(H) showed a cell voltage of 1.37 V and 1.43 V @100 mA $cm^{-2}$ whereas $Ru_{0.8}Nb_{0.2}O_2$(A) and $Ru_{0.8}Nb_{0.2}O_2$(H) showed cell voltage of 1.43 V and 1.47 V @100 mA $cm^{-2}$ respectively. At low current density (100 mA $cm^{-2}$) the activity was in the order $RuO_2$(A) > $Ru_{0.8}Nb_{0.2}O_2$(A) = $RuO_2$(H) > $Ru_{0.8}Nb_{0.2}O_2$(H) as is clear from Figure 5-17. The trend was similar to the active area calculated from the CV studies (Figure 5-13). The lower performance of $Ru_{0.8}Nb_{0.2}O_2$(A) compared to $RuO_2$(A) may be attributed to the lower $RuO_2$ content as well as the Na-Nb oxide formation. The crystallite size and conductivity was also lower for $RuO_2$(A) (8.7 nm, 5.3 S $cm^{-1}$) compared to $Ru_{0.8}Nb_{0.2}O_2$(A) (12.4 nm, 1.3 S $cm^{-1}$). The significantly lower performance of $Ru_{0.8}Nb_{0.2}O_2$(H) can be attributed to their larger crystallite size and poor conductivity (25.5 nm, 0.37 S $cm^{-1}$) compared to other catalysts. It is clear that the $Nb_2O_5$ addition decrease the activity of $RuO_2$ in both the methods of preparation due to the dilution of the active $RuO_2$.

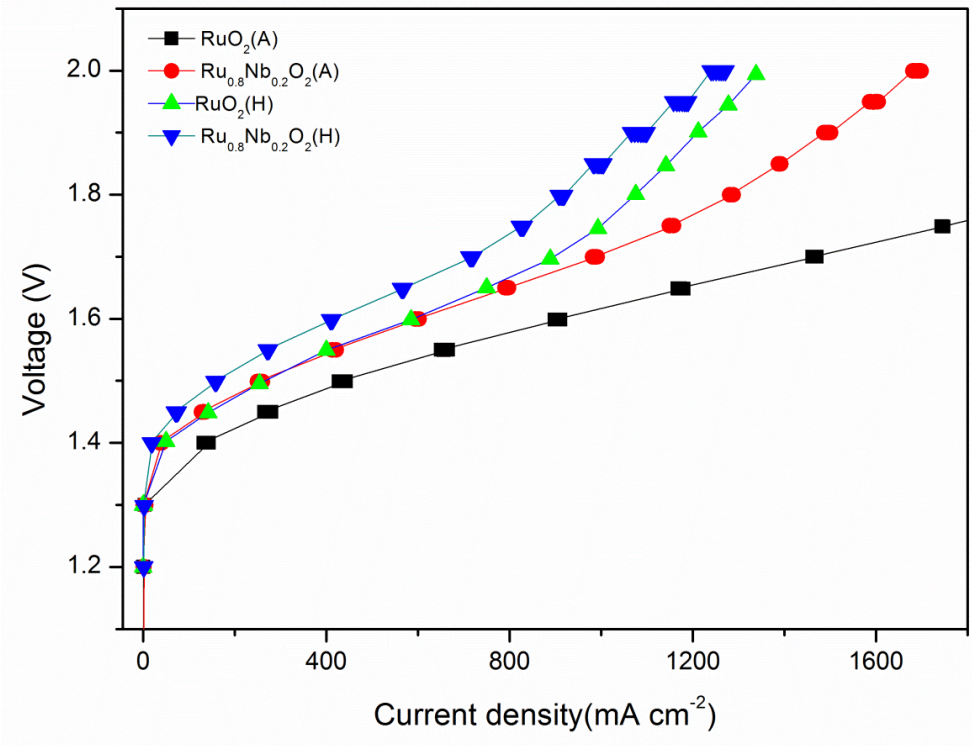


*Figure 5-17. MEA performance of $Ru_xNb_{1-x}O_2$ (A) and $Ru_xNb_{1-x}O_2$ (H) at 80°C. Nafion®-115 membrane, Pt/C(40%) cathode.*

The stability of the $RuO_2$(A) and $Ru_{0.8}Nb_{0.2}O_2$(A) in the MEA was tested at 1 A $cm^{-2}$ and 80°C for 24 hours (Figure 5-18). The voltage remains unaltered for about 20 hr for both $RuO_2$(A) and $Ru_{0.8}Nb_{0.2}O_2$(A). The potential for $RuO_2$(A) increased drastically from the initial value of ~1.75 V to > 2 V after 21 hr of operation, whereas $Ru_{0.8}Nb_{0.2}O_2$(A) showed a relatively stable voltage of ~1.9 V under the same conditions. The increase in voltage may be attributed to the erosion/dissolution of the catalyst from the electrode [102, 244, 256]. The $RuO_2$ can electrochemically oxidise at high potential according to equation (5-2 to form soluble $RuO_4$ [257, 258] which will contribute to the increase in overvoltage of the $RuO_2$ electrode. This indicate that the $RuO_2$(A) is quite unstable at the usual current density of operation (1 A $cm^{-2}$) whereas the addition of Nb increases its stability. However the potential starts to increase slowly after 23 hr of operation for $Ru_{0.8}Nb_{0.2}O_2$(A) indicating that, though the stability of $Ru_{0.8}Nb_{0.2}O_2$(A) is better than $RuO_2$(A), it may not be satisfactory for long term operation. Such a steep increase in potential after certain time was also observed for the DSA type electrode [257, 259, 260] and was explained based on the passivation of the titanium base metal as well as $RuO_2$ dissolution [257, 260].

$$RuO_2 + 2H_2O \rightarrow RuO_4 + 4H^+ + 4e^- \qquad (5\text{-}2)$$

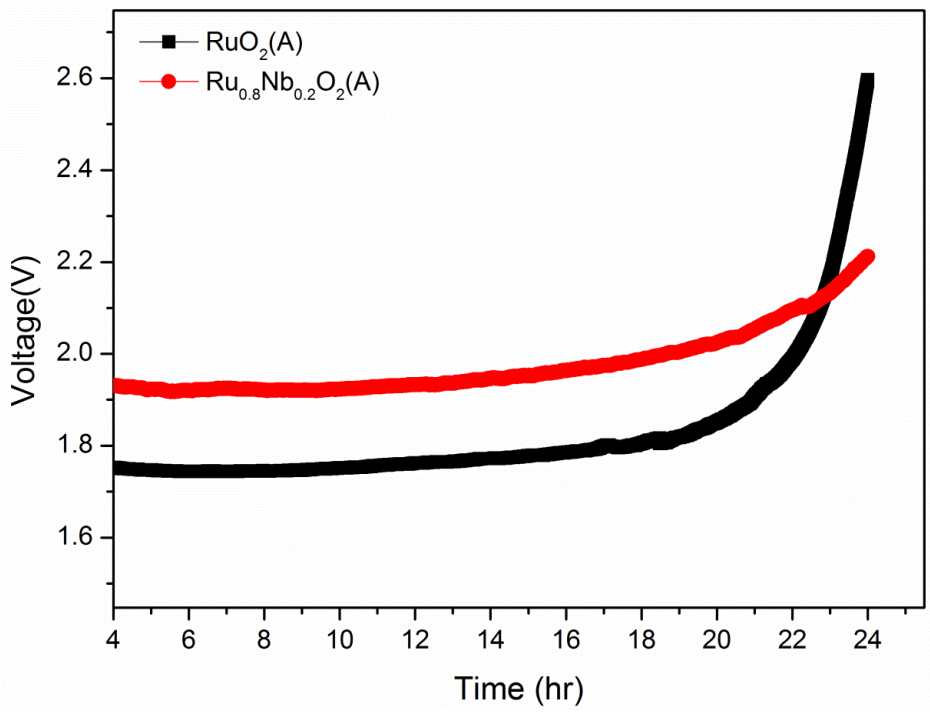


*Figure 5-18. MEA stability test of $RuO_2$(A) and $Ru_{0.8}Nb_{0.2}O_2$(A) at 1 $Acm^{-2}$ and 80°C for 24 hr. Nafion®-115 membrane, Pt/C(40%) cathode.*

## 5.5 $Ir_xNb_{1-x}O2$ catalyst

In order to study the effect of Nb addition on $IrO_2$, an $Ir_xNb_{1-x}O_2$(H) catalyst was prepared by the hydrolysis method. The hydrolysis method was adopted as the Adams method was found to form sodium-niobium oxide during the synthesis.

### 5.5.1 Structure and morphology

The XRD spectra of the $Ir_xNb_{1-x}O_2$(H) catalyst is given in Figure 5-19. The crystallinity decreased as the Nb content increased. $Nb_2O_5$ peak was not visible in any of the sample as for $Ru_xNb_{1-x}O_2$. The $Ir_{0.4}Nb_{0.6}O_2$(H) showed a broad peak indicating lower crystallinity due to the amorphous nature of $Nb_2O_5$ in the prepared condition [245]. In bimetallic oxide systems where one of the oxides is amorphous, the complete crystallisation of the other oxide will be affected. The $IrO_2$-$Ta_2O_5$ film prepared at 450$^o$C calcination temperature using $IrCl_3$ was reported to contain 35% $IrO_2$ as distorted $IrO_2.xH_2O$ phase [99]. Hence, the catalyst prepared here can be considered as mixture of crystalline and amorphous particles [245]. The two intense peaks at ~28$^o$ and ~34.7$^o$ were used to calculate the average crystallite size of $IrO_2$ using Scherrer equation (equation 2-4) and are tabulated in Table 5-4. The $IrO_2$(H) showed a crystallite size of 3 nm which increased on Nb addition up to13.1 nm for $Ir_{0.4}Nb_{0.6}O_2$(H) . No significant change in the position of the XRD peak were observed indicating that no solid solution was formed between the two metal oxides [208].

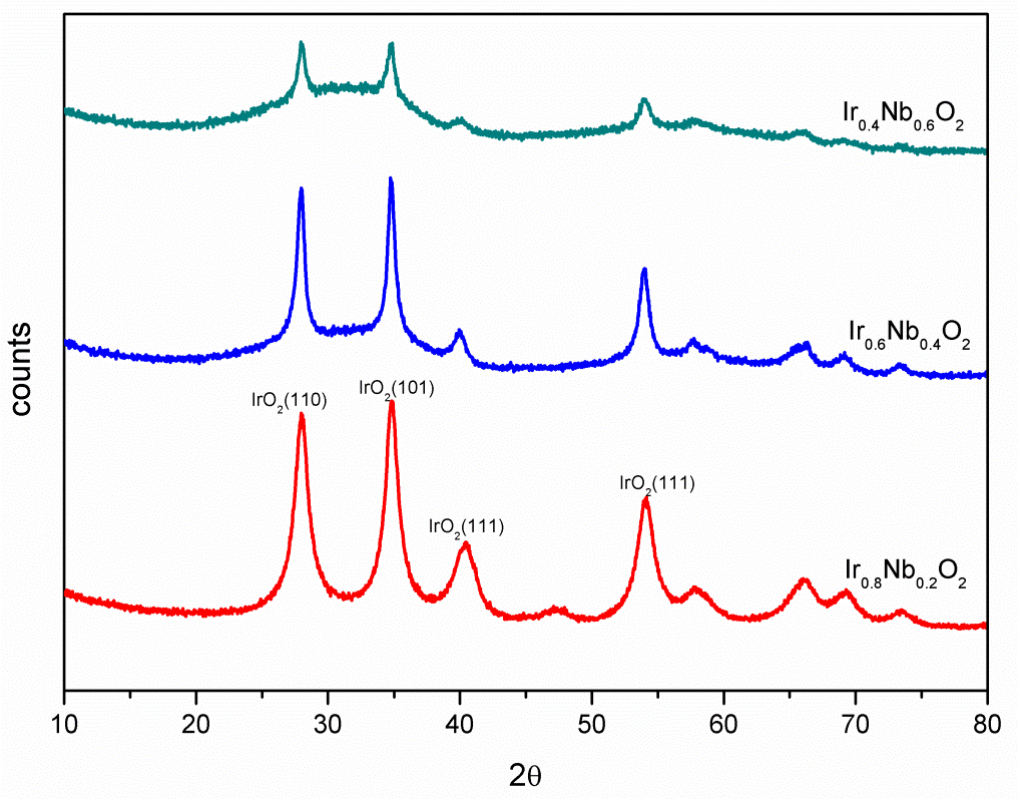


*Figure 5-19. XRD spectra of $Ir_xNb_{1-x}O_2$(H) catalyst.*

The SEM images of the samples prepared are given in Figure 5-20. The $IrO_2$(H) and $Ir_{0.8}Nb_{0.2}O_2$(H) have similar morphology. It was difficult to distinguish $RuO_2$ and $Nb_2O_5$ from the SEM. Very uniform particles are observed for both the catalysts similar to $Ru_xNb_{1-x}O_2$(H) in Figure 5-6. The EDX analysis of $Ir_{0.8}Nb_{0.2}O_2$(H) is given in Figure 5-21. No impurities were found in the EDX analysis. The Ir mol% obtained from the EDX is given in the Figure 5-21 inset. Composition was slightly different from the composition expected from the precursor used. This may be due to the loss of some of the precursors during the synthesis and/or washing.

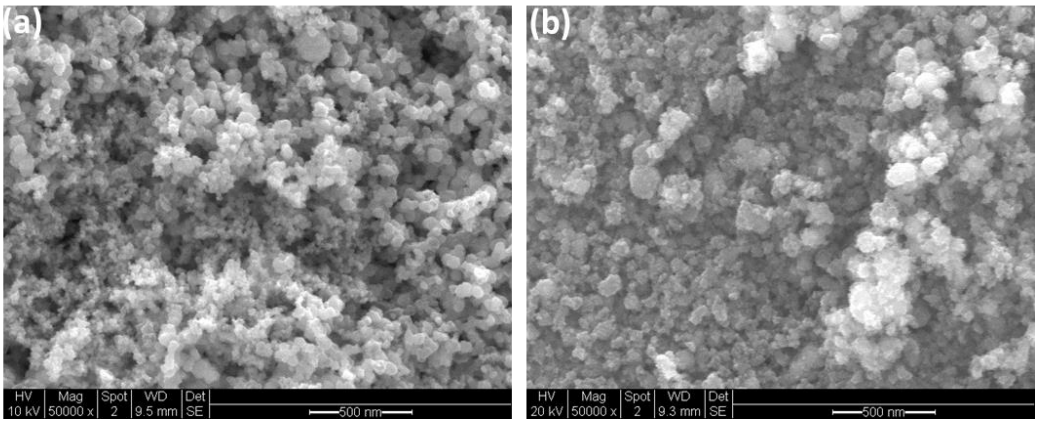


*Figure 5-20. SEM images of (a) $IrO_2$(H) (b) $Ir_{0.8}Nb_{0.2}O_2$(H).*

### 5.5.2 **Powder conductivity**

The powder conductivities of the catalyst measured are given in Table 5-4. The conductivity behaviour was similar to that of the $Ru_xNb_{1-x}O_2$ catalyst. The conductivity decreased on $Nb_2O_5$ addition. The $IrO_2$(H) and $Ir_{0.8}Nb_{0.2}O_2$(H) showed a conductivity of 3.2 S $cm^{-1}$ and 3 S $cm^{-1}$ respectively. A decrease of one order of magnitude in conductivity was observed from $Ir_{0.8}Nb_{0.2}O_2$(H) (3 S $cm^{-1}$) to $Ir_{0.6}Nb_{0.4}O_2$(H) ($4.9\times10^{-1}$ S $cm^{-1}$) indicating the Nb > 20 mol% failed to form a conducting network.

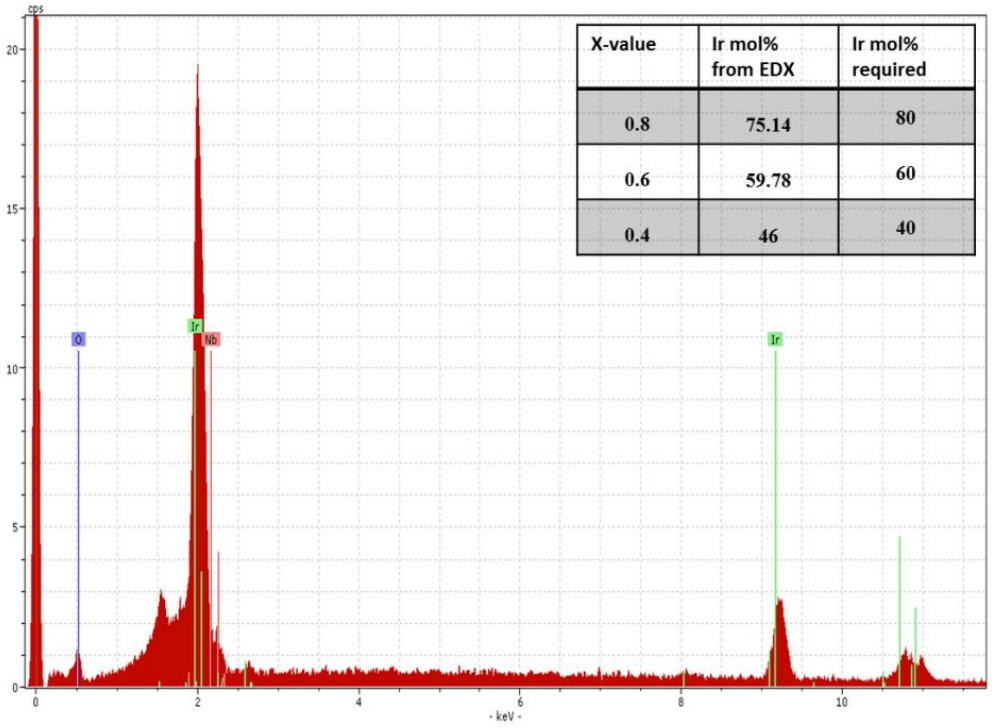


*Figure 5-21. EDX spectra of $Ir_{0.8}Nb_{0.2}O_2$ (H). Inset gives the Ir mol% obtained for various $Ir_xNb_{1-x}O_2$(H) catalyst.*

*Table 5-4. Powder conductivity and crystallite size of the $Ir_xNb_{1-x}O_2$(H) catalyst.*

| Catalyst | Powder conductivity (S $cm^{-1}$) | Crystallite size (nm) |
|---|---|---|
| $IrO_2$(H) | 3.2 ± 0.3 | 3.0 ± 0.2 |
| $Ir_{0.8}Nb_{0.2}O_2$(H) | 3.0 ± 0.3 | 7.2 ± 0.4 |
| $Ir_{0.6}Nb_{0.4}O_2$(H) | $4.9\times10^{-1}$ | 12.6 ± 0.6 |
| $Ir_{0.4}Nb_{0.6}O_2$(H) | $6.5\times10^{-3}$ | 13.1 ± 0.7 |
| $IrO_2$(A) | 4.9 ± 0.5 | 6.5 ± 0.3 |
| $RuO_2$(A) | 5.3 ± 0.5 | 8.5 ± 0.4 |
| $RuO_2$(H) | 2.1 ± 0.2 | 12.8 ± 0.6 |

### 5.5.3 **MEA performance**

MEAs prepared with the prepared catalyst as anode were tested in an electrolyser set up using Nafion-115 membrane and commercial Pt/C(40%) as cathode. The MEA performance of $IrO_2$(H) and $Ir_{0.8}Nb_{0.2}O_2$(H) at 80°C is compared in Figure 5-22. The Nb addition decreased the performance of the $IrO_2$(H). The $IrO_2$(H) and $Ir_{0.8}Nb_{0.2}O_2$(H) showed a cell voltage of 1.44 V and 1.5 V respectively at 100 mA $cm^{-2}$. It was also evident from section 5.4.7 that addition of $Nb_2O_5$ decreased the activity of the $RuO_2$ catalyst. The lower performance of $Ir_{0.8}Nb_{0.2}O_2$(H) can be attributed to its lower $IrO_2$ content and larger crystallite size (7.2 nm) compared to $IrO_2$(H) (3 nm) (Table 5-4). Pristine monometallic oxide showed higher activity over both $Ru_xNb_{1-x}O_2$ and $Ir_xNb_{1-x}O_2$ bimetallic catalysts. The performance of the various MEA prepared is compared in Table 5-5. Both $RuO_2$ and $Ru_{0.8}Nb_{0.2}O_2$ showed higher performance compared to their Ir counterpart at low current density in both methods of preparation. The best performance obtained among all the MEA prepared was with $RuO_2$(A) and $IrO_2$(A) with a cell voltage of 1.37 V @ 100 mA $cm^{-2}$ and 80°C.

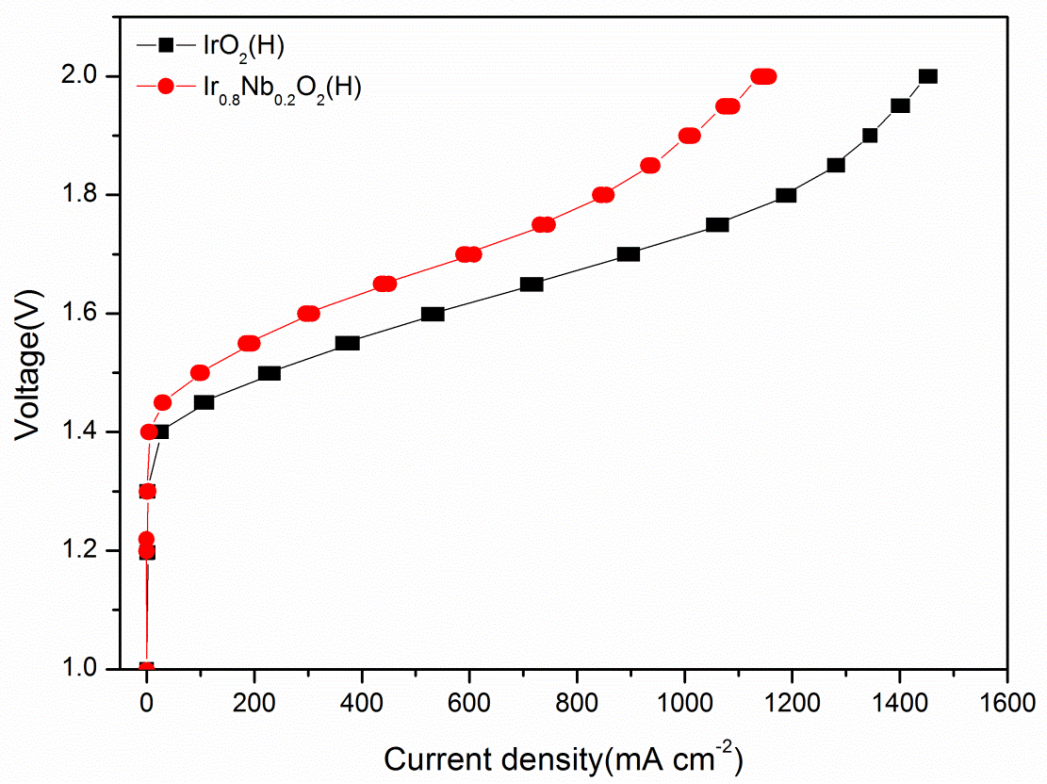


*Figure 5-22. MEA analysis of $IrO_2$(H) and $Ir_{0.8}Nb_{0.2}O_2$(H) at 80°C. Nafion-115 membrane, Pt/C(40%) cathode.*

The stability of the MEA prepared was tested for 24 hour in galvanostatic mode at 1 A $cm^{-2}$ and 80$^{o}$C (Figure 5-23). All the catalysts showed a better performance with no significant variation of voltage with time from the initial value of ~1.92 and ~2.2 respectively for $IrO_2$(H) and $Ir_{0.8}Nb_{0.2}O_2$(H) unlike the $RuO_2$ based catalyst in Figure 5-18. This confirms the excellent stability of $IrO_2$ over $RuO_2$ at acurrent density of 1 A $cm^{-2}$. Since the experimental conditions were the same for both the stability test in Figure 5-18 and Figure 5-23, the increase in voltage for the Ru based catalyst can be attributed to the dissolution of $RuO_2$ at high potential to form soluble $RuO_4$ according to equation (5-2 [257, 258] whereas for the $IrO_2$ containing electrode, such reactions are unlikely to occur at the potential experienced by the electrode in Figure 5-23 [257].

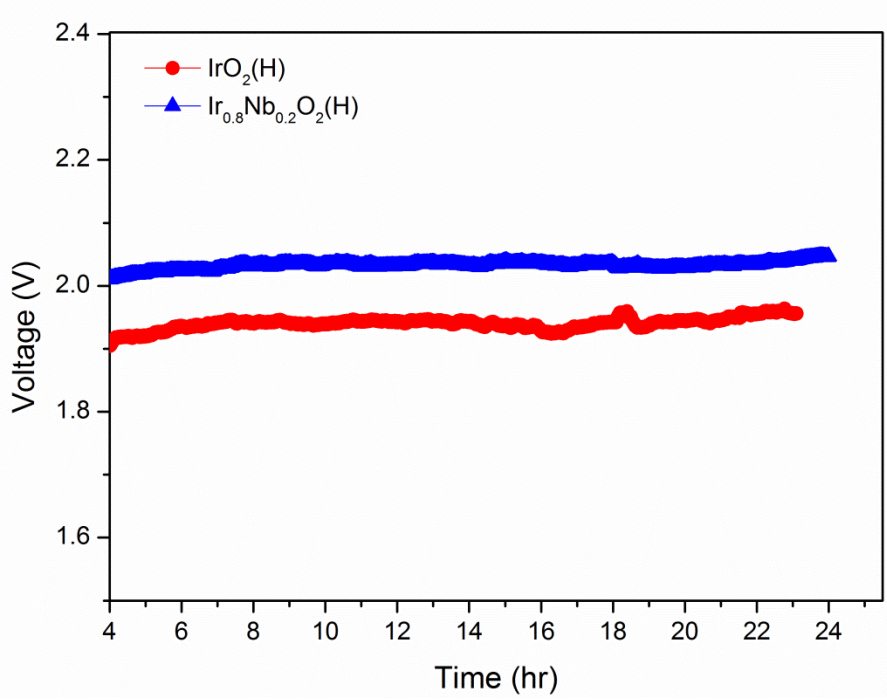


*Figure 5-23. MEA stability test of $IrO_2$(H) and $Ir_{0.8}Nb_{0.2}O_2$(H) catalyst at 1 $Acm^{-2}$ current density and 80$^{o}$C for 24 hr. Nafion®-115 membrane, Pt/C(40%) cathode.*

*Table 5-5.MEA performance comparison of various MEA at 80$^{o}$C.*

| Anode catalyst | Voltage @1A cm$^{-2}$ (V) | Voltage @ 0.1 A cm$^{-2}$ (V) | Current density @ 1.6 V (mA cm$^{-2}$) |
|---|---|---|---|
| $IrO_2$ (H) | 1.73 | 1.44 | 536 |
| $Ir_{0.8}Nb_{0.2}O_2$ (H) | 1.89 | 1.50 | 308 |
| $RuO_2$ (A) | 1.62 | 1.37 | 915 |
| $Ru_{0.8}Nb_{0.2}O_2$ (A) | 1.71 | 1.43 | 609 |
| $RuO_2$ (H) | 1.75 | 1.43 | 585 |
| $Ru_{0.8}Nb_{0.2}O_2$ (H) | 1.85 | 1.47 | 422 |

## 5.6 **Conclusion**

A bimetallic $Ru_xNb_{1-x}O_2$ catalyst was prepared as an OER catalyst using the Adam's and the hydrolysis methods. The Adams method of synthesis was found to form a sodium-niobium complex oxide during the synthesis (Figure 5-2). No $Nb_2O_5$ peaks were observed from the XRD in any catalyst indicating that $Nb_2O_5$ was amorphous in the prepared condition for both the Adams and hydrolysis methods. $RuO_2$(A) and $RuO_2$(H) showed the lowest crystallite sizes of 8.7 nm and 13.4 nm respectively. The crystallite size increased with Nb addition in both the Adams and the hydrolysis methods of synthesis. The addition of $Nb_2O_5$ decreased the voltammetric charge (Figure 5-13) and the electronic conductivity (Figure 5-9) of the catalysts. The NaNb oxide complex oxide was formed at temperatures ≥450$^{o}$C in the Adams method and significantly influenced the conductivity and active area of the catalyst. The MEA analysis also showed a similar trend to CV analysis. The pristine $RuO_2$(A) (1.37 V @0.1 A cm$^{-2}$) and $RuO_2$(H) (1.43 @ 0.1 A cm$^{-2}$) showed the best performance compared to the bimetallic catalysts in both methods of preparation. The stability of $RuO_2$ was found to improve on the addition of $Nb_2O_5$ in the continuous CV cycling test. The MEA stability test at 1 A cm$^{-2}$ and 80$^{o}$C showed that 20 mol% Nb addition slightly improve the stability but was not be satisfactory for long term operation (Figure 5-18).

A $Ir_xNb_{1-x}O_2$ (H) catalyst was also investigated prepared by the hydrolysis method. The crystallite size of $IrO_2$ was found to be increasing on Nb addition as for the $R_xNb_{1-x}O_2$ system. Powder conductivity also decreased on Nb addition. At high $Nb_2O_5$ concentration $Ir_xNb_{1-x}O_2$ (H) resulted in an amorphous structure similar to $Ru_xNb_{1-}$

$_xO_2$(H) catalysts indicating that the crystallisation of the $IrO_2$ and $RuO_2$ was affected by $Nb_2O_5$ addition in the hydrolysis method. The MEA analysis give lower performance for $Ir_{0.8}Nb_{0.2}O_2$(H) (1.5 V @0.1 A $cm^{-2}$) compared to $IrO_2$(H) (1.44 V@0.1 A $cm^{-2}$). The stability test at 1 A $cm^{-2}$ showed excellent stability for the $IrO_2$ based catalyst with no significant variation of cell voltage with time (Figure 5-23). It may be concluded from the results that $Nb_2O_5$ addition gave no enhancement in activity of the $RuO_2$ and $IrO_2$ catalyst but still has a stabilisation effect towards the $RuO_2$ catalyst. Monometallic $RuO_2$ and $IrO_2$ showed better performance than the bimetallic catalysts. The maximum amount of Nb that can be added is limited to 20 mol% below which significant decrease in conductivity and activity was observed.

# Chapter 6. Preliminary investigation of organic acids doped PBI membrane

This chapter describes the preparation and conductivity analysis of some organic acid doped PBI membrane.

## 6.1 Introduction

Solid proton exchange membrane (SPE) is an integral part of the PEM water electrolyser and fuel cells. State of the art PEMWE uses perfluoro sulfonated membrane Nafion® as the SPE. The conductivity of the Nafion® membrane depends on the water content and hence the temperature of operation is limited up to the boiling point of water. High pressure operation is proposed in order to retain water at high temperature. However high pressure operation is energy extensive process as it requires extra components for the pressurisation. Acid-base complexation was found to be one of the best options for a high temperature membrane fuel cell [261, 262]. Introduction of polybenzimidazole (PBI) polymer (Figure 6-1) as a proton conducting membrane was a breakthrough in the high temperature PEM fuel cell [263]. PBI is relatively cheap, non perflourinated commercially available polymer having excellent chemical and thermal stability [264]. Phosphoric acid (PA) doped PBI is an acid-base type membrane having good conductivity at temperatures > 100$^{o}$C ($10^{-2}$ S $cm^{-1}$) and is a suitable alternative to Nafion® up to a temperature of 200$^{o}$C [264, 265]. It has many advantages [266] such as good proton conductivity, low gas permeability, zero electro osmotic drag, oxidative and thermal stability, good mechanical flexibility at elevated temperature, low acid and water vapour pressure of PA [267]. But it also has disadvantages such as poor mass transport properties (low $O_2$ solubility, diffusivity and ionic conductivity) [267-269], slow kinetics for ORR [267, 268], leaching of acid from the membrane, and strong adsorption of $H_3PO_4$ on a Pt catalyst [269]. An alternate dopant to $H_3PO_4$ with superior properties still remains a challenge and is of interest to high temperature PEMFC and PEMWE.

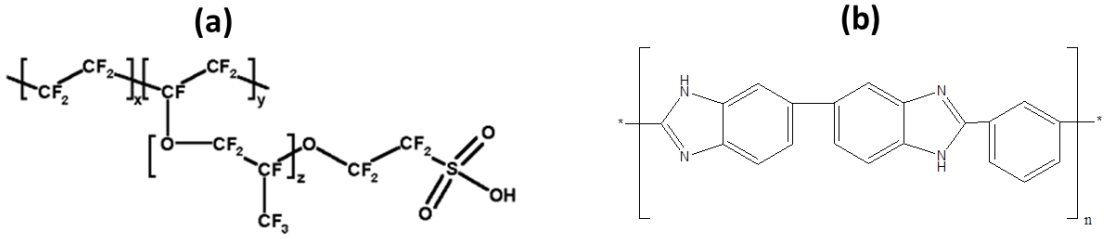


*Figure 6-1. Chemical structure of (a) Nafion [270] and (b) polybenzimidazole [266].*

The proton conductivity of the pristine PBI membrane is very low ($10^{-10}$ – $10^{-9}$ S $cm^{-1}$) [271, 272], but doping with acids gives good proton conductivity in the range of $10^{-2}$ S $cm^{-1}$ even in the anhydrous state [271]. Several inorganic acids have been studied as dopant by various groups. Xing and Savadogo [272] studied different inorganic acids $H_2SO_4$, $HClO_4$, HCl, $HNO_3$ and $H_3PO_4$ as a PBI membrane dopant. The conductivity of the membrane was found to depend on the type of the acid and its concentration. The highest conductivity was obtained for PBI doped in $H_2SO_4$ and $H_3PO_4$. At higher concentrations of the acids ($\geq$ 8 M), the conductivities were in the order $H_2SO_4$ > $H_3PO_4$ > $HClO_4$ > $HNO_3$ > HCl [272]. Kawahara et al [273] studied $H_2SO_4$, $H_3PO_4$, HCl, $CH_3$-$SO_3H$, $C_2H_5$-$SO_3H$ as dopants to PBI membranes. The PBI/$H_3PO_4$ complex was found to be thermally the most stable up to 500$^oC$ whereas all other acid doped membranes lose acid molecules at high temperature [273]. It was confirmed that an acid content of more than 2 moles per repeating unit (PRU) is required for the proton conductivity and a doping level of 5-7 is generally used for fuel cell application [273, 274]. The conductivity of $H_3PO_4$ doped PBI increases with temperature [273]. High conductivity can only be obtained with amphoteric acids, such as phosphoric or phosphonic acids and $H_3PO_4$ is considered to be the best dopant for PBI because of its high boiling point, low volatility, thermal stability and high proton conductivity even in anhydrous form [275]. The blend between PBI and $H_3PO_4$ is ideal and the conduction mechanism is same irrespective of the concentration of the $H_3PO_4$ used [276]. Since they are amphoteric, having both proton donor (acidic) and proton acceptor (basic) groups, it can form dynamic 3-D H-bonded networks which makes the proton transport through the hopping of proton (Figure 6-2). This type of conduction mechanism is called Grotthus mechanism [261, 266, 276] and is different from vehicle mechanism in which the solvent acts as vehicle for the proton transport (e.g. proton conduction in Nafion®). Grotthus mechanism is not possible with mono protic strong acids [269]. Also PBI/$H_3PO_4$ membranes retain good mechanical strength up to 200°C [277]. $H_2SO_4$ on the other hand is much more acidic and the

oxidative and thermal stability of $H_2SO_4$ doped PBI membrane is poor [278] and is not suitable for fuel cells at temperatures above about 80°C [268, 273]. At elevated temperatures $H_3PO_4$ starts dehydrating in many stages and the first two stages are given in equations *(6-1*) and *(6-2*) [279]. The polymerisation reduces the conductivity of the membrane.

$$2H_3PO_4 \rightleftharpoons H_4P_2O_7 + H_2O \qquad (6\text{-}1)$$

$$H_4P_2O_7 + H_3PO_4 \rightleftharpoons H_5P_3O_{10} + H_2O \qquad (6\text{-}2)$$

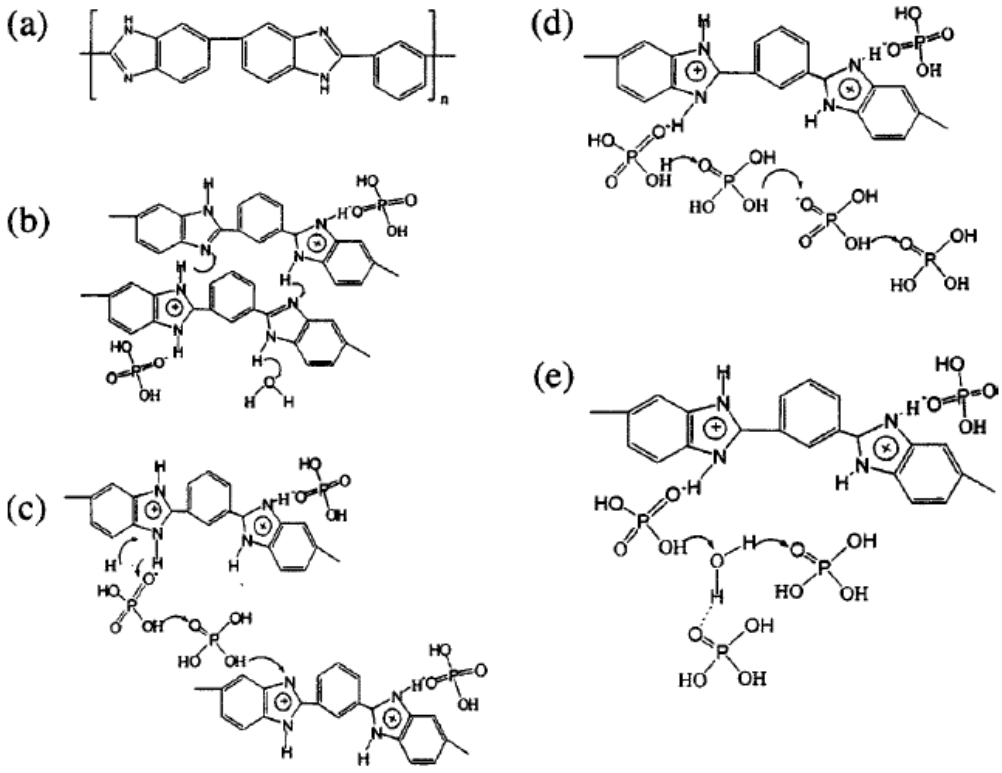


*Figure 6-2. Schematic of proton conduction in phosphoric acid doped PBI membrane. (a) PBI )(b) protonated PBI (c) proton transfer along acid-BI-acid (d) proton transfer along acid-acid (e) proton transfer along acid-$H_2O$[266].(Reproduced by permission of The Electrochemical Society).*

### 6.1.1 **Alternate acid to Phosphoric acid**

Several studies have been carried out to find suitable alternative to $H_3PO_4$ electrolyte in the 1970's for phosphoric acid fuel cells (PAFC). Many organic acids were studied as the

flexibility of the organic compound gives the freedom to alter their structure which is not available with inorganic systems [280].

The most studied alternate electrolyte to $H_3PO_4$ was trifluoro methane sulfonic acid (TFMSA) [268, 281-283]. Adams and Barger [283] studied the potential of TFMSA monohydrate (TFMSA-MH) for hydrogen oxidation and propane oxidation. TFMSA showed a higher reaction rate for propane and $H_2$ oxidation than 85% $H_3PO_4$ at 135$^o$C [283]. Appleby and Foley [284] also observed a higher reaction rate for the various low molecular weight hydrocarbon oxidation and ORR in TFMSA-MH than in $H_3PO_4$ [268, 285]. The higher kinetics on TFMSA compared to $H_3PO_4$ was attributed to the higher oxygen solubility and lower specific adsorption of the $CF_3SO_3^-$ anion compared to $H_2PO_4^-$ [286, 287] whereas $H_3PO_4$ has higher anionic adsorption and lower oxygen solubility [285, 287, 288]. The solubility and diffusivity of oxygen in perfluorosulfonic acid is higher than that in $H_3PO_4$ [269], however the high volatility and low ionic conductivity (aqueous solution) of TFMSA compared to $H_3PO_4$ makes it unsuitable as an electrolyte above 150$^o$C [269, 281, 283]. The lower conductivity at higher concentrations is due to the lack of a hydrogen bonded network, as proton conduction occurs by migration through a highly viscous medium unlike the Grotthus mechanism in $H_3PO_4$ [288].

Analogous compounds to TFMSA with a general formula $HSO_3$-$(CF_2)_n$-$SO_3H$ with n=1, 2 and 6 were also studied [287]. It was found that as the 'n' value increases, the solubility in water and conductivity of aqueous solution decreases and the specific adsorption of the anion increases. At constant pH, the ORR on Pt decreases with an increase in n-value due to the increased anion adsorption. This increased adsorption was attributed to the weaker hydration of the anion due to its large size. As the anion is less solvated the adsorption will be higher since the solvent displacement from the inter nuclear region of ion and metal will be easier.

Ahmad et al [280] studied the electrochemical properties of three organic sulfonic acids - ethane sulfonic acid, methane sulfonic acid and sulfoacetic acid as alternate fuel cell electrolyte. It was found that methane sulfonic acid is unstable as it decomposes at 0.9 V and 100$^o$C [280]. Ethane sulfonic acid was found to be strongly adsorbed on the Pt electrode inhibiting the hydrogen and oxidation reaction and is thus cannot be a suitable electrolyte for fuel cell. Sulfoacetic acid on other hand did not show any significant adsorption on Pt electrode, but the commercially available sulfoacetic acid was not pure

and also is chemically unstable at temperatures above 85$^{o}$C. From these studies it was concluded that unprotected C-H group containing compounds are strongly adsorbed on Pt and so the molecule has to be protected against the electrolytic oxidation or reduction in order to be used as fuel cell electrolytes [280].

Kanamura et al [269] studied perfluoro-ethylene-1,2-bis-phosphonic acid as fuel cell electrolyte. The diprotic phosphono group helps in the proton transport by Grotthus mechanism and the perfluoro group gives higher oxygen solubility [269]. CV studies showed that, bisphosphonic acid has higher hydrogen adsorption current density indicating that bisphononic adsorbs weakly on Pt catalysts [269]. The bis-phosphonic acid showed higher performance for ORR compared to $H_3PO_4$ at low current density (< 200 mA cm$^{-2}$) at 100$^{o}$C and slightly lower performance at higher current density due to the lower $O_2$ diffusion coefficient. As temperature increased from 100$^{o}$C to 200$^{o}$C the performance of bis-phosphonic acid increased due to the decrease in viscosity and the increase in $O_2$ diffusivity. This makes it a promising acid for high temperature fuel cells.

The studies on organic acids discussed above were mainly carried out before the introduction of PBI membrane in fuel cells by Savinell in 1996 [263, 265] and was mainly for the application in phosphoric acid fuel cell. Nowadays the high temperature fuel cell researchers are mainly concentrating on the $H_3PO_4$ doped PBI membrane because of its high proton conductivity at high temperature as discussed before. The objective of this chapter was to investigate the suitability of organic acid as alternate dopant to phosphoric acid doped PBI membrane. Introducing hydrophobicity by the organic group to the dopant structure will partially help to reduce the leaching out of the dopant from the membrane.

## 6.2 Experimental

Commercial PBI powder (Between, batch Lot 101/08) was used for the preparation of the PBI membrane. PBI powder was dissolved in dimethyl acetamide (DMAc) (Sigma Aldrich) to make 10 -12 wt.% solutions in a Teflon digestion vessel (Savillex, USA). The solution was then heat treated in the microwave oven (Cook works EM717CKL, 700W) at power = 50% with certain interval of cooling until most of the powder dissolved in the solvent. The undissolved powder was separated out by centrifuge and the solution was cast on a glass plate using a doctor blade and dried at 110$^{o}$C to obtain a membrane with the required thickness (~40 µm).

### 6.2.1 **Doping of the membrane**

Benzoic acid (BA) (fluka analytical), benzene sulfonic acid (BSA) (sigma aldrich) and phosphonoacetic acid (PAA) (alfa aesar) were used as PBI membrane dopants. Due to its lower solubility in water, benzoic acid solution was prepared in dimethyl formamide (DMF) [289] and all other acids were prepared in DI-water. Solutions of various concentrations were prepared and the PBI membrane was doped in it. The doping time was maintained to 12-14 days in order to have maximum adsorption of the acid by the membrane.

A saturated solution of PAA was prepared by dissolving the acid in DI water and a concentration of about 7.3 M was obtained. A lower concentration of the acid (3 M, 5 M and 6 M) were obtained by the subsequent dilution of the saturated solution. The PBI membrane was initially weighed, immersed into each of these solutions and kept in an oven at $80^{o}$C.

A saturated solution of BA (6.5 M) was prepared in DMF at $80^{o}$C and used for the membrane doping. Since BA has good solubility in DMAc, a direct casting method was also adopted to prepare the doped PBI membrane. For this, a 12.5% PBI-DMAc solution was mixed with BA to obtain 4, 6 and 8 PRU doping levels. This solution was cast on a flat glass plate using a doctor blade and dried in the air oven at $80^{o}$C for 1 hour.

BSA solutions (4 M, 5 M, and 6 M) were prepared in DI water. A melt of the BSA was also prepared and used for doping the PBI membrane at $80^{o}$C.

The doping level was calculated by weighing the membrane before and after the doping. The doped membrane was taken out from the solution and dried using tissue paper before weighing. The molar acid uptake was calculated from the weight difference before and after doping and is expressed as per repeating unit (PRU), i.e. the number of acid molecules per repeating unit of PBI polymer. The membrane conductivity of the doped PBI membrane was measured using the two point probe technique (section 2.3.4).

## 6.3 **Results and Discussions**

Three organic acids- BSA, BA and PAA were selected as dopants for PBI based on their melting point (MP) and boiling point (BP). Out of this the PAA contains both phosphonic acid and acetic acid group. It also contains an active methylene group (acidic hydrogen). The properties of the organic acids studied are given in Table 6-1. The doping level and doping time of three organic acids BA, BSA and PAA are given in Table 6-2.

*Table 6-1. Properties of organic acids studied as membrane dopant.*

| Acid | Structure | Melting point (MP) ($^{o}$C) | Boiling point (BP) ($^{o}$C) | Molecular weight (MW) (g mol$^{-1}$) |
|---|---|---|---|---|
| PA | 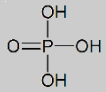 | 42 | 158$^{o}$C | 98 |
| PAA | 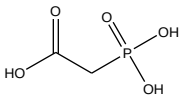 | 143-146 | 490$^{o}$C | 140.0 |
| BA | 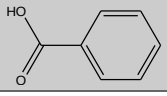 | 118 | 249$^{o}$C | 122.1 |
| BSA | 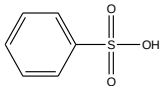 | 45 -46$^{o}$C | 174$^{o}$C | 158.2 |

*Table 6-2. Organic acids studied as dopants for PBI membrane and their doping conditions.*

| Acid | Concentration (M) | Doping time (days) | Doping Temperature ($^{o}$C) | Doping level (PRU) | Conductivity at 160$^{o}$C, S cm$^{-1}$ (order of magnitude) |
|---|---|---|---|---|---|
| BSA | 4 | 12 | 75-80 | 3.0 | $10^{-3}$ |
| | 5 | 12 | 75-80 | 5.6 | $10^{-3}$ |
| | 6 | 12 | 75-80 | 4.9 | $10^{-3}$ |
| | Melt | 5 | 75-80 | - | 0 |
| BA | 6.5 | 13 | 75-80 | 3.7 | $10^{-3}$ |
| PAA | 3 | 12 | 75-80 | 7.1 | $10^{-3}$ |
| | 5 | 12 | 75-80 | 8 | $10^{-3}$ |
| | 6 | 12 | 75-80 | 14.7 | $10^{-2}$ |
| | 7.3 | 12 | 75-80 | 19.7 | $10^{-2}$ |

### 6.3.1 Benzene sulfonic acid

A doping of PBI membrane in BSA melt was tried, but the membrane was found to be dissolving in the melt and no further testing was carried out. It was also observed in this study that the PBI membrane dissolves in the concentrated $H_2SO_4$ (98%) and TFMSA solution. Three different concentration of the BSA (4 M, 5 M and 6 M) were prepared and the conductivities of the doped membranes measured are given in Figure 6-3. The 4M BSA doped PBI membrane showed conductivity in the range of $10^{-4}$ S $cm^{-1}$ at all temperatures whereas 5M and 6M showed conductivity in the order of $10^{-3}$ S $cm^{-1}$ at 80°C and decreased with increase in temperature. The conductivity of the BSA doped PBI was one order of magnitude lower than the $H_3PO_4$ doped PBI membrane (Figure 6-5).

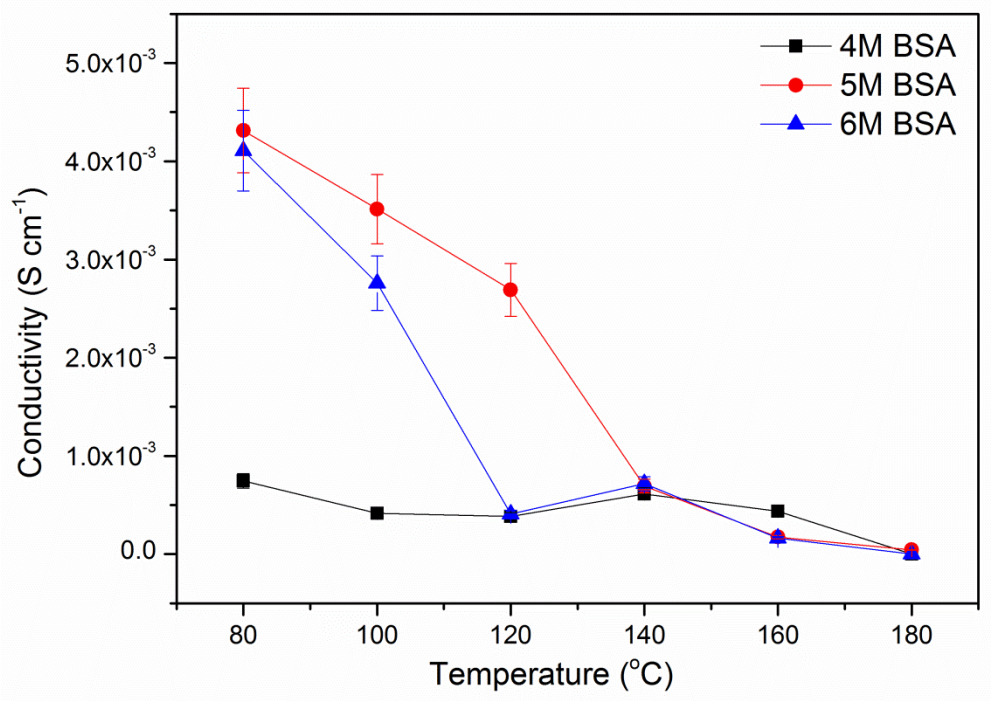


*Figure 6-3. Conductivity of BSA doped PBI membrane at different temperatures.*

Unlike the $H_3PO_4$ doped membrane, the conductivity of the BSA doped membrane decreased with an increase in temperature. As temperature increases from 120°C there was a tenfold decrease in conductivity for 5 M and 6 M BSA doped membranes. This might be due to the loss of water from the acid and the anhydrous acid being unable to provide sufficient proton conductivity. Anhydrous sulfonic acids are poor ionic conductors [280]. At temperature ≥ 140°C the conductivity of 4 M, 5 M and 6 M doped PBI membranes were more or less the same and was in the range of $10^{-4}$ S $cm^{-1}$ which is unacceptable for fuel cell application. A doping level of 3.0, 5.6 and 4.9 were obtained for

4M, 5M and 6M respectively. A higher doping level was obtained with 5M than 6M which explains the higher conductivity of 5M than 6M.

### 6.3.2 **Benzoic acid**

Two procedures have been adopted to prepare for BA doped PBI membrane, direct casting and the immersion method (section 6.2.1). The former method resulted in a very fragile membrane which was not able to be used for testing. The thickness of the so obtained membrane was 87 µm. The latter method of doping PBI membrane in saturated solution of BA in DMF (6.5 M) produced a mechanically more stable membrane and the conductivity values measured are given in Figure 6-4. The conductivity obtained was in the range of $10^{-3}$ S $cm^{-1}$ which was lower than $H_3PO_4$ doped PBI membrane. No significant change in conductivity with temperature was observed. This may be because the solution was prepared in DMF instead of water and the proton conductivity was contributed only by the –COOH group in the BA.

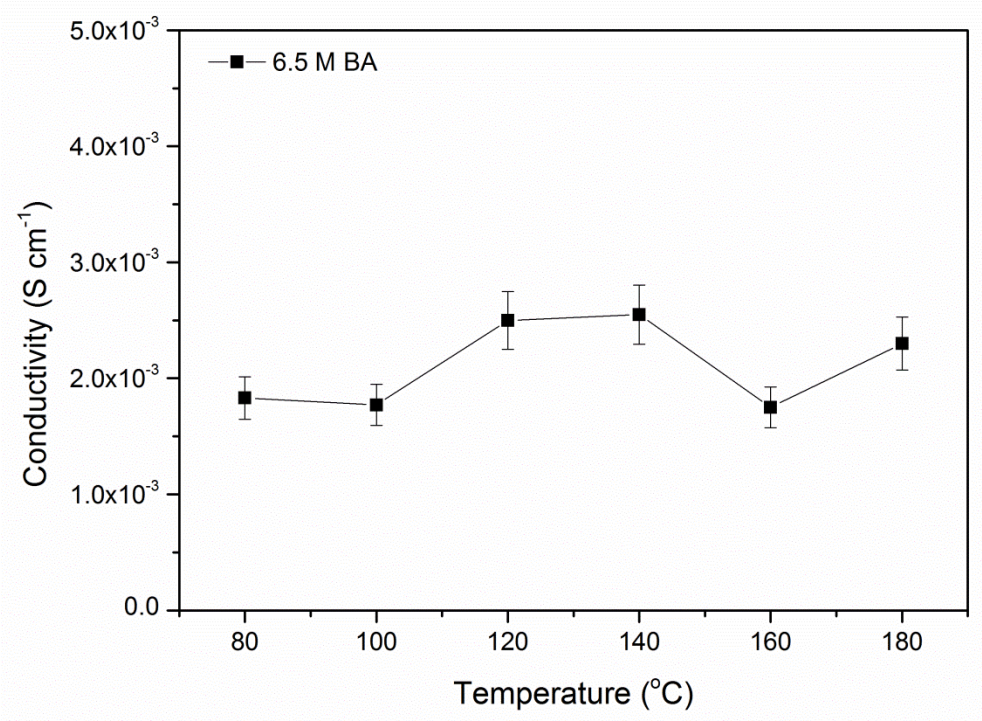


*Figure 6-4 Conductivity of 6.5M BA at different temperatures.*

No lower concentration solution was prepared due to the poor conductivity obtained with saturated solution. The low conductivity of BA and BSA could be the result of higher resistivity of these acids in their anhydrous form as reported elsewhere [290].

### 6.3.3 **Phosphonoacetic acid**

The PBI doped in 6M PAA solution at room temperature was tested for conductivity after 1, 3 and 10 days of doping and negligible conductivity were observed. So a higher doping temperature of 80°C and doping time 12 days were used for doping. The negligible conductivity of the membrane doped at room temperature may be due to the lack of diffusion of the acid into the membrane whereas at high temperature the acid present on the surface can migrate inside to the membrane. The conductivity of the doped PBI membrane was measured at temperature varying from 80°C to 200°C. The result obtained is given in Figure 6-5. The conductivity of the membrane increased with an increase in acid concentration. The highest conductivity was obtained for the 7.3 M doped PBI membrane ($1.45\times10^{-2}$ S $cm^{-1}$ at 140°C). At 100°C all PAA doped PBI membranes showed conductivity in the order of $10^{-3}$ S $cm^{-1}$. Interestingly the conductivity of the membrane increased with an increase in temperature for all concentration. The conductivity below 140°C was of the same order of magnitude whereas a large increase in conductivity was observed above 140°C. All the membranes doped at PAA concentration > 3 M showed conductivity in the order of $10^{-2}$ S $cm^{-1}$ at temperature > 160°C which is of the same order of magnitude as that of the PA doped PBI membrane. The conductivity of PBI membrane doped in 11.5 M $H_3PO_4$ at the same conditions is also given for comparison in Figure 6-5.

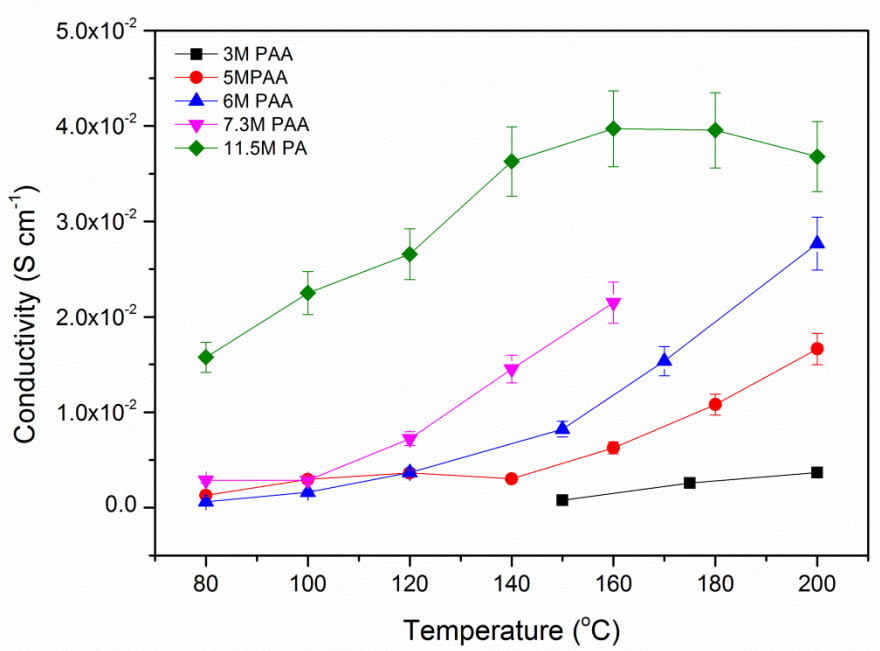


*Figure 6-5. Conductivity of PAA doped PBI membrane with respect to temperature. PBI doped with 11.5M $H_3PO_4$ (PA) is also shown for comparison.*

The conductivity of PAA doped PBI was higher than that of the BSA (Figure 6-3) and BA (Figure 6-4) doped PBI membranes. However it was lower than that of $H_3PO_4$ doped PBI membrane at all concentrations. It has to be noted that $H_3PO_4$ conductivity decreases at >160$^oC$ (due to the polymerisation of PA) whereas PAA conductivity increases with temperature and at high temperature the conductivity may reach a value similar to PA doped PBI. The boiling point of PAA (490$^oC$) is also higher than $H_3PO_4$ (158$^oC$). This makes PAA an interesting alternate to $H_3PO_4$ at high temperature. The doping level of the PAA doped PBI increased with concentration (Table 6-2). Since water content was higher at lower concentration, there could be both water and acid uptake resulting in less acid content in the polymer membrane. A conductivity of $2\times10^{-2}$ S cm$^{-1}$ was obtained at 160$^oC$ for a membrane doped with 7.3 M PAA. Except the 3M PAA doped PBI membrane, all other membranes showed a conductivity in the order of $10^{-2}$ S cm$^{-1}$ at temperature >140$^oC$. The conductivity increase for temperature > 140$^oC$ may be attributed to the melting of the acid. The melted acid on the surface provides a better ionic conduction path and thus increases the protonic conductivity. Also the melted acid can penetrate into the membrane giving a higher doping level and better ionic conduction path. Unlike BSA, the anhydrous PAA is conducting due to the presence of phosphono group. The membrane after doping was found to contain solid particles of acid on the surface. The doping level for PAA was higher compared to other acids which might be due to the better interaction with PBI membrane by the phosphono group.

## 6.4 **Conclusion:**

A preliminary investigation of the suitability of organic acids as alternate to the $H_3PO_4$ was carried out. Three organic acids BSA, BA and PAA were selected based on their melting and boiling point. Various concentrations of the acids were prepared and their conductivities at different temperatures were studied. Benzoic acid ($2.5\times10^{-3}$ S cm$^{-1}$, 120$^oC$, 6.5 M) and benzene sulfonic acid ($2.7\times10^{-3}$ S cm$^{-1}$, 120$^oC$, 5 M) showed lower conductivity compared to phosphonoacetic acid ($7.5\times10^{-3}$ S cm$^{-1}$, 120$^oC$, 7.3 M). The conductivities of the doped PBI membrane were in the order PA>PAA>BSA>BA. Phosphonoacetic acid was the only studied acid that showed conductivity ($2.2\times10^{-2}$ S cm$^{-1}$, 160$^oC$, 7.3 M) in the range of $H_3PO_4$ ($2.6\times10^{-2}$ S cm$^{-1}$, 120$^oC$, 11.5 M). Its conductivity also increased with increase in temperature (Figure 6-5). Since the conductivity of PAA doped PBI membrane increased continuously at temperatures > 160$^oC$ unlike phosphoric acid, PAA may be considered as suitable dopant to PBI membrane at temperature > 160$^oC$. Since only the conductivity of the doped membrane is considered here, a

definitive conclusion is not possible to make on the applicability of the PAA as alternate to phosphoric acid. More electrochemical studies are required to find out the adsorption of these acids on Pt or $IrO_2$ catalysts and its effect on the activity of the catalyst to reach to a definitive conclusion.

# Conclusion and future work

## 7.1 Conclusion

This thesis tried to explore various possibilities of producing a stable and active OER catalyst with reduced precious metal loading in order to make the PEMWE system cost effective. Supporting the catalyst on a cheap support material is one of the methods to reduce the precious metal loading on the electrode. Antimony doped tin oxide (ATO) and indium tin oxide (ITO) were investigated as supports for $IrO_2$ in PEMWE anodes in chapter 3 and chapter 4. The surface area and the conductivity of the supported catalysts were predominantly contributed by the $IrO_2$ as the support materials used have lower conductivity and surface area than the pristine $IrO_2$ catalyst. From the ATO supported catalysts it was clear that a loading of lower than 60 wt.% $IrO_2$ decreased the conductivity and surface area significantly which in turn decreased the performance of the MEA. The CV in 85% $H_3PO_4$ at room temperature showed that all the supported catalysts have higher normalised voltammetric charge compared to the pristine $IrO_2$ indicating that the support helps in the dispersion of the catalyst and smaller crystallites of $IrO_2$ formed on the support. MEA analysis with Nafion 115 membrane at 80$^oC$ was also in agreement with the CV analysis. The pristine $IrO_2$ and 90% $IrO_2$-ATO showed best performance with a cell voltage of 1.73 V @ 1A $cm^{-2}$ at 80$^oC$. Normalising the current density with the $IrO_2$ loading indicated that the $IrO_2$ loading ≥60% $IrO_2$-ATO gives better performance than the pristine $IrO_2$. A similar study on the ITO supported $IrO_2$ catalyst showed significant agglomeration for loading ≤ 60% $IrO_2$-ITO and a large decrease in the catalytic performance was observed in CV and MEA tests. This shows the influence of the $IrO_2$ particle size on the performance of the MEA. Interestingly the 60 wt.% $IrO_2$ supported on a non-conducting $TiO_2$ gave a conductivity of the same order of magnitude to that of its ITO counterpart. This implies that the support conductivity is not significant as long as a conducting film is formed on it. Comparing the results of ITO, ATO and $TiO_2$ supported $IrO_2$ catalyst, it can be proposed that 60 wt.% $IrO_2$ can be considered as optimum loading on supports with good catalytic performance. Complete coverage of the support with smaller active catalyst particles is important to produce catalysts with high active surface area and good conductivity.

$Nb_2O_5$ addition to $RuO_2$ and $IrO_2$ was studied in order to produce a stable catalyst for low temperature PEMFC. The addition of $Nb_2O_5$ did not enhance the activity of the catalyst but decreased the activity due to the dilution of active component. Two synthesis methods-Adams method and hydrolysis method were adopted to prepare the bimetallic catalyst. The Adams method was found to be forming NaNb oxide complex oxides which decrease the conductivity and activity of the catalyst. Thus the Adams method is not a suitable method to prepare Nb based catalysts. In both methods of preparation, > 20 mol% Nb lowers the electrical conductivity and activity. The monometallic $RuO_2$(A), . The pristine $RuO_2$(A) (1.62 V @1 A $cm^{-2}$) and $RuO_2$(H) (1.75 V @1 A $cm^{-2}$) and $IrO_2$(A) (1.63 V@ 1 A $cm^{-2}$) showed best performance in the MEA analysis with Nafion 115 membrane at 80$^oC$ compared to the bimetallic catalysts in both methods of preparation. The stability, on the other hand was found to be increasing on $Nb_2O_5$ addition. MEA stability tests on ruthenium oxide based catalysts showed that the stability of $RuO_2$ is poor whereas Nb addition slightly improve the stability but is not significant enough whereas iridium oxide based catalysts showed extremely good stability in the MEA stability test. 20 mol% Nb can be added to iridium oxide and ruthenium oxide with slight compromise in the activity while reducing the precious metal loading by 20 mol%.

Preliminary investigations of some of the possible organic acids were carried out as dopant for a PBI membrane. Phosphonoacetic acid (PAA) doped PBI was found to be giving comparable conductivity as that of phosphoric acid doped PBI (in the order of $10^{-2}$ S $cm^{-1}$). The conductivity of the PAA doped PBI membrane increased with an increase in temperature. Unlike PA, no drop in conductivity was observed above 160$^oC$ indicating that the conductivity may reach to that of PA at high temperature (> 160$^oC$). More electrochemical studies are required to understand the activity of the catalyst on this electrolyte.

## 7.2 Recommendation for future work

1. Since 60 wt.% was proposed to be an optimum loading for a supported catalyst, a long term stability test of 60% $IrO_2$-ATO and 60% $IrO_2$-$TiO_2$ catalyst needs to be compared with the pristine $IrO_2$ to investigate the stability of the supported catalyst for long term operation.
2. Phosphoric acid doped PBI membrane is proposed to be a promising membrane for high temperature membrane. The MEA performance of the supported catalyst can be investigated in a PBI membrane based MEA in steam electrolysis.

3. The potential of the supported catalyst at high temperature can be studied in half-cell set up using 85% $H_3PO_4$ electrolyte. An experimental set up need to design with a provision for uniform heating. Thermally stable binders such as PTFE solution need to be studied for this purpose.
4. Phosphonoacetic acid was found to be promising organic acid from its conductivity at high temperature. Detailed electrochemical studies required to investigate its applicability as alternate dopant to phosphoric acid in PBI-phosphoric acid membrane system. The phosphonoacetic acid doped PBI membrane can also be studied in full cell set up to study the MEA performance.

# Appendix

## 8.1 Crystallite size calculation by Scherrer equation from XRD

Scherrer equation was used to calculate the crystallite size from the XRD spectra.

$$t = \frac{0.9\lambda}{\beta cos\theta}$$

Where t is the crystallite size, $\lambda = 0.154\ nm$ is the wavelength of the X-ray, $\beta$ is the full width at half maximum (FWHM), $\theta$ is the peak position in radians.

E.g For peak at $2\theta$=33.94$^o$ and FWHM of 1.97$^o$ ,

$$\theta = \frac{33.94}{2} = 16.97^o = 16.97 \times \frac{\pi}{180}\ radian = 0.296\ radians$$

$$ie.\theta = 0.296\ and\ cos\theta = 0.956$$

Similarly $FWHM\ = 1.97 \times \frac{\pi}{180} = 0.034\ radians$

Substituting in Scherrer equation,

$$t = \frac{0.9 \times 0.154}{0.034 \times 0.956} = \mathbf{4.26\ nm}$$

## 8.2 Conductivity measurement

Powder conductivity of the powder catalyst samples were measured using the set up described in section 2.3.1. The thickness vs. resistance gives a linear relationship and slope of which gives the resistivity.

For e.g. The linear vs. thickness plot of 60% $IrO_2$-ATO is given below. The slope of the linear fit is 0.3188.

The resistivity can be calculated from the equation (2-14),

$$\rho = \frac{\Delta R}{\Delta l}.A$$

Where $\rho$ is the resitivity and $\frac{\Delta R}{\Delta l}$ is the slope of the resistance. Vs thickness plot, A is the area of cross section of sample which is 0.19625 cm$^2$ in our set up. Thus

$$\rho = 0.3188 \times 0.19625 \times 10 = 6.26 \times 10^{-1}\ \Omega.cm$$

Conductivity ($\sigma$) can be calculated taking reciprocal of resistivity,

$$\sigma = \frac{1}{\rho} = \frac{1}{6.26 \times 10^{-1}} = \mathbf{1.60\ S.cm^{-1}}$$

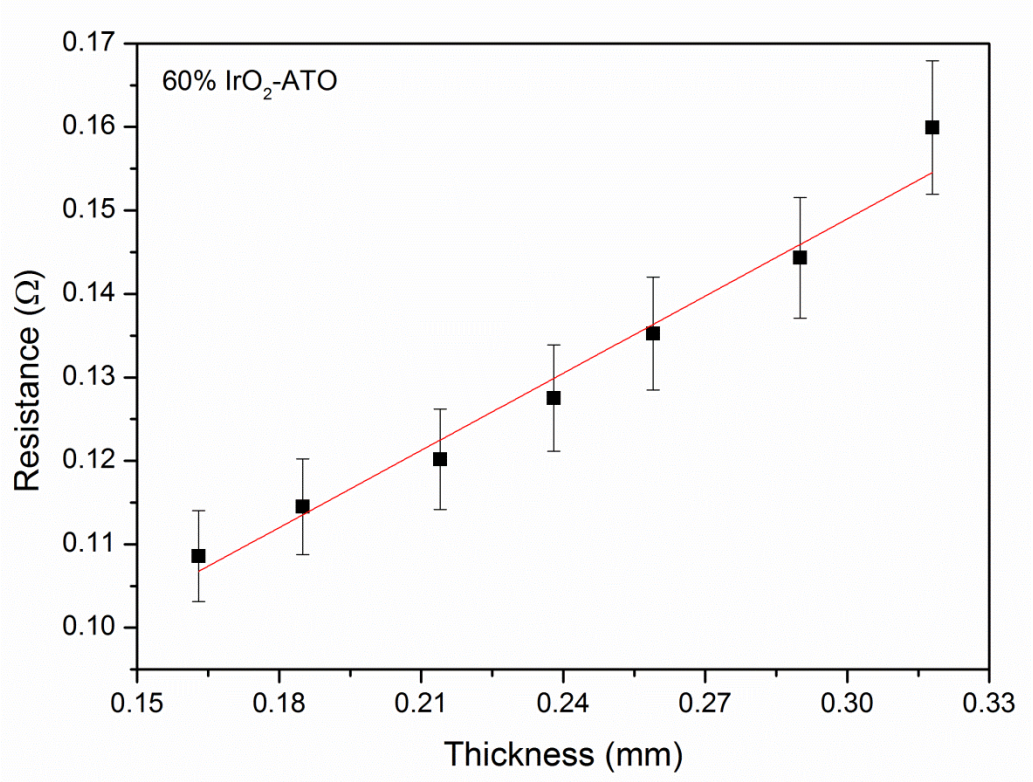


## 8.3 Cell efficiency calculation

Reversible potential at any temperature without the pressure effect can be written as [30-34],

$$E^{o}_{rev,t} = 1.5184 - 1.5421 \times 10^{-3}T + 9.523 \times 10^{-5}T\ ln\ T + 9.84 \times 10^{-8}T^{2}$$

The reversible potential calculated according to this equation is given in the table below.

| Temperature | $E_{rev}$ (V) |
|---|---|
| 25 | 1.229 |
| 50 | 1.208 |
| 80 | 1.184 |

The efficiency ($\varepsilon_{\Delta G}$) is defined as below,

$$\varepsilon_{\Delta G} = \frac{E_{rev}}{E_{cell}}$$

Where $E_{rev}$ is the thermodynamic reversible potential and $E_{cell}$ is the cell voltage obtained. Substituting the reversible voltage from the table above at 80$^{o}$C, and cell potential obtained (e.g. 1.73 V), the efficiency can be calculated as,

$$\varepsilon_{\Delta G} = \frac{E_{rev}}{E_{cell}} = \frac{1.184}{1.73} = \mathbf{68.4}\%$$

## 8.4 Energy consumption for $H_2$ production

The $H_2$ evolution can be written as,

$$2H^+ + 2e^- \rightarrow H_2$$

ie, for one mole of $H_2$ production 2 moles of electrons is required.

Considering current density as $j$ A cm$^{-2}$ passed for $t$ hour, the number of moles of electrons passed ($n$) will be (Total charge passed/charge of one moles),

$$n = \frac{j \times t}{F}$$

Where j is the current density (A cm$^{-2}$), t is the time (seconds), F is the faradays constant (96487 C). The no of moles of $H_2$ produced are half of the moles of electron (from the stoichiometric equation for HER above),

$$\text{No of moles of } H_2 = \frac{n}{2}$$

We know that one of mole of ideal gas at STP possess a volume of 22.4 litres,

Considering the $H_2$ as ideal gas, the volume of $H_2$ produced at STP will be,

$$Volume\ of\ H_2\ produced = No\ of\ moles\ of\ H_2 \times 22.4\ litre$$

$$Hydrogen\ production\ rate = \frac{Volume\ of\ H_2\ produced}{time}$$

$$Energy\ required = Cell\ voltage \times current\ density$$

$$Energy\ consumption = \frac{Energy\ required}{H_2\ production\ rate}\ \ \boldsymbol{kWh\ Nm^{-3}}$$

An example of the calculation is given in table below

| Current density | Time | Cell voltage | No of moles of $e^-$ | No of moles of $H_2$ | Volume of $H_2$ | $H_2$ production rate | Energy required | Energy consumption |
|---|---|---|---|---|---|---|---|---|
| 1 A $cm^{-2}$ | 1 hr | 1.62 V | 0.037 | 0.0187 | 0.418 litre | 0.000418 $Nm^3/h$ | 1.62 W | **3.877 kWh $Nm^{-3}$** |

## 8.5 Final state screening

Final state screening in XPS is due to the relaxation of the final state configuration (due to the loss of screening effect of core level electron which underwent photoemission) [291]. There is a sudden change in the effective charge due to the loss of shielding electrons (This perturbation induces a transition in which an electron from a bonding orbital can be transferred to an anti-bonding orbital simultaneously with core ionization) [291, 292]. This produces line which is split asymmetrically into several components. The relaxation energy used to excite electrons in the valence state to bound state (monopole excitation or **shake up satellite**) or unbound state (monopole ionization or shake off satellite) [292]. Shake up features appear at high BE side of main XPS peak and are common among transition metal oxides associated with paramagnetic species (eg: $Ir^{4+}$).

Two types of satellites are detected,

**Shake up**: The outgoing electron interacts with a valence electron and excites (shake up) it to a higher energy level. As a consequence, the core electron energy is reduced and a satellite structure appears a few eV lower KE (higher BE) of core level electron [291, 292].

**Shake off**: The valence electron ejected from the ion completely (to the continuum). Appears as a broadening of the core level peak or contribute to the inelastic background [291, 292].

Schematic of the two types of satellite is given in Figure 8-1.

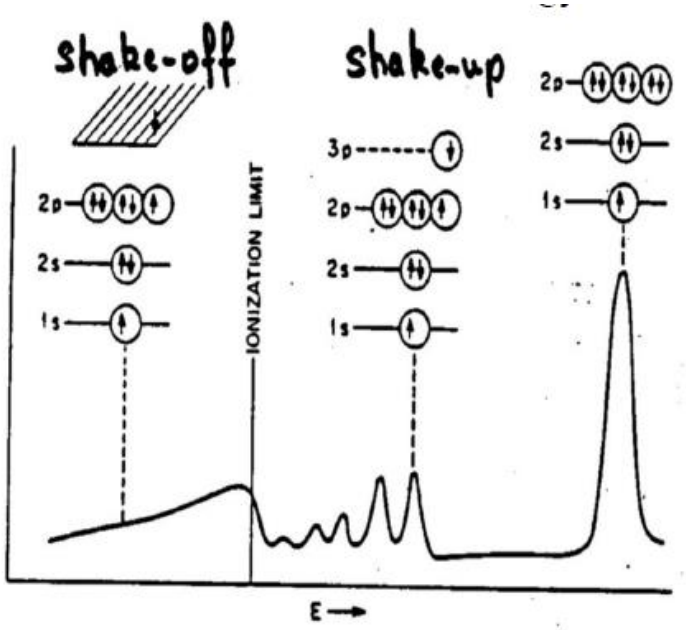


*Figure 8-1. Schematic of final state screening in XPS [291].*

## 8.6 **Calculation of acid doping level in the membrane**

Consider,

Weight of the membrane before doping = $m_1$

Weight of the membrane after acid doping = $m_2$

$$The\ weight\ of\ the\ acid\ absorbed = m_2 - m_1 = W$$

The molecular weight of the phosphoric acid = $w_2$ g mol$^{-1}$

$$The\ no\ of\ moles\ of\ phosphoric\ acid\ absorbed = \frac{W}{w_2} = x\ M$$

Molecular weight of the PBI =308 g mol$^{-1}$

$$The\ no\ of\ moles\ of\ PBI\ used = \frac{m_1}{308} = y\ M$$

$$Doping\ level = \frac{No\ of\ moles\ of\ acid}{No\ of\ moles\ of\ PBI} = \frac{x}{y}$$

## 8.7 Some major electrolyser manufactures

Some of the major commercial electrolyser manufacturers and their hydrogen production efficiencies are given in the Table 8-1.

*Table 8-1. Some of the major commercial electrolyser manufacturers and their hydrogen production specifications.*

| Manufacturer | Type of electrolyser | Model | Rate of production ($Nm^3h^{-1}$) | Energy consumption ($kWhNm^{-3}$) | Pressure (bar) | Country of origin | Ref |
|---|---|---|---|---|---|---|---|
| AccaGen | Alkaline | | 150 | 5 | 40 | Switzerland | [293] |
| Hydrogenics | PEM | HyLZER 1&2 | 1-2 | 6.7 | 0-8 | US/EU | [294] |
| | Alkaline | HySTAT 10 | 4-10 | 4.9 | 10-30 | | |
| | Alkaline | HySTAT 15 | 6-15 | 4.9 | 10-30 | | |
| | Alkaline | HySTAT 20 | 8-20 | 4.9 - 5 | 10 | | |
| | Alkaline | HySTAT 30 | 12-30 | 4.9-5 | 10 | | |
| | Alkaline | HySTAT 60 | 24-60 | 4.9 | 10 | | |
| Protononsite | PEM | HoGEN S | 0.265 - 1.05 | 6.7 | 13.8 | USA | [295] |
| | | HoGEN H | 2 - 6 | 6.8 - 7.3 | 15 | | |
| | | HoGEN C | 10 -30 | 5.8 - 6.2 | 30 | | |
| Norsk hydro electrolyser | Alkaline | Atm. (4000A) | 0 - 377 | 4.1 | 0.02 | Norway | [296] |
| | | Atm. (5150A) | 0 - 485 | 4.3 | 0.02 | | |
| | | HPE | 10-65 | 4.8 | 12 | | |
| | | NEL-A atm | 50 - 485 | 4.4 | 250 | | [297] |
| IHT | Alkaline | Lurgi system | 110 - 760 | 4.3-4.6 | 32.4 | Switzerland | [296] |
| | | Bamag system | 3-330 | 3.9 - 4.5 | | | |
| | Alkaline | EC 500,600,750, 1000 | 28-56 | | 10 | | |
| Giner | PEM | High pressure electrolyser | 3.7 | 5.4 | 85 | USA | [298] |
| H-tec systems | PEM | EL-30 | 0.33-3.6 | 5 - 5.5 | 30 | Germany | [299] |

# List of publications

## 9.1 Peer-reviewed publications

1. Puthiyapura, V.K., S. Pasupathi, S. Basu, X. Wu, H. Su, N. Varagunapandiyan, B. Pollet, and K. Scott, *$Ru_xNb_{1-x}O_2$ catalyst for the oxygen evolution reaction in proton exchange membrane water electrolysers.* International Journal of Hydrogen Energy, 2013. **38**(21): p. 8605-8616.
2. Wu, X., K. Scott, and V. Puthiyapura, *Polymer electrolyte membrane water electrolyser with Aquivion® short side chain perfluorosulfonic acid ionomer binder in catalyst layers.* International Journal of Hydrogen Energy, 2012. **37**(18): p. 13243-13248.
3. Puthiyapura, V.K., S. Pasupathi, H. Su, B. Pollet, X. Liu, and K. Scott, *Investigation of supported $IrO_2$ as electrocatalyst for the oxygen evolution reaction in Proton exchange membrane water electrolyser*. International Journal of Hydrogen Energy, 2014. **39**(5): p. 1905-1913.
4. Puthiyapura, V.K., M. Mamlouk, S. Pasupathi and K. Scott, *Physical and electrochemical studies of ATO supported $IrO_2$ catalyst for PEM water electrolyser*. Journal of Power Sources (Submitted).

## 9.2 Conference presentations

1. UKIERI – British council- Research Industry Workshop -10th May 2011, Hotel Taj Mansingh, New Delhi, India (Poster presentation)

2. $I^2$-tech-2011, open house posters – March 2011, IIT-Delhi, India (Poster presentation).

3. Electrochemical Horizons, 5-6 september-2011, University of Bath, United Kingdom (Poster presentation)

4. PG research conference, Research Beehive, Newcastle University, UK, 22-March-2012 (Oral presentation)

5. Symposium on Water electrolysis and hydrogen as part of the future Renewable Energy System, 10-11 May 2012, Gamle Carlsberg, Copenhagen-Denmark (Poster presentation)

6. PG research conference, Research Beehive, Newcastle University, UK 25 March 2013. (Oral presentation).

7. Electrochem-2013, 1-3 September 2013, University of Southampton, United Kingdom (Poster presentation).

# References


1. Mazloomi, K. and C. Gomes, *Hydrogen as an energy carrier: Prospects and challenges.* Renewable and Sustainable Energy Reviews, 2012. **16**(5): p. 3024-3033.
2. Momirlan, M. and T.N. Veziroglu, *Current status of hydrogen energy.* Renewable and Sustainable Energy Reviews, 2002. **6**(1–2): p. 141-179.
3. Conte, M., A. Iacobazzi, M. Ronchetti, and R. Vellone, *Hydrogen economy for a sustainable development: state-of-the-art and technological perspectives.* Journal of Power Sources, 2001. **100**(1–2): p. 171-187.
4. Laguna-Bercero, M.A., *Recent advances in high temperature electrolysis using solid oxide fuel cells: A review.* Journal of Power Sources, 2012. **203**(0): p. 4-16.
5. Turner, J., G. Sverdrup, M.K. Mann, P.-C. Maness, B. Kroposki, M. Ghirardi, R.J. Evans, and D. Blake, *Renewable hydrogen production.* International Journal of Energy Research, 2008. **32**(5): p. 379-407.
6. Balat, M., *Potential importance of hydrogen as a future solution to environmental and transportation problems.* International Journal of Hydrogen Energy, 2008. **33**(15): p. 4013-4029.
7. O'Hayre, R., S.-W. Cha, W. Colella, and F. B.Prinz, *Fuel Cell Fundamentals*2006: John Wiley and Sons.Inc. 409.
8. Lu, P.W.T. and S. Srinivasan, *Advances in water electrolysis technology with emphasis on use of the solid polymer electrolyte.* Journal of Applied Electrochemistry, 1979. **9**(3): p. 269-283.
9. Edwards, P.P., V.L. Kuznetsov, and W.I.F. David, *Hydrogen energy.* Philosophical Transactions of the Royal Society a-Mathematical Physical and Engineering Sciences, 2007. **365**(1853): p. 1043-1056.
10. Barreto, L., A. Makihira, and K. Riahi, *The hydrogen economy in the 21st century: a sustainable development scenario.* International Journal of Hydrogen Energy, 2003. **28**(3): p. 267-284.
11. Zeng, K. and D. Zhang, *Recent progress in alkaline water electrolysis for hydrogen production and applications.* Progress in Energy and Combustion Science, 2010. **36**(3): p. 307-326.
12. Holladay, J.D., J. Hu, D.L. King, and Y. Wang, *An overview of hydrogen production technologies.* Catalysis Today, 2009. **139**(4): p. 244-260.
13. Bičáková, O. and P. Straka, *Production of hydrogen from renewable resources and its effectiveness.* International Journal of Hydrogen Energy, 2012. **37**(16): p. 11563-11578.
14. Fayaz, H., R. Saidur, N. Razali, F.S. Anuar, A.R. Saleman, and M.R. Islam, *An overview of hydrogen as a vehicle fuel.* Renewable and Sustainable Energy Reviews, 2012. **16**(8): p. 5511-5528.
15. A, F. and H. K, *Electrochemical photolysis of water at a semiconductor electrode.* Nature, 1972. **238**: p. 37-38.

16. Grimes, C.A., O.K. Varghese, and S. Ranjan, *Light, Water, Hydrogen: The Solar Generation of Hydrogen by Water Photoelectrolysis*2008: Springer, USA. 546.

17. Ma, L., S. Sui, and Y. Zhai, *Investigations on high performance proton exchange membrane water electrolyzer.* International Journal of Hydrogen Energy, 2009. **34**(2): p. 678-684.

18. Grigoriev, S.A., V.I. Porembsky, and V.N. Fateev, *Pure hydrogen production by PEM electrolysis for hydrogen energy.* International Journal of Hydrogen Energy, 2006. **31**(2): p. 171-175.

19. Dunn, S., *Hydrogen futures: toward a sustainable energy system.* International Journal of Hydrogen Energy, 2002. **27**(3): p. 235-264.

20. de Souza, R.F., J.C. Padilha, R.S. Gonçalves, M.O. de Souza, and J. Rault-Berthelot, *Electrochemical hydrogen production from water electrolysis using ionic liquid as electrolytes: Towards the best device.* Journal of Power Sources, 2007. **164**(2): p. 792-798.

21. Marshall, A., *Electrocatalysts for the oxygen evolution electrode in water electrolysers using proton exchange membranes : synthesis and characterization.*,Thesis in *Norwegian University of Science and Technology, Faculty of Natural Sciences and Technology* 2005, Norwegian University of Science and Technology. p. 233.

22. Lopez, M., A. Schleunung, and P. Biberbach, *Precious Metal Oxide catalyst for water electrolysis.*, in *EUROPEAN PATENT*2009.

23. Grimes, C.A., O.K. Varghese, and S. Ranjan, *Light, Water, Hydrogen:The Solar Generation of Hydrogen by Water Photoelectrolysis*2008: Springer.

24. Sandstede, G., E.J. Cairns, V.S. Bagotsky, and K. Wiesener, *History of low temperature fuel cells*, in *Handbook of Fuel Cells*2010, John Wiley & Sons, Ltd.

25. Kreuter, W. and H. Hofmann, *Electrolysis: The important energy transformer in a world of sustainable energy.* International Journal of Hydrogen Energy, 1998. **23**(8): p. 661-666.

26. Santos, D.M.F., C.A.C. Sequeira, and J.L. Figueiredo, *Hydrogen production by alkaline water electrolysis.* Química Nova, 2013. **36**: p. 1176-1193.

27. Ursua, A., L.M. Gandia, and P. Sanchis, *Hydrogen Production From Water Electrolysis: Current Status and Future Trends.* Proceedings of the IEEE, 2012. **100**(2): p. 410-426.

28. Zhang, J., ed. *PEM Fuel Cell Electrocatalysts and Catalyst Layers-Fundamentals and Applications*. 2008, Springer.

29. Pletcher, D. and X. Li, *Prospects for alkaline zero gap water electrolysers for hydrogen production.* International Journal of Hydrogen Energy, 2011. **36**(23): p. 15089-15104.

30. LeRoy, R.L., *Industrial water electrolysis: Present and future.* International Journal of Hydrogen Energy, 1983. **8**(6): p. 401-417.

31. Laoun, B., *Thermodynamics aspect of high pressure hydrogen production by water electrolysis* Revue des Energies Renouvelables, 2007. **10**(3): p. 435-444.

32. Harrison, K.W., E. Hernandez-Pacheco, M. Mann, and H. Salehfar, *Semiempirical Model for Determining PEM Electrolyzer Stack Characteristics.* Journal of Fuel Cell Science and Technology, 2006. **3**(2): p. 220-223.

33. GarcÃa-Valverde, R., N. Espinosa, and A. Urbina, *Simple PEM water electrolyser model and experimental validation.* International Journal of Hydrogen Energy, 2012. **37**(2): p. 1927-1938.

34. Roy, A., S. Watson, and D. Infield, *Comparison of electrical energy efficiency of atmospheric and high-pressure electrolysers.* International Journal of Hydrogen Energy, 2006. **31**(14): p. 1964-1979.

35. Millet, P., R. Ngameni, S.A. Grigoriev, N. Mbemba, F. Brisset, A. Ranjbari, and C. Etievant, *PEM water electrolyzers: From electrocatalysis to stack development.* International Journal of Hydrogen Energy, 2010. **35**(10): p. 5043-5052.

36. Bard, A.J. and L.R. Faulkner, *Electrochemical Methods: Fundamentals and Applications*. 2 ed2001: John Wiley & Sons, Inc. 833.

37. Onda, K., T. Kyakuno, K. Hattori, and K. Ito, *Prediction of production power for high-pressure hydrogen by high-pressure water electrolysis.* Journal of Power Sources, 2004. **132**(1–2): p. 64-70.

38. Zhang, H., G. Lin, and J. Chen, *Evaluation and calculation on the efficiency of a water electrolysis system for hydrogen production.* International Journal of Hydrogen Energy, 2010. **35**(20): p. 10851-10858.

39. Wendt, H. and G. Imarisio, *Nine years of research and development on advanced water electrolysis. A review of the research programme of the Commission of the European Communities.* Journal of Applied Electrochemistry, 1988. **18**(1): p. 1-14.

40. Sørensen, B., *Hydrogen and Fuel Cells-emerging technologies and applications*. Sustainable World Series2005: Elsevier. 450.

41. M.A, L.-B., *Recent advances in high temperature electrolysis using solid oxide fuel cells: A review.* Journal of Power Sources, 2012. **203**(0): p. 4-16.

42. Marangio, F., M. Pagani, M. Santarelli, and M. Calì, *Concept of a high pressure PEM electrolyser prototype.* International Journal of Hydrogen Energy, 2011. **36**(13): p. 7807-7815.

43. Rasten, E., G. Hagen, and R. Tunold, *Electrocatalysis in water electrolysis with solid polymer electrolyte.* Electrochimica Acta, 2003. **48**(25-26): p. 3945-3952.

44. McElroy, J.F., *Recent advances in SPE(R) water electrolyzer.* Journal of Power Sources, 1994. **47**(3): p. 369-375.

45. Marshall, A., B. Børresen, G. Hagen, M. Tsypkin, and R. Tunold, *Hydrogen production by advanced proton exchange membrane (PEM) water electrolysers--Reduced energy consumption by improved electrocatalysis.* Energy, 2007. **32**(4): p. 431-436.

46. Barbir, F., *PEM electrolysis for production of hydrogen from renewable energy sources.* Solar Energy, 2005. **78**(5): p. 661-669.

47. Millet, P., F. Andolfatto, and R. Durand, *Design and performance of a solid polymer electrolyte water electrolyzer.* International Journal of Hydrogen Energy, 1996. **21**(2): p. 87-93.

48. Zhang, J., Z. Xie, J. Zhang, Y. Tang, C. Song, T. Navessin, Z. Shi, D. Song, H. Wang, D.P. Wilkinson, Z.-S. Liu, and S. Holdcroft, *High temperature PEM fuel cells.* Journal of Power Sources, 2006. **160**(2): p. 872-891.

49. Qian, G., D.W. Smith Jr, and B.C. Benicewicz, *Synthesis and characterization of high molecular weight perfluorocyclobutyl-containing polybenzimidazoles (PFCB-PBI) for high temperature polymer electrolyte membrane fuel cells.* Polymer, 2009. **50**(16): p. 3911-3916.

50. Aili, D., M.K. Hansen, C. Pan, Q. Li, E. Christensen, J.O. Jensen, and N.J. Bjerrum, *Phosphoric acid doped membranes based on Nafion®, PBI and their blends - Membrane preparation, characterization and steam electrolysis testing.* International Journal of Hydrogen Energy, 2011. **36**(12): p. 6985-6993.

51. Hansen, M.K., D. Aili, E. Christensen, C. Pan, S.r. Eriksen, J.O. Jensen, J.H. von Barner, Q. Li, and N.J. Bjerrum, *PEM steam electrolysis at 130°C using a phosphoric acid doped short side chain PFSA membrane.* International Journal of Hydrogen Energy, 2012. **37**(15): p. 10992–11000.

52. Nikiforov, A.V., I.M. Petrushina, E. Christensen, A.L. TomÃ¡s-GarcÃa, and N.J. Bjerrum, *Corrosion behaviour of construction materials for high temperature steam electrolysers.* International Journal of Hydrogen Energy, 2011. **36**(1): p. 111-119.

53. Jensen, J.O., V. Bandur, N.J. Bjerrum, S.H. Jensen, S. Ebbesen, M. Mogensen, N. Tophøj, and L. Yde, *Pre-investigation of water electrolysis*,Report 2008, KI DTU,Risø DTU,DONG Energy:PSO-F&U 2006-1-6287.

54. Carmo, M., D.L. Fritz, J. Mergel, and D. Stolten, *A comprehensive review on PEM water electrolysis.* International Journal of Hydrogen Energy, 2013. **38**(12): p. 4901-4934.

55. Trasatti, S., *Physical electrochemistry of ceramic oxides.* Electrochimica Acta, 1991. **36**(2): p. 225-241.

56. Koper, M.T.M. and H.A. Heering, *Comparison of Electrocatalysis and Bioelectrocatalysis of Hydrogen and Oxygen Redox Reactions*, in *Fuel Cell Science: Theory, Fundamentals, and Biocatalysis*, A. Wieckowski and J.K. Nørskov, Editors. 2010, John Wiley & Sons, Inc.

57. Tseung, A.C.C. and S. Jasem, *Oxygen evolution on semiconducting oxides.* Electrochimica Acta, 1977. **22**(1): p. 31-34.

58. Rasiyah, P. and A.C.C. Tseung, *The Role of the Lower Metal Oxide/Higher Metal Oxide Couple in Oxygen Evolution Reactions.* Journal of The Electrochemical Society, 1984. **131**(4): p. 803-808.

59. Rasten, E., *Electrocatalysis in Water Electrolysis with Solid Polymer Electrolyte.*,Thesis in *Department of Materials Technology and Electrochemistry* 2001, Norwegian University of Science and Technology: Trondheim.

60. Comninellis, C. and G.P. Vercesi, *Characterization of DSA-type oxygen evolving electrodes: Choice of a coating.* Journal of Applied Electrochemistry, 1991. **21**(4): p. 335-345.

61. Millet, P., *Water electrolysis using eme technology: electric potential distribution inside a nafion membrane during electrolysis.* Electrochimica Acta, 1994. **39**(17): p. 2501-2506.

62. Trasatti, S., *Electrocatalysis in the anodic evolution of oxygen and chlorine.* Electrochimica Acta, 1984. **29**(11): p. 1503-1512.

63. Sergio, T., *Electrocatalysis by oxides — Attempt at a unifying approach.* Journal of Electroanalytical Chemistry and Interfacial Electrochemistry, 1980. **111**(1): p. 125-131.

64. Owe, L.-E., *Characterization of Iridium Oxides for Acidic Water Electrolysis*,Thesis in *Faculty of Natural Sciences and Technology, Department of Materials Science and Engineering* 2011, Norwegian University of Science and Technology.

65. Balko, E.N. and C.R. Davidson, *Solid solutions of $RuO_2$ and $IrO_2$.* Journal of Inorganic and Nuclear Chemistry, 1980. **42**(12): p. 1778-1781.

66. Kötz, R. and S. Stucki, *Stabilization of $RuO_2$ by $IrO_2$ for anodic oxygen evolution in acid media.* Electrochimica Acta, 1986. **31**(10): p. 1311-1316.

67. Sedlak, J.M., R.J. Lawrance, and J.F. Enos, *Advances in oxygen evolution catalysis in solid polymer electrolyte water electrolysis.* International Journal of Hydrogen Energy, 1981. **6**(2): p. 159-165.

68. Damjanovic, A., A. Dey, and J.O.M. Bockris, *Kinetics of oxygen evolution and dissolution on platinum electrodes.* Electrochimica Acta, 1966. **11**(7): p. 791-814.

69. Bockris, J.O.M., *Kinetics of Activation Controlled Consecutive Electrochemical Reactions: Anodic Evolution of Oxygen.* The Journal of Chemical Physics, 1956. **24**(4): p. 817-827.

70. Trasatti, S. and G. Lodi, *Electrodes of conductive metallic oxides, Part B*1980: Elsevier scientific publishing company.

71. Riddiford, A.C., *Mechanisms for the evolution and ionization of oxygen at platinum electrodes.* Electrochimica Acta, 1961. **4**(2-4): p. 170-178.

72. Scarr, R.F., *The Mechanism of Oxygen Evolution on Nickel, Platinum, and Other Metals and Alloys.* Journal of The Electrochemical Society, 1969. **116**(11): p. 1526-1532.

73. Beer, H.B., *The Invention and Industrial Development of Metal Anodes.* Journal of The Electrochemical Society, 1980. **127**(8): p. 303C-307C.

74. Comninellis, C. and G.P. Vercesi, *Problems in DSA coating deposition by thermal decomposition.* Journal of Applied Electrochemistry, 1991. **21**(2): p. 136-142.

75. Marshall, A., B. Børresen, G. Hagen, S. Sunde, M. Tsypkin, and R. Tunold, *Iridium oxide-based nanocrystalline particles as oxygen evolution electrocatalysts.* Russian Journal of Electrochemistry, 2006. **42**(10): p. 1134-1140.

76. Song, S., H. Zhang, X. Ma, Z. Shao, R.T. Baker, and B. Yi, *Electrochemical investigation of electrocatalysts for the oxygen evolution reaction in PEM water*

*electrolyzers.* International Journal of Hydrogen Energy, 2008. **33**(19): p. 4955-4961.

77. Kadakia, K., M.K. Datta, O.I. Velikokhatnyi, P. Jampani, S.K. Park, P. Saha, J.A. Poston, A. Manivannan, and P.N. Kumta, *Novel (Ir,Sn,Nb)O2 anode electrocatalysts with reduced noble metal content for PEM based water electrolysis.* International Journal of Hydrogen Energy, 2012. **37**(4): p. 3001-3013.

78. Trasatti, S., *Work function, electronegativity, and electrochemical behaviour of metals: III. Electrolytic hydrogen evolution in acid solutions.* Journal of Electroanalytical Chemistry and Interfacial Electrochemistry, 1972. **39**(1): p. 163-184.

79. Laursen, A.B., A.S. Varela, F. Dionigi, H. Fanchiu, C. Miller, O.L. Trinhammer, J. Rossmeisl, and S. Dahl, *Electrochemical Hydrogen Evolution: Sabatier's Principle and the Volcano Plot.* Journal of Chemical Education, 2012. **89**(12): p. 1595-1599.

80. Conway, B.E. and G. Jerkiewicz, *Relation of energies and coverages of underpotential and overpotential deposited H at Pt and other metals to the 'volcano curve' for cathodic H2 evolution kinetics.* Electrochimica Acta, 2000. **45**(25-26): p. 4075-4083.

81. Cheng, J., H. Zhang, H. Ma, H. Zhong, and Y. Zou, *Study of carbon-supported IrO2 and RuO2 for use in the hydrogen evolution reaction in a solid polymer electrolyte electrolyzer.* Electrochimica Acta, 2010. **55**(5): p. 1855-1861.

82. Sheng, W., H.A. Gasteiger, and Y. Shao-Horn, *Hydrogen Oxidation and Evolution Reaction Kinetics on Platinum: Acid vs Alkaline Electrolytes.* Journal of The Electrochemical Society, 2010. **157**(11): p. B1529-B1536.

83. Adams, R. and R.L. Shriner, *Platinum Oxide as a catalyst in the reduction of of organic compounds.III.Preparation and Properties of the oxide of Platinum obtained by the fusion of chloroplatinic acid with sodium nitrate.* Journal of the American Chemical Society, 1923. **45**(9): p. 2171-2179.

84. Marshall, A.T., S. Sunde, M. Tsypkin, and R. Tunold, *Performance of a PEM water electrolysis cell using $Ir_xRu_yTa_zO_2$ electrocatalysts for the oxygen evolution electrode.* International Journal of Hydrogen Energy, 2007. **32**(13): p. 2320-2324.

85. Mamaca, N., E. Mayousse, S. Arrii-Clacens, T.W. Napporn, K. Servat, N. Guillet, and K.B. Kokoh, *Electrochemical activity of ruthenium and iridium based catalysts for oxygen evolution reaction.* Applied Catalysis B: Environmental, 2011. **111-112**(0): p. 376-380.

86. Marshall, A., B. Børresen, G. Hagen, M. Tsypkin, and R. Tunold, *Electrochemical characterization of $Ir_xSn1\text{-}xO_2$ powders as oxygen evolution electrocatalysts.* Electrochimica Acta, 2006. **51**(15): p. 3161-3167.

87. Marshall, A., M. Tsypkin, B. Børresen, G. Hagen, and R. Tunold, *Nanocrystalline $Ir_xSn_{(1-x)}O_2$ Electrocatalysts for Oxygen Evolution in Water Electrolysis with Polymer Electrolyte – Effect of Heat Treatment.* Journal of New Materials for Electrochemical Systems, 2004. **7**(3): p. 197-204.

88. Wu, X., J. Tayal, S. Basu, and K. Scott, *Nano-crystalline $Ru_xSn_{1-x}O_2$ powder catalysts for oxygen evolution reaction in proton exchange membrane water*

*electrolysers.* International Journal of Hydrogen Energy, 2011. **36**(22): p. 14796-14804.

89. Cheng, J., H. Zhang, H. Ma, H. Zhong, and Y. Zou, *Preparation of $Ir_{0.4}Ru_{0.6}Mo_xO_y$ for oxygen evolution by modified Adams' fusion method.* International Journal of Hydrogen Energy, 2009. **34**(16): p. 6609-6613.

90. Papazisi, K.M., A. Siokou, S. Balomenou, and D. Tsiplakides, *Preparation and characterization of IrxPt1−xO2 anode electrocatalysts for the oxygen evolution reaction.* International Journal of Hydrogen Energy, 2012(0).

91. Chenga, J., H. Zhanga, G. Chena, and Y. Zhang, *Study of $Ir_xRu_{1-x}O_2$ oxides as anodic electrocatalysts for solid polymer electrolyte water electrolysis.* Electrochimica Acta, 2009. **54**: p. 6250–6256.

92. Ma, H., C. Liu, J. Liao, Y. Su, X. Xue, and W. Xing, *Study of ruthenium oxide catalyst for electrocatalytic performance in oxygen evolution.* Journal of Molecular Catalysis A: Chemical, 2006. **247**(1–2): p. 7-13.

93. Cheng, J.B., H.M. Zhang, H.P. Ma, H.X. Zhong, and Y. Zou, *Study of carbon-supported IrO2 and RuO2 for use in the hydrogen evolution reaction in a solid polymer electrolyte electrolyzer.* Electrochimica Acta, 2010. **55**(5): p. 1855-1861.

94. Yoshinaga, N., W. Sugimoto, and Y. Takasu, *Oxygen reduction behavior of rutile-type iridium oxide in sulfuric acid solution.* Electrochimica Acta, 2008. **54**(2): p. 566-573.

95. Hutchings, R., K. Müller, R. Kötz, and S. Stucki, *A structural investigation of stabilized oxygen evolution catalysts.* Journal of Materials Science, 1984. **19**(12): p. 3987-3994.

96. Morris, D.F.C. and T.J. Ritter, *Reduction of hexachloroiridate (IV) with borohydride.* Journal of the Less Common Metals, 1978. **59**(2): p. P73-P82.

97. Zheng, J.P., P.J. Cygan, and T.R. Jow, *Hydrous Ruthenium Oxide as an Electrode Material for Electrochemical Capacitors.* Journal of The Electrochemical Society, 1995. **142**(8): p. 2699-2703.

98. Davidson, L., Y. Quinn, and D.F. Steele, *Ruthenium-Mediated Electrochemical Destruction of Organic Wastes.* Platinum metals review, 1998. **42**(3): p. 90-98.

99. Roginskaya, Y.E. and O.V. Morozova, *The role of hydrated oxides in formation and structure of DSA-type oxide electrocatalysts.* Electrochimica Acta, 1995. **40**(7): p. 817-822.

100. Ioroi, T., N. Kitazawa, K. Yasuda, Y. Yamamoto, and H. Takenaka, *Iridium Oxide/Platinum Electrocatalysts for Unitized Regenerative Polymer Electrolyte Fuel Cells.* Journal of The Electrochemical Society, 2000. **147**(6): p. 2018-2022.

101. da Silva, L.A., V.A. Alves, M.A.P. da Silva, S. Trasatti, and J.F.C. Boodts, *Oxygen evolution in acid solution on $IrO_2$ + $TiO_2$ ceramic films. A study by impedance, voltammetry and SEM.* Electrochimica Acta, 1997. **42**(2): p. 271-281.

102. Iwakura, C., K. Hirao, and H. Tamura, *Preparation of ruthenium dioxide electrodes and their anodic polarization characteristics in acidic solutions.* Electrochimica Acta, 1977. **22**(4): p. 335-340.

103. Luxton, T.P., M.J. Eick, and K.G. Scheckel, *Characterization and dissolution properties of ruthenium oxides.* Journal of Colloid and Interface Science, 2011. **359**(1): p. 30-39.

104. Jenkins, R. and R. Snyder, *Introduction to X-Ray Powder Diffractometry*1996: John Wiley and Sons,Inc.

105. Smart, L. and E. Moore, *Solid state chemistry: an introduction*. 3rd ed2005: Taylor & Francis.

106. Cullity, B.D., *Elements of X-ray diffraction*1956, US: Addison-Wesley.

107. Chusuel, C.D. and D.W. Goodman, *X-ray photoelectron spectroscopy*, in *Encyclopedia of physical science and technology* 2002, Academic press. p. 921-938.

108. Hercules, D.M. and S.H. Hercules, *Analytical chemistry of surfaces. Part II. Electron spectroscopy.* Journal of Chemical Education, 1984. **61**(6): p. 483.

109. Reimschuessel, A.C., *Scanning electron microscopy - Part I.* Journal of Chemical Education, 1972. **49**(8): p. A413.

110. Brunauer, S., P.H. Emmett, and E. Teller, *Adsorption of Gases in Multimolecular Layers.* Journal of the American Chemical Society, 1938. **60**(2): p. 309-319.

111. Marshall, A., B. Børresen, G. Hagen, M. Tsypkin, and R. Tunold, *Preparation and characterization of nanocrystalline $Ir_xSn_{1-x}O2$ electrocatalytic powders.* Materials Chemistry and Physics, 2005. **94**(2-3): p. 226-232.

112. Nikiforov, A.V., A.L. Tomás García, I.M. Petrushina, E. Christensen, and N.J. Bjerrum, *Preparation and study of IrO2/SiC-Si supported anode catalyst for high temperature PEM steam electrolysers.* International Journal of Hydrogen Energy, 2011. **36**(10): p. 5797-5805.

113. Espinola, A., P.M. Miguel, M.R. Salles, and A.R. Pinto, *Electrical properties of carbons-resistance of powder materials.* Carbon, 1986. **24**(3): p. 337-341.

114. Celzard, A., J.F. MarÃªchÃ©, F. Payot, and G. Furdin, *Electrical conductivity of carbonaceous powders.* Carbon, 2002. **40**(15): p. 2801-2815.

115. Sánchez-González, J., A. Macías-García, M.F. Alexandre-Franco, and V. Gómez-Serrano, *Electrical conductivity of carbon blacks under compression.* Carbon, 2005. **43**(4): p. 741-747.

116. Pantea, D., H. Darmstadt, S. Kaliaguine, and C. Roy, *Electrical conductivity of conductive carbon blacks: influence of surface chemistry and topology.* Applied Surface Science, 2003. **217**(1â€“4): p. 181-193.

117. Pantea, D., H. Darmstadt, S. Kaliaguine, L. SÃ¼mmchen, and C. Roy, *Electrical conductivity of thermal carbon blacks: Influence of surface chemistry.* Carbon, 2001. **39**(8): p. 1147-1158.

118. Rusling, J.F. and S.L. Suib, *Characterizing Materials with Cyclic Voltammetry.* Advanced Materials, 1994. **6**(12): p. 922-930.

119. Kissinger, P.T. and W.R. Heineman, *Cyclic voltammetry.* Journal of Chemical Education, 1983. **60**(9): p. 702.

120. Van Benschoten, J.J., J.Y. Lewis, W.R. Heineman, D.A. Roston, and P.T. Kissinger, *Cyclic voltammetry experiment.* Journal of Chemical Education, 1983. **60**(9): p. 772.

121. Doña Rodríguez, J.M., J.A. Herrera Melián, and J. Pérez Peña, *Determination of the Real Surface Area of Pt Electrodes by Hydrogen Adsorption Using Cyclic Voltammetry.* Journal of Chemical Education, 2000. **77**(9): p. 1195.

122. Randles, J.E.B., *A cathode ray polarograph. Part II.-The current-voltage curves.* Transactions of the Faraday Society, 1948. **44**: p. 327-338.

123. Jürgen, H., *Cyclic Voltammetry - "Electrochemical Spectroscopy". New Analytical Methods (25).* Angewandte Chemie International Edition in English, 1984. **23**(11): p. 831-847.

124. Nicholson, R.S., *Theory and Application of Cyclic Voltammetry for Measurement of Electrode Reaction Kinetics.* Analytical Chemistry, 1965. **37**(11): p. 1351-1355.

125. Wang, J., *Analytical Electrochemistry*2000: Wiley-VCH.

126. Bott, A.W., *Practical problem in voltammetry-2.Electrode capacitance.* Current seperations, 1993. **12**(1): p. 10-13.

127. Pozio, A., M. De Francesco, A. Cemmi, F. Cardellini, and L. Giorgi, *Comparison of high surface Pt/C catalysts by cyclic voltammetry.* Journal of Power Sources, 2002. **105**(1): p. 13-19.

128. Trasatti, S. and P. Kurzweil, *Electrochemical Supercapacitors as Versatile Energy Stores-Potential use for platinum metals.* Platinum metals review, 1994. **38**(2): p. 46.

129. Ardizzone, S., G. Fregonara, and S. Trasatti, *"Inner" and "outer" active surface of RuO2 electrodes.* Electrochimica Acta, 1990. **35**(1): p. 263-267.

130. Elsen, H.A., *Thermodynamic and Dynamic Investigations of Hydrated Iridium Oxide potentuimetric pH micro-sensors*,Thesis in *Chemistry* 2007, University of California,Berkeley.

131. Conway, B.E., V. Birss, and J. Wojtowicz, *The role and utilization of pseudocapacitance for energy storage by supercapacitors.* Journal of Power Sources, 1997. **66**(1–2): p. 1-14.

132. Shukla, A.K., S. Sampath, and K. Vijayamohanan, *Electrochemical supercapacitors: Energy storage beyond batteries.* CURRENT SCIENCE, 2000. **79**(12): p. 1656-1661.

133. Conway, B.E. and W.G. Pell, *Double-layer and pseudocapacitance types of electrochemical capacitors and their applications to the development of hybrid devices.* Journal of Solid State Electrochemistry, 2003. **7**(9): p. 637-644.

134. Trasatti, S. and G. Buzzanca, *Ruthenium dioxide: A new interesting electrode material. Solid state structure and electrochemical behaviour.* Journal of Electroanalytical Chemistry and Interfacial Electrochemistry, 1971. **29**(2): p. A1-A5.

135. Wen, T.-C. and C.-C. Hu, *Hydrogen and Oxygen Evolutions on Ru-Ir Binary Oxides.* Journal of The Electrochemical Society, 1992. **139**(8): p. 2158-2163.

136. Kong, F.-D., S. Zhang, G.-P. Yin, Z.-B. Wang, C.-Y. Du, G.-Y. Chen, and N. Zhang, *Electrochemical studies of Pt/Ir-IrO2 electrocatalyst as a bifunctional oxygen electrode.* International Journal of Hydrogen Energy, 2011(0).

137. Li, G., H. Yu, X. Wang, S. Sun, Y. Li, Z. Shao, and B. Yi, *Highly effective IrxSn1-xO2 electrocatalysts for oxygen evolution reaction in the solid polymer electrolyte water electrolyser*. Physical Chemistry Chemical Physics, 2013. **15**(8): p. 2858-2866.

138. Tischer, R., *The anodic behavior of gold in phosphoric acid at elevated temperatures.* Fresenius' Zeitschrift für analytische Chemie, 1966. **224**(1): p. 93-99.

139. Xu, C., L. Ma, J. Li, W. Zhao, and Z. Gan, *Synthesis and characterization of novel high-performance composite electrocatalysts for the oxygen evolution in solid polymer electrolyte (SPE) water electrolysis.* International Journal of Hydrogen Energy, 2012. **37**(4): p. 2985-2992.

140. Leimin, X., L. Shijun, Y. Lijun, and L. Zhenxing, *Investigation of a Novel Catalyst Coated Membrane Method to Prepare Low-Platinum-Loading Membrane Electrode Assemblies for PEMFCs.* Fuel Cells, 2009. **9**(2): p. 101-105.

141. Su, H., B.J. Bladergroen, V. Linkov, S. Pasupathi, and S. Ji, *Study of catalyst sprayed membrane under irradiation method to prepare high performance membrane electrode assemblies for solid polymer electrolyte water electrolysis.* International Journal of Hydrogen Energy, 2011. **36**(23): p. 15081-15088.

142. Wikander, K., H. Ekström, A.E.C. Palmqvist, A. Lundblad, K. Holmberg, and G. Lindbergh, *Alternative Catalysts and Carbon Support Material for PEMFC.* Fuel Cells, 2006. **6**(1): p. 21-25.

143. Mayousse, E., F. Maillard, F. Fouda-Onana, O. Sicardy, and N. Guillet, *Synthesis and characterization of electrocatalysts for the oxygen evolution in PEM water electrolysis.* International Journal of Hydrogen Energy, 2011. **36**(17): p. 10474-10481.

144. Song, S., H. Zhang, X. Ma, Z.G. Shao, Y. Zhang, and B. Yi, *Bifunctional oxygen electrode with corrosion-resistive gas diffusion layer for unitized regenerative fuel cell.* Electrochemistry Communications, 2006. **8**(3): p. 399-405.

145. Liu, C.-Y., L.-H. Hu, and C.-C. Sung, *Micro-protective layer for lifetime extension of solid polymer electrolyte water electrolysis.* Journal of Power Sources, 2012. **207**(0): p. 81-85.

146. Li, M.-Q., Z.-G. Shao, and K. Scott, *A high conductivity $Cs_{2.5}H_{0.5}PMo_{12}O_{40}$/polybenzimidazole (PBI)/$H_3PO_4$ composite membrane for proton-exchange membrane fuel cells operating at high temperature.* Journal of Power Sources, 2008. **183**(1): p. 69-75.

147. Yuan, X.-Z., C. Song, H. Wang, and J. Zhang, *Electrochemical Impedance Spectroscopy in PEM Fuel Cells-Fundamentals and Applications*2010: Springer.

148. Owe, L.-E., M. Tsypkin, K.S. Wallwork, R.G. Haverkamp, and S. Sunde, *Iridium–ruthenium single phase mixed oxides for oxygen evolution: Composition dependence of electrocatalytic activity.* Electrochimica Acta, 2012. **70**(0): p. 158-164.

149. Tseung, A.C.C. and S.C. Dhara, *Loss of surface area by platinum and supported platinum black electrocatalyst.* Electrochimica Acta, 1975. **20**(9): p. 681-683.

150. Ma, L., S. Sui, and Y. Zhai, *Preparation and characterization of Ir/TiC catalyst for oxygen evolution.* Journal of Power Sources, 2008. **177**(2): p. 470-477.

151. Lee, K.-S., I.-S. Park, Y.-H. Cho, D.-S. Jung, N. Jung, H.-Y. Park, and Y.-E. Sung, *Electrocatalytic activity and stability of Pt supported on Sb-doped SnO2 nanoparticles for direct alcohol fuel cells.* Journal of Catalysis, 2008. **258**(1): p. 143-152.

152. Chhina, H., S. Campbell, and O. Kesler, *An oxidation-resistant indium tin oxide catalyst support for proton exchange membrane fuel cells.* Journal of Power Sources, 2006. **161**(2): p. 893-900.

153. Roen, L.M., C.H. Paik, and T.D. Jarvi, *Electrocatalytic Corrosion of Carbon Support in PEMFC Cathodes.* Electrochemical and Solid-State Letters, 2004. **7**(1): p. A19-A22.

154. Maillard, F., A. Bonnefont, and F. Micoud, *An EC-FTIR study on the catalytic role of Pt in carbon corrosion.* Electrochemistry Communications, 2011. **13**(10): p. 1109-1111.

155. Sharma, S. and B.G. Pollet, *Support materials for PEMFC and DMFC electrocatalysts-A review*. Journal of Power Sources, 2012. **208**(0): p. 96-119.

156. Avasarala, B. and P. Haldar, *On the stability of TiN-based electrocatalysts for fuel cell applications.* International Journal of Hydrogen Energy, 2011. **36**(6): p. 3965-3974.

157. Sui, S., L. Ma, and Y. Zhai, *Investigation on the proton exchange membrane water electrolyzer using supported anode catalyst.* Asia-Pacific Journal of Chemical Engineering, 2009. **4**(1): p. 8-11.

158. Ignaszak, A., C. Song, W. Zhu, J. Zhang, A. Bauer, R. Baker, V. Neburchilov, S. Ye, and S. Campbell, *Titanium carbide and its core-shelled derivative TiC@TiO2 as catalyst supports for proton exchange membrane fuel cells.* Electrochimica Acta, 2012. **69**(0): p. 397-405.

159. Pierson, H.O., *Handbook of Refractory Carbides and Nitrides-Properties, Characteristics,Processing and Applications*, 1996, Noyes Publications: United States of America.

160. Cowling, R.D. and H.E. Hintermann, *The Anodic Oxidation of Titanium Carbide.* Journal of The Electrochemical Society, 1971. **118**(12): p. 1912-1916.

161. Cowling, R.D. and H.E. Hintermann, *The Corrosion of Titanium Carbide.* Journal of The Electrochemical Society, 1970. **117**(11): p. 1447-1449.

162. J. Polonský, J., I.M. Petrushina, E. Christensen, K. Bouzek, C.B. Prag, J.E.T. Andersen, and N.J. Bjerrum, *Tantalum carbide as a novel support material for anode electrocatalysts in polymer electrolyte membrane water electrolysers.* International Journal of Hydrogen Energy, 2012. **37**(3): p. 2173-2181.

163. Chhina, H., S. Campbell, and O. Kesler, *Thermal and electrochemical stability of tungsten carbide catalyst supports.* Journal of Power Sources, 2007. **164**(2): p. 431-440.

164. Levy, R.B. and M. Boudart, *Platinum-Like Behavior of Tungsten Carbide in Surface Catalysis.* Science, 1973. **181**(4099): p. 547-549.

165. Bennett, L.H., J.R. Cuthill, A.J. McAlister, N.E. Erickson, and R.E. Watson, *Electronic Structure and Catalytic Behavior of Tungsten Carbide*. Science, 1974. **184**(4136): p. 563-565.

166. Hu, F., G. Cui, Z. Wei, and P.K. Shen, *Improved kinetics of ethanol oxidation on Pd catalysts supported on tungsten carbides/carbon nanotubes.* Electrochemistry Communications, 2008. **10**(9): p. 1303-1306.

167. Lee, K., A. Ishihara, S. Mitsushima, N. Kamiya, and K.-i. Ota, *Stability and electrocatalytic activity for oxygen reduction in WC + Ta catalyst.* Electrochimica Acta, 2004. **49**(21): p. 3479-3485.

168. Liu, Y., T.G. Kelly, J.G. Chen, and W.E. Mustain, *Metal Carbides as Alternative Electrocatalyst Supports.* ACS Catalysis, 2013. **3**(6): p. 1184-1194.

169. Antolini, E. and E.R. Gonzalez, *Ceramic materials as supports for low-temperature fuel cell catalysts.* Solid State Ionics, 2009. **180**(9-10): p. 746-763.

170. Weidman, M.C., D.V. Esposito, Y.-C. Hsu, and J.G. Chen, *Comparison of electrochemical stability of transition metal carbides (WC, W2C, Mo2C) over a wide pH range.* Journal of Power Sources, 2012. **202**(0): p. 11-17.

171. Liu, Y. and W.E. Mustain, *Evaluation of tungsten carbide as the electrocatalyst support for platinum hydrogen evolution/oxidation catalysts.* International Journal of Hydrogen Energy, 2012. **37**(11): p. 8929-8938.

172. Avasarala, B. and P. Haldar, *Electrochemical oxidation behavior of titanium nitride based electrocatalysts under PEM fuel cell conditions.* Electrochimica Acta, 2010. **55**(28): p. 9024-9034.

173. Fuentes, R.E., J. Farell, and J.W. Weidner, *Multimetallic Electrocatalysts of Pt, Ru, and Ir Supported on Anatase and Rutile TiO2 for Oxygen Evolution in an Acid Environment.* Electrochemical and Solid-State Letters, 2011. **14**(3): p. E5-E7.

174. Siracusano, S., V. Baglio, C. D'Urso, V. Antonucci, and A.S. Aricò, *Preparation and characterization of titanium suboxides as conductive supports of IrO2 electrocatalysts for application in SPE electrolysers.* Electrochimica Acta, 2009. **54**(26): p. 6292-6299.

175. Chen, G., S.R. Bare, and T.E. Mallouk, *Development of Supported Bifunctional Electrocatalysts for Unitized Regenerative Fuel Cells.* Journal of The Electrochemical Society, 2002. **149**(8): p. A1092-A1099.

176. Shekarchizade, H. and M.K. Amini, *Effect of Elemental Composition on the Structure, Electrochemical Properties, and Ozone Production Activity of Ti/SnO2-Sb-Ni Electrodes Prepared by Thermal Pyrolysis Method.* International Journal of Electrochemistry, 2011. **2011**.

177. Datta, M.K., K. Kadakia, O.I. Velikokhatnyi, P.H. Jampani, S.J. Chung, J.A. Poston, A. Manivannan, and P.N. Kumta, *High performance robust F-doped tin oxide based oxygen evolution electro-catalysts for PEM based water electrolysis.* Journal of Materials Chemistry A, 2013. **1**(12): p. 4026-4037.

178. Mishra, K.C., K.H. Johnson, and P.C. Schmidt, *Electronic structure of antimony-doped tin oxide*. Physical Review B, 1995. **51**(20): p. 13972-13976.

179. Zheng, M. and B. Wang, *One-step synthesis of antimony-doped tin dioxide nanocrystallites and their property.* Transactions of Nonferrous Metals Society of China, 2009. **19**(2): p. 404-409.

180. Liu, T.J., Z.G. Jin, L.R. Feng, and T. Wang, *Conducting antimony-doped tin oxide films derived from stannous oxalate by aqueous sol–gel method.* Applied Surface Science, 2008. **254**(20): p. 6547-6553.

181. Vicent, F., E. Morallo´n, C. Quijada, J.L. Va´zquez, A. Aldaz, and F. Cases, *Characterization and stability of doped SnO2 anodes.* Journal of Applied Electrochemistry, 1998. **28**(6): p. 607-612.

182. Marshall, A. and R. Haverkamp, *Nanoparticles of $IrO_2$ or Sb–$SnO_2$ increase the performance of iridium oxide DSA electrodes.* Journal of Materials Science, 2012. **47**(3): p. 1135-1141.

183. Marshall, A.T. and R.G. Haverkamp, *Electrocatalytic activity of $IrO_2$-$RuO_2$ supported on Sb-doped $SnO_2$ nanoparticles.* Electrochimica Acta, 2010. **55**(6): p. 1978-1984.

184. Haverkamp, R.G., A.T. Marshall, and B.C.C. Cowie, *Energy resolved XPS depth profile of (IrO2, RuO2, Sb2O5, SnO2) electrocatalyst powder to reveal core-shell nanoparticle structure.* Surface and Interface Analysis, 2011. **43**(5): p. 847-855.

185. Yin, M., J. Xu, Q. Li, J.O. Jensen, Y. Huang, L.N. Cleemann, N.J. Bjerrum, and W. Xing, *Highly active and stable Pt electrocatalysts promoted by antimony-doped SnO2 supports for oxygen reduction reactions.* Applied Catalysis B: Environmental, 2014. **144**(0): p. 112-120.

186. Cruz, J.C., S. Rivas, D. Beltran, Y. Meas, R. Ornelas, G. Osorio-Monreal, L. Ortiz-Frade, J. Ledesma-GarcÃa, and L.G. Arriaga, *Synthesis and evaluation of ATO as a support for Pt-$IrO_2$ in a unitized regenerative fuel cell.* International Journal of Hydrogen Energy, 2012. **37**(18): p. 13522-13528.

187. Chen, G., X. Chen, and P.L. Yue, *Electrochemical Behavior of Novel Ti/IrOx−Sb2O5−SnO2 Anodes.* The Journal of Physical Chemistry B, 2002. **106**(17): p. 4364-4369.

188. Chen, Y., H. Zhang, D. Ma, J. Ma, H. Ye, G. Qian, and Y. Ye, *Synthesis, thermal stability, and photocatalytic activity of nanocrystalline titanium carbide.* Materials Research Bulletin, 2011. **46**(11): p. 1800-1803.

189. Lavrenko, V.A., L.A. Glebov, A.P. Pomitkin, V.G. Chuprina, and T.G. Protsenko, *High-temperature oxidation of titanium carbide in oxygen.* Oxidation of Metals, 1975. **9**(2): p. 171-179.

190. Preiss, H., B. Meyer, and C. Olschewski, *Preparation of molybdenum and tungsten carbides from solution derived precursors.* Journal of Materials Science, 1998. **33**(3): p. 713-722.

191. Fuentes, R.E., B.L. García, and J.W. Weidner, *Effect of Titanium Dioxide Supports on the Activity of Pt-Ru toward Electrochemical Oxidation of Methanol.* Journal of The Electrochemical Society, 2011. **158**(5): p. B461-B466.

192. Lodi, G., C. de Asmundis, S. Ardizzone, E. Sivieri, and S. Trasatti, *Resistivity and temperature coefficient of resistivity of ruthenium oxide layers influence of morphology.* Surface Technology, 1981. **14**(4): p. 335-343.

193. Mazúr, P., J. Polonský, M. Paidar, and K. Bouzek, *Non-conductive TiO2 as the anode catalyst support for PEM water electrolysis.* International Journal of Hydrogen Energy, 2012. **37**(17): p. 12081-12088.

194. Xu, J., G. Liu, J. Li, and X. Wang, *The electrocatalytic properties of an IrO2/SnO2 catalyst using SnO2 as a support and an assisting reagent for the oxygen evolution reaction.* Electrochimica Acta, 2011. **59**(0): p. 105-112.

195. Chen, X., G. Chen, and P.L. Yue, *Stable Ti/IrOx−Sb2O5−SnO2 Anode for O2 Evolution with Low Ir Content.* The Journal of Physical Chemistry B, 2001. **105**(20): p. 4623-4628.

196. Galizzioli, D., F. Tantardini, and S. Trasatti, *Ruthenium dioxide: a new electrode material. I. Behaviour in acid solutions of inert electrolytes.* Journal of Applied Electrochemistry, 1974. **4**(1): p. 57-67.

197. Atanasoska, L., R. Atanasoski, and S. Trasatti, *XPS and AES study of mixed layers of $RuO_2$ and $IrO_2$.* Vacuum, 1990. **40**(1-2): p. 91-94.

198. Rubel, M., R. Haasch, P. Mrozek, A. Wieckowski, C. De Pauli, and S. Trasatti, *Characterization of IrO2 • SnO2 thin layers by electron and ion spectroscopies.* Vacuum, 1994. **45**(4): p. 423-427.

199. Chen, R.S., H.M. Chang, Y.S. Huang, D.S. Tsai, S. Chattopadhyay, and K.H. Chen, *Growth and characterization of vertically aligned self-assembled $IrO_2$ nanotubes on oxide substrates.* Journal of Crystal Growth, 2004. **271**(1-2): p. 105-112.

200. Slavcheva, E.P., *Magnetron sputtered iridium oxide as anode catalyst for PEM hydrogen generation.* Macedonian Journal of Chemistry and Chemical Engineering; Vol 30, No 1 (2011), 2011.

201. Rubel, M., R. Haasch, P. Mrozek, A. Wieckowski, C. De Pauli, and S. Trasatti, *Characterization of $IrO_2$-$SnO_2$ thin layers by electron and ion spectroscopies.* Vacuum, 1994. **45**(4): p. 423-427.

202. Zhao, J.S., J.S. Sim, H.J. Lee, D.-Y. Park, and C.S. Hwang, *Investigation of the Deposition Behavior of a Lead Oxide Thin Film on Ir Substrates by Liquid Delivery Metallorganic Chemical Vapor Deposition.* Electrochemical and Solid-State Letters, 2006. **9**(2): p. C29-C31.

203. Hara, M., K. Asami, K. Hashimoto, and T. Masumoto, *An X-ray photoelectron spectroscopic study of electrocatalytic activity of platinum group metals for chlorine evolution.* Electrochimica Acta, 1983. **28**(8): p. 1073-1081.

204. Kötz, R., H. Neff, and S. Stucki, *Anodic Iridium Oxide Films: XPS ‐Studies of Oxidation State Changes and.* Journal of The Electrochemical Society, 1984. **131**(1): p. 72-77.

205. De Pauli, C.P. and S. Trasatti, *Electrochemical surface characterization of $IrO_2$ + $SnO_2$ mixed oxide electrocatalysts.* Journal of Electroanalytical Chemistry, 1995. **396**(1-2): p. 161-168.

206. Sharma, S., A.M. Volosin, D. Schmitt, and D.-K. Seo, *Preparation and electrochemical properties of nanoporous transparent antimony-doped tin oxide (ATO) coatings.* Journal of Materials Chemistry A, 2013. **1**(3): p. 699-706.

207. Owe, L.-E., M. Tsypkin, and S. Sunde, *The effect of phosphate on iridium oxide electrochemistry.* Electrochimica Acta, 2011. **58**(1): p. 231-237.

208. Grupioni, A.A.F., E. Arashiro, and T.A.F. Lassali, *Voltammetric characterization of an iridium oxide-based system: the pseudocapacitive nature of the $Ir_{0.3}Mn_{0.7}O_2$ electrode.* Electrochimica Acta, 2002. **48**(4): p. 407-418.

209. Li, G., H. Yu, X. Wang, S. Sun, Y. Li, Z.-G. Shao, and B. Yi, *Highly effective IrxSn1-xO2 electrocatalysts for oxygen evolution reaction in the solid polymer electrolyte water electrolyser.* Physical Chemistry Chemical Physics, 2012. **15**(8): p. 2858-2866.

210. Dunwoody, D. and J. Leddy, *Proton Exchange Membranes: The View Forward and Back.* The Electrochemical Society Interface, 2005. **14**(3): p. 37-39.

211. Siracusano, S., V. Baglio, A. Di Blasi, N. Briguglio, A. Stassi, R. Ornelas, E. Trifoni, V. Antonucci, and A.S. Aricò, *Electrochemical characterization of single cell and short stack PEM electrolyzers based on a nanosized IrO2 anode electrocatalyst.* International Journal of Hydrogen Energy, 2010. **35**(11): p. 5558-5568.

212. Awasthi, A., K. Scott, and S. Basu, *Dynamic modeling and simulation of a proton exchange membrane electrolyzer for hydrogen production.* International Journal of Hydrogen Energy, 2011. **36**(22): p. 14779-14786.

213. Siracusano, S., V. Baglio, A. Stassi, R. Ornelas, V. Antonucci, and A.S. Aricò, *Investigation of IrO2 electrocatalysts prepared by a sulfite-couplex route for the O2 evolution reaction in solid polymer electrolyte water electrolyzers.* International Journal of Hydrogen Energy, 2011. **36**(13): p. 7822-7831.

214. Cruz, J., V. Baglio, S. Siracusano, R. Ornelas, L. Ortiz-Frade, L. Arriaga, V. Antonucci, and A. Aricò, *Nanosized $IrO_2$ electrocatalysts for oxygen evolution reaction in an SPE electrolyzer.* Journal of Nanoparticle Research, 2011. **13**(4): p. 1639-1646.

215. Polonský, J., I.M. Petrushina, E. Christensen, K. Bouzek, C.B. Prag, J.E.T. Andersen, and N.J. Bjerrum, *Tantalum carbide as a novel support material for anode electrocatalysts in polymer electrolyte membrane water electrolysers.* International Journal of Hydrogen Energy, 2012. **37**(3): p. 2173-2181.

216. Li, H., T. Arita, S. Takami, and T. Adschiri, *Rapid synthesis of tin-doped indium oxide microcrystals in supercritical water using hydrazine as reducing agent.* Progress in Crystal Growth and Characterization of Materials, 2011. **57**(4): p. 117-126.

217. Cho, Y.-S., G.-R. Yi, J.-J. Hong, S.H. Jang, and S.-M. Yang, *Colloidal indium tin oxide nanoparticles for transparent and conductive films.* Thin Solid Films, 2006. **515**(4): p. 1864-1871.

218. Matveeva, E., *Electrochemistry of the Indium-Tin Oxide Electrode in 1 M NaOH Electrolyte.* Journal of The Electrochemical Society, 2005. **152**(9): p. H138-H145.

219. Folcher, G., H. Cachet, M. Froment, and J. Bruneaux, *Anodic corrosion of indium tin oxide films induced by the electrochemical oxidation of chlorides.* Thin Solid Films, 1997. **301**(1–2): p. 242-248.

220. Goebbert, C., H. Bisht, N. Al-Dahoudi, R. Nonninger, M.A. Aegerter, and H. Schmidt, *Wet Chemical Deposition of Crystalline, Redispersable ATO and ITO Nanoparticles.* Journal of Sol-Gel Science and Technology, 2000. **19**(1-3): p. 201-204.

221. Ho, S.I., D.P. Whelan, K. Rajeshwar, A. Weiss, M. Murley, and R. Reid, *Electrocatalytic Modification of Indium Tin Oxide Electrode Surfaces: Surface Analyses and Electrochemistry.* Journal of The Electrochemical Society, 1988. **135**(6): p. 1452-1457.

222. Goebbert, C., R. Nonninger, M.A. Aegerter, and H. Schmidt, *Wet chemical deposition of ATO and ITO coatings using crystalline nanoparticles redispersable in solutions.* Thin Solid Films, 1999. **351**(1–2): p. 79-84.

223. Kyung-Soo, P., C. Young-Jin, K. Jin-Gu, S. Yun-Mo, and P. Jae-Gwan, *The effect of the concentration and oxidation state of Sn on the structural and electrical properties of indium tin oxide nanowires.* Nanotechnology, 2011. **22**(28): p. 285712.

224. Terrier, C., J.P. Chatelon, R. Berjoan, and J.A. Roger, *Sb-doped SnO2 transparent conducting oxide from the sol-gel dip-coating technique.* Thin Solid Films, 1995. **263**(1): p. 37-41.

225. Santana, M.H.P. and L.A. De Faria, *Oxygen and chlorine evolution on $RuO_2 + TiO_2 + CeO_2 + Nb_2O_5$ mixed oxide electrodes.* Electrochimica Acta, 2006. **51**(17): p. 3578-3585.

226. Trasatti, S. and G. Lodi, *Electrodes of conductive metallic oxides, Part A*, ed. S. Trasatti1980: Elsevier Scientific publishing company.

227. Terezo, A.J. and E.C. Pereira, *Preparation and characterization of $Ti/RuO_2$-$Nb_2O_5$ electrodes obtained by polymeric precursor method.* Electrochimica Acta, 1999. **44**(25): p. 4507-4513.

228. Sergio, T., *Physical electrochemistry of ceramic oxides.* Electrochimica Acta, 1991. **36**(2): p. 225-241.

229. Marshall, A., M. Tsypkin, B. Borresen, G. Hagen, and R. Tunold, *Nanocrystalline IrxSn(1-x)O2 electrocatalysts for oxygen evolution in water electrolysis with polymer electrolyte - Effect of heat treatment.* Journal of New Materials for Electrochemical Systems, 2004. **7**(3): p. 197-204.

230. Brumbach, M.T., T.M. Alam, R.H. Nilson, P.G. Kotula, B.B. McKenzie, R.G. Tissot, and B.C. Bunker, *Ruthenium oxide-niobium hydroxide composites for pseudocapacitor electrodes.* Materials Chemistry and Physics, 2010. **124**(1): p. 359-370.

231. Gaudet, J., A.C. Tavares, S. Trasatti, and D. Guay, *Physicochemical Characterization of Mixed $RuO_2$-$SnO_2$ Solid Solutions.* Chemistry of Materials, 2005. **17**(6): p. 1570-1579.

232. Li, B.-s., A. Lin, and F.-x. Gan, *Preparation and electrocatalytic properties of Ti/IrO2-Ta2O5 anodes for oxygen evolution.* Transactions of Nonferrous Metals Society of China, 2006. **16**(5): p. 1193-1199.

233. Di Blasi, A., C. D'Urso, V. Baglio, V. Antonucci, A. Arico', R. Ornelas, F. Matteucci, G. Orozco, D. Beltran, Y. Meas, and L. Arriaga, *Preparation and evaluation of RuO2–IrO2, IrO2–Pt and IrO2Ta2O5 catalysts for the oxygen evolution reaction in an SPE electrolyzer.* Journal of Applied Electrochemistry, 2009. **39**(2): p. 191-196.

234. Zhou, W., Z. Zhou, S. Song, W. Li, G. Sun, P. Tsiakaras, and Q. Xin, *Pt based anode catalysts for direct ethanol fuel cells.* Applied Catalysis B: Environmental, 2003. **46**(2): p. 273-285.

235. Hu, J.M., H.M. Meng, J.Q. Zhang, and C.N. Cao, *Degradation mechanism of long service life Ti/IrO2-Ta2O5 oxide anodes in sulphuric acid.* Corrosion Science, 2002. **44**(8): p. 1655-1668.

236. Hu, J.-M., J.-Q. Zhang, and C.-N. Cao, *Oxygen evolution reaction on IrO2-based DSA® type electrodes: kinetics analysis of Tafel lines and EIS.* International Journal of Hydrogen Energy, 2004. **29**(8): p. 791-797.

237. Xu, L.K. and J.D. Scantlebury, *Microstructure and Electrochemical Properties of IrO[sub 2]-Ta[sub 2]O[sub 5]-Coated Titanium Anodes.* Journal of The Electrochemical Society, 2003. **150**(6): p. B254-B261.

238. Morimitsu, M., R. Otogawa, and M. Matsunaga, *Effects of cathodizing on the morphology and composition of IrO2-Ta2O5/Ti anodes.* Electrochimica Acta, 2000. **46**(2–3): p. 401-406.

239. Comninellis, C. and G.P. Vercesi, *Problems in DSA® coating deposition by thermal decomposition.* Journal of Applied Electrochemistry, 1991. **21**(2): p. 136-142.

240. Vercesi, G.P., J.Y. Salamin, and C. Comninellis, *Morphological and microstructural the Ti/IrO2 · Ta2O5 electrode: effect of the preparation temperature.* Electrochimica Acta, 1991. **36**(5 – 6): p. 991-998.

241. Vercesi, G.P., J.Y. Salamin, and C. Comninellis, *Morphological and microstructural study of the Ti/$IrO_2$-$Ta_2O_5$ electrode: effect of the preparation temperature.* Electrochimica Acta, 1991. **36**(5-6): p. 991-998.

242. Krysa, J., J. Maixner, R. Mraz, and I. Rousar, *Effect of coating thickness on the properties of IrO2–Ta2O5 anodes.* Journal of Applied Electrochemistry, 1998. **28**(3): p. 369-372.

243. Santana, M.H.P., L.A. De Faria, and J.F.C. Boodts, *Investigation of the properties of Ti/[IrO2-Nb2O5] electrodes for simultaneous oxygen evolution and electrochemical ozone production, EOP.* Electrochimica Acta, 2004. **49**(12): p. 1925-1935.

244. Terezo, A.J. and E.C. Pereira, *Fractional factorial design applied to investigate properties of Ti/IrO2-Nb2O5 electrodes.* Electrochimica Acta, 2000. **45**(25-26): p. 4351-4358.

245. Santana, M.H.P., L.A. De Faria, and J.F.C. Boodts, *Investigation of the properties of Ti/[IrO2–Nb2O5] electrodes for simultaneous oxygen evolution and electrochemical ozone production, EOP.* Electrochimica Acta, 2004. **49**(12): p. 1925-1935.

246. Kung, H.H., *Transition metal oxides: Surface Chemistry and Catalysis*. Studies in Surface Science and Catalysis 45, ed. B.D.a.J.T. Yates. Vol. 45. 1989: Elsevier.

247. Santana, M.H.P., L.M. Da Silva, and L.A. De Faria, *Investigation of surface properties of Ru-based oxide electrodes containing Ti, Ce and Nb.* Electrochimica Acta, 2003. **48**(13): p. 1885-1891.

248. Alquier, C., M.T. Vandenborre, and M. Henry, *Synthesis of niobium pentoxide gels.* Journal of Non-Crystalline Solids, 1986. **79**(3): p. 383-395.

249. Robin, A., *Corrosion Behaviour of Niobium in Sodium Hydroxide Solutions.* Journal of Applied Electrochemistry, 2004. **34**(6): p. 623-629.

250. Faria, L.A., J.F.C. Boodts, and S. Trasatti, *Electrocatalytic properties of ternary oxide mixtures of composition $Ru_{0.3}Ti_{(0.7-x)}Ce_xO_2$ oxygen evolution from acidic solution.* Journal of Applied Electrochemistry, 1996. **26**(11): p. 1195-1199.

251. Ardizzone, S., M. Falciola, and S. Trasatti, *Effect of the Nature of the Precursor on the Electrocatalytic Properties of Thermally Prepared Ruthenium Oxide.* Journal of The Electrochemical Society, 1989. **136**(5): p. 1545-1550.

252. Arikado, T., C. Iwakura, and H. Tamura, *Electrochemical behaviour of the ruthenium oxide electrode prepared by the thermal decomposition method.* Electrochimica Acta, 1977. **22**(5): p. 513-518.

253. Kim, H. and B.N. Popov, *Characterization of hydrous ruthenium oxide/carbon nanocomposite supercapacitors prepared by a colloidal method.* Journal of Power Sources, 2002. **104**(1): p. 52-61.

254. Zheng, J.P. and C.K. Huang, *Electrochemical Behavior of Amorphous and Crystalline Ruthenium Oxide Electrodes.* Journal of New Materials for Electrochemical Systems, 2002. **5**(1): p. 41-46.

255. Kötz, R., S. Stucki, D. Scherson, and D.M. Kolb, *In-situ identification of RuO4 as the corrosion product during oxygen evolution on ruthenium in acid media.* Journal of Electroanalytical Chemistry and Interfacial Electrochemistry, 1984. **172**(1–2): p. 211-219.

256. Vuković, M., D. Čukman, M. Milun, L.D. Atanasoska, and R.T. Atanasoski, *Anodic stability and electrochromism of electrodeposited ruthenium-iridium coatings on titanium.* Journal of Electroanalytical Chemistry, 1992. **330**(1–2): p. 663-673.

257. Martelli, G.N., R. Ornelas, and G. Faita, *Deactivation mechanisms of oxygen evolving anodes at high current densities.* Electrochimica Acta, 1994. **39**(11–12): p. 1551-1558.

258. Kötz, R., H.J. Lewerenz, P. Brüesch, and S. Stucki, *Oxygen evolution on Ru and Ir electrodes: XPS-studies.* Journal of Electroanalytical Chemistry and Interfacial Electrochemistry, 1983. **150**(1–2): p. 209-216.

259. Loučka, T., *The reason for the loss of activity of titanium anodes coated with a layer of RuO2 and TiO2.* Journal of Applied Electrochemistry, 1977. **7**(3): p. 211-214.

260. Tamura, H. and C. Iwakura, *Metal oxide anodes for oxygen evolution.* International Journal of Hydrogen Energy, 1982. **7**(11): p. 857-865.

261. Li, Q.F., J.O. Jensen, R.F. Savinell, and N.J. Bjerrum, *High temperature proton exchange membranes based on polybenzimidazoles for fuel cells.* Progress in Polymer Science, 2009. **34**(5): p. 449-477.

262. *Membranes for Energy Conversion*, ed. K.-V. Peinemann and S.P. Nunes. Vol. 2. 2008: WILEY-VCH Verlag GmbH & Co. KGaA, Weinheim. 286.

263. Savinell, *Proton conducting Polymers used as Membranes*, in *US Patent*, U.S. Patent, Editor 1996, Case Western Reserve University: USA. p. 12.

264. Wainright, J.S., J.T. Wang, D. Weng, R.F. Savinell, and M. Litt, *Acid‐Doped Polybenzimidazoles: A New Polymer Electrolyte.* Journal of The Electrochemical Society, 1995. **142**(7): p. L121-L123.

265. Wainright, J.S., J.T. Wang, D. Weng, R.F. Savinell, and M. Litt, *Acid-Doped Polybenzimidazoles: A New Polymer Electrolyte.* Journal of The Electrochemical Society, 1995. **142**(7): p. L121-L123.

266. Ma, Y.L., J.S. Wainright, M.H. Litt, and R.F. Savinell, *Conductivity of PBI Membranes for High-Temperature Polymer Electrolyte Fuel Cells.* Journal of The Electrochemical Society, 2004. **151**(1): p. A8-A16.

267. Saffarian, H., P. Ross, F.E. Behr, and G.L. Gard, *Electrochemical Evaluation of Bis(trifluoromethylsulfonyl) Methane as a Fuel Cell Electrolyte.* Journal of The Electrochemical Society, 1990. **137**(5): p. 1345-1348.

268. Appleby, A.J. and B.S. Baker, *Oxygen Reduction on Platinum in Trifluoromethane Sulfonic Acid.* Journal of The Electrochemical Society, 1978. **125**(3): p. 404-406.

269. Kanamura, K., A. Tanaka, D. Gervasio, V. Kennedy, R. Adzic, E.B. Yeager, D. Burton, and R. Guneratne, *Perfluoro-ethylene-1,2-bis-phosphonic Acid Fuel Cell Electrolyte.* Journal of The Electrochemical Society, 1996. **143**(9): p. 2765-2770.

270. Catalano, J., T. Myezwa, M.G. De Angelis, M.G. Baschetti, and G.C. Sarti, *The effect of relative humidity on the gas permeability and swelling in PFSI membranes.* International Journal of Hydrogen Energy, 2012. **37**(7): p. 6308-6316.

271. Zhang, J., Y. Tang, C. Song, and J. Zhang, *Polybenzimidazole-membrane-based PEM fuel cell in the temperature range of 120-200 °C.* Journal of Power Sources, 2007. **172**(1): p. 163-171.

272. Xing, B.Z. and O. Savadogo, *The effect of acid doping on the conductivity of polybenzimidazole (PBI).* Journal of New Materials for Electrochemical Systems, 1999. **2**(2): p. 95-101.

273. Kawahara, M., J. Morita, M. Rikukawa, K. Sanui, and N. Ogata, *Synthesis and proton conductivity of thermally stable polymer electrolyte: poly(benzimidazole) complexes with strong acid molecules.* Electrochimica Acta, 2000. **45**(8–9): p. 1395-1398.

274. He, R., Q. Che, and B. Sun, *The acid doping behavior of polybenzimidazole membranes in phosphoric acid for proton exchange membrane fuel cells.* Fibers and Polymers, 2008. **9**(6): p. 679-684.

275. Kongstein, O.E., T. Berning, B. Børresen, F. Seland, and R. Tunold, *Polymer electrolyte fuel cells based on phosphoric acid doped polybenzimidazole (PBI) membranes.* Energy, 2007. **32**(4): p. 418-422.

276. Bouchet, R. and E. Siebert, *Proton conduction in acid doped polybenzimidazole.* Solid State Ionics, 1999. **118**(3-4): p. 287-299.

277. Hogarth, M. and X. Glipa, *High temperature membranes for solid polymer fuel cells.*,Report 2001, Johnson Matthey Technology Centre:ETSU F/02/00189/REP

DTI/Pub URN 01/893.

278. Ma, Y., *The Fundamental studies of Polybenzimidazole/Phosphoric Acid Polymer Electrolyte for Fuel cells.*,Thesis 2004, Case Western University.

279. Mamlouk, M., *Investigation of High Temperature Polymer Electrolyte Membrane Fuel Cells.*,Thesis in *School of Chemical Engineering & Advanced Materials.* 2008, Newcastle University: Newcastle. p. 344.

280. Ahmad, J., T.H. Nguyen, and R.T. Foley, *Evaluation of Organic Acids as Fuel Cell Electrolytes.* Journal of The Electrochemical Society, 1981. **128**(11): p. 2257-2261.

281. Sarada, T., R.D. Granata, and R.T. Foley, *Properties of Trifluoromethanesulfonic Acid Monohydrate Pertinent to Its Use as a Fuel Cell Electrolyte.* Journal of The Electrochemical Society, 1978. **125**(12): p. 1899-1906.

282. R.C Bhardwaj, M.A.E., J.O'M.Bockris, *Proton activities in concentrated Phosphoric acid and Trifluoromethane Sulfonic Acid at Elevated Temperature in relation to Acid Fuel cells.* J.Electrochem.Soc., 1990. **137**(7): p. 2070-2076.

283. Adams, A.A. and J.H.J. Barger, *A New Electrolyte for Hydrocarbon Air Fuel Cells.* Journal of The Electrochemical Society, 1974. **121**(8): p. 987-990.

284. Adams, A.A. and R.T. Foley, *The Electrochemical Behavior of Low Molecular Weight Hydrocarbons in Trifluoromethanesulfonic Acid Monohydrate.* Journal of The Electrochemical Society, 1979. **126**(5): p. 775-778.

285. Ross, P.N. and P.C. Andricacos, *The effect of H2PO4- anion on the kinetics of oxygen reduction on Pt.* Journal of Electroanalytical Chemistry and Interfacial Electrochemistry, 1983. **154**(1-2): p. 205-215.

286. Ross, J.P.N., *Evaluation of Tetrafluoroethane-1,2-Disulfonic Acid as a Fuel Cell Electrolyte.* Journal of The Electrochemical Society, 1983. **130**(4): p. 882-885.

287. Saffarian, H., P. Ross, F. Behr, and G. Gard, *Electrochemical Properties of Perfluoroalkane Disulfonic [$HSO_3(CF2)_nSO_3H$] Acids Relevant to Fuel Cell Technology.* Journal of the Electrochemical Society, 1992. **139**(9): p. 2391-2397.

288. Razaq, M., A. Razaq, E. Yeager, D.D. Desmarteau, and S. Singh, *Oxygen electroreduction in perfluorinated sulphonyl imides.* Journal of Applied Electrochemistry, 1987. **17**(5): p. 1057-1064.

289. Fuentes, R.E., S. Rau, T. Smolinka, and J. Weidner, *Ir-Ru Supported Electrocatalysts for Oxygen Evolution Reaction in a PEM Water Electrolyzer.* ECS Meeting Abstracts, 2011. **1101**(30): p. 1654-1654.

290. Rebert, N., B.G. Ateya, T. Poweigha, and L.G. Austin, *Some Electrochemical Properties of Strong Organic Acids for Use as Fuel Cell Electrolytes: Methane Sulfonic, Methane Di-sulfonic, Trichloroacetic, Chloro-Difluoroacetic, Pentafluoropropanoic, Benzoic, and Benzene Sulfonic Acids.* Journal of The Electrochemical Society, 1980. **127**(12): p. 2641-2646.

291. Scudiero, L. *X-Ray Photoelectron Spectroscopy (XPS)-2*. Available from: http://public.wsu.edu/~scudiero/documents/571-XPS-Lecture2_003.pdf.

292. Veal, B.W. and A.P. Paulikas, *Final-state screening and chemical shifts in photoelectron spectroscopy.* Physical Review B, 1985. **31**(8): p. 5399-5416.

293. *Accagen*. Available from: http://www.accagen.com/.

294. *Hydrogenics*. Available from: http://hydrogenics.com/home.

295. *Protonsite*. Available from: http://www.protononsite.com/.

296. *On-site Electrolysis*. Available from: http://www.ika.rwth-aachen.de/r2h/index.php/On-site_Electrolysis.

297. *NEL Hydrogen*. Available from: http://www.nel-hydrogen.com/home/?pid=54.

298. *Giner*. Available from: http://www.ginerinc.com/.

299. *H-TEC SYSTEMS GmbH*. Available from: http://www.h-tec.com/en/systems/home/.